# The Physics Case and Proposed Detector Technologies for MINERvA, a High Statistics Neutrino Scattering Experiment Using a Fine-grained Detector in the NuMI Beam

*23 December 2004*

**Abstract**

The NuMI facility at Fermilab will provide an extremely intense beam of neutrinos for the MINOS neutrino-oscillation experiment. The spacious and fully-outfitted MINOS near detector hall will be the ideal venue for a high-statistics, high-resolution $\nu$ and $\nu$–nucleon/nucleus scattering experiment. The experiment described here will measure neutrino cross-sections and probe nuclear effects essential to present and future neutrino-oscillation experiments. Moreover, with the high NuMI beam intensity, the experiment will either initially address or significantly improve our knowledge of a wide variety of neutrino physics topics of interest and importance to the elementary-particle and nuclear-physics communities.

# The MINER$\nu$A Collaboration


D. Drakoulakos, P. Stamoulis, G. Tzanakos, M. Zois
*University of Athens; Athens, Greece*

D. Casper, J. Dunmore, C. Regis, B. Ziemer
*University of California, Irvine; Irvine, California, USA*

E. Paschos
*University of Dortmund, Dortmund, Germany*

D. Harris, M. Kostin, J.G. Morfín*, P. Shanahan
*Fermi National Accelerator Laboratory; Batavia, Illinois, USA*

M.E. Christy, W. Hinton, C.E. Keppel[1]
*Hampton University; Hampton, Virginia, USA*

R. Burnstein, O. Kamaev, N. Solomey
*Illinois Institute of Technology; Chicago, Illinois, USA*

S. Kulagin
*Institute for Nuclear Research, Moscow, Russia*

W.K. Brooks, A. Bruell, R. Ent, D. Gaskell, W. Melnitchouk, S.A. Wood
*Thomas Jefferson National Accelerator Facility; Newport News, Virginia, USA*

I. Niculescu, G. Niculescu
*James Madison University, Harrisonburg, Virginia, USA*

G. Blazey, M.A.C. Cummings, V. Rykalin
*Northern Illinois University; DeKalb, Illinois, USA*

S. Boyd, D. Naples, V. Paolone
*University of Pittsburgh; Pittsburgh, Pennsylvania, USA*

A. Bodek, H. Budd, J. Chvojka, P. deBarbaro, S. Manly, K. McFarland*, I. Park, W. Sakumoto, R. Teng
*University of Rochester; Rochester, New York, USA*

R. Gilman, C. Glashausser, X. Jiang, G. Kumbartzki, R.D. Ransome
*Rutgers, The State University of New Jersey; Piscataway, New Jersey, USA*

H. Gallagher, T. Kafka, W.A. Mann, W. Oliver
*Tufts University; Boston, Massachusetts, USA*

A. Chakravorty
*St. Xavier College, Chicago, Illinois, USA*

[1] Also at Thomas Jefferson National Accelerator Facility
* Co-spokespersons

# Contents

**List of Figures** ix

**List of Tables** xiii

**I Physics Motivation and Goals** 1

**1 Neutrino Scattering and Long-Baseline Oscillation Experiments** 3
1.1 Introduction . . . 3
1.2 $\nu_\mu$ Disappearance . . . 3
1.2.1 Kinematic neutrino energy recontruction . . . 4
1.2.2 Calorimetric neutrino energy reconstruction . . . 5
1.3 $\nu_e$ Appearance . . . 7
1.3.1 Signal and backgrounds . . . 7
1.3.2 Cross-section uncertainties with a near detector . . . 8
1.4 Conclusions . . . 10

**2 Quasi-Elastic Scattering** 11
2.1 Introduction . . . 11
2.2 Nucleon Form-factors in Quasi-elastic Scattering . . . 11
2.2.1 Vector form-factors . . . 11
2.2.2 Axial form-factor . . . 12
2.2.3 Physics of vector and axial form-factors . . . 13
2.2.4 Quark/hadron and local duality . . . 14
2.2.5 Axial form-factor measurement in MINER$\nu$A . . . 14
2.2.6 Results . . . 16
2.3 Nuclear Effects in Quasi-elastic Scattering . . . 19
2.3.1 Fermi gas model . . . 19
2.3.2 Bound nucleon form-factors . . . 20
2.3.3 Intra-nuclear rescattering . . . 20

**3 Coherent Pion Production** 21
3.1 Introduction . . . 21
3.2 Theory . . . 22
3.3 Experimental Studies of Coherent Production . . . 22
3.3.1 Charged-current cross-section . . . 23
3.3.2 A-dependence of the coherent cross-section . . . 26
3.3.3 Neutral-current cross-section . . . 27

**4 Resonant Pion Production** 31
4.1 Introduction . . . 31
4.2 Analysis of Existing Data . . . 31
4.3 MINER$\nu$A Performance . . . 32
4.4 Conclusion . . . 33

**5 Strange and Charm Particle Production** **37**
5.1 Backgrounds to Nucleon Decay . . . 37
5.2 Measurement of $\sigma(\nu\Lambda K^+)$ . . . 37
5.3 Strangeness-changing Neutral Currents . . . 37
5.4 Hyperon Beta-decay and Exotic Quark States . . . 38
5.5 Charm Production . . . 38

**6 Perturbative/Non-Perturbative Interface** **39**
6.1 Quark/Hadron Duality . . . 39
6.2 Structure Functions . . . 41
6.2.1 Measurement of $xF_3$ . . . 41
6.2.2 High $x_{Bj}$ measurements . . . 43
6.3 Testing Lattice QCD . . . 45
6.4 Summary . . . 46

**7 Generalized Parton Distributions** **47**
7.1 The Nucleon Spin Puzzle and GPDs . . . 47
7.2 Deeply-virtual Compton Scattering . . . 47
7.3 Measurement of GPDs in MINER$\nu$A . . . 49

**8 Nuclear Effects in Neutrino Scattering** **51**
8.1 Introduction . . . 51
8.2 Modified Interaction Probabilities . . . 51
8.2.1 Nuclear effects in the incoherent regime at large $x$ . . . 52
8.2.2 Nuclear effects at small $x$ . . . 53
8.2.3 Determination of $\sin^2\theta_W$ . . . 55
8.3 Final-state Interactions . . . 56
8.3.1 Overview . . . 56
8.3.2 Nuclear transparency . . . 58
8.4 Nuclear Effects in MINER$\nu$A . . . 58
8.4.1 Measuring modified interaction probabilities . . . 59
8.4.2 Measuring final state interactions . . . 59

**II The MINER$\nu$A Project** **63**

**9 NuMI Beam and Hall** **65**
9.1 The MINOS Near Detector Hall . . . 65
9.1.1 Utilities . . . 65
9.1.2 Detector placement . . . 66
9.1.3 Impact on MINOS . . . 66
9.2 The NuMI Beam and MINER$\nu$A Event Sample . . . 69
9.2.1 Energy options . . . 69
9.2.2 MINER$\nu$A event rates . . . 70
9.2.3 Baseline MINOS run plan . . . 70
9.2.4 Precision of neutrino flux prediction . . . 71

**10 The MINER$\nu$A Detector** **73**
10.1 Overview of Detector Design . . . 73
10.2 Scintillator . . . 78
10.2.1 Scintillator extrusions . . . 78
10.2.2 Wavelength-shifting fibers . . . 79
10.2.3 Scintillator plane design . . . 81
10.2.4 Scintillator plane assembly . . . 83
10.3 Detector Modules . . . 84
10.3.1 Module frames . . . 84
10.3.2 Calorimeters . . . 85
10.3.3 Module assembly . . . 86
10.3.4 Module response mapping . . . 86
10.3.5 Detector stand . . . 89
10.3.6 Module installation . . . 89
10.4 Magnetic Coil . . . 90
10.4.1 Manufacture and installation . . . 92
10.4.2 Cooling systems . . . 93
10.4.3 Power system . . . 94
10.4.4 Magnetic calibration . . . 94
10.5 PMT's, Optical Boxes and Cables . . . 94
10.5.1 Multi-anode PMT's . . . 94
10.5.2 PMT testing . . . 96
10.5.3 PMT optical boxes . . . 97
10.5.4 Fiber connectors and optical cables . . . 101
10.6 Electronics . . . 102
10.6.1 Electronics overview . . . 102
10.6.2 Front-end electronics . . . 103
10.6.3 Data acquisition and slow control . . . 107
10.7 Power and Safety Systems . . . 109
10.7.1 Quiet power . . . 109
10.7.2 Magnet power supply . . . 110
10.7.3 Power distribution . . . 110
10.7.4 Safety considerations . . . 110

**11 Detector Simulation and Performance** **113**
11.1 Event Generators . . . 113
11.2 Detector Response Simulation . . . 116
11.2.1 GNuMI flux interface . . . 116
11.2.2 Event generator interface . . . 116
11.2.3 Geometry . . . 116
11.2.4 Hits and digitizations . . . 117
11.2.5 Photon transport . . . 117
11.3 Optical Simulation . . . 117
11.4 Performance of Reconstruction Algorithms . . . 119
11.4.1 Pattern recognition . . . 119

11.4.2 Coordinate reconstruction . . . . . 120
11.4.3 Track reconstruction . . . . . 120
11.4.4 Vertex reconstruction . . . . . 122
11.4.5 Particle identification . . . . . 122
11.4.6 Energy reconstruction and containment . . . . . 124
11.4.7 Event categorization . . . . . 128
11.5 R&D Studies . . . . . 128
11.5.1 Scintillator extrusions . . . . . 129
11.5.2 Optical fibers . . . . . 129
11.5.3 Front-end prototype . . . . . 131
11.5.4 Vertical-slice test . . . . . 131

# List of Figures


1 Nuclear effects on calorimetric neutrino energy reconstruction . . . 7
2 Effect of neutrino scattering uncertainties in MINOS . . . 8
3 NO$\nu$A statistical and systematic errors . . . 10
4 BPA-2003 fits to $G_E^p/G_D$ . . . 12
5 Form-factor contributions to quasi-elastic scattering in MINER$\nu$A. . . . 13
6 Simulated charged-current quasi-elastic interaction . . . 15
7 Cuts for low- and high-$Q^2$ quasi-elastic events . . . 16
8 Quasi-elastic neutrino cross-sections . . . 17
9 Extraction of $F_A$ in MINER$\nu$A . . . 18
10 Suppression of bound cross-sections in Fermi gas model . . . 19
11 Charged-current coherent scattering cross-sections . . . 21
12 Topological and kinematic quantities for coherent signal and background . . . 25
13 MINER$\nu$A coherent scattering measurements and existing data . . . 26
14 Simulated neutral-current $\pi^0$-production event . . . 27
15 Backgrounds to coherent $\pi^0$ production . . . 28
16 Selection of neutral-current single-$\pi^0$ production . . . 29
17 Angular distribution of neutral-current single-$\pi^0$ sample . . . 30
18 Fits to BNL resonant cross-section $d\sigma/dQ^2$ . . . 32
19 Correlation of reconstructed $W$ and $Q^2$ with true quantities . . . 33
20 Resolution of $W$ and $Q^2$ for charged-current resonant events . . . 34
21 True and reconstructed $W$ distributions for resonant pion production . . . 35
22 Existing $xF_3$ data, and expected MINER$\nu$A results . . . 39
23 $F_2$ vs. $\xi$, illustrating quark/hadron duality . . . 40
24 Variation in $xF_3$ due to $Q^2$ resolution . . . 42
25 $F_2$ data compared to fits . . . 43
26 Ratio of nuclear and deuterium cross-sections vs. $\xi$ . . . 46
27 Forward virtual Compton and "Handbag" diagrams . . . 48
28 The DVCS process and interfering diagrams . . . 48
29 Reactions sensitive to GPDs in neutrino scattering. . . . 48
30 Ratio of iron to deuterium structure functions . . . 52
31 Ratio of iron to nucleon and lead to carbon structure functions . . . 55
32 Ratio of lead to carbon structure functions for two models . . . 56
33 Pion absorption cross-sections for different nuclei . . . 57
34 Event samples for nuclear interaction probability study . . . 59
35 Multiplicity variation with different nuclear absorption . . . 60
36 Fractional change in multiplicity for different nuclear absorption . . . 61
37 Fractional change in visible hadron energy with pion absorption . . . 62
38 Isometric view of MINER$\nu$A . . . 66
39 Plan view of MINER$\nu$A . . . 67
40 Front view of MINER$\nu$A . . . 68
41 Layout of NuMI beamline components and near detector hall (not to scale). . . . 69
42 Charged-current interaction spectra for the LE, sME and sHE beams . . . 70
43 Side view schematic of MINER$\nu$A detector . . . 74

44 Outline of MINER$\nu$A . . . 74
45 View of downstream active detector region . . . 75
46 View of an upstream active detector module . . . 76
47 View of an upstream hadron calorimeter module . . . 76
48 View of a downstream hadron calorimeter module . . . 77
49 View of an upstream electromagnetic calorimeter module . . . 77
50 View of a downstream electromagnetic calorimeter module . . . 78
51 Specification for MINER$\nu$A inner-detector scintillator extrusions . . . 79
52 Prototype scintillator extrusion die for MINER$\nu$A . . . 80
53 Prototype MINER$\nu$A scintillator bars . . . 80
54 Setup for fiber polishing . . . 81
55 Schematic of a full (inner + outer) detector plane . . . 82
56 Schematic cross-section of an inner-detector plane . . . 82
57 Schematic cross-section of an outer-detector plane . . . 82
58 Schematic of one tower showing scintillator placement. . . . 84
59 Module assembly work for MINOS at the New Muon Lab . . . 87
60 The MINOS source scanner . . . 88
61 Expected magnetic field map . . . 90
62 Magnetic field in a radial slice . . . 91
63 Cross-section of an aluminum conductor element . . . 91
64 Cross-section of a MINOS coil plank . . . 92
65 Complete MINOS coil planks with lap joint end pieces . . . 93
66 Schematic of MINOS PMT test stand and electronics . . . 96
67 Front view of a MINOS “Alner” PMT box . . . 99
68 Rear view of a MINOS “Alner” PMT box . . . 100
69 Interior of a MINOS “Alner” PMT box . . . 100
70 DDK optical connector parts . . . 101
71 Light-tight boot for DDK connectors . . . 102
72 Simplified schematic of the front end electronics final board. . . . 104
73 Simplified schematic of the front end electronics of the TRiP chip. . . . 105
74 Existing charged-current $\nu_\mu$ cross-section data . . . 114
75 Total neutrino and anti-neutrino cross-sections . . . 115
76 Relative light collection efficiency across the scintillator strips . . . 118
77 Relative light yields for different strip widths and fiber diameters . . . 119
78 Light yield vs. distance along MINER$\nu$A scintillator strips . . . 120
79 Tracking performance for muons from quasi-elastic interactions . . . 121
80 Vertex resolution for charged-current quasi-elastic interactions . . . 122
81 Topological electron/$\gamma$ separation in MINER$\nu$A . . . 123
82 $dE/dx$ vs. range from stopping point for $\pi^\pm$, $K^\pm$ and protons . . . 125
83 Particle identification performance for stopping tracks, using $dE/dx$. . . . 126
84 Fraction of hadronic energy escaping detector . . . 127
85 Probability of visible hadronic energy leakage. . . . 128
86 Fit and resolution of $E_h$ determination . . . 129
87 Prototype readout board . . . 131
88 Schematic of vertical slice test readout . . . 132

89 Measured single-pe peak . . . . . 133
90 Vertical slice test noise measurement . . . . . 133
91 Measured cosmic-ray light yields . . . . . 134

# List of Tables


1 Signal and background processes in NO$\nu$A . . . . . 9
2 Efficiency and purity vs. $Q^2$ for quasi-elastic analysis . . . . . 18
3 Existing data on coherent pion production . . . . . 23
4 Coherent scattering cuts . . . . . 25
5 Event rates for exclusive strangeness production reactions in MINER$\nu$A . . . . . 38
6 MINER$\nu$A charged-current interaction rates . . . . . 70
7 Hypothetical four-year proton luminosity scenario . . . . . 71
8 MINER$\nu$A samples for different reaction types . . . . . 71
9 Electronics design requirements and parameters for MINER$\nu$A . . . . . 103
10 MINER$\nu$A front-end board channel summary. . . . . 104
11 Parts count for MINER$\nu$A electronics design . . . . . 109
12 R&D results for 1.2 mm optical fibers . . . . . 130
13 R&D results for 1.5 mm optical fibers . . . . . 130

# Part I
# Physics Motivation and Goals

# 1 Neutrino Scattering and Long-Baseline Oscillation Experiments

The field of oscillation physics is about to make an enormous leap forward in statistical precision: first with MINOS in the coming year, and later in T2K and the proposed NO$\nu$A experiment. Unfortunately, our relatively poor understanding of neutrino interaction physics in the relevant energy range of these experiments gives rise to systematic uncertainties that could be as large as, or even larger than, their corresponding statistical uncertainties. We have studied the origin of some of these systematic effects, and how MINER$\nu$A's measurements can reduce them to well below the statistical level.

## 1.1 Introduction

Over the past five years the field of neutrino oscillation has moved from seeing decades-old anomalies in cosmic ray [1] and solar [2] neutrino data to powerful cross checks of these anomalies (SNO data [3] and angular distributions in atmospheric neutrino data [4]), and most recently to terrestrial confirmation of the oscillation hypothesis (Kamland [5] and K2K [6]). The next steps in this field are to move to precision measurement of the mass splittings and mixing angles already observed, and search for other non-zero off-diagonal elements in the neutrino mixing matrix.

New, extremely-intense beams being built or planned will greatly increase the statistical reach and ultimate measurement precision for oscillation parameters. With these tremendous improvements in statistical accuracy, however, come new concerns about systematic uncertainties that until now have been a secondary concern. In particular, uncertainties in neutrino cross-sections and nuclear effects lead to systematic uncertainty in the extraction of mixing parameters. Although near detectors are a critical part of precision long-baseline oscillation measurements, they are often ill-suited to make the needed cross-section measurements because they tend to be similar to the coarse and massive far detectors. A near detector can at best constrain the convolution of the near flux, cross-section and detection efficiency. Uncertainties on all of these quantities must be incorporated into the analysis. The cross-section uncertainties we consider are only a subset of the whole, but when flux and efficiency are also taken into account, near-detector performance must be worse than we estimate here.

This chapter is divided into two sections. The first addresses uncertainties relevant for $\nu_\mu$ disappearance experiments, whose aim is to precisely measure the mass splitting $\Delta m^2_{23}$, and the mixing angle which has already been determined to be large, $\theta_{23}$. To achieve these goals the experiments must measure oscillation probabilities as a function of neutrino energy. Two important concerns here are uncertainties in charged-current inelastic processes, and the scale of nuclear effects. Both inelastic channels and the nuclear environment alter the relationship between the true and measured neutrino energies. The second section discusses searches for $\nu_e$ appearance, which if observed at accelerator energies would indicate a non-zero value of $\theta_{13}$ or more exotic new physics. Because the size of the signal is unknown, the final sample may be dominated by signal (charged-current) cross-sections, and/or background (neutral- and charged-current) processes. In both cases, the experiments of the past are inadequate to precisely predict the far detector event samples.

## 1.2 $\nu_\mu$ Disappearance

Precision measurement of the mass splitting between two neutrino eigenstates requires analysis of the oscillation probability as a function of neutrino energy ($E_\nu$) divided by baseline ($L$). The muon neutrino disappearance probability (in the standard 3-generation oscillation parameterization [7]) is

$$P(\nu_\mu \to \nu_\mu) = 1 - \cos^4\theta_{13}\sin^2 2\theta_{23}\sin^2\left(\frac{1.27\Delta m^2_{23}(eV^2)L(km)}{E_\nu(GeV)}\right) - ... \quad (1)$$

where the additional terms are $\mathcal{O}(\sin^2 2\theta_{13})$ or smaller. Currently $\Delta m^2_{23}$ is known to within a factor of two and $\cos^4\theta_{13}\sin^2 2\theta_{23}$ must be larger than 0.9, at 90% confidence level [8]. Since $\sin^2 2\theta_{13}$ has been constrained below 0.1 by the CHOOZ reactor experiment[9], this means $\sin^2 2\theta_{23}$ itself is very close to 1. The fact that $\theta_{23}$ is close to $45°$ has been cited as a hint of the underlying symmetry that generates neutrino mass and mixing. Precise measurement of this angle is important because the level at which the mixing deviates from maximal may again give hints about the mechanisms responsible for the breaking that symmetry [10].

More precise measurements of $\Delta m^2_{23}$ are required to extract mixing angles from eventual $\nu_e$ appearance experiments. The challenge of $\Delta m^2_{23}$ lies in measuring the true neutrino energy in both near and far detectors. Even if the two detectors have an identical design, any uncertainty in the "neutrino energy scale" of the $\nu_\mu$ charged-current signal translates directly into an uncertainty in the extracted value of $\Delta m^2_{23}$.

There are two different ways of measuring neutrino energies: kinematic or calorimetric reconstruction. We discuss both techniques here, and then explain how uncertainties in neutrino interactions lead to energy scale uncertainties and ultimately $\Delta m^2_{23}$ uncertainties.

The first experiment to provide a precision measurement of $\Delta m^2_{23}$ will be MINOS [11], which will start taking data early in 2005. MINOS will use both far and near detectors, which are magnetized steel-scintillator calorimeters with 2.54 cm longitudinal segmentation. The transverse segmentation of the 1 cm thick scintillator planes is 4 cm. MINOS will use Fermilab's NuMI beam, with a baseline of 735 km, which can provide a variety of broad-band neutrino spectra. In its lowest-energy configuration, where MINOS expects to do most of its running, the peak neutrino energy in the $\nu_\mu$ interaction spectrum is about 3.5 GeV.

T2K will use Super-Kamiokande, a water Cherenkov detector, and focus on single-ring muon-like events, for which the neutrino energy is reconstructed kinematically under the hypothesis of two-body scattering. T2K will use a narrow band off-axis neutrino beam from J-PARC in Tokai, whose peak flux is close to 700 MeV, and which originates some 295 km away [13]. The design of the near detectors has not been finalized, but should include a fine-grained tracker and a water Cherenkov detector.

The proposed NO$\nu$A experiment will use a calorimetric detector to improve measurement of $\Delta m^2_{23}$. Because NO$\nu$A is optimized for $\nu_e$ appearance rather than $\nu_\mu$ disappearance, it will use near and far calorimeters made of scintillator planes interspersed with particle board or other scintillator planes. The longitudinal segmentation should be about 1/3 to 1/6 of a radiation length, and the transverse segmentation of the scintillator will be about 4 cm[12]. NO$\nu$A will also use the NuMI beam, but will place its detectors 12–14 mrad off the beam axis, to receive a narrow-band neutrino spectrum. NO$\nu$A with a baseline of 810 km, will run with a peak neutrino energy of about 2 GeV.

### 1.2.1 Kinematic neutrino energy recontruction

Kinematic reconstruction assumes that a given event was produced by a particular process (for example, quasi-elastic scattering) and determines the neutrino energy based on a sufficiently constraining subset of the final-state particles under that hypothesis.

This technique is well-suited to water Cherenkov detectors, which perform best for single-ring topologies. In Super-Kamiokande detector, for example, the $\nu_\mu$ charged-current signal consists of

single-ring, muon-like events, which are primarily quasi-elastic interactions. The energy of the incoming neutrino in that case can be determined using only the outgoing muon momentum ($p_\mu$) and direction ($\theta_\mu$):

$$E_\nu = \frac{m_N E\mu - m_\mu^2/2}{m_N - E_\mu + p_\mu \cos\theta_\mu} \tag{2}$$

Since the absolute energy scale for muons can be fixed to within 2–3% by a variety of calibration techniques [107], and the reconstruction algorithms measure ring directions extremely well, it seems plausible that the neutrino energy scale could be determined with comparable precision. However, not all events producing a single muon-like ring are quasi-elastic interactions. Resonant excitation, and even deep-inelastic scattering, where pions are absorbed in the oxygen nucleus or emerge below Cherenkov threshold can lead to the same topology. Such events will have a reconstructed energy well below the true neutrino energy, because the recoiling hadronic mass is larger than assumed. The effect of this inelastic background could be corrected, if the energy-dependent ratio of quasi-elastic and resonant cross-sections were perfectly known, but since it is not, an uncertainty in the effective neutrino energy scale of the detector results.

Because the $\nu_\mu$ disappearance probability is nearly 100% for T2K, the relative abundance of quasi-elastic and inelastic events will be very different at Super–K than for the unoscillated beam sampled by a near detector.

Precision measurement of the differential cross-sections for single- and multi-pion production, as a function of neutrino energy, will reduce uncertainties in the subtraction of inelastic background, improving T2K's neutrino energy resolution, and ultimately the precision of its oscillation measurements. Since the event samples are so different between near and far detectors, and because water Cherenkov technology cannot entirely eliminate the inelastic background, additional measurements with fine-grained detectors are required. Ideally, these measurements would include not only exclusive inelastic reactions, but also quasi-elastic scattering, with a well-modeled efficiency relative to the inelastic channels. Because the reconstructed energy for inelastic background is lower than the true neutrino energy (the background "feeds down"), it is essential to measure these cross-sections both at and above the T2K beam energy. Chapters 2 and 4 discuss MINER$\nu$A's measurements of quasi-elastic and resonant cross-sections.

### 1.2.2 Calorimetric neutrino energy reconstruction

At neutrino energies above 1 GeV, calorimetric energy reconstruction is more efficient than kinematic reconstruction. In a low-threshold calorimetric device, the reconstructed or visible neutrino energy is simply the sum of all observed secondary particles' energies. For a $\nu_\mu$ charged-current interaction, the muon energy can be determined by measuring its momentum by either range or curvature (if the calorimeter is magnetized), and the remaining activity can be summed to estimate the hadron energy. Scintillating calorimeters have a lower charged-pion detection threshold than Cherenkov detectors, so more of the total kinetic energy is visible for multi-pion interactions, which dominate the cross-section above a few GeV. As a result, neutrino energy reconstruction is less susceptible to bias from inelastic reactions than Cherenkov detectors.

For MINOS, the absolute energy scale for muons is fixed by knowledge of the steek plate thickness and muon energy loss processes. The thickness of each plate has been measured to better than 0.1% and they vary with an RMS of 0.4% [108]. In a muon test beam at CERN a 2% absolute scale calibration

was achieved [109]. The hadronic and electromagnetic energy scales have been calibrated with test beams on a prototype detector at CERN, and have been measured relative to the muon scale within better than 5% [110, 111]. It is still necessary to translate from the raw response to pions and muons to the energy of interacting neutrinos, however.

At neutrino energies of a few GeV and below, three effects become significant in translation between visible and and neutrino energies. Uncertainties in these effects must be understood and included in any precise measurement of $\Delta m^2_{23}$. One effect, independent of the target nucleus, is the rest masses of the secondary charged pions. Since MINOS lacks the granularity to measure the multiplicity of final state particles, a hadron-energy dependent multiplicity distribution must be assumed. The second and third effects are due to secondary particle scattering or complete absorption in the nucleus. All three effects reduce the visible hadronic energy, which in turn lowers the reconstructed neutrino energy. Importance of these effects grows larger as the parent neutrino energy decreases,[76] due to strong enhancement of the pion–nucleon cross-section near the $\Delta(1232)$ resonace [113].

To quantify the magnitude of nuclear effects on measurement of $\Delta m^2_{23}$ in a MINOS-like detector, a simple detector simulation was combined with the NEUGEN event generator [114] and NuMI fluxes at 735 km [115]. In this simulation the visible energy is simply defined as the sum of kinetic energies for all charged final-state particles, plus the total energy for the neutral pions, and photons, which are assumed to deposit all their energy as electromagnetic showers.

Figure 1 shows the variation of the ratio of visible to total neutrino energy for changes in nuclear absorption and scattering separately. In the plot on the left the target is assumed to be steel, and the parameter controlling pion absorption is set to zero or doubled. In the plot on the right all pion absorption is turned off, and the differences that remain are due to rescattering effects in steel, carbon, and lead. These rescattering effects have not been measured with neutrinos on high $Z$ nuclei, so the rescattering variation can be considered as an error on extrapolation from the low-$Z$ measurements that do exist. Because the $\nu_\mu$ disappearance probability should be large, the far and near detector energy spectra will be very different, and these effects will only partially cancel in a ratio between near and far detectors. The extent to which they do not cancel represents a systematic error on $\Delta m^2_{23}$.

If these pion absorption $Z$ extrapolation effects are treated as the total systematic uncertainty due to nuclear effects, we can compare it to the expected MINOS statistical error. In this more complete analysis, the detector acceptance must also be taken into account. One cut which could reduce the error due to nuclear effects significantly would be to require a minimum muon energy. The less visible energy attributable to hadrons, the smaller the relative effect of nuclear uncertainties on the total neutrino energy measurement. Requiring the muon to take up most of the energy in an event lowers efficiency, of course, and reduces the statistical power of the far-detector data sample. Here a minimum muon energy of 0.5 GeV was required, in an attempt to approximate the acceptance of a real analysis.

If the uncertainties from nuclear effects correspond to the differences in Figure 1, then for a 0.5 GeV muon momentum cut they induce a $\Delta m^2_{23}$ error only slightly smaller than the statistical error expected by MINOS with $7.6 \times 10^{20}$ protons on target (POT) (see Figure 2).

As described in Chapter 8, MINER$\nu$A will measure neutrino interactions on steel, carbon, and lead and collect about 750K events on each target over the four year run. This represents an enormous improvement in both the statistics and the range of target nuclei over previous experiments, and would improve our level of understanding of nuclear effects dramatically. With sufficient data on several different nuclei, the error on $Z$ extrapolation would be reduced since the nuclear models would be better constrained. The remaining uncertainties on the detector energy scale are likely due to uncertainties in pion rescattering in steel. Systematic uncertainty in $\Delta m^2_{23}$ with this new data in hand would be small

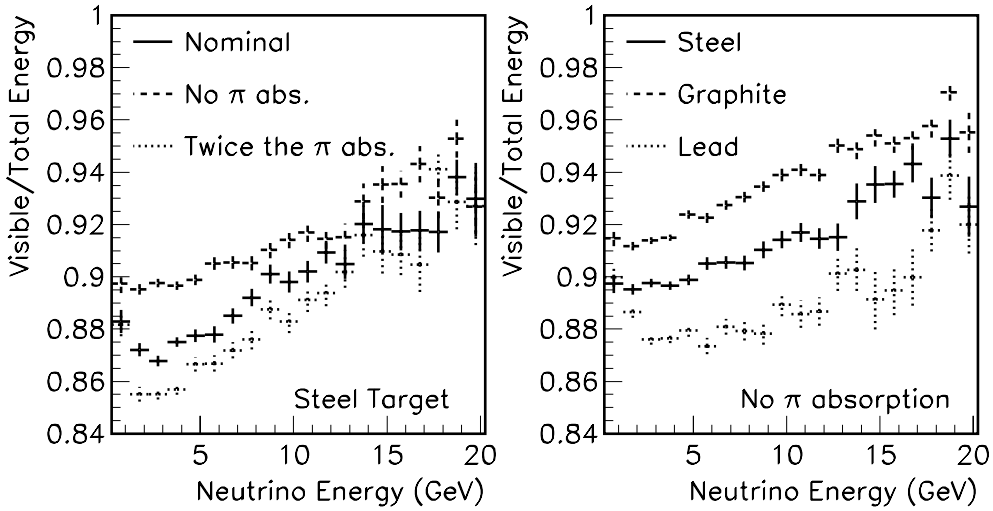


Figure 1: Ratio of visible (reconstructed) to true neutrino energy for several different models of nuclear effects. The left plot shows the ratio for steel (solid) with the nominal pion absorption, as well as the same ratio for the pion absorption turned off or doubled from what is expected. The right plot shows the differences the ratio for three different target nuclei, where pion absorption is turned off to isolate the effects of pion rescattering.

compared to the statistical error, as is shown in Figure 2.

## 1.3 $\nu_e$ Appearance

### 1.3.1 Signal and backgrounds

The goal of the next generation of neutrino oscillation experiments is to determine whether the last unmeasured neutrino mixing matrix element, (called $|U_{e3}|$ or $\sin\theta_{13}$) is non-zero. If $\theta_{13}$ is in fact non-zero future experiments could measure the neutrino mass hierarchy search for CP violation in the lepton sector. T2K and NO$\nu$Awill probe this matrix element by measuring the $\nu_\mu \to \nu_e$ oscillation probability at a "frequency" corresponding to $\Delta m^2_{23}$. The oscillation probability for $\nu_\mu \to \nu_e$ in vacuum can be expressed [7]

$$P(\nu_\mu \to \nu_e) = \sin^2\theta_{23}\sin^2 2\theta_{13}\sin^2\left(\frac{1.27\Delta m^2_{23}(eV^2)L(km)}{E_\nu(GeV)}\right) + ... \tag{3}$$

where the additional terms not shown are due to small effects from the solar mass splitting, $\Delta m^2_{12}$.

Identifying $\nu_e$ appearance in a $\nu_\mu$ beam is quite challenging for several reasons. From the CHOOZ reactor neutrino limit on $\sin^2 2\theta_{13}$ [9] the appearance probability must be less than about 5% at 90% confidence level. Also, the beams contain an intrinsic $\nu_e$ contamination as large as a few per cent. Finally, neutral-current and high-$y$ charged-current $\nu_\mu$ interactions can produce energetic $\pi^0$, leading to electromagnetic showers that may resemble a $\nu_e$ charged-current event.

T2K and NO$\nu$A will reduce some of these backgrounds significantly below the level in current long baseline experiments by using detectors optimized for electron appearance, and by placing those

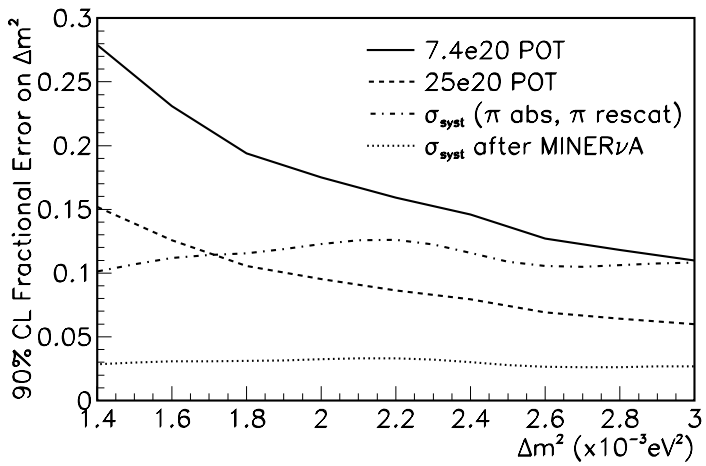


Figure 2: Fractional size of the statistical 90% confidence level region at $\sin^2 2\theta_{23} = 1$ for MINOS. Also shown are possible systematic uncertainties due to uncertainties in nuclear effects: the dot-dashed line are those effects described in the text, and the dotted line assumes uncertainties after dedicated nuclear effect measurements where pion rescattering and absorption are measured on the target nucleus (steel). Detector acceptance is modelled by requiring muons above 0.5 GeV. Also shown are the statistical errors for two different integrated proton intensities.

detectors off the beam axis. In two-body decay of the charged pion, the neutrino energy spectrum at small angles from the beam axis are narrower than the on-axis spectrum. Also, at these small angles the peak energy itself is reduced. The narrowest neutrino energy spectrum occurs when the far detector is placed at an angle corresponding to $90^\circ$ in the pion center of mass. In this configuration, the $\nu_e$ flux comes from the three-body muon decays, so the intrinsic $\nu_e$ flux at lower energies does not increase at higher angles like the $\nu_\mu$ flux does. Also, the neutral-current background is always a steeply falling function of visible energy because the outgoing neutrino always takes some fraction of the incoming neutrino's energy.

With this "off-axis" strategy, T2K and NO$\nu$A still expect some background after all analysis cuts, even in the absence of $\nu_\mu \to \nu_e$ oscillation. Measurement of the $\nu_\mu \to \nu_e$ probability requires accurate knowledge of this remaining background, and the cross-section and detection efficiencies for the $\nu_e$ signal.

### 1.3.2 Cross-section uncertainties with a near detector

Both T2K and NO$\nu$A will use near-detector measurements to predict the expected backgrounds at the far detector. In T2K, an on-axis near detector 280 m from the proton target will measure the spectrum and transverse beam profile, and at least one other off-axis detector will be focused on cross-section measurements. There are also plans to build a water Cherenkov detector 2 km from the proton target, but even then near- and far-detector efficiencies may not be identical. For NO$\nu$A, the near detector will be very similar in design to the far detector, and can be placed in a wide range of angles with respect to the beam. By making the near detector similar, NO$\nu$A hopes to minimize uncertainties in the detector response and efficiency. However, because the near detector will be as coarse as the far, it is

not optimized for cross-section measurements.

To see how any uncertainties (cross-section, detector acceptance, or flux) will arise in the far detector prediction based on the near detector data, it is useful to think about how the event samples are likely to change between near and far. At a near detector, the flux of muon neutrinos will have a very strong peak at a particular energy, while at the far detector that peak will (by design) have oscillated to mostly $\nu_\tau$. At these energies, $\nu_\tau$ cannot produce charged-current interactions, only neutral-current. Neutral-current samples are likely to be similar from near to far, provided the near detector is at a similar off-axis angle. Electron neutrino events at the peak are primarily from muon decays in the beam, which occur on average substantially farther downstream than the pion decays. Therefore, the extrapolation from the near to far detector tends to be different for all three event samples. If the relative population of the background sample among different categories cannot be predicted accurately (due to cross-section, detector or flux uncertainties), the far detector extrapolation will be wrong.

The MINOS and NO$\nu$A near detectors will both provide important constraints on neutrinos coming from NuMI. However, neither will be able to measure the charged- and neutral-current near detector backgrounds precisely. A finer-grained detector with improved timing resolution will be extremely useful to distinguish these two contributions which change so dramatically between near and far detectors.

A quantitative case study of how cross-section uncertainties may not completely cancel between near and far detectors, was performed using the simulation for an early design [116] of NO$\nu$A. Although NO$\nu$A's final design will be different, the fundamental arguments remain unchanged: the mixture of contributing cross-sections at the far detector cannot, even in principle, be identical to the mixture at the near detector.

| | | QE | RES | COH | DIS |
|---|---|---|---|---|---|
| | | cross-section Uncertainty | | | |
| | | 20% | 40% | 100% | 20% |
| Process | Statistics | Composition after all cuts in far detector | | | |
| Signal $\nu_e$ | 175 ($\sin^2 2\theta_{13} = 0.1$) | 55% | 35% | n/I | 10% |
| NC | 15.4 | 0 | 50% | 20% | 30% |
| $\nu_\mu CC$ | 3.6 | 0 | 65% | n/I | 35% |
| Beam $\nu_e$ | 19.1 | 50% | 40% | n/I | 10% |

Table 1: Rate of signal and background processes in a 50 kton NO$\nu$A far detector, assuming $\Delta m^2_{23} = 2.5 \times 10^{-3}$ eV$^2$. Also listed are the present cross-section uncertainties for those processes. Charged-current coherent production was not included since it is should be unimportant compared to other charged-current processes.

The signal and background samples for the nominal 5 year run are listed in Table 1 along with the fractional contribution of each process to events of a given type passing all cuts, and the relative cross-section uncertainties [117]. Without a near detector, the total error on the background prediction from cross-section uncertainties, in the absence of $\nu_\mu$ oscillation, is 16%, which is equal to the statistical error. For oscillation at the level indicated in the table, the statistical error on the probability would be 8%, while the errors from cross-section uncertainties alone are 31% .

Figure 3 shows the projected error on $\sin^2 2\theta_{13}$ as a function of $\sin^2 2\theta_{13}$ itself, for present cross-section uncertainties. Should NO$\nu$A find a large signal, even in its first phase the measurement will be

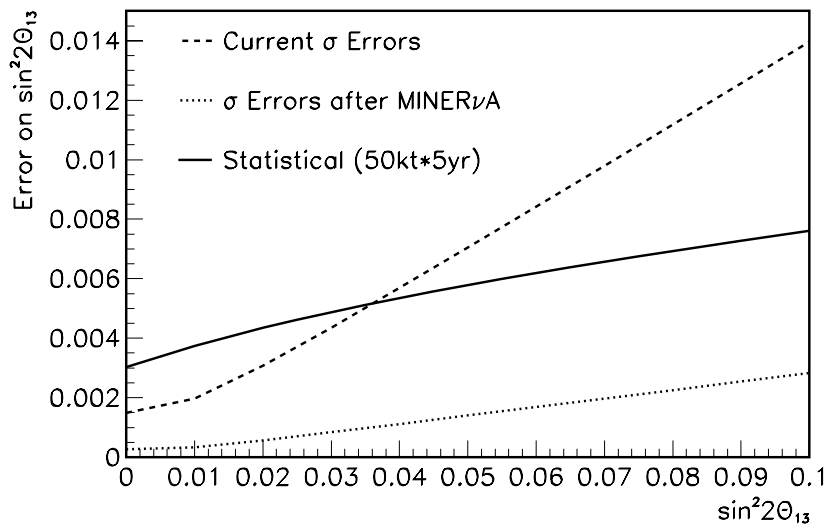


Figure 3: Statistical error, present cross-section systematic error, and post-MINER$\nu$A cross-section systematic error in NO$\nu$A measurement of $\sin^2 2\theta_{13}$, as a function of $\sin^2 2\theta_{13}$.

systematics limited with existing knowledge of relevant cross-sections. Chapters 2, 4, and 6 explain how different channels will be isolated, and give the size of the expected samples. MINER$\nu$A should be able to reduce cross-section uncertainties for NO$\nu$A to about 5% for all charged- and neutral-current deep-inelastic scattering processes, 10% for neutral-current resonant processes, and 20% for neutral-current coherent $\pi^0$ processes. If these uncertainties were achieved, then systematic errors due to cross-section uncertainties would be well below the statistical errors, as shown in Figure 3.

## 1.4 Conclusions

It is clear from even these preliminary studies that MINER$\nu$A will play an important and potentially decisive role in helping current and future precision oscillation experiments reach their ultimate sensitivity. To get the most precise values of $\Delta m^2_{23}$ (which is eventually necessary to extract mixing angles and the CP-violating phase) our field must better understand and quantify the processes that occur between interaction of an incoming neutrino and measurement of the outgoing particles in a detector. Although the issues are different depending on whether the detector is a water Cherenkov or calorimetric devices, in both cases more information is needed. Extracting mixing parameters like $\theta_{13}$ and ultimately the neutrino mass hierarchy and CP-violation requires much better understanding of resonant cross-sections. Even setting limits on these parameters will require better measurements of neutral-current processes. The cost of curing our present ignorance pales in comparison to the possibility that an entire generation of oscillation experiments might miss out on an exciting discovery or end in a morass of inconclusive, ambiguous, contradictory or even wrong results because we have failed to invest the effort needed to understand the most basic interactions of the particle whose exotic behavior they were built to study. Precision measurement of exclusive cross-sections and nuclear effects will finally put a field making tremendous strides in luminosity and statistical power on a sound systematic foundation.

# 2 Quasi-Elastic Scattering

## 2.1 Introduction

Quasi-elastic scattering dominates the total $\nu$–N interaction rate in the threshold regime $E_\nu \leq 2$ GeV. Precision measurement of the cross-section for this reaction, including its energy dependence and variation with target nuclei, is essential to current and future neutrino-oscillation experiments.

## 2.2 Nucleon Form-factors in Quasi-elastic Scattering

MINER$\nu$A's large quasi-elastic samples will probe the $Q^2$ response of the weak nucleon current with unprecedented accuracy. The underlying V-A structure of this current includes vector and axial-vector form-factors. The essential formalism is given in reference [14].

$$< p(p_2)|J_\lambda^+|n(p_1) >= \overline{u}(p_2)\left[\gamma_\lambda F_V^1(q^2) + \frac{i\sigma_{\lambda\nu}q^\nu \xi F_V^2(q^2)}{2M} + \gamma_\lambda\gamma_5 F_A(q^2)\right]u(p_1),$$

where $q = k_\nu - k_\mu$, $\xi = (\mu_p - 1) - \mu_n$, and $M = (m_p + m_n)/2$. Here, $\mu_p$ and $\mu_n$ are the proton and neutron magnetic moments. The pseudoscalar form-factor is not shown since it is small for $\nu_\mu$.

The vector part of this matrix element can be expressed using $G_E^p(q^2)$, $G_E^n(q^2)$, $G_M^p(q^2)$, and $G_M^n(q^2)$. It has been generally assumed that the $q^2$ dependence of these form-factors can be described by the dipole approximation:

$$G_D(q^2) = \frac{1}{\left(1 - \frac{q^2}{M_V^2}\right)^2}, \quad M_V^2 = 0.71 \text{ (GeV/c)}^2, \quad F_A(q^2) = \frac{g_A}{\left(1 - \frac{q^2}{M_A^2}\right)^2}$$

$$G_E^p = G_D(q^2), \quad G_E^n = 0, \quad G_M^p = \mu_p G_D(q^2), \quad G_M^n = \mu_n G_D(q^2).$$

As discussed below, the dipole parameterization is far from perfect. MINER$\nu$A will be able to measure deviations of $F_A$ from this form. In general, the axial form-factor $F_A(q^2)$ can only be extracted from quasi-elastic neutrino scattering.[1]

### 2.2.1 Vector form-factors

Electron scattering experiments at SLAC and Jefferson Lab (JLab) have measured the proton and neutron electromagnetic (vector) form-factors with high precision. The vector form-factors can be determined from electron scattering cross-sections using the standard Rosenbluth separation technique[15], which is sensitive to (two-photon) radiative corrections, or from polarization measurements using the newer polarization transfer technique[16]. Polarization measurements do not directly measure form-factors, but rather the ratio $G_E/G_M$. Recently, discrepancies in electron scattering measurements of some vector form-factors have appeared; study of quasi-elastic reactions in MINER$\nu$A may help reveal the origin these discrepancies. Figure 4 shows the BBA-2003 (Bodek, Budd, Arrington 2003) fits to $G_E^p/G_D$. There appears to be a difference between the two methods of measuring this ratio. The newer polarization transfer technique yields a much lower value at high $Q^2$ and indicates a difference between the electric charge and magnetization distributions. The polarization transfer technique is believed to be

[1] At low $Q^2$, below 0.1 (GeV/c)$^2$, its behavior can also be inferred from pion electroproduction data.

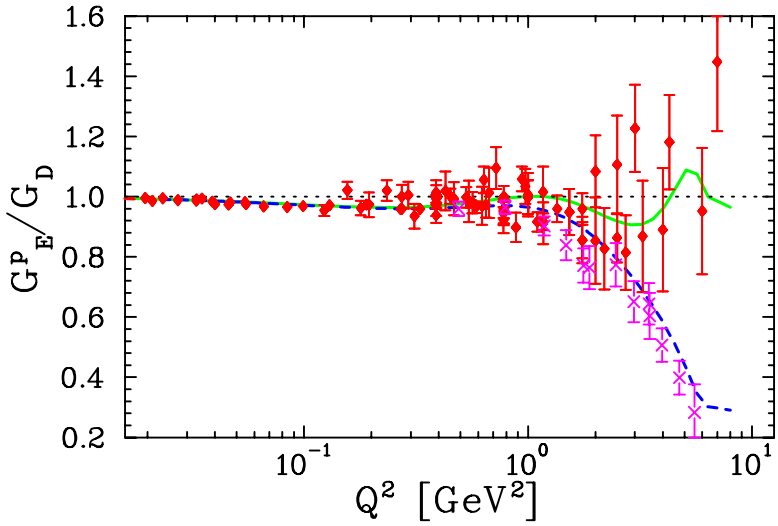


Figure 4: The (BBA-2003) fits to $G_E^p/G_D$, using cross-section data only (solid), and with both the cross-section and polarization transfer data (dashed). The diamonds are the from Rosenbluth extractions and the crosses are the Hall A polarization transfer data.

more reliable and less sensitive to radiative effects from two-photon corrections. In addition, Figure 4 shows that dipole amplitudes provide only a first-order description of form-factor behavior at high $Q^2$. In general, these deviations are different for each of the form-factors and are shown in [17].

If the electric charge and magnetization distributions of the proton are indeed different, accurate measurement of the axial form-factor's high-$Q^2$ shape in MINER$\nu$A can provide important new input to help resolve differences in electron scattering data.

To obtain the correct neutrino cross-sections [17], the input form-factors must be correct. The $Q^2$ distribution measured in neutrino scattering is sensitive to both the vector and axial form-factors. However, using an incorrect *axial* form-factor to match the the $Q^2$ distribution in neutrino scattering (to compensate for old dipole *vector* form-factors) results in a 6–8% error in the calculated neutrino cross-section. Therefore, updated vector form-factors *and* better-measured axial form-factors are required. MINER$\nu$A will measure the $Q^2$ dependence of $F_A$ in neutrino scattering and compare the calculated cross-section with the measured cross-section.

### 2.2.2 Axial form-factor

Neutrino scattering provides the only practical route to precision measurement of the axial form-factor above $Q^2 = 0$, and the functional form of $F_A(Q^2)$. The fall-off of the form-factor strength with increasing $Q^2$ is traditionally parameterized (approximately) using an effective axial-vector mass $M_A$. Uncertainty in the value of $M_A$ contributes directly to uncertainty in the total quasi-elastic cross-section. Earlier neutrino measurements, mostly bubble-chamber experiments on deuterium, extracted $M_A$ using the best vector form-factors, other parameters, and models available at the time. Changing these input assumptions changes the extracted value of $M_A$. Hence, precision extractions of $M_A$ and $F_A$ require using the best possible vector form-factors and coupling constants. The value of $M_A$ is $\approx 1.00$ GeV/c$^2$, to an accuracy of perhaps 5%. This value agrees with the theoretically-corrected value from pion electroproduction[18], $1.014 \pm 0.016$ GeV$/c^2$.

The fractional contributions of $F_A$, $G_M^p$, $G_M^n$, $G_E^p$, and $G_E^n$ to the $Q^2$ distribution for quasi-elastic neutrino and anti-neutrino scattering cross-sections in energy range of the NuMI beam are shown in Figure 5. The contributions are determined by comparing the BBA-2003 cross-sections with and without each of the form-factors included. MINER$\nu$A will be the first systematic study of $F_A$, which accounts for roughly half of the quasi-elastic cross-section, over the entire range of $Q^2$ shown in the figure.

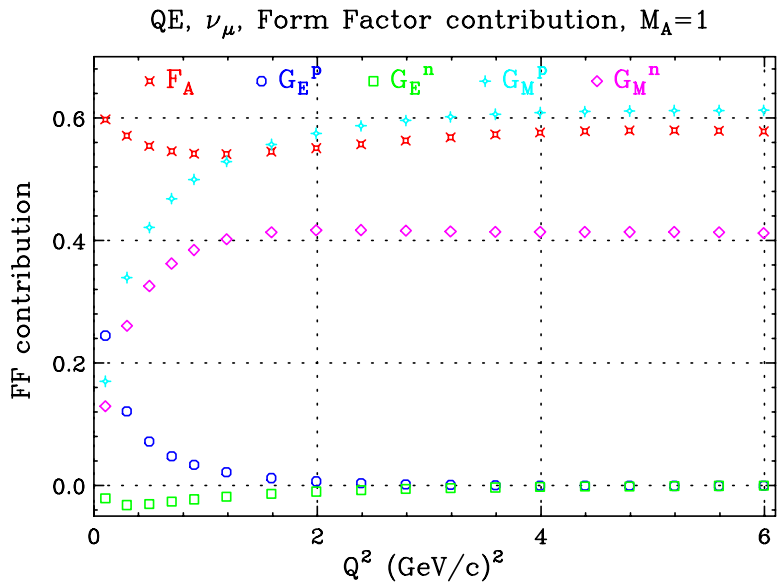


Figure 5: Fractional contributions of $G_M^p$, $G_M^n$, $G_E^p$, $G_E^n$, and $F_A$ to the $Q^2$ distributions for quasi-elastic neutrino samples in the energy range of the NuMI beam. Because of interference terms, the sum of the fractions does not necessarily add up to 100%.

### 2.2.3 Physics of vector and axial form-factors

In deep-inelastic charged-current scattering from quarks, the vector and axial couplings are equal (V-A). Similarly, in electron scattering from quarks (vector current), there is a well-defined ratio between electric and magnetic scattering from point-like Dirac quarks. At low momentum transfers, all of these relations break down. For example in quasielastic and resonant production at very low momentum transfers, the charge and anomalous magnetic moments of the neutron and proton mean the ratio of electric and magnetic scattering for the vector current is not the same as for free quarks. Similarly, from neutron decay, we know that $g_a(Q^2 = 0) = 1.267$ instead of 1.0, so vector and axial scattering differ at $Q^2 = 0$.

There are efforts in progress by lattice gauge programs to calculate the anomalous vector and axial magnetic moments of the proton and neutron, and the $Q^2$ dependence of all the form-factors in the low- and high-$Q^2$ regions. The normalization of the magnetic form-factors at $Q^2$=0 are constrained to equal the charge and anomalous (vector and axial) magnetic moment. The slope at low $Q^2$ is related to the mean square charge radius of the proton and neutron. The dipole form assumes that the charge and magnetization distributions of the various types of quarks and antiquarks have an exponential form. For $Q^2$ above 0.5–1.0 (GeV/c)$^2$ this non-relativistic picture breaks down. The ratio $G_E/\mu G_M \approx 1.0$ (at low $Q^2$) implies that the charge and magnetization distribution of the proton are the same, but at higher

$Q^2$ the ratio becomes much smaller, and more sophisticated models are required (e.g. lattice gauge theories). Therefore, measurement of the axial form-factor over a wide range of $Q^2$ is of great interest. In this section, we show MINER$\nu$A's sensitivity to three different models of the axial form-factor:

- Model 1: A simple dipole approximation currently used for the magnetic form-factor of the proton, with different axial and vector radii. This is the current standard assumption.
- Model 2: A model in which the ratios $G_M^p/G_D$ and $G_E^p/G_D$ are equal, and decrease with $Q^2$.
- Model 3: A model based on duality, which requires the axial and vector parts of $W_1^{elastic}$ to be equal above $Q^2$=0.5 (GeV/$c$)$^2$, and therefore increase with $Q^2$, as described briefly in the next section.

### 2.2.4 Quark/hadron and local duality

In modern language, the concept of quark-hadron duality can be related to the momentum sum rule in QCD, and various other moments of the structure functions. It has been shown by Bodek and Yang that with inclusion of target mass corrections, NNLO QCD describes deep-inelastic scattering and the average resonant cross-section down to $Q^2 = 0.5$ (GeV/c)$^2$. The concept of local duality implies that the integral of the QCD predictions (including target mass) in the threshold region up to pion threshold, should be equal to the integral of the elastic peak. Since for QCD, the vector and axial contributions to $W_1$ and $W_2$ are equal, local duality predicts that vector and axial part of the quasi-elastic form-factors should become equal around $Q^2 = 0.5$ (GeV/c)$^2$. This means that the dipole approximation must break down for both vector and axial form-factors.

The vector and axial components of $W_1^{elastic}$ become equal at $Q^2 \sim 0.5$ (GeV/c)$^2$ for both BBA and dipole form-factors. The requirement that this vector/axial ratio remains equal to 1.0 for higher $Q^2$ yields a definite prediction that the axial form-factor is 1.4 times larger than the dipole prediction at higher $Q^2$.

### 2.2.5 Axial form-factor measurement in MINER$\nu$A

Figure 6 shows a typical quasi-elastic event, as simulated in MINER$\nu$A.

In $\nu n \rightarrow \mu^- p$, the outgoing proton carries kinetic energy of approximately $Q^2/2M_N$. So for low $Q^2$, the challenge is identifying events with a very soft recoil proton; for high $Q^2$, this proton is high energy and may interact in the detector, making particle identification more challenging. The main strategies of the current analysis are:

- At low $Q^2$, accept quasi-elastic candidates with a single (muon) track, and discriminate from background by requiring low activity in the remainder of the detector
- At higher $Q^2$, reconstruct both the proton and the muon, and require kinematic consistency with $x = 1$ and $p_T^{tot} = 0$

Simple cuts based on these ideas yield reasonable efficiency and good purity, even at high $Q^2$.

This analysis uses the NEUGEN generator and the hit-level MINER$\nu$A detector simulation and tracking package to model signal selection and background processes.

Initial event identification requires one or two tracks in the active target. One of these tracks must be long range (400 g/cm$^2$) as expected for a muon. If a second track forms a vertex with this track,

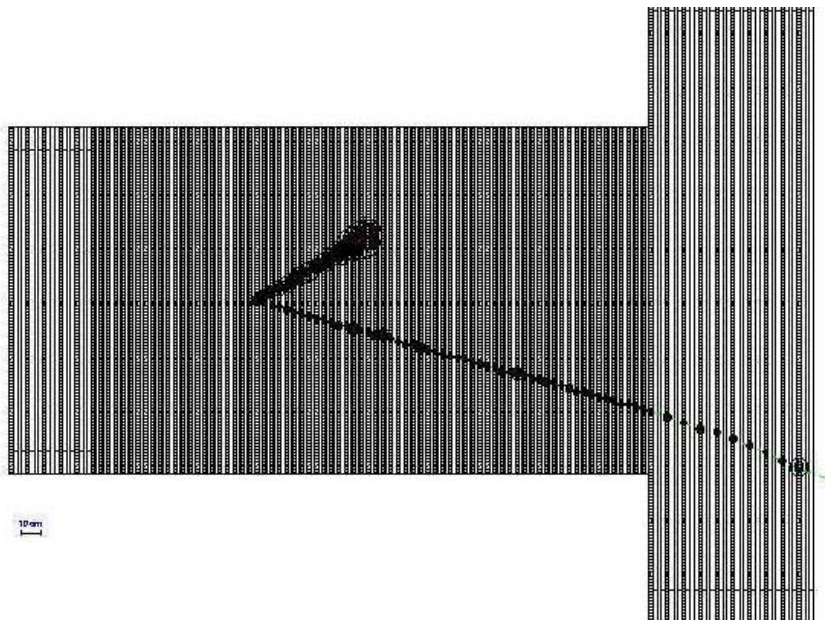

Figure 6: A simulated charged-current quasi-elastic interaction in MINER$\nu$A. The proton (upper) and muon (lower) tracks are well resolved. In this display, hit size is proportional to energy loss within a strip. The increased energy loss of the proton as it slows and stops is clear. For clarity the outer detector is not drawn.

it is assumed to be the proton. No other tracks may be associated with this vertex. The muon track momentum is reconstructed with a fractional uncertainty of 10–20%.

For low $Q^2$, the proton track (if found) is effectively required to lose energy by $dE/dx$ alone, since only limited detector activity not associated with the primary tracks is allowed by the selection criteria. We attempt to recover some of the resulting efficiency loss by allowing hits on tracks near the proton track to be associated with it. Figure 7 shows the fraction of hits not associated with the lepton or proton in the quasi-elastic events and in expected background processes. For higher-$Q^2$ events a similar procedure could be applied, but it is not particularly effective nor efficient.

The energy of the proton for the high-$Q^2$ sample (where the proton almost always interacts) is reconstructed calorimetrically with an expected fractional energy resolution of $35\%/\sqrt{E_{proton}}$.

Although muons are identified by requiring a single long track, no attempt was made (in this initial analysis) to improve particle identification by requiring a $dE/dx$ consistent with the muon or proton tracks. This requirement should be particularly effective for protons of $\mathcal{O}(1)$ GeV momentum[2], and such a requirement can be imposed to optimize the analysis in the future. In addition, it may be possible to improve the efficiency by allowing a shorter muons, with a $dE/dx$ requirement, without sacrificing purity.

If a quasi-elastic interaction is assumed, one can reconstruct the event kinematics from only the

[2]See Section 11.4.5.

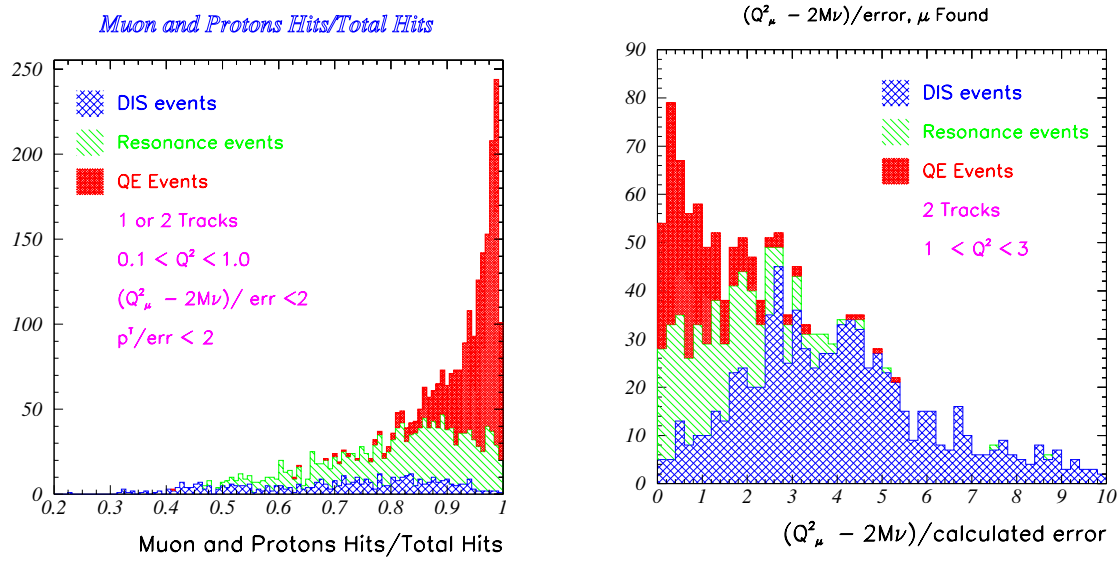


Figure 7: Left: The fraction of hits associated with the muon and the proton tracks in quasi-elastic candidates, for events with one or two vertex tracks, and measured $Q^2$ between 0.1 and 1 (GeV/c)$^2$. Right: Significance of the difference between $Q^2$ from the quasi-elastic hypothesis and $Q^2$ from the final state energy, for quasielastic candidates with measured $Q^2$ above 1 GeV$^2$.

momentum and direction of the final state $\mu$. Neglecting the binding energy of the final-state proton,

$$E_\nu^{QE} = \frac{M_N E_\mu - \frac{m_\mu^2}{2}}{M_N - E_\mu + p_\mu \cos\theta_\mu}.$$

If a proton track is identified and its angle and energy are also measured, one can additionally require consistency with the quasi-elastic hypothesis. Two constraints are possible, one on the $x$ of the reconstructed interaction and one on the total $p_T$ of the observed final state.

If the interaction is truly quasi-elastic, then $x = 1$, and therefore $Q^2 = 2M_N\nu$ where $\nu$ = $E_{had}$ - $M_N$, and $E_{had}$ is the energy of the hadronic final state. In this analysis, we test this by comparing $Q^2$ reconstructed from the lepton kinematics under the quasi-elastic hypothesis to $2M_N\nu$ and forming $(Q_\mu^2 - 2M_N\nu)/\sigma$ where the dominant part of the calculated error $\sigma$ for this term comes from the smearing of hadronic final-state energy. Figure 7 shows the significance of this $Q^2$ difference for two track quasi-elastic candidates with observed 1 $(GeV/c)^2 < Q^2 < 3$ $(GeV/c)^2$, for quasi-elastic, resonant and deep-inelastic events. This cut can be applied without identifying a proton track if the visible energy, less the muon energy, is assumed to be $\nu$.

The $Q^2$ significance ($x$) cut does not use information on the proton direction, and so we impose a second kinematic cut on the total transverse momentum $p_T$ relative to the incoming neutrino direction. This selection requires that a proton track is identified, and we cut on the significance of the difference from $p_T = 0$: $p_T^{tot} < 2\sigma_{p_T}$ if $Q^2 < 3$ (GeV/c)$^2$, and $p_T^{tot} < 3\sigma_{p_T}$ for higher $Q^2$.

### 2.2.6 Results

Table 2 shows the efficiency and purity of the quasi-elastic sample for different $Q^2$ bins after each cut. Using these efficiencies and purities, we have determined uncertainties on $F_A$ including efficiency and

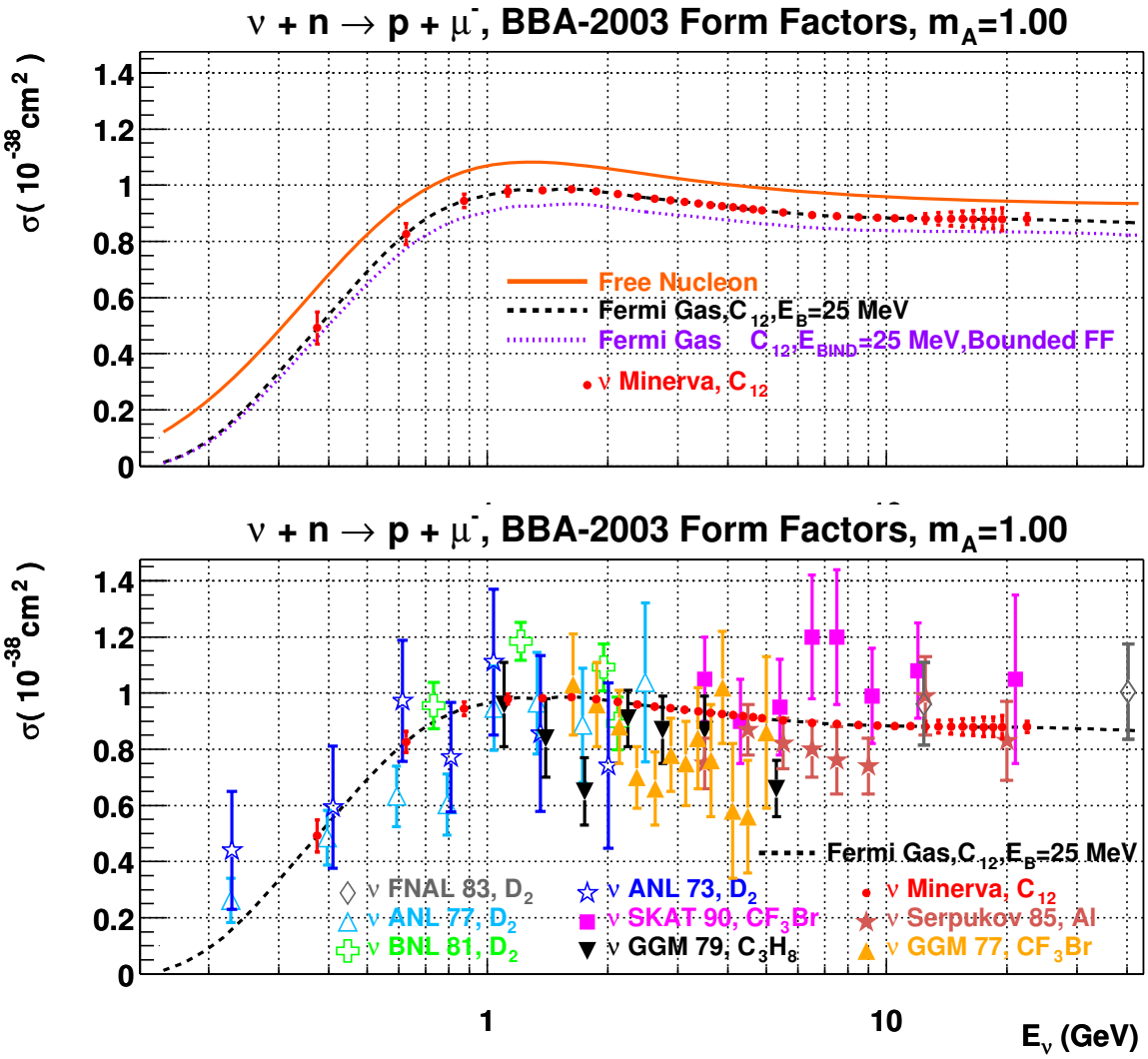


Figure 8: The quasi-elastic neutrino cross-section along with data from various experiments. Representative calculations are shown using BBA-2003 form-factors with $M_A = 1.00$ GeV/c$^2$. The solid curve uses no nuclear correction, while the dashed curve [19] uses a Fermi gas model for carbon with 25 MeV binding energy and 220 MeV/c Fermi momentum. The dotted curve is the prediction for carbon including both Fermi gas Pauli blocking and the effect of nuclear binding on the nucleon form-factors [20](bounded form-factors). The predicted MINER$\nu$A points, with errors, are shown. The data shown in the bottom plot are from FNAL 1983 [21], ANL 1977 [22], BNL 1981 [23], ANL 1973 [24], SKAT 1990 [25], GGM 1979 [26], LSND 2002 [27], Serpukov 1985 [28], and GGM 1977 [29]. The data have large errors and are only marginally consistent throughout the $E_\nu$ range.

| | $\mu$ | | $(Q^2_\mu - 2M\nu)$/err | | $p_T$ /err | | Hits | |
|---|---|---|---|---|---|---|---|---|
| $Q^2$ bin | Effic | Purity | Effic | Purity | Effic | Purity | Effic | Purity |
| 0.1-0.5 | 0.926 | 0.246 | 0.918 | 0.442 | 0.866 | 0.559 | 0.775 | 0.842 |
| 0.5 - 1 | 0.775 | 0.199 | 0.765 | 0.410 | 0.624 | 0.486 | 0.528 | 0.685 |
| 1 - 2 | 0.600 | 0.199 | 0.541 | 0.416 | 0.397 | 0.555 | 0.338 | 0.598 |
| 2 - 3 | 0.456 | 0.146 | 0.400 | 0.375 | 0.344 | 0.554 | 0.278 | 0.676 |
| 3 - 10 | 0.689 | 0.123 | 0.600 | 0.310 | 0.467 | 0.420 | 0.311 | 0.700 |

Table 2: Efficiency and purity in $Q^2$ bins for quasi-elastic candidates

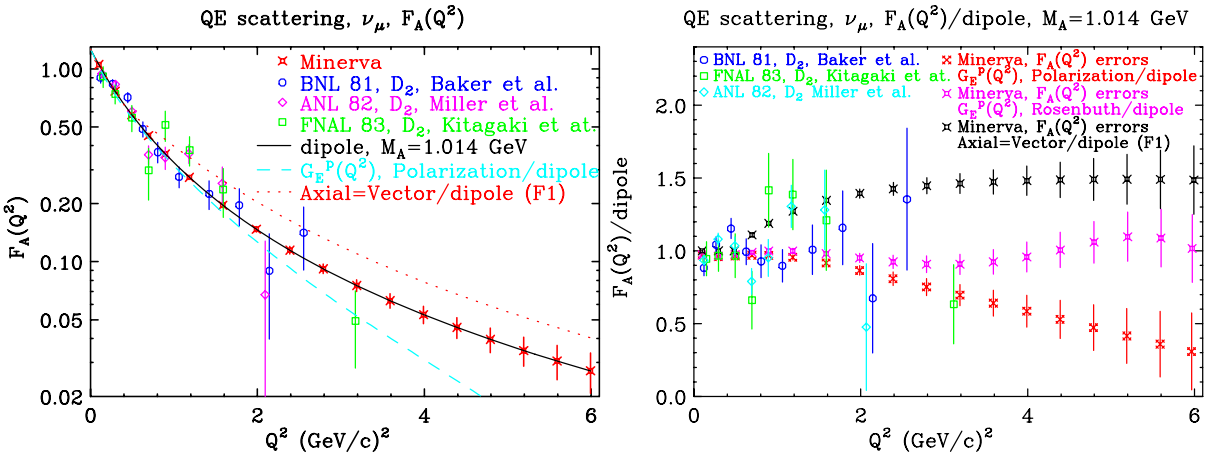


Figure 9: Left: Estimation of $F_A$ (left) and $F_A$/dipole (right) from a four year MINER$\nu$A run, in the quasielastic analysis described in the text, where (left) assumes a pure dipole form-factor with $M_A = 1.014$ GeV/c$^2$. Also shown is $F_A$ extracted from deuterium bubble chamber experiments using the $d\sigma/dq^2$ from the papers of FNAL 1983 [21] BNL 1981 [23], and ANL 1982 [30]. Also shown is the expectations from Model 2 (dashed line) and Model 3 (dotted line) for the axial form-factor.

background effects.

Figure 8 shows predictions for the cross-section assuming the BBA-2003 form-factors, with $M_A =$ 1.00 (GeV/c)$^2$. The predicted MINER$\nu$A points are shown along with their expected errors. The MIPP experiment will measure particle production off the NuMI target, and from this, we expect an additional overall uncertainty of 4% from the flux. Figure 8 summarizes current knowledge of neutrino quasi-elastic cross-sections. Among the results shown, there are typically 10–20% normalization uncertainties from knowledge of the fluxes. This plot shows that existing measurements have large errors throughout the $E_\nu$ range accessible to MINER$\nu$A and especially in the threshold regime crucial to future oscillation experiments.

Figure 9 shows the expected values and errors of $F_A$ in bins of $Q^2$ for the MINER$\nu$A active carbon target, after a four-year exposure in the NuMI beam. The method to extract $F_A$ from $d\sigma/dq^2$ is given in [32]. Clearly the high-$Q^2$ regime, which is inaccessible to K2K, MiniBooNE and T2K, will be well-resolved in MINER$\nu$A. Figure 9 shows these results as a ratio of $F_A$/$F_A$(Dipole), demonstrating MINER$\nu$A's ability to distinguish between different models of $F_A$. We show the three different models (described earlier) for $F_A$ as a function of $Q^2$ . Model 2 is a factor of 5 lower at high $Q^2$, as indicated

by $G_E^p/G_M^p$ data, while model 3 (based on duality) is a factor of 1.4 higher. MINER$\nu$A will be able to measure the axial nucleon form-factor with precision comparable to vector form-factor measurements at JLab. Note that resolution effects are not included in this extraction of $F_A$, but the typical $Q^2$ resolution for quasi-elastic events at high $Q^2$ is $\lesssim 0.2\ (GeV/c)^2$ which is smaller than the bin size.

Figure 9 shows the extraction of $F_A$ from Miller, Baker, and Kitagaki, using their plots of $d\sigma/dq^2$. For $Q^2 > 2$ (GeV/$c$)$^2$ there is essentially no measurement of $F_A$. Even the measurements of $F_A(Q^2)$ below 2 (GeV/c)$^2$ have significant errors, hence one cannot assume $F_A$ is a dipole for low $Q^2$. The maximum $Q^2$ values that can be achieved with incident neutrino energies of 0.5, 1.0, 1.5 and 2 GeV are 0.5, 1.2, 2.1 and 3.0 (GeV/c)$^2$, respectively. Since K2K, MiniBooNE, and T2K energies are in the 0.7–1.0 GeV range, these experiments probe the low $Q^2 < 1$ (GeV/c)$^2$ region where nuclear effects are large (see Figures 10). The low-$Q^2$ ($Q^2 < 1$ (GeV/c)$^2$) MiniBooNE and K2K experiments have begun to investigate the various nuclear effects in carbon and oxygen. However, higher $Q^2$ data are only accessible in experiments like MINER$\nu$A, which can span the 2–8 GeV neutrino energy range. MINER$\nu$A's measurement of the axial form-factor at high $Q^2$ will be essential to a complete understanding of the vector and axial structure of the neutron and proton.

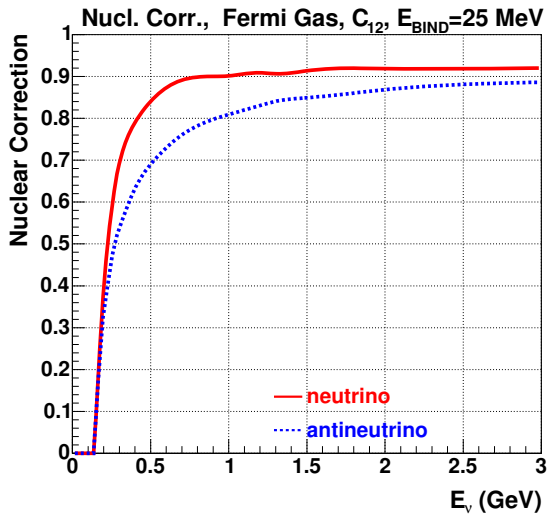


Figure 10: Pauli suppression in a Fermi gas model for carbon with binding energy $\epsilon = 25$ MeV and Fermi momentum $k_f = 220$ MeV/c. A similar suppression is expected for quasi-elastic reactions in MINER$\nu$A.

## 2.3 Nuclear Effects in Quasi-elastic Scattering

### 2.3.1 Fermi gas model

There are three important nuclear effects in quasi-elastic scattering from bound targets: Fermi motion, Pauli blocking, and corrections to the nucleon form-factors due to distortion of the nucleon's size and its pion cloud in the nucleus. Figure 10 shows the nuclear suppression versus $E_\nu$ from a NUANCE[33] calculation[19] using the Smith and Moniz[34] Fermi gas model for carbon. This nuclear model includes Pauli blocking and Fermi motion but not final state interactions. The Fermi gas model uses a

nuclear binding energy $\epsilon = 25$ MeV and Fermi momentum $k_f = 220$ MeV/c. Reference [34] shows how the effective $k_f$ and nuclear potential binding energy $\epsilon$ (within a Fermi-gas model) for various nuclei is determined from electron scattering data.

### 2.3.2 Bound nucleon form-factors

The predicted distortions of nucleon form-factors due to nuclear binding are can be as large as 10% at $Q^2 = 1$ (GeV/c)$^2$ to 15% at $Q^2 = 2$ (GeV/c)$^2$. With carbon, iron and lead targets, MINER$\nu$A can compare measured form-factors for a range of light to heavy nuclei. Figure 8 shows the cross-section suppression due to bound form-factors. As is described in [20], these effects can cause variations up to 10% in the differential cross-sections at MiniBooNE, K2K and T2K energies.

Requiring vector and axial contributions to $W_1$ be equal for $Q^2 > 0.5$ (GeV/c)$^2$ introduces further suppression at low $Q^2$. Changing the various assumptions in $d\sigma/dq^2$ as calculated with dipole form-factors introduces 5–10% effects on the $Q^2$ distributions these experiments will see.

### 2.3.3 Intra-nuclear rescattering

In neutrino experiments, detection of the recoil nucleon helps distinguish quasi-elastic scattering from inelastic reactions. Knowledge of the probability for outgoing protons to reinteract with the target remnant is therefore highly desirable. Similarly, quasi-elastic scattering with nucleons in the high-momentum tail of the nuclear spectral function needs to be understood. More sophisticated treatments than the simple Fermi gas model are required. Conversely, inelastic reactions may be misidentified as quasi-elastic if a final-state pion is absorbed in the nucleus. With its constrained kinematics, low-energy neutrino-oscillation experiments use the quasi-elastic channel to measure the (oscillated) neutrino energy spectrum at the far detector; uncertainty in estimation of non-quasi-elastic background due to proton intra-nuclear rescattering is currently an important source of systematic error in K2K.

The best way to study these effects is to analyze electron scattering on nuclear targets (including the hadronic final states) and test the effects of the experimental cuts on the final-state nucleons. MINER$\nu$A can address proton intra-nuclear rescattering by comparing nuclear binding effects in neutrino scattering on carbon to electron data in similar kinematic regions. Indeed, MINER$\nu$A members will be working with the CLAS collaboration to study hadronic final states in electron scattering on nuclear targets using existing JLab Hall B data. This analysis will allow theoretical models used in both electron and neutrino experiments to be tested. Other work in progress, with the Ghent[35] nuclear physics group, will develop the theoretical tools needed to extract the axial form-factor of the nucleon using MINER$\nu$A quasi-elastic data on carbon. The ultimate aim is to perform nearly identical analyses on both neutrino and electron scattering data in the same range of $Q^2$.

# 3 Coherent Pion Production

MINER$\nu$A will be able to study both charged- and neutral-current coherent neutrino-nucleus scattering with unprecedented precision. This chapter summarizes several preliminary studies to estimate the efficiencies and backgrounds in neutral- and charged-current analyses for different nuclei. MINER$\nu$A's high rates, range of nuclear targets, fine granularity, strong pattern recognition capabilities, and good electromagnetic calorimetry make it ideal for measurement of charged and neutral-current coherent processes.

## 3.1 Introduction

Coherent neutrino-nucleus reactions, in which the neutrino scatters coherently from an entire nucleus with small energy transfer, leave a relatively clean experimental signature and have been studied in both charged-current ($\nu_\mu + A \rightarrow \mu^- + \pi^+$) and neutral-current ($\nu_\mu + A \rightarrow \nu + \pi^0$) interactions of neutrinos and anti-neutrinos. Although the coherent interaction rates are typically an order of magnitude or more lower than other single-pion production mechanisms, the distinct kinematic characteristics of these events allow them to be cleanly identified. Because the outgoing pion generally follows the incoming neutrino direction, this reaction is an important background to searches for $\nu_\mu \rightarrow \nu_e$ oscillation, as these events can easily mimic the oscillation signature of a single energetic electron shower. Neutral-current coherent production will be discussed in more detail in Section 3.3.3; we first turn our attention to the charged-current channel where the kinematics can be fully measured and the underlying dynamics explored.

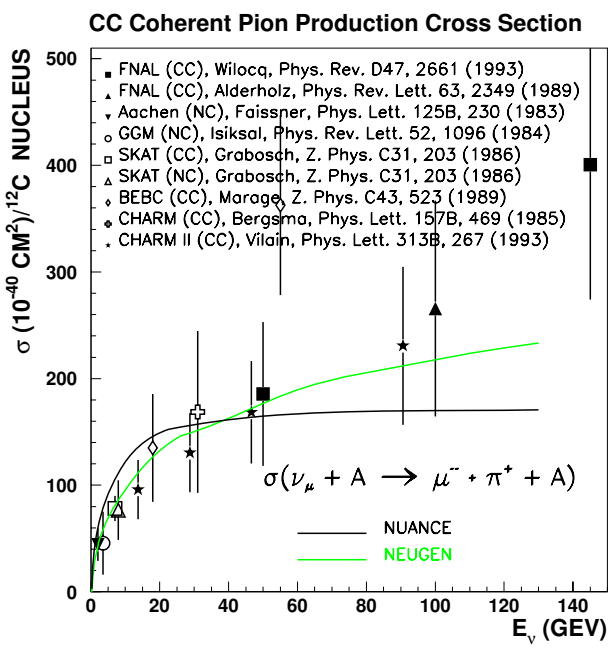


Figure 11: Charged-current neutrino–carbon coherent cross-sections. Results have all been scaled to carbon assuming an $A^{1/3}$ dependence, and $\sigma(CC) = 2\sigma(NC)$ [36].

### 3.2 Theory

It is well known from electron scattering that at low $Q^2$ and high $\nu$, vector mesons are abundantly produced through diffractive mechanisms. These interactions are interpreted as fluctuation of the virtual photon intermediary into a virtual meson with the same quantum numbers, which by the uncertainty principle can travel a length

$$l \sim \frac{\nu}{Q^2 + m^2} \tag{4}$$

where $m$ is the mass of the meson in question. For the weak current, similar fluctuations can occur, into both vector- and axial-vector mesons. From the Adler relation and "partially-conserved axial current" (PCAC) hypothesis, it is known that the hadronic current at low $Q^2$ is proportional to the pion field. The hadronic properties of the weak current in these kinematic regions have been investigated through study of nuclear shadowing at low $x$ and coherent production of $\pi$, $\rho$, and $a_1$ mesons. Coherent scattering therefore allows investigation of the PCAC hypothesis and hadron dominance models of the weak current in detail [37].

A number of calculations of coherent scattering, involving substantially different procedures and assumptions, have been made over the past thirty years[38, 39, 40, 41]. These calculations factorize the problem in terms of the hadron-like component of the weak current and the scattering of this hadron with the nucleus. The calculations assume PCAC as a starting point but quickly diverge when it comes to the number of hadronic states required to describe the weak current and how the hadron–nucleus scattering should be treated. The Rein-Sehgal model, used by both NUANCE and NEUGEN, describes the weak current only in terms of the pion field; the $Q^2$ dependence of the cross-section is assumed to have a dipole form. Other calculations rely on meson-dominance models[40] which include the important contributions from the $\rho$ and $a_1$ mesons. Figure 11 shows the coherent charged-current cross-section as a function of energy, compared to the model of Rein and Sehgal as implemented in NEUGEN and the calculation in [41].

### 3.3 Experimental Studies of Coherent Production

MINER$\nu$A, with its high-intensity, wide-band beam, excellent pattern recognition capabilities, good electromagnetic calorimetry, and variety of nuclear targets, has the potential to greatly improve our experimental understanding of coherent neutrino scattering processes. The variety of nuclear targets - from carbon to lead - in MINER$\nu$A make possible a detailed measurement of the A-dependence of the coherent cross-section. An additional strength of the experiment is its strong pattern recognition capabilities for both the neutral-current and charged-current channels. Identified samples of charged-current coherent events can be used to study the differential cross-sections for coherent scattering. Comparion of the total rates for neutral- and charged-current production, and their pion energy and angular distributions will also provide useful tests of the various models. Several recent models predict CC/NC ratios differing by around 20% [38, 41].

Systematic comparison of charged- and neutral-current coherent production is currently a topic of considerable interest. In the low energy range there is very limited data on either process from bubble chamber experiments, and data from K2K and MiniBoone is only now exploring at least the neutral-current process at $\sim$ 1 GeV in carbon and oxygen. While data on single $\pi^0$ production from these experiments are in reasonable agreement with predictions [42, 43], study of the charged-current process is limited by detector capabilities and because the $Q^2$ distribution for all inelastic events shows a strong

| Experiment | Reaction | Energy (GeV) | A | Signal | Ref |
|---|---|---|---|---|---|
| Aachen-Padova | NC | 2 | 27 | 360 | [47] |
| Gargamelle | NC | 2 | 30 | 101 | [48] |
| CHARM | NC | 20-30 | 20 | 715 | [49] |
| CHARM II | CC | 20-30 | 20 | 1379 | [50] |
| BEBC (WA59) | CC | 5-100 | 20 | 158 | [51, 52] |
| SKAT | CC (NC) | 3-20 | 30 | 71 (14) | [53] |
| FNAL 15' | NC | 2-100 | 20 | 28 | [54] |
| FNAL 15' E180 | CC | 10-100 | 20 | 61 | [55] |
| FNAL 15' E632 | CC | 10-100 | 20 | 52 | [56] |

Table 3: Existing measurements of coherent pion production[37].

depletion at low $Q^2$ compared to Monte Carlo predictions [44, 45]. Numerous explanations for this low $Q^2$ anomaly have been suggested [17, 46]. Since coherent events occur at low $Q^2$, they have been under scrutiny as a possible contributor to the disagreement. Empirically it has been noted that the discrepancy could be largely resolved by eliminating charged-current coherent interactions from the Monte Carlo entirely. While this suggestion is a drastic one, it does point out the need for better understanding of charged-current coherent scattering in the several-GeV region. The remainder of this section summarizes simulated analyses carried out on coherent interactions in MINER$\nu$A.

### 3.3.1 Charged-current cross-section

The kinematics of coherent scattering are quite distinct compared to the more common deep-inelastic and resonant interactions. Because the coherence condition requires that the nucleus remain intact, low-energy transfers to the nuclear system, $|t|$, are needed. Events are generally defined as coherent by making cuts on the number of prongs emerging from the event vertex followed by an examination of the t distribution, where t is approximated by:

$$-|t| = -(q - p_\pi)^2 = (\Sigma_i(E_i - p_i^{||}))^2 - (\Sigma_i(p_i^{\perp}))^2 \tag{5}$$

With its excellent tracking capabilities, MINER$\nu$A's inner detector can measure this kinematic variable well.

To quantify MINER$\nu$A's ability to measure the charged-current coherent cross-section, a Monte Carlo study was carried out using the GEANT detector simulation described in Section 11.2. Analysis cuts were tuned on a sample of coherent interactions corresponding to a four-year run with the three-ton fiducial volume (24630 events). Events were generated according to the appropriate mix of low, medium, and high energy beams. This study used the Rein-Seghal [38] model of coherent production, as implemented in NEUGEN3. A low-energy beam sample containing all reaction channels was used for background determination. Based on published bubble chamber analyses, charged-current reactions should be the largest background contributor, in particular quasi-elastic and $\Delta$-production reactions where the baryon is mis-identified as a pion or not observed. To isolate a sample of coherent interactions, a series of cuts are placed on event topology and kinematics.

**Topological cuts** An initial set of topological cuts are applied to isolate a sample of events which contain only a muon and charged pion. These cuts are based on the hit-level and truth information as provided by the GEANT simulation.

1. **2 Charged Tracks:** The event is required to have 2 visible charged tracks emerging from the event vertex. A track is assumed to be visible if it produces at least 8 hit strips in the fully active region of the detector which are due to this track alone.

2. **Track Identification:** The two tracks must be identified as a muon and pion. The muon track is taken to be the most energetic track in the event which does not undergo hadronic interactions. The pion track is identified by the presence of a hadronic interaction. The pion track is required not to have ionization characteristic of a stopping proton (which is assumed can be identified 95% of the time).

3. **$\pi^0$/neutron Energy:** Because MINER$\nu$A is nearly hermetic we also assume that neutral particles will produce visible activity which can be associated with the event and used to exclude it. Events with more than 500 MeV of neutral energy ($\pi^0$ or neutron) produced in the initial neutrino interaction are rejected.

4. **Track Separation:** To make good measurements of the two tracks, the interaction point of the pion must be more than 30 cm from the primary vertex, and at this interaction point, at least 4 must strips separate the two tracks in at least one view.

**Kinematic cuts** Because coherent and background processes have very different kinematics, cuts on kinematic variables are effective in isolating the final sample. In this analysis, the true pion and muon 4-momenta were used as the reconstruction values. For the final event rates we reduce our overall signal sample by 0.65 to account for this short-cut. The difference between true and reconstructed variables obviously depends strongly on the pattern recognition and reconstruction capabilities of the detector, and this value is considered reasonable for reconstruction of the event kinematics for coherent events. Figure 17 shows the true and reconstructed angular distributions for neutral pions produced via the neutral-current reaction, in this case the difference between truth and reconstructed quantities is negligible.

1. **$x_{Bj} < 0.2$:** Requiring Bjorken-$x$ (as reconstructed from the observed pion and muon 4-momenta) less than 0.2 eliminates much of the background from quasi-elastic reactions with $x_{Bj} \sim 1$.

2. **$t < 0.2$ (GeV/c)$^2$:** The most powerful variable for the identification of coherent events is the square of the 4-momentum transfer to the nucleus. Equation 5 relating t to the observed particles in the event is used as the estimator of this quantity.

3. **$p_\pi > 600$ MeV:** Requiring $p_\pi > 600$ MeV effectively eliminates background from $\Delta$ excitation, which tends to produce lower energy pions.

The cumulative effect of these cuts on the signal and background samples is shown in Table 3.3.1, and the signal and background distributions for several of the important cut variables are shown in Figure 13. The relative normalizations of the two distributions in the initial plot is arbitrary; subsequent plots show the effect of the applied cuts.

| Cut | Signal Sample | Background Sample |
|---|---|---|
| | 5000 | 10000 |
| 2 Charged Tracks | 3856 | 3693 |
| Track Identification | 3124 | 3360 |
| $\pi^o$/neutron Energy | 3124 | 1744 |
| Track Separation | 2420 | 500 |
| x<0.2 | 2223 | 100 |
| t<0.2 | 2223 | 19 |
| $p_\pi < 600$ MeV | 1721 | 12 |

Table 4: Analysis cuts to isolate a sample of coherent interactions. The cuts are described in the text.

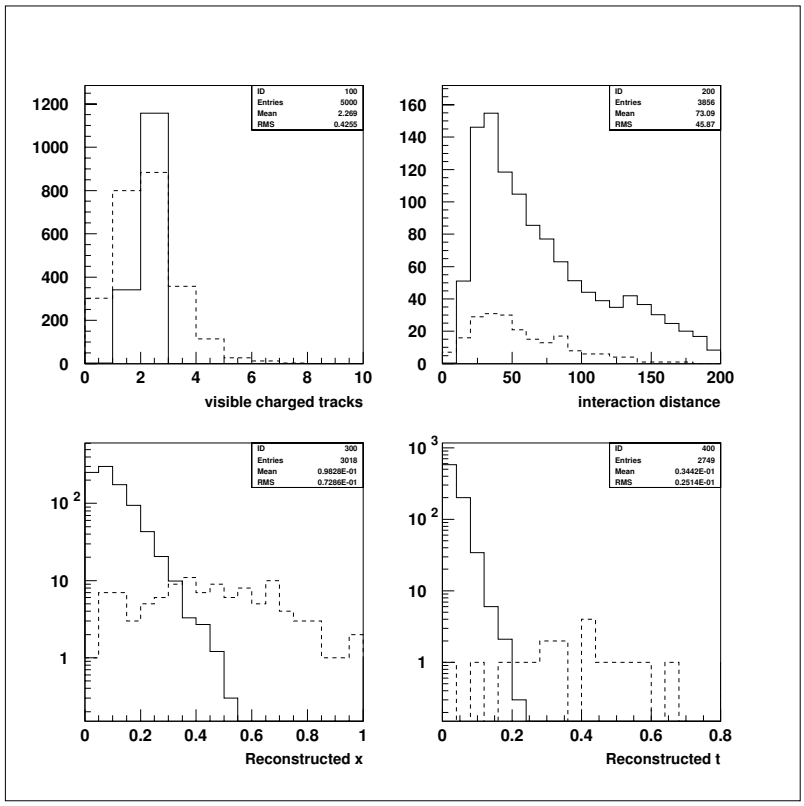


Figure 12: Topological and kinematic quantities for signal (solid) and background (dashed) processes. Top Left: Visible charged tracks. Top Right: Distance between the event vertex and the location of the pion interaction (in cm). Bottom Left: Bjorken-x as computed from the true pion and muon 4-momenta. Bottom Right: Square of the 4-momentum transfer to the nucleus (in $\mathrm{GeV}^2$) as calculated from the pion and muon 4-momenta.

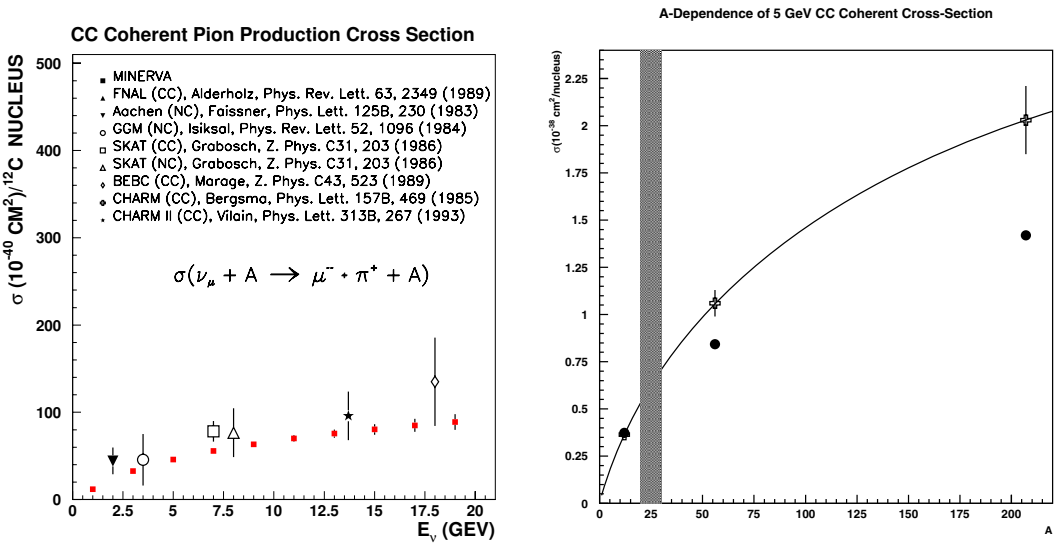


Figure 13: Left: Coherent cross-sections measured by MINER$\nu$A compared with existing published results. MINER$\nu$A errors here are statistical only. Right: Measurement of the coherent cross-section as a function of atomic number in MINER$\nu$AṪhe shaded band indicates the range of previous measurements. Error bars indicate the size of the experimental errors in a single 1-GeV bin. The curve shows the prediction from the Rein-Seghal model. Crosses are the prediction of the Rein-Seghal model for scattering from carbon, iron, and lead, circles are the predictions of the Paschos-Kartavtsev model.

Applying this set of cuts to our signal sample we find that 7698 signal events pass all cuts, which gives an overall efficiency of 31%. Applying the factor 0.65 to account for the fact that we have not used fully reconstructed quantities for our kinematic cuts gives us a final event sample of 5004 events. Applying these cuts to the background sample we find that 12 events out of 20k pass all cuts. Normalized to the total event rate, this gives an expected background of 4400 events. We note that in this analysis other important variables for background rejection, related to associated activity around the vertex, were not used. Figure 13 shows the expected precision of the MINER$\nu$A measurement as a function of neutrino energy. Here we have only included the statistical error on the signal and assumed that the measured value is that predicted by Rein-Seghal. No attempt has not been made to quantify the systematic errors on this measuerment other than that resulting from the background subtraction. Previous measurements of the coherent cross-section were statistics limited.

### 3.3.2 A-dependence of the coherent cross-section

Another task for MINER$\nu$A will be comparison of reaction rates for lead and carbon. The expected yield from lead will be $\approx$ 1800 charged-current events, assuming the same efficiency. The A-dependence of the cross-section depends mainly on the model assumed for the hadron–nucleus interaction, and serves as a crucial test for that component of the predictions. No experiment to date has been able to perform this comparison. For reference, the predicted ratio of carbon to lead neutral-current cross-sections at 10 GeV in the Rein-Sehgal and Paschos models are 0.223 and 0.259, respectively [57]. Figure 13 shows the predicted A-dependence according to the model of Rein and Sehgal.

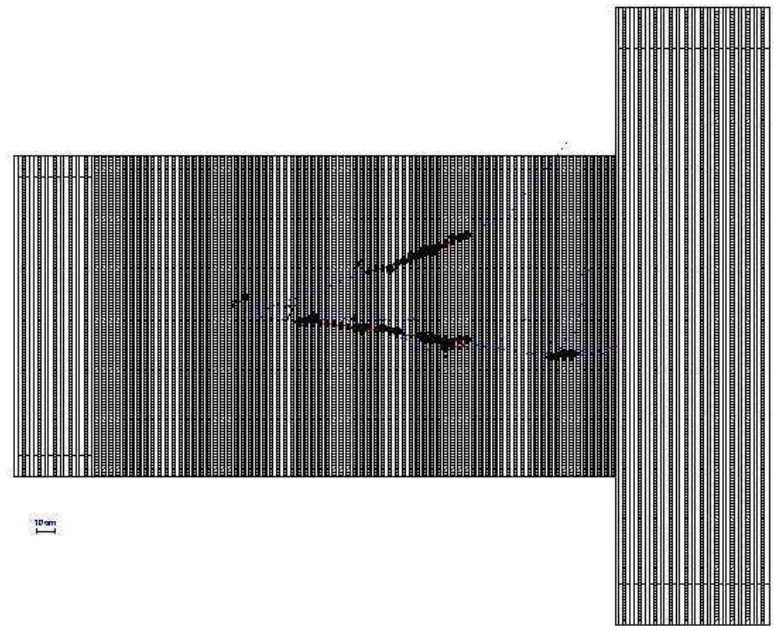

Figure 14: A simulated neutral-current coherent $\pi^0$ production event in MINER$\nu$A. The position of the $\pi^0$ decay vertex can be determined accurately by extrapolating the two photons backward. Notice that both photons pass through a number of planes before beginning to shower, distinguishing them from electrons.

### 3.3.3 Neutral-current cross-section

Neutral-current $\pi^0$ production can occur through a number of mechanisms - resonant production, coherent production, and deep-inelastic scattering. Figure 14 shows a striking example of MINER$\nu$A's response to coherent $\pi^0$ production.

By requiring two well-separated electromagnetic clusters that shower in the scintillator target, and extend at least 6 scintillator planes, about 30% of the coherent $\pi^0$ events produced in the detector are retained. Furthermore, by requiring the ratio of the energy in the two clusters to that of the total event energy to be above 90%, and requiring any extra energy to be less than 100 MeV, reduces both the $\nu_e$ ($\nu_\mu$) charged-current contamination to a few (less than one) events. Figure 15 shows these two last variables, where the coherent $\pi 0$ peak is clearly visible in the plot on the right. The resulting sample in this simple analysis (1000 events per year in 3 tons of fiducial mass) is roughly half resonant $\pi^0$ production and half coherent $\pi^0$ events, which can be separated by studying the angular and energy distribution of the events, as well as the presence or absence of additonal particles at the production vertex identified by the two photon showers.

Neutral pions from resonance excitation are neither as energetic nor as collinear as those produced coherently. Resonant $\pi^0$ are particularly susceptible to final-state nuclear interaction and rescattering, which will be studied in detail by MINER$\nu$A using charged-current reactions.

As a proof-of-concept, a sample of neutral-current single-$\pi^0$ events has been selected using simple cuts. For events with two well-separated electromagnetic clusters ($E_\pi \equiv E_1 + E_2$), each passing through at least six planes of the fully-active region, requiring $E_\pi/E_{tot} > 90\%$ and $E_{tot} - E_\pi <$ 100 MeV efficiently isolates a neutral-current $\pi^0$ sample, as shown in Figure 16. After these cuts, the contamination of $\nu_e$ and $\nu_\mu$ charged-current interactions (combined) is less than 1%. The resulting sample contains about 2400 neutral-current $\pi^0$ events per 3 ton-yr, of which half are resonant and half

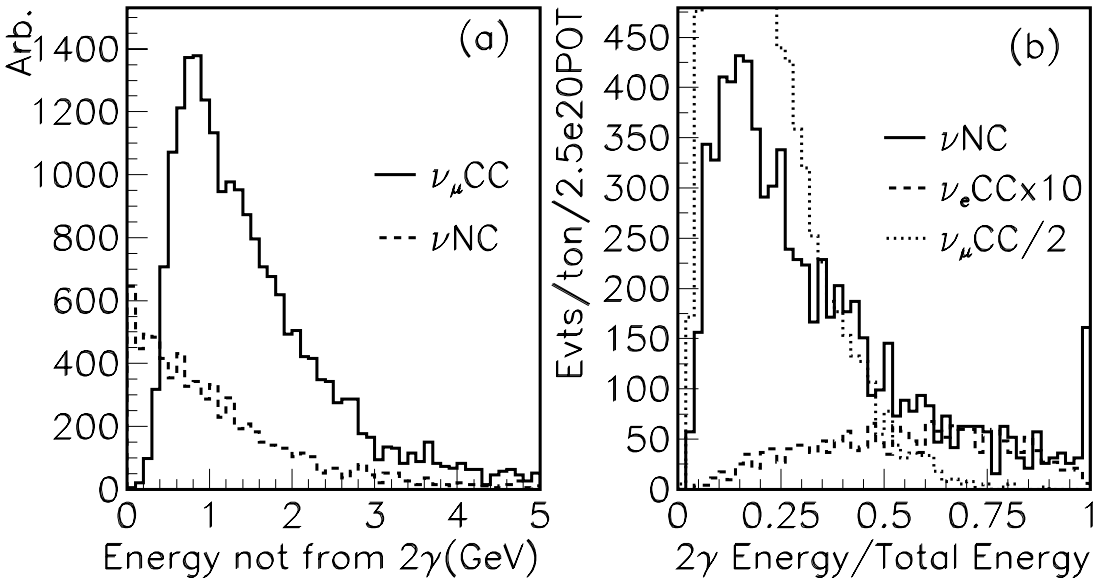


Figure 15: Variables that reject backgrounds to coherent $\pi^0$ measurements: (a) Other energy in the event for $\nu_\mu$ charged- and neutral-current events, and (b) Ratio of two photon energy to total event energy for $\nu_\mu$ charged-current sample (reduced by factor of 2), $\nu_e$ charged-current (increased by a factor of 10) and the neutral-current sample (normalized per ton per year, acceptance calculated for 3 tons fiducial volume)

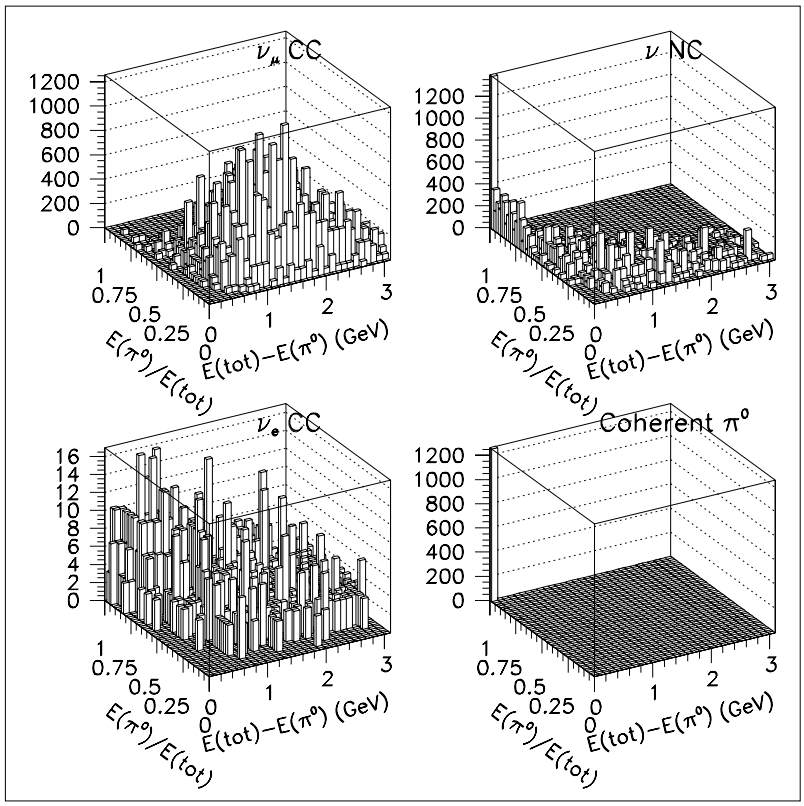


Figure 16: Selection of neutral-current single-$\pi^0$ production. The variables plotted are the fraction of visible energy carried by the $\pi^0$ candidate ($E_\pi/E_{tot}$) and the residual energy $E_{tot} - E_\pi$. The left-hand plots show backgrounds from $\nu_\mu$(top) and $\nu_e$(bottom). The plot at top right shows the same distribution for true neutral-current $\pi^0$ production, and the lower right shows the subset from coherent scattering. In the neutral-current plots, notice the dramatic concentration of the coherent $\pi^0$ signal in a single bin, in the left-most corner of the graph. All samples shown are normalized to a 3 ton-yr exposure of MINER$\nu$A.

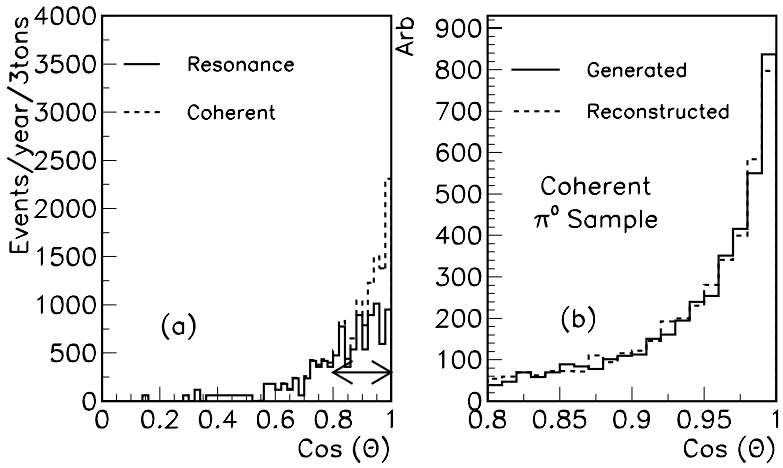


Figure 17: Angular distribution of neutral-current single-$\pi^0$ sample. The plot at left shows all events passing the cuts on $E_\pi/E_{tot}$ and $E_{tot}-E_\pi$ described in the text, broken down into coherent and resonant reactions. The coherent sample is strongly forward-peaked. The plot at right is a close-up of the forward region comparing the true and reconstructed $\pi^0$ angular distributions from the beam direction. The distributions are nearly identical, highlighting the MINER$\nu$A's excellent angular resolution.

coherent.

Coherent and resonant interactions can be cleanly separated by cutting on the $\pi^0$ angle to the beam direction, as shown in Figure 17, which also highlights MINER$\nu$A's excellent $\pi^0$ angular resolution. The overall efficiency for selecting coherent neutral-current $\pi^0$ is about 40%.

# 4 Resonant Pion Production

## 4.1 Introduction

Simulations of resonant reactions rely on an early theoretical model by Rein & Sehgal [58] or results from electro-production experiments, since existing neutrino-induced resonant production data is inadequate. The theoretical and experimental pictures of the resonant and transition regions are far more obscure than quasi-elastic and deep-inelastic scattering. Since important backgrounds to present and proposed neutrino oscillation experiments originate from this poorly-understood regime, resonant pion production, careful study by MINER$\nu$A is vital.

Analysis of resonance production in MINER$\nu$A [59] will focus on several experimental channels, including inclusive scattering in the resonant region ($W < 2$ GeV) and exclusive charged- and neutral-pion production. To date, efforts have focused on MINER$\nu$A's performance for inclusive resonant production, particularly near the $\Delta(1232)$ resonance. This preliminary analysis indicates that the resolution on $W$ is about 100 MeV around the $\Delta$, and the $Q^2$ resolution is better than 20%. Despite this resolution smearing, and distortion introduced by Fermi motion of bound nucleons in carbon, the $\Delta$ peak is still clearly visible in the reconstructed $W$ distribution.

## 4.2 Analysis of Existing Data

Inclusive electron- and neutrino-nucleon scattering with $W < 2$ GeV is dominated by resonance excitation. The large number of possible form-factors can be reduced through several assumptions. The prominent resonances are $P_{33}(1232)$, $S_{11}(1535)$, $P_{11}(1440)$ and $D_{13}(1520)$. The $P_{33}(1232)$ has the largest contribution and must be understood. In electroproduction, the magnetic dipole term dominates, and emphasizes to one of the vector form-factors, $C_3^V$, with a $Q^2-$dependence steeper than the dipole parameterization. The contribution of $C_5^A$ is determined by PCAC and also has a steeper $Q^2-$dependence than the phenomenological dipole form. It is worth pursuing this program to see if these two form-factors are sufficient. Current wisdom is that form-factors steeper than the dipole reflect the larger size of the resonant states, due to the mesonic cloud surrounding them. A simplified model has been developed by Paschos, Sakuda and Yu[60], and describes existing data (within the large experimental uncertainties and inconsistencies mentioned below).

One inconsistency concerns the $Q^2-$dependence. Two older experiments at ANL[61] and BNL[62] have noticed a difference between the data and theoretical predictions for $Q^2 < 0.2$ (GeV/c)$^2$. It appears that the same problem is apparent in newer experiments like K2K[64] in the same region of $Q^2$. The BNL data can be fitted with the form-factors used in [60], except for $Q^2 < 0.2$ (GeV/c)$^2$ where the data falls faster than the theoretical curve (see Figure 18).

The muon mass, which influences the results in this region of $Q^2$, was neglected in previous theoretical calculations.[3] The effect of the muon mass can be seen from the Figure 18: it reduces the cross-section at small $Q^2$, in agreement with the experimental trends. Summarizing these results: older measurements of $d\sigma/dQ^2$ at ANL and BNL show a suppression at low $Q^2$ which is not understood, and the $Q^2$ dependence of the form-factors is steeper in the ANL data. Thus, new experiments are needed to resolve this discrepancy and better constrain theoretical models.

Better understanding of resonant production is also vital for quasi-elastic measurements. The pion

[3] The muon mass has always been included in recent, experimentally-developed Monte Carlo programs like NEUGEN and NUANCE, however.

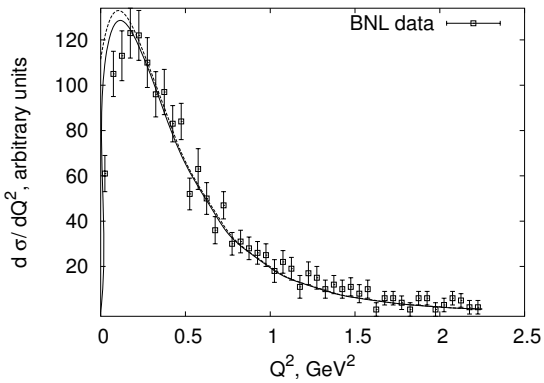


Figure 18: The cross-section $d\sigma/dQ^2$ from BNL compared with fits from PSY[60]. The full lines are for $m_\mu = 0.105$ GeV/c$^2$, the dashed lines are for the approximation $m_\mu = 0$.

from a resonant excitation can be absorbed in the nucleus, resulting in an important experimental background to quasi-elastic scattering.

More issues remain to be investigated in resonant production. Near the $\Delta$, an isospin-1/2 amplitude is observed in electroproduction. As higher resonances cannot contribute much strength in this region, the amplitude must be a non-resonant background. The importance of this background grows with $Q^2$, to become the dominant term in deep-inelastic scattering.

Nuclear effects are significant in resonant reactions, via pion absorption and charge-exchange processes. A good "rule of thumb" is that in lepton-nucleus reactions on a light target such as $^{12}$C or $^{16}$O, pions with the same charge as the exchanged current are suppressed by $30-40\%$, and pions of different charge are slightly enhanced. For instance, in the neutrino charged-current reactions the $\pi^+$ yield is reduced. Half of this reduction is due to absorption and the remainder comes from change exchange of $\pi^+$ into $\pi^0$ and $\pi^-$. Since single-pion production is an important background to be subtracted in $\nu_e$ appearance and nucleon decay searches, uncertainties in final-state interactions will directly affect their ultimate sensitivity.

MINER$\nu$A can improve the situation with precision measurements of $d\sigma/dQ^2$, $d\sigma/dW$ and total cross-sections, to further constrain the form-factors and test final-state interaction models.

### 4.3 MINER$\nu$A Performance

Analysis of resonant production in MINER$\nu$A will focus on several experimental channels including inclusive scattering $(\nu, \mu^-)$ for $W < 2$ GeV, neutral-pion production $(\nu, \mu^-\pi^0)$ and charged-pion production $(\nu, \mu^-\pi^\pm)$. Unlike inclusive charged-lepton scattering (i.e. $(e, e')$), measurements of neutrino inclusive scattering with wide-band neutrino beams cannot rely solely the outgoing lepton kinematics, since the incident neutrino's exact energy is *a priori* unknown. This section focuses on performance for inclusive resonance production, particularly near the $\Delta(1232)$. A brief discussion of more sophisticated kinematic reconstruction possibilities is included at the end of this chapter. In an inclusive analysis, reconstructing the kinematics of an event ($Q^2$, $W$ and $y$) requires calculating the neutrino energy by estimating the hadronic energy and adding it to the much more precisely known $E_\mu$.

$E_h$ can be estimated by tracking and identifying every particle emerging from the scattering vertex,

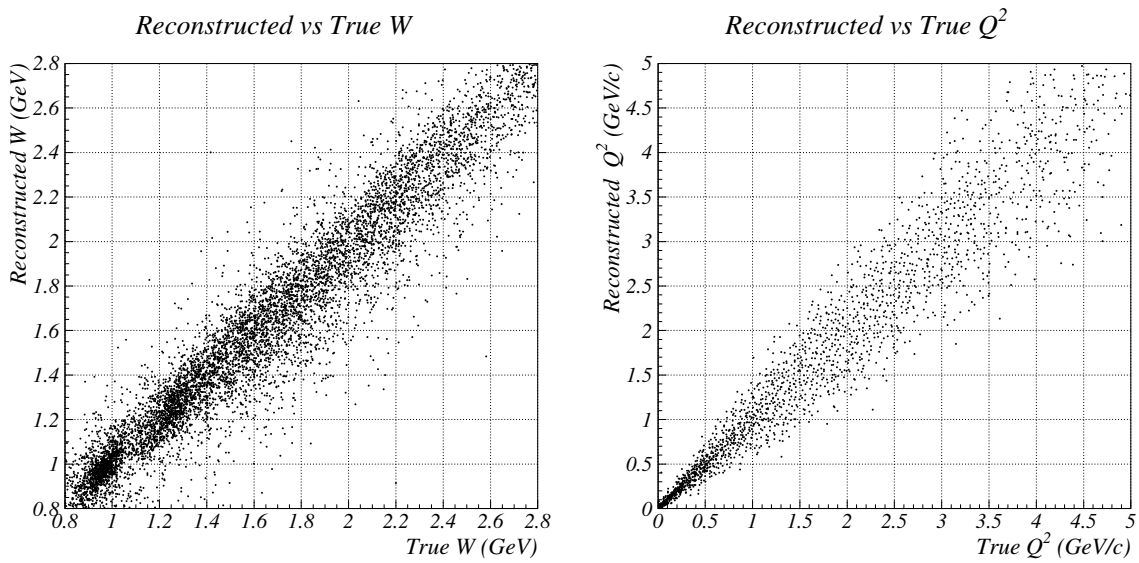


Figure 19: Correlation between true and reconstructed $W$ (left) and $Q^2$ (right).

or by summing up the $dE/dx$ energy deposited by all the reaction products (other than the muon). Tracking will be an important technique for analysis of resonance production, as primary vertex multiplicities will be low (typically $\mu + \pi + N$). However, calorimetric measurement of $E_h$ will be essential for inclusive resonance production, to minimize biases and because pions have a non-negligible probability of interaction or decay before stopping. For interacting and decaying particles, the energy not seen by active detector elements must be estimated.

As described in Section 11.4.6, MINER$\nu$A is an excellent hadronic calorimeter, with full hermeticity up to $E_h \sim 8$ GeV, and 90% containment up to $E_h \sim 15$ GeV, far above the region of interest for resonance channels. The $E_h$ resolution measured with simulated data can be described by

$$\frac{\Delta E_h}{E_h} = 4\% + \frac{18\%}{\sqrt{E_h(\mathrm{GeV})}}.$$

The kinematics of resonant events are reconstructed using $E_h$, and an assumed muon momentum resolution $dP/P = 9\%$. Figure 19 shows the good correlation of true $W$ and $Q^2$ with reconstructed quantities based on measured $E_h$. The $W$ and $Q^2$ resolutions obtained from the fit are shown in Figure 20. The $W$ resolution is about 100 MeV in the region of the $\Delta$, and the $Q^2$ resolution is slightly better than $0.2\ Q^2$. The effect of this smearing is shown in Figure 21 where the $\Delta$ peak is still visible in the $W$ spectrum from reconstructed kinematics. It is important to note that the $\Delta(1232)$ is already somewhat smeared by Fermi motion, as most scatterings take place on bound nucleons in carbon. Also note that a more mature analysis could correct for resolution smearing, yielding an even better measurement of the line-shape.

## 4.4 Conclusion

Thanks to its enormous samples and excellent resolution, MINER$\nu$A will perform the world's best measurements of resonant pion production by neutrinos, a process of primary importance to future

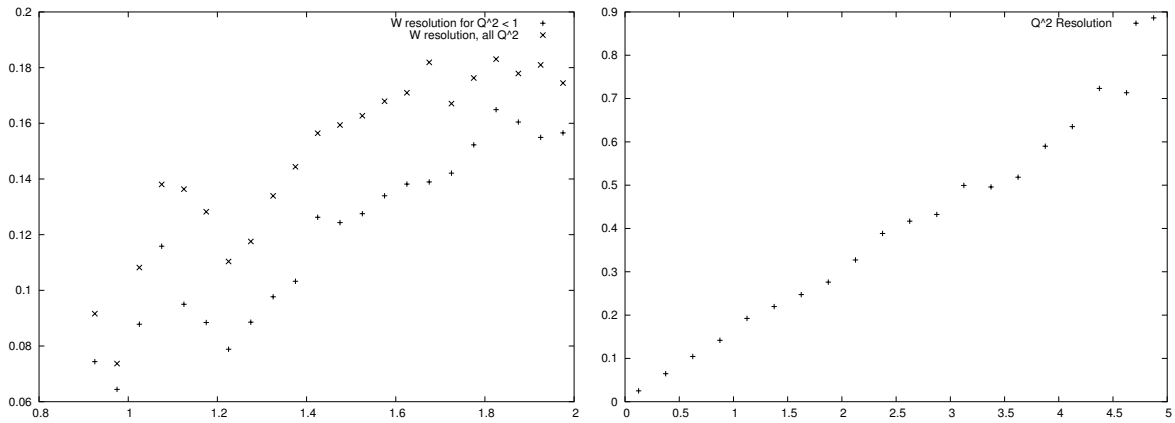


Figure 20: Resolution of $W$ (left: units of GeV) and $Q^2$ (right: $(\mathrm{GeV/c})^2$) for fully-contained resonant interactions. $W$ resolution is shown for all events ($\times$) and events with $Q^2 < 1$ (GeV/c)$^2$ ($+$).

oscillation and nucleon-decay experiments, and essential to better understanding the axial structure of the nucleon.

Analysis methods are being developed to exploit MINER$\nu$A's tracking capability and refine the kinematic reconstruction of low-multiplicity resonant events. For instance, $E_\nu$, $W$ and $Q^2$ can also be estimated if only a single hadron's momentum and direction are measured (in addition to the lepton). Reconstruction is also possible if the directions of both hadrons (but neither momentum) is measured. These kinematic fitting techniques will complement the calorimetric approach described above. A fully-developed analysis will leverage all available information, including measurement errors, for optimal performance, permitting a more accurate determination of $W$ in the neighborhood of the $\Delta$ and improving the analysis of resonant events.

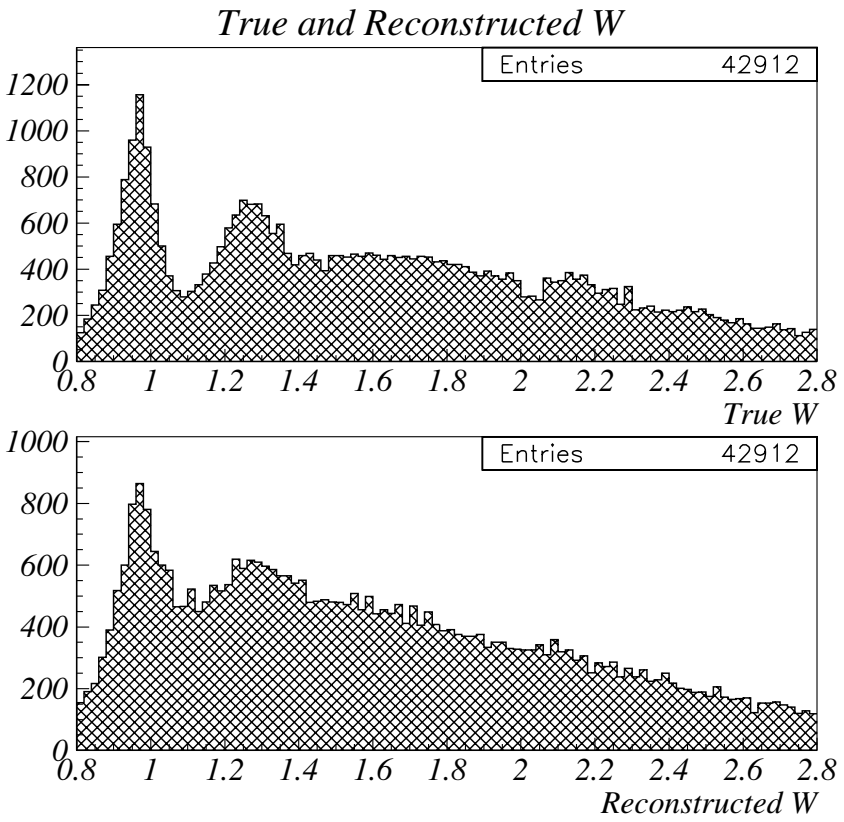


Figure 21: (Top) True $W$ distribution for resonant events with $Q^2 < 1$ (GeV/c)$^2$. (Bottom) Reconstructed $W$ distribution for the same $Q^2$ range.

# 5 Strange and Charm Particle Production

High-statistics studies of exclusive strange-particle production by neutrinos will be possible for the first time in MINER$\nu$A. Sample sizes for several channels accessible to MINER$\nu$A in a four-year $\nu_\mu$ run are summarized in Table 5.3. Our results will impact other areas of particle physics, for example in estimation of atmospheric neutrino $\Delta S$ backgrounds to nucleon-decay searches. MINER$\nu$A's physics program will also include searches for new processes, *e.g.* strangeness-changing neutral-current reactions and unusual baryon resonances such as the recently reported candidate pentaquark state in $K^+n$ and $K_s^0p$ systems. Extended running of the NuMI beam with $\bar{\nu}$ exposures will provide valuable data for many neutrino topics. Anti-neutrino exposure will facilitate study of $\Delta S = 1$ single-hyperon production $(\Lambda, \Sigma, Y^*)$, and would permit a novel measurement of CKM matrix elements. The major topics and their motivations are described below.

## 5.1 Backgrounds to Nucleon Decay

Current lifetime limits for nucleon decay ($\tau/\beta \geq 10^{33}$ years) have not diminished hopes for the eventual success of super-symmetric grand unification (SUSY GUTs). Indeed, there is strong motivation to proceed with more ambitious experimental searches. For the near future, improved searches will be carried out by Super–Kamiokande. Eventually these will be taken up by a next generation of underground detectors. Continued progress, either by improving limits to $10^{34}$ year lifetimes or discovering nucleon decay, hinges upon improved knowledge of certain neutrino interactions which, when initiated by atmospheric neutrinos, can imitate nucleon-decay signals. The most problematic of background reactions to SUSY GUT modes arise with neutral-current associated production of strangeness at threshold energies.

## 5.2 Measurement of $\sigma(\nu\Lambda K^+)$

We propose to measure the exclusive $\Delta S = 0$ neutral-current channel

$$\frac{d\sigma}{dE_\nu}(\nu_\mu p \to \nu_\mu K^+\Lambda), \tag{6}$$

from its threshold at $\approx 1$ GeV through its rise and plateau at $E_\nu$ between 10-15 GeV. For purposes of comparison and as a valuable check on systematics[65], we will simultaneously measure the the $\Delta S = 0$ companion charged-current reaction

$$\frac{d\sigma}{dE_\nu}(\nu_\mu n \to \mu^- K^+\Lambda). \tag{7}$$

## 5.3 Strangeness-changing Neutral Currents

Strangeness-changing neutral-current reactions have never been observed. Their occurrence at rates accessible in NuMI would imply new physics beyond the Standard Model. Existing limits on NC $\Delta S = 1$ processes are based upon searches for rare $K$ decays. Although there are experimental difficulties with unambiguous identification of such processes in neutrino reactions, there is nevertheless an opportunity for a search in the neutrino sector. A search for strangeness-changing neutral-current neutrino interactions can usefully clarify the extent to which new physics parameters may be missing from the analysis of weak radiative hyperon decays. It is plausible that neutrino reactions, in contrast to hyperon weak decays, may provide cleaner signals for a new weak current, since multi-loop quark-gluon diagrams which complicate hyperon decay analysis would be absent.

| Reaction Type | Exclusive Channel | No. Events ($\geq 0$ constraint) |
|---|---|---|
| $\Delta S = 0$ CC | $\nu_\mu n \rightarrow \mu^- K^+ \Lambda^0$ | 10,500 |
| | $\nu_\mu n \rightarrow \mu^- \pi^0 K^+ \Lambda^0$ | 9,300 |
| | $\nu_\mu n \rightarrow \mu^- \pi^+ K^0 \Lambda^0$ | 6,300 |
| | $\nu_\mu n \rightarrow \mu^- K^- K^+ p$ | 5,100 |
| | $\nu_\mu p \rightarrow \mu^- K^0 K^+ \pi^0 p$ | 1,500 |
| $\Delta S = 1$ CC | $\nu_\mu p \rightarrow \mu^- K^+ p$ | 15,900 |
| | $\nu_\mu n \rightarrow \mu^- K^0 p$ | 2,400 |
| | $\nu_\mu n \rightarrow \mu^- \pi^+ K^0$ | 2,100 |
| $\Delta S = 0$ NC | $\nu_\mu p \rightarrow \nu K^+ \Lambda^0$ | 3,600 |
| | $\nu_\mu n \rightarrow \nu K^0 \Lambda^0$ | 1,100 |
| | $\nu_\mu n \rightarrow \nu K^0 \Lambda^0$ | 2,800 |

Table 5: Event samples for kinematically constrainable exclusive strangeness production reactions, in a four-year exposure of MINER$\nu$A's three-ton inner fiducial volume.

### 5.4 Hyperon Beta-decay and Exotic Quark States

Hyperon beta-decay $A \rightarrow B\, e^- \, \bar{\nu}_e$ provides a window onto weak hadronic current form-factors and their underlying structure. Recent high-statistics measurements of these form-factors using KTeV $\Xi^0$ hyperon beta-decays have been reported[66]; the results show that the level of SU(3) breaking is very small compared to expectations of modern theories[67]. These new results have been used to extract the CKM matrix elements $V_{us}$[68] [69]. Similar studies are possible anti-neutrino interactions that produce hyperons. The hyperon decays have the added feature of a self-analyzing power of the polarization vector. Thus the fundamental form-factors and CKM matrix elements will be accessible without the hindrance of double solutions due to the missing neutrino energy.

$\Delta S = 1$ production of pentaquark states like those recently announced[70], could be greatly extended here. In regard to these pentaquark states, with the production of hyperons and mesons together, a wealth of combinations can be throughly examined to search for the full spectrum of the pentaquark family[71] of particles as well as other exotic quark combinations such as di-baryons.

### 5.5 Charm Production

Charm production in MINER$\nu$A is suppressed by the relatively low energy of its beams, hence our reach will be limited. Nevertheless, the cross-section turn-on just above threshold is is very sensitive to the bare charm mass and MINER$\nu$A can still make a valuable contribution. With the proposed beam running schedule for MINER$\nu$A we expect $\sim 6500$ charm events for a three-ton detector over the first five years, with an additional $\sim 3200$ from anti-neutrino beam running for $x_F > 0$.

# 6 Perturbative/Non-Perturbative Interface

## 6.1 Quark/Hadron Duality

Three decades after the establishment of QCD as the theory of the strong nuclear force, understanding *how* QCD works remains one of the great challenges in nuclear and particle physics. A major obstacle arises because the degrees of freedom observed in nature (hadrons and nuclei) are totally different from those appearing in the QCD Lagrangian (current quarks and gluons). The remarkable feature of QCD at large distances — quark confinement — prevents the individual quark and gluon constituents making up hadronic bound states from being examined in isolation. Making the transition from quark and gluon to hadron degrees of freedom is therefore essential to a description of nature based on first principles.

Experimentally, exploring this transition requires high-quality data in three kinematic regimes: in the scaling domain of large-$Q^2$ deep-inelastic scattering; in the hadronic region of resonances and quasi-elastic scattering; and, most importantly, in the moderate $Q^2$ region between the two, where the transition occurs. MINER$\nu$A can address this compelling topic with neutrinos for the first time. As Figure 22 demonstrates, MINER$\nu$A's pioneering measurement will span all three regimes, and provide crucial data in the transition region.

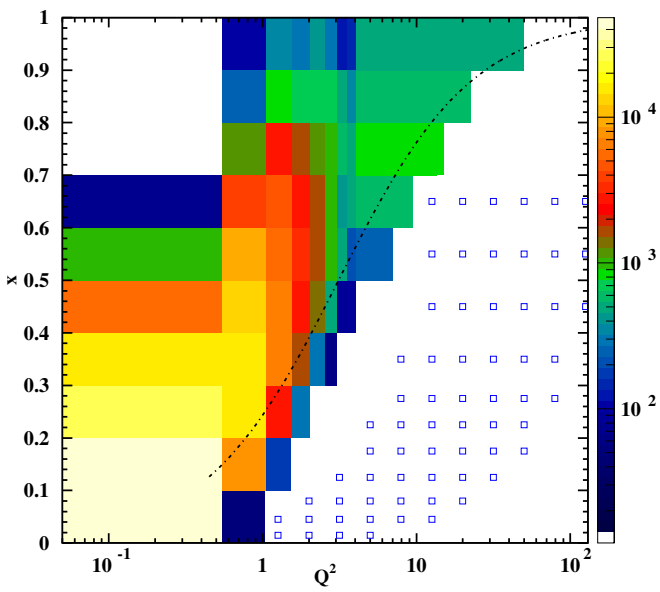


Figure 22: Available $xF_3$ data (open symbols) and the anticipated (resonant region) MINER$\nu$A data (colored distributions) in $x_{Bj}$ vs. $Q^2$. The curve indicates the commonly-accepted $W^2$ = 4 GeV$^2$ boundary between the resonant and deep-inelastic regimes. The color key to the right shows the corresponding, expected MINER$\nu$A statistics.

Despite the apparent dichotomy between the partons and hadrons, in some cases the kinematic dependence of low-energy cross-sections (averaged over appropriate energy intervals) closely follows the scaling behavior at high energies, which is expressed in terms of quark and gluon degrees of freedom. This phenomenon, *quark/hadron duality*, reflects the relationship between confinement and asymptotic freedom, and the transition between perturbative and nonperturbative QCD regimes. Such duality is

quite general and arises in other physical processes, for instance $e^+e^-$ annihilation into hadrons, and semi-leptonic decays of heavy mesons.

In electron–nucleon scattering, quark/hadron duality links the physics of resonance production to the physics of scaling; it is the focus of renewed interest in understanding the structure of the nucleon [118, 119, 120, 121, 122]. Over 10 approved experiments at Jefferson Lab address this topic, and it is a major focus area of a planned energy upgrade there. Figure 23 illustrates duality in the $F_2$ structure function measured at Jefferson Lab citereport, for nucleons and nuclei. Data in the (hadronic) resonance region average to the perturbative scaling prediction, most dramatically in the nucleus where Fermi motion facilitates the required averaging and the partonic curve and hadronic data are indistinguishable.

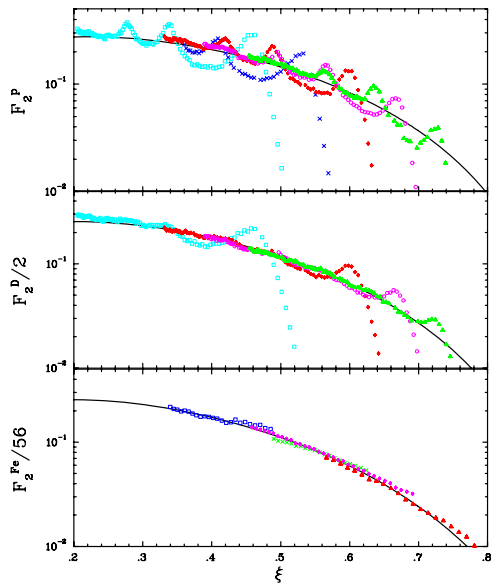


Figure 23: $F_2$ structure function per nucleon vs $\xi$ (the Nachtmann scaling variable, accounting for target mass effects) for hydrogen (top), deuterium, and iron (bottom). The data are all in the resonance region. The curves are based on a perturbative parameterization of GRV parton distribution functions at $Q^2$ = 1.0 GeV$^2$, corrected for the EMC effect. Uncertainties shown are statistical only.

Weak currents can provide complementary information (not accessible to electromagnetic probes) on the quark structure of hadrons, and allow important consistency checks on the validity of duality. While deep-inelastic neutrino structure functions are built on the same universal parton distribution functions as charged lepton scattering, the structure of resonant excitations by neutrino beams is sometimes strikingly different than those produced by virtual photons. On general grounds, duality should exist for weak structure functions [123], but its features may be quite unlike those observed in electron scattering.

Differences between electron and neutrino scattering can easily understood by considering specific resonance transitions. While a neutrino beam can convert a neutron into a proton, it cannot convert a proton into a neutron, (and *vice versa* for an anti-neutrino beam). Similarly, there are dramatic differences for inelastic production near the $\Delta$ resonance [124, 125] — because of charge conservation, only transitions to isospin-$3/2$ states from the proton are allowed.

Unfortunately, existing neutrino data are sparse in the resonance region [126], and thanks to the

small weak cross-section, often limited to heavy nuclei (since large target volumes are easier to handle and more affordable than light nuclei) [127]. As a result, no conclusive studies of duality in neutrino scattering have been possible.

The high-intensity NuMI beam at Fermilab makes possible a valuable complement to duality and resonance studies in electron scattering, and MINER$\nu$A will be an exceptional tool for such measurements. With its enormous data samples and fine-grained resolution specifically designed to accurately measure low-energy neutrino-nucleus interactions across the resonant and deep-inelastic regimes, MINER$\nu$A will be the premiere facility for exploring quark/hadron duality in neutrino scattering.

## 6.2 Structure Functions

Neutrino scattering plays a crucial role in extraction of fundamental parton distribution functions (PDFs). These PDFs describe parton constituents of protons and other hadrons, and (in the $\overline{MS}$ convention) are precisely defined in terms of operator matrix elements. The necessity of neutrino measurements is obvious, because only neutrinos can resolve the flavor of the nucleon's constituents: $\nu$ interacts with $d$, $s$, $\overline{u}$ and $\overline{c}$ while the $\overline{\nu}$ interacts with $u$, $c$, $\overline{d}$ and $\overline{s}$. The weak current's unique ability to "taste" only particular quark flavors significantly enhances the study of parton distribution functions. MINER$\nu$A's high-statistics measurement of the nucleon's partonic structure, using neutrinos, will complement ongoing studies with electromagnetic probes at other laboratories.

Large samples, and dedicated effort to minimizing beam-related systematics allow MINER$\nu$A to independently isolate all the structure functions $F_1^{\nu N}(x,Q^2)$, $F_1^{\bar{\nu} N}(x,Q^2)$, $F_2^{\nu N}(x,Q^2)$, $F_2^{\bar{\nu} N}(x,Q^2)$, $xF_3^{\nu N}(x,Q^2)$ and $xF_3^{\bar{\nu} N}(x,Q^2)$ for the first time. By taking differences and sums of these structure functions, specific parton distribution functions in a given $(x,Q^2)$ bin can in turn be determined. With the manageable systematic uncertainties expected, this experiment will dramatically improve the isolation of individual PDFs by measuring the full set of $\nu$ and $\bar{\nu}$ structure functions.

Extracting this full set of structure functions will rely on the $y$-variation of the structure function coefficients in the expression for the cross-section. In the helicity representation, for example:

$$\begin{aligned}\frac{d^2\sigma^\nu}{dxdQ^2} &= \frac{G_F^2}{2\pi x}\Big[\frac{1}{2}\left(F_2^\nu(x,Q^2)+xF_3^\nu(x,Q^2)\right)+ \\ &\quad \frac{(1-y)^2}{2}\left(F_2^\nu(x,Q^2)-xF_3^\nu(x,Q^2)\right)- \\ &\quad 2y^2F_L^\nu x,Q^2)\Big]. \end{aligned} \tag{8}$$

By analyzing the data as a function of $(1-y)^2$ in a given $(x,Q^2)$ bin, all six structure functions can be extracted.[4]

### 6.2.1 Measurement of $xF_3$

Our studies indicate that systematic uncertainties in extraction of the $xF_3$ structure function are dominated by determination of the incident neutrino energy. For high-multiplicity, deep-inelastic scattering in MINER$\nu$A this energy will be measured indirectly, by summing the energy deposited by hadrons ($E_{had}$) and the outgoing muon:

$$E_\nu = E_{had} + E_\mu - M,$$

[4]Note that for this type of parton distribution function study, anti-neutrino running will be essential.

where $M$ is the nucleon mass. Hence the neutrino energy resolution is dominated, in turn, by hadronic calorimetry.

In our Monte Carlo study of resonant scattering the hadronic energy resolution is approximately $20\%/\sqrt{E_{had}}$, with $E_{had}$ in GeV. This results in a 4–7% uncertainty for the four-momentum transfer, $Q^2$. A projected $xF_3$ structure function computed from CTEQ6M PDFs is shown in Figure 24 for three $Q^2$ values (1, 2, and 4 (GeV/c)$^2$) and a 7% $Q^2$ smearing.

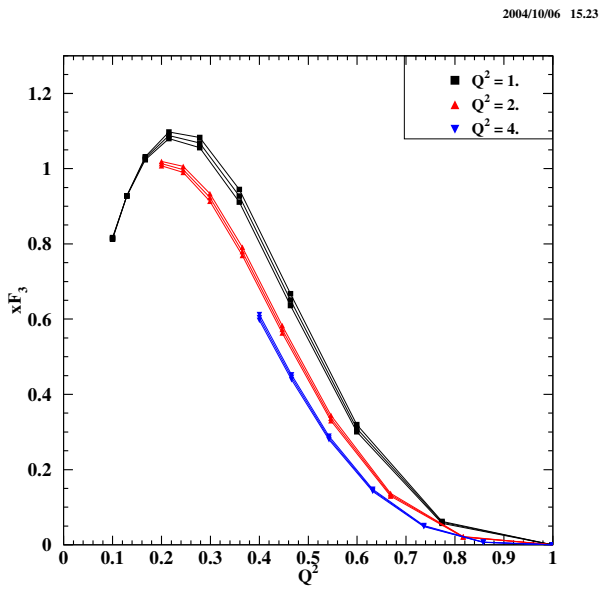


Figure 24: Variation in $xF_3$ due to uncertainty on the four-momentum transfer, $Q^2$, as described in the text.

While the variations in Figure 24 are small, $xF_3$ itself is not directly observable. In practice, yields will be measured and used to extract differential cross-sections. The neutrino/anti-neutrino differential cross-section can be expressed as a linear combination of structure functions. The helicity representation of the differential cross-section can be used to extract $xF_3$ using the the y-dependence in a given $(x, Q^2)$ bin. MINER$\nu$A is clearly capable of precision measurement in the pivotal large-$x$ region.

Note the fully active region of MINER$\nu$A provides a wealth of information for each neutrino interaction. The fine segmentation provides excellent topological identification capability, and the optical system and read-out electronics are designed to provide accurate position, pulse height, and timing information for each strip to further enhance particle identification and reconstruction. Fully exploiting this abundance of information requires sophisticated pattern recognition and reconstruction software whose development is labor-intensive and becomes a high priority only after an experiment moves out of the design/construction phase. The reconstruction software developed for this proposal was intended for optimization of the detector design rather than high-level physics analyses. It is clear that more mature reconstruction algorithms allowing full reconstruction of many-particle final states will significantly improve the performance of this analysis.

### 6.2.2 High $x_{Bj}$ measurements

MINER$\nu$A's precision measurements of parton distribution functions at high $x$ will complement a remarkable range of other experiments, from Jefferson Lab to LHC, as well as theoretical efforts to understand the dynamics of SU(6) spin/flavor symmetry breaking. The key obstacle to determining these PDFs has been accumulation of sufficient statistical power at high $x$, for light targets. As Figure 22 shows, MINER$\nu$A will probe precisely this low-$Q^2$, high-$x$ kinematic region, with a large data sample made possible by the unprecedented intensity of the NuMI beam.

Uncertainties in nucleon parton distribution functions at high $x$ arise from the flavor ratio $d(x)/u(x)$, as $x \to 1$ and the role of leading power corrections (higher twist) in extraction of high-$x$ quark behavior.

**$d(x)/u(x)$ ratio at high $x$** Available leptoproduction data on hydrogen and deuterium have been unable to pin down the high $x$ behavior of $d(x)/u(x)$. Bodek and Yang's analysis [132] indicates that $d(x)/u(x)$ approaches 0.2 as $x \to 1$. On the other hand, global QCD analyses, such as the CTEQ fits [133], do not indicate the need for this higher value.

There are several indications that current PDF parameterizations are not correct at high $x$. Comparing Drell-Yan pair production off hydrogen and deuterium (Fermilab E866 [137]) to the latest CTEQ global fits, CTEQ6 [138], suggests the valence distributions are *overestimated* at high $x$. Recent NuTeV results [139], on the other hand, imply that the valence distributions are underestimated at high $x$. As $x$ increases from 0.35, NuTeV's measurements of $F_2(x)$ deviate in the positive direction from CCFR values currently used in global fits such as CTEQ and MRST (see Figure 25). NuTeV measurements at $x$ = 0.65 are 20% higher than CCFR values for $\nu$ and almost 30% higher for $\overline{\nu}$, albeit with larger uncertainties. Since CCFR and NuTeV used the same detector, the difference is not attributable to nuclear effects.

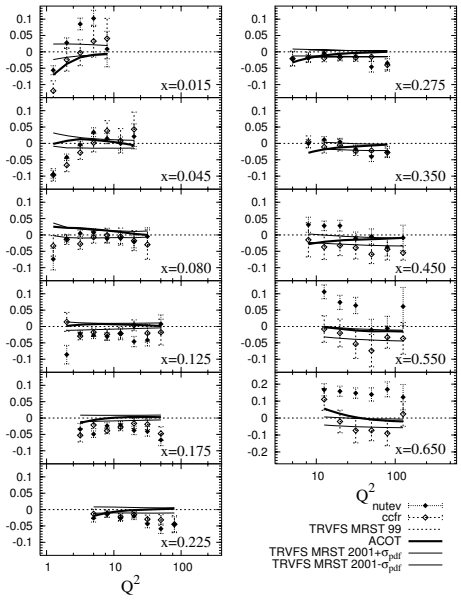


Figure 25: $F_2$ data compared to fits, from [139]. Shown is $(F_2 - F_2^{model})/F_2^{model}$

Efforts are underway to understand how the $d(x)/u(x)$ ratio affects this comparison. The flavor mixture in Drell-Yan scattering, measured in E866, approaches $4u(x) + d(x)$ as $x_{beam} \rightarrow 1$. This would suggest that $u(x)$ is overestimated and $d(x)/u(x)$ is underestimated as $x \rightarrow 1$. Full radiative corrections are only now being applied to the E866 results, however, and still-unresolved deuterium nuclear corrections have not been applied to either the E866 results or the deuterium data in the global fits. MINER$\nu$A's large sample of high-$x$ events could be valuable in resolving this anomaly.

**Higher twist corrections** PDF measurements at high $x$ are closely related to leading power corrections known as "higher twist effects". $n^{th}$-order higher twist effects are proportional to $1/Q^{2n}$ and reflect the transverse momentum of quarks within the nucleon and increased probability of multiple-quark interactions with a larger scale (or equivalently, smaller $Q^2$) probe.

As with the $d/u$ ratio, different analyses of higher twist corrections leave unresolved questions that new data may help resolve. Recent work by Yang and Bodek [134] suggests that what has been measured as "higher-twist" in charged-lepton scattering can be explained by increasing the order (NNLO) of the perturbative expansion used in the analysis.

The only measurements of a higher-twist term with neutrinos are two low-statistics bubble chamber experiments: Gargamelle [135] with freon and BEBC [136] with $NeH_2$. Both analyses were complicated by nuclear corrections at high-$x$, but found a twist-4 contribution smaller in magnitude than for charged leptoproduction and, significantly, negative.

**SU(6) symmetry breaking** Although a large body of structure function data exists over a wide range of $x$ and $Q^2$, the region $x > 0.6$ is not well sampled. MINER$\nu$A offers the first opportunity for precision measurement of this large $x$ regime with neutrinos. For $x \geq 0.4$, $q\bar{q}$ sea contributions become negligible, and the structure functions are dominated by valence quarks. Better knowledge of these valence quark distributions at large $x$ is vital for several reasons.

The simplest SU(6) quark model predicts a $d/u$ quark distribution ratio of $1/2$ for the proton, but after breaking this symmetry (as in nature), the ratio becomes much smaller. Various mechanisms have been suggested to explain why the $d(x)$ distribution is softer than $u(x)$. If the interaction between spectator quarks in a deep-inelastic collision is dominated by one-gluon exchange, for instance, the $d$-quark distribution will be suppressed, and the $d/u$ ratio will tend to zero in the limit $x \rightarrow 1$ [129]. This assumption is built into most global analyses of parton distribution functions, but has never been tested independently.

On the other hand, if the dominant mechanism in deep-inelastic scattering involves scattering from a quark with the same spin orientation as the nucleon, as predicted by perturbative QCD counting rules, $d/u$ tends to $\approx 1/5$ as $x \rightarrow 1$ [130]. Precision measurement of structure functions at large $x$ should give us new insights into the dynamics of spin/flavor symmetry breaking.

The ratio of neutron to proton structure functions at large $x$ will be a particularly interesting MINER$\nu$A measurement. Valence quark dynamics similar to charged lepton scattering are probed, but with different sensitivity to quark flavors. At the hadronic level, quark model studies reveal distinct patterns of resonance transitions to the lowest-lying positive and negative parity multiplets of SU(6) [124, 141, 142, 143]. Summing $N \rightarrow N^*$ matrix element contributions to the proton and neutron $F_1$ and $g_1$ structure functions in the SU(6) quark model yields the expected SU(6) quark-parton model results, providing explicit confirmation of duality. On the other hand, some models of spin-flavor symmetry breaking ($\lambda \neq \rho$) yield neutrino structure function ratios at the parton level which are in obvious conflict with

values from electroproduction. Neutrino data can therefore provide valuable checks on the appearance of duality and its consistency between electromagnetic and weak probes.

**LHC backgrounds** Quark distributions at large $x$ are essential to estimating backgrounds in searches for physics beyond the Standard Model at colliders on the energy frontier [131]. QCD evolution of parton distribution functions takes high-$x_{Bj}$ PDFs at low $Q^2$ and evolves them down to moderate- and low-$x$ at higher $Q^2$. One of the larger contributions to background uncertainties at LHC will be the very poorly known high-$x$ PDFs at the lower-$Q^2$ values accessible to NuMI.

**Synergy with Jefferson Lab measurements** Global analyses and MINER$\nu$A's own studies will both benefit from the significant kinematic overlap between Jefferson Lab and MINER$\nu$A data. High-precision structure function measurements at Jefferson Lab over the same $x$ and $Q^2$ ranges will provide valuable constraints on the vector coupling when extracting structure functions and PDFs from MINER$\nu$A data. In addition, Jefferson Lab data will help disentangle nuclear effects to obtain free-nucleon PDFs from bound targets.

Figure 26 shows the same $A$-dependence in low-$Q^2$ structure function data from Jefferson Lab (in the resonance regime) and high-$Q^2$ (deep-inelastic) data from CERN and SLAC [128]. This suggests that nuclear modulation of the structure functions, an easily parameterizable if not well understood effect, should be the same for MINER$\nu$A's frontier kinematic range as in the well-measured deep-inelastic regime.

Other Jefferson Lab experiments will directly address issues of final state interactions and on-shell extrapolation, which are particularly important at large $x$. A major reason the $d(x)/u(x)$ ratio is not better known is the difficulty of accessing the structure of the neutron, due to the uncertainties in extracting information from neutrons bound in nuclei. To overcome this problem, the BONUS experiment at Jefferson Lab [140] has been approved to measure inclusive electron scattering on quasi-free neutrons using a novel recoil detector with low proton momentum threshold and high rate capability. These measurements will provide unambiguous neutron structure measurements, and reveal which of the available models best describe, for instance, on-shell extrapolation for bound neutrons. This information will be invaluable for extracting nucleon structure information with MINER$\nu$A, and facilitate our own unique ability to provide flavor decomposition information.

## 6.3 Testing Lattice QCD

Finally, MINER$\nu$A can measure the structure function moments calculable in lattice QCD. Predicted moments are currently available for $Q^2 = 4$ (GeV/c)$^2$, which is accessible to MINER$\nu$A. Comparing measured moments with calculations on the lattice over a range $Q^2 \approx 1 - 10$ (GeV/c)$^2$ would allow the size of higher twist corrections and quark-gluon correlations in the nucleon to be determined. An appreciable fraction of the strength of these moments falls in resonance region. While a broad reach in $x$ at fixed $Q^2$ is required to obtain the moments, precise resonance region data are imperative. Since the first moment is an integral over all $x$, energy resolution will have a smaller effect on this moment than on structure function measurements. Flavor decomposition for PDF moments and structure functions at large $x$ and low $Q^2$ offer MINER$\nu$A a clear and unique role in testing the results of lattice QCD.

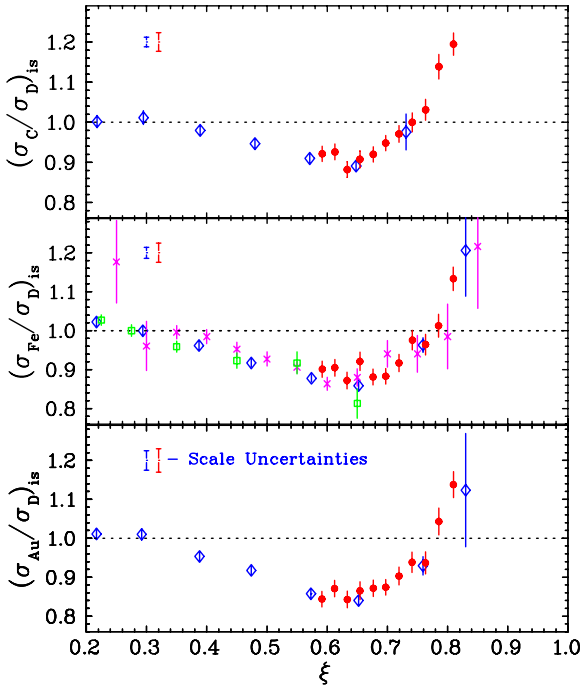


Figure 26: Ratio of nuclear to deuterium cross-sections per nucleon, corrected for neutron excess, for Carbon (top), Iron (center) and Gold (bottom) versus $\xi$. The resonance data at low $W$ and $Q^2$ from Jefferson Lab (circles) are compared with the deep inelastic data at high $W$ and $Q^2$ from SLAC E139 (diamonds), SLAC E87 (crosses), and BCDMS (squares). The scale uncertainties for the SLAC (left) and JLab (right) data are shown in the figure.

## 6.4 Summary

MINER$\nu$A is uniquely poised to provide a wealth of information crucial to carrying our understanding of the nucleon beyond a perturbative description. MINER$\nu$A is the only experiment capable of investigating quark/hadron duality in neutrino scattering. Extraction of parton distribution functions at large $x$ is becoming an increasingly important and controversial topic, in which MINER$\nu$A's contributions as the only precision neutrino experiment could be decisive. MINER$\nu$A can also investigate large-$x$ evolution, PDF ratios, and PDF moments - all part of a rich physics program at the perturbative/non-perturbative frontier.

# 7 Generalized Parton Distributions

One of the main goals of subatomic physics is to understand the structure of hadrons, and in particular the structure of the nucleon. The primary approach to this problem has been measurement of the nucleon form-factors, with (quasi-)elastic scattering (for $Q^2$ up to a few (GeV/c)$^2$), parton densities, through inclusive deep-inelastic scattering (DIS), and distribution amplitudes, through exclusive processes. However, the usual parton densities extracted from DIS are only sensitive to the longitudinal component of the parton distributions and do not give information on the transverse component, or other contributions to the nucleon angular momentum.

## 7.1 The Nucleon Spin Puzzle and GPDs

In the late 1980's, results from polarized DIS showed that a relatively small fraction, about 20%, of the nucleon spin is carried by the valence quarks. The obvious candidates for the missing spin were the quark and gluon orbital momentum and gluon helicity. However, information on those quantities cannot be extracted from DIS.

In 1997, Ji [144, 145] showed that a new class of nucleon observables, which he called "off-forward parton distributions", could be used to determine the spin structure of the nucleon. This work, along with developments by others, especially Radyuskin [146, 147] and Collins [148] showed that these distributions, now called generalized parton distributions (GPDs), had the potential to give a full three-dimensional picture of the nucleon structure. This exciting development has led to an immense amount of theoretical work in the last few years. Short reviews can be found in [149, 150] and a comprehensive review can be found in [151].

Ji showed that in leading twist there are four GPDs, which he called $H$, $\tilde{H}$, $E$, and $\tilde{E}$, for each quark flavor. $H$ and $\tilde{H}$ are nucleon helicity-conserving amplitudes and $E$ and $\tilde{E}$ are helicity-flipping amplitudes. The GPDs are functions of $x$, $\xi$ (a factor determining the "off-forwardness" of the reaction), and the total momentum-transfer squared, $t$. The GPDs can be accessed experimentally through reactions proceeding via the "handbag" diagram shown in Figure 27.

## 7.2 Deeply-virtual Compton Scattering

The most promising reaction to measure GPDs identified so far is deeply-virtual Compton scattering (DVCS). The DVCS reaction is shown in Figure 28a. An interesting feature of DVCS is that it can interfere with the Bethe-Heitler process, Figure 28b, which is completely calculable in terms of the nucleon elastic form-factors. This interference causes an asymmetry in the azimuthal distribution of the scattered proton allowing some quantities to be determined that would otherwise require a polarized target. However, DVCS involves a combination of the four GPD amplitudes, which cannot be separated using DVCS alone. Some complementary information can also be obtained from nucleon form-factor measurements and deep exclusive meson electroproduction.

Neutrino scattering provides a very similar reaction to DVCS. In this case, the virtual mediator is a $W^{\pm}$ with the production of an energetic photon, a $\mu^{\pm}$, with either a recoiling nucleon or nucleon resonance, as shown in Fig. 29. This "weak DVCS" reaction is very promising theoretically because it provides access to different GPDs than DVCS. It will help resolve the individual flavors, e.g. $d$ in neutrino scattering and $u$ in anti-neutrino scattering, and the interference of the $V$ and $A$ currents will give access to C-odd combinations of GPDs.

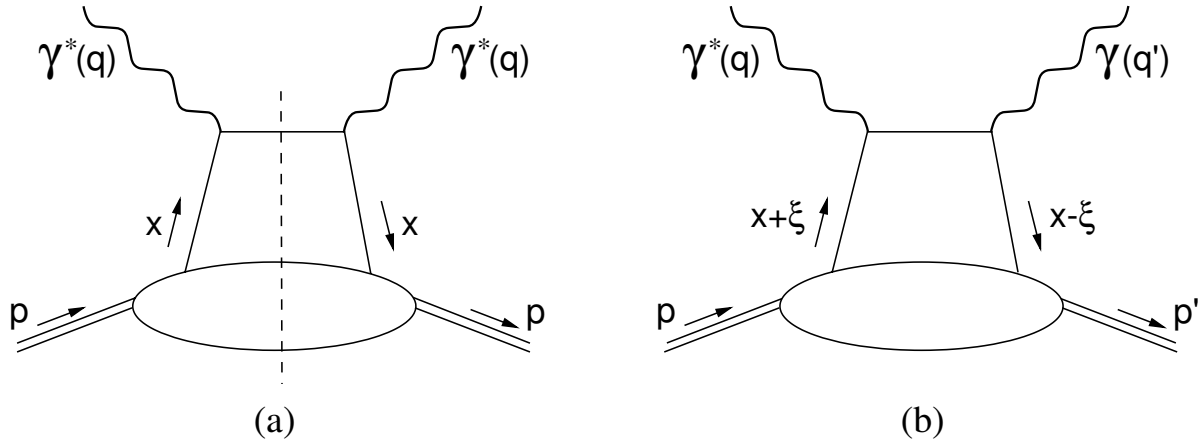


Figure 27: (a) Forward virtual Compton amplitude which describes the DIS *cross-section* via the optical theorem ($x_B = x$); (b) Handbag diagram occurring in the DVCS *amplitude*.

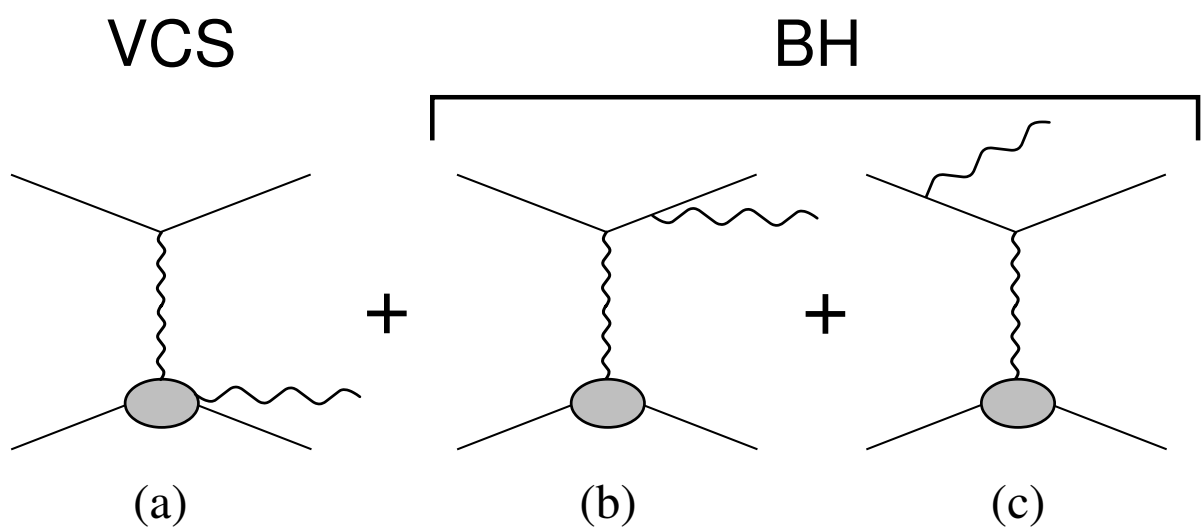


Figure 28: The DVCS process (a) along with the interfering Bethe-Heitler diagrams (b) and (c).

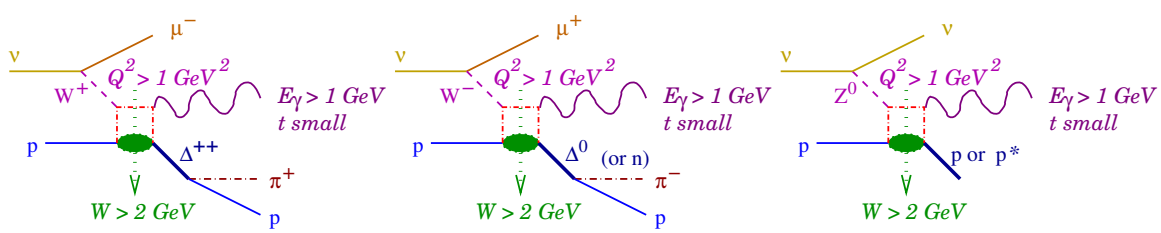


Figure 29: Reactions sensitive to GPDs in neutrino scattering.

### 7.3 Measurement of GPDs in MINER$\nu$A

Measurement of the GPDs requires measurement of exclusive processes. In addition, certain kinematic limits must be imposed to allow reliable calculations. In particular, the reaction should be above the resonance region ($W^2 > 4$ GeV$^2$), the momentum transfer should be small ($t < 0.2$ (GeV/c)$^2$), and $Q^2$ should be large ($Q^2 > 2$ (GeV/c)$^2$), which implies a high-energy photon and low-energy nucleon in the final state. Although this does present certain experimental difficulties, it should be possible to detect these for charged currents in MINER$\nu$A. A. Psaker, a student of A. Radyuskin, has made detailed calculations of the weak DVCS process for neutrinos in the 5-20 GeV range with the above kinematic constraints. He finds a cross-section of about $10^{-41}$ cm$^2$/neutron for CC reactions, with a relatively small energy dependence (the useful cross section increases slightly from 5 to 20 GeV). The cross section for protons (giving a $\Delta^{++} \rightarrow p\pi^+$ in the final state would be about half the neutron cross section. This would yield a few thousand events for the full four-year run with a 3-4 kiloton active target.

Background studies have not yet been performed, but the most significant background should be events with a photon radiated by the out-going muon. It should be pointed out that these will be primarily for reactions on neutrons in carbon, not free nucleons. We are still studying this reaction to assess the effect of extracting GPDs from a bound nucleon.

# 8 Nuclear Effects in Neutrino Scattering

## 8.1 Introduction

Most neutrino experiments, including neutrino oscillation experiments, require massive nuclear targets/detectors to obtain useful reaction rates. Analysis of neutrino reactions with nuclear media requires understanding the nuclear environment's effect on the process [72]. There are two general categories of such nuclear effects:

- The neutrino interaction probability on nuclei is modified relative to free nucleons. Nuclear effects of this type have been extensively studied using muon and electron beams, but have not been explored with neutrinos. Depending on the kinematic region, these nuclear effects can be quite different for neutrinos [73], and are important for neutrino energies typical of oscillation experiments.
- Hadrons produced in a nuclear target may undergo final-state interactions (FSI), including rescattering and absorption. These effects may significantly alter the observed final-state configuration and measured energy [74, 75], and are sizable at neutrino energies typical of current and planned neutrino oscillation experiments [112].

The hadron shower observed in neutrino experiments is actually the *convolution* of these two effects. FSI effects are dependent on the specific final states that, even for free protons, differ for neutrino and charged-lepton reactions. The suppression or enhancement of particular final states by nuclear effects also differs for neutrino and charged lepton reactions. For these reasons, measurements of nuclear effects with charged leptons cannot be applied to neutrino-nucleus interactions without considerable care.

To study these questions in MINER$\nu$A, carbon, iron and lead targets will be installed upstream of the pure scintillator active detector. To measure the overall effect of the nucleus, the observed interaction rate, hadron spectrum and multiplicity will be measured for all three targets.

## 8.2 Modified Interaction Probabilities

Pronounced nuclear effects have been measured in *charged-lepton* scattering from a number of nuclear targets. The experimental situation is discussed in review papers [77, 78].

The mechanisms of nuclear scattering have also been studied theoretically. These mechanisms appear to be different for small and large Bjorken $x$ as viewed from the laboratory system. Bjorken $x$ is defined as $x = Q^2/2M\nu$, where $\nu$ and $\boldsymbol{q}$ are energy and three-momentum transfer to the target and $Q^2 = \boldsymbol{q}^2 - \nu^2$. The physical quantity discriminating between large and small $x$ regions is a characteristic scattering time, which is also known as Ioffe time (or length) $\tau_I = \nu/Q^2$ [79]. If $\tau_I$ is smaller than the average nuclear separation between nucleons, the process can be viewed as incoherent scattering off bound nucleons. This occurs for larger $x(> 0.2)$.

At small Bjorken $x$ the space-time picture is different. The underlying physical mechanism in the laboratory reference frame can be sketched as a two-stage process. In the first stage, the virtual photon $\gamma^*$ (or $W^*$ or $Z^*$ for neutrino interactions) fluctuates into a quark-antiquark (or hadronic) state. This hadronic state then interacts with the target. The uncertainty principle allows an estimate of the average lifetime of such a fluctuation as

$$\tau = 2\nu/(m^2 + Q^2), \tag{9}$$

where $m$ is the invariant mass of the hadrons into which the virtual boson converts. The same scale $\tau$ also determines the characteristic longitudinal distances involved in the process. At small $x$, $\tau$ exceeds the average distance between bound nucleons and coherent multiple interactions of this hadronic fluctuation in a nucleus are important. It is well known that the nuclear shadowing effect for structure functions results from coherent nuclear interactions by hadronic fluctuations of virtual intermediate bosons (for a recent review of nuclear shadowing see, e.g., [78]).

### 8.2.1 Nuclear effects in the incoherent regime at large $x$

If $x$ is large enough to neglect coherent nuclear shadowing, lepton scattering off a nucleus can be approximated as incoherent scattering from bound protons and neutrons. The most pronounced nuclear effects in this region are due to Fermi-motion, nuclear binding [80, 81, 82, 83, 84, 85, 86], and off-shell modification of nucleon structure functions [85, 86, 87, 88, 91].

A widely used approximation in description of nuclear structure functions is to neglect the final state interactions of resulting hadrons with the recoiling nucleus. In this approximation the nuclear structure functions can be written as the bound nucleon structure function averaged (convoluted) with the nuclear spectral function (for derivation and more details see [82, 85, 91]). Since bound nucleons are off-shell particles their quark distributions generally depend on nucleon virtuality $k^2$ as an additional variable. Off-shell effects in structure functions can be viewed as a way to describe in-medium modification of structure functions. This effect was discussed in terms of different approaches in the literature [84, 88, 85, 87, 90, 91].

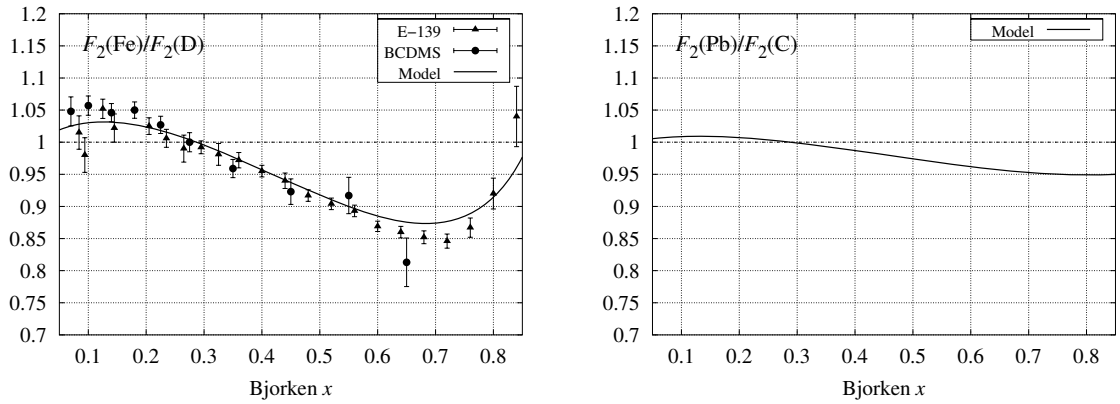


Figure 30: The ratio of iron to deuterium structure functions as measured by SLAC E-139 and CERN BCDMS collaborations in experiments with electron and muon beams (left panel). Also shown are the results of model calculation at fixed $Q^2 = 10\ \mathrm{GeV}^2$ which account for binding, Fermi-motion and off-shell effects in nuclear deep-inelastic scattering [91]. The ratio of lead and carbon structure functions calculated at fixed $Q^2 = 10\ \mathrm{GeV}^2$ within the same approach is presented in the right panel.

Predictions of the convolution approach are compared to data on charged-lepton deep-inelastic scattering in Figure 30. Model calculations of nuclear structure functions use realistic nuclear spectral functions. Data seem to indicate that some off-shell modification of bound nucleon structure function is necessary [91]. The right panel of Figure 30 displays the ratio of lead and carbon structure functions calculated within the same approach. It appears nuclear effects at large $x$ are practically saturated

in carbon. Similar effects are predicted for neutrino structure functions $F_2$ and $xF_3$. MINER$\nu$A will provide valuable information on nuclear effects in this region.

### 8.2.2 Nuclear effects at small $x$

Nuclear shadowing effects have been discussed extensively in the literature. A recent paper [78] reviews both experimental data and theoretical models of nuclear shadowing for charged-lepton scattering. This effect is interpreted as the coherent interaction of a hadronic component of the virtual photons with the target nucleus. The structure functions at small $x$ can be represented as a superposition of contributions from different hadronic states.

In fixed-target experiments events with small Bjorken $x$ are correlated with low four-momentum transfer ($Q^2$). At low $Q^2$ the vector meson dominance model (VMD) appears to be a good tool to study nuclear corrections to structure functions [78, 92]. In VMD the structure functions are saturated by contributions from a few low-mass vector meson states. For the interactions driven by the electromagnetic current usually only the isovector $\rho$ and the isoscalar $\omega$ and $\phi$ mesons are important at low $Q^2 < 1\ \mathrm{GeV}^2$ [92]. The structure functions in this model have strong $Q^2$ dependence. In the generalized versions of VMD, higher-mass states including the continuum have also been considered, making the model applicable at higher $Q^2$ [78, 92].

The VMD approach has also been applied to weak interactions [93]. The vector current, in close analogy with the electromagnetic current, is assumed to be saturated by $\rho$ meson contribution at low $Q^2$. The axial-vector channel requires inclusion of contributions from the axial-vector meson $a_1$. There are still a number of interesting physics questions related to the analysis of the axial-vector channel for neutrino interactions.

It should be emphasized that neutrino scattering at low $Q^2$ is dominated by the axial current. Indeed, contributions to the structure functions (and cross-sections) from the vector current vanish as $Q^2 \to 0$ due to vector-current conservation. The axial current is not conserved and for this reason the longitudinal structure function $F_L$ does not vanish at low $Q^2$. It was observed long ago by Adler that neutrino cross-sections at low $Q^2$ are dominated by the contribution from the divergence of the axial current [94]. The latter, because of PCAC, is saturated by the pion contribution, so low $Q^2$ neutrino cross-sections and structure functions are determined by pion cross-sections. For the longitudinal structure function at low $Q^2$ the Adler relation is

$$2xF_L^{\mathrm{PCAC}} = \frac{f_\pi^2}{\pi}\sigma_\pi(s, Q^2), \tag{10}$$

where $f_\pi = 0.93 m_\pi$ is the pion decay constant ($m_\pi$ is the pion mass) and $\sigma_\pi(s, Q^2)$ the total pion cross-section at the center-of-mass energy $s = Q^2(1/x - 1) + M^2$ for an off-shell pion with mass $\sqrt{Q^2}$. Equation (10) determines the dominant contribution to $F_2$ and neutrino cross-sections at small $Q^2$ for nucleon and nuclear targets.

It is important to realize that Eq. (10) is not a consequence of the pion dominance of the axial current, i.e. fluctuation of the axial current to a pion which interacts with the target [97]. Indeed, the single-pion fluctuation of the axial current gives a vanishing contribution to the neutrino cross-section. Instead, the axial current in neutrino interactions can produce heavy states such as the $a_1$ meson and $\rho\pi$ pair, which interact with the target. The overall contribution of all such states is described by the PCAC relation. The detailed mechanism of this phenomenon is not fully understood and MINER$\nu$A can provide new insights on physics driven by the axial current in neutrino interactions.

The strength of nuclear shadowing is controlled by mesonic cross-sections $\sigma_v$ for the vector current. In the axial-vector channel the relevant quantity is the pion cross-section. To quantitatively understand nuclear effects, the multiple scattering effect on the cross-section is calculated using Glauber–Gribov multiple scattering theory [95, 96, 92, 97]. If $l_f$ is small compared with the nuclear radius, as is the case for heavy nuclei, then multiple scattering effects are important. It should be emphasized that the multiple scattering correction is negative because destructive interference of the forward scattering amplitudes on the upstream nucleons causes *shadowing* of virtual hadron interactions on the back-face nucleons.

The onset of coherent nuclear effects can be estimated by comparing the coherence length of hadronic fluctuation $L_c$ with the average distance between bound nucleons in the nucleus $d$. For hadronic fluctuation of the vector current $L_c$ is similar to the fluctuation time $\tau$ from Eq. (9), where $m$ is the mass of hadronic state in question. Coherent nuclear effects occur if the fluctuation time is large enough $\tau > d$. This condition requires high energy transfer $\nu$ and, as is clear from Eq. (9), the coherent region begins at lower energy for smaller masses $m$. Since $\tau < 2\nu/Q^2$ for any intermediate state, the region of coherent nuclear effects is limited to small $x$ for any $Q^2$, $x < 1/Md$. Nuclear shadowing saturates if $L_c \gg R$, which happens at small $x$, and the condition $L_c \sim R$ defines the transition region with strong $x$ dependence of the ratio $\delta\sigma_A/\sigma_N$.

For the axial-vector current, the fluctuation time $\tau$ is also given by Eq. (9). However, as argued in [97], the fluctuation and coherence lengths are not the same in this case. In particular, the coherence length is determined by the pion mass $m_\pi$ in Eq. (9) because of the dominance of off-diagonal transitions like $a_1 N \to \pi N$ in nuclear interactions. Since the pion mass is much smaller than typical masses of intermediate hadronic states for the vector current ($m_\rho,\ m_\omega$, etc.), the coherence length $L_c$ of intermediate states of the axial current at low $Q^2$ will be much larger than $L_c$ for the vector current. A direct consequence of this observation is early onset of nuclear shadowing in neutrino scattering at lower energy and $Q^2$ compared to charged-lepton scattering.

Figure 31 shows the calculated ratios of iron to nucleon and lead to carbon structure functions at two different $Q^2$ values as a function of $x$. We also compare the nuclear shadowing effect for muon and neutrino scattering. The basic reason for the earlier onset of nuclear shadowing in neutrino scattering and different behavior in the transition region is the difference in correlation lengths of hadronic fluctuations between the vector and axial-vector currents. This is also illustrated by the observation that for a given $Q^2$ the cross-section suppression due to shadowing occurs for much lower energy transfer ($\nu$) in neutrino interactions than for charged leptons.

The relative nuclear shadowing effect for the structure function $xF_3$ should be substantially different than that of $F_2$ [98]. This is because $xF_3$ describes the correlation between the vector and the axial-vector current in neutrino scattering. In terms of helicity cross-sections, $xF_3$ is given by the cross-section asymmetry between the left- and right-polarized states of the virtual $W$ boson. It is known that such a difference of cross-sections is strongly affected by Glauber multiple scattering corrections in nuclei. This leads to enhanced nuclear shadowing of $xF_3$.

The resulting ratio of lead and carbon structure functions are shown in Figure 32. Unlike nuclear effects at large Bjorken $x$ (Figure 30), there are substantial, structure-function dependent nuclear effects at small $x$. MINER$\nu$A can provide a unique tool to study these effects.

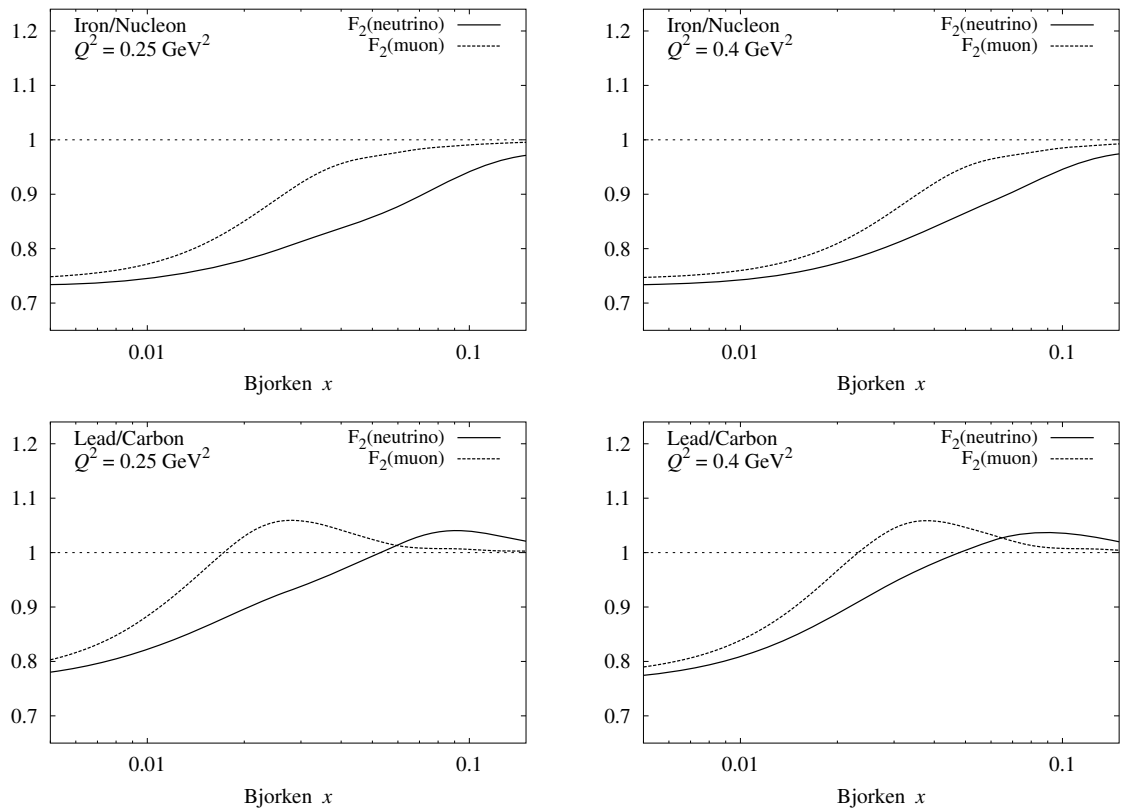


Figure 31: The ratio of iron to nucleon (upper row) and lead to carbon neutrino CC structure functions $F_2^\nu$ calculated at two different $Q^2$ within an approach based on PCAC and VMD (solid line). The dashed line shows similar ratios for the muon structure function $F_2^\mu$.

### 8.2.3 Determination of $\sin^2\theta_W$

The rates of neutral-current (anti-)neutrino scattering are directly determined by $\sin^2\theta_W$. Therefore the measurement of NC/CC ratios of neutrino cross-sections provides a valuable tool for determination of $\sin^2\theta_W$. For an isoscalar target (e.g. the isoscalar combination of proton and neutron, or for deuterium) a relation between neutrino–antineutrino asymmetries in the NC and CC DIS cross-sections was derived by Paschos and Wolfenstein [99]

$$R^- = \frac{\sigma^\nu_{\rm NC} - \sigma^{\bar\nu}_{\rm NC}}{\sigma^\nu_{\rm CC} - \sigma^{\bar\nu}_{\rm CC}} = \frac{1}{2} - \sin^2\theta_W, \tag{11}$$

where $\theta_W$ is the weak mixing angle. A similar relation also holds for the NC/CC ratio of structure functions

$$F_3^{\rm NC}(x,Q^2)/F_3^{\rm CC}(x,Q^2) = 1 - 2\sin^2\theta_W, \tag{12}$$

where $F_3^{\rm CC}$ is the neutrino and antineutrino averaged structure function, $F_3^{\rm CC} = (F_3^\nu + F_3^{\bar\nu})$.

If only the contributions of light quarks are taken into account, the PW relationship is a direct result of isospin symmetry. This ensures that various strong interaction effects, including nuclear effects,

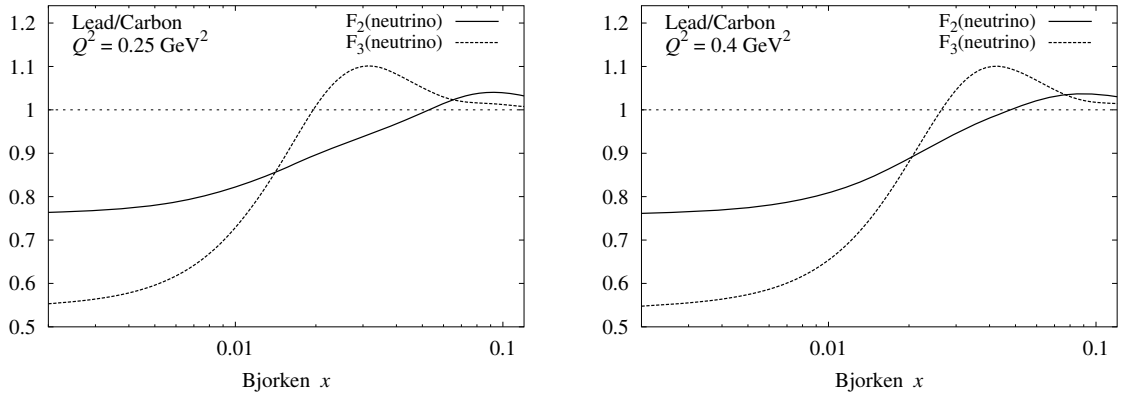


Figure 32: The ratio of lead to carbon neutrino charged-current structure functions $F_2$ calculated in an approach based on PCAC and VMD at two different $Q^2$ (solid line). The corresponding ratio for $xF_3$ is shown by the dashed curve.

cancel out in $R^-$ for an isoscalar target, making Eq. (11) a powerful tool for measurement of the mixing angle in neutrino scattering.

The targets used in neutrino experiments are usually heavy nuclei, such as iron in the NuTeV experiment [100]. Heavy nuclei typically have an excess of neutrons over protons and therefore are not isoscalar targets. For a non-isoscalar target the relations (11) and (12) are violated by contributions from isovector components of nuclear parton distribution functions. Nuclear corrections to relations (11) and (12) were recently studied in [101, 102, 103], which showed that nuclear effects enter through non-isoscalar effects in the target. These studies suggest that nuclear corrections should be greatly reduced for isoscalar targets like carbon. MINER$\nu$A, with its lead, iron, and carbon targets, can directly measure the NC/CC ratio for several nuclear targets to explore these effects experimentally.

## 8.3 Final-state Interactions

### 8.3.1 Overview

Interactions of few-GeV neutrinos with nuclei often produce resonances which decay to pions. Any attempt to reconstruct the incident neutrino energy based on the total observed energy must account for pion interactions within the target nucleus. Existing neutrino interaction Monte Carlos (such as INTRANUKE [104]) handle intra-nuclear pion interactions crudely and have generally not incorporated the latest knowledge of pion interactions.

The concern is mainly with pions in the 100–500 MeV range, where the interaction cross-sections are highest. In this range the pion/nucleon cross-section is dominated by the strong $\Delta(1232)$ resonance. The $\Delta$ is a fairly narrow (about 100 MeV) resonance, and the pion-nucleon cross-section reflects this, with a peak near 200 MeV pion energy which drops quickly above and below this. The pion/nucleus cross-section exhibits a similar behavior, with a less pronounced drop-off at higher energy. The charged-pion/nucleus cross-section has four important components in the intermediate energy range: elastic scattering (nucleus left in the ground state), inelastic scattering (nucleus left in an excited state or nucleon knocked out), true absorption (no pion in the final state), and single charge exchange (neutral pion

in the final state).

Neutrino detectors are mainly iron (absorber), oxygen (water) and carbon (scintillator). The total pion–carbon cross-section is 600 mb, with elastic and inelastic cross-sections about 200 mb each, and absorption about 160 mb. The total pion-iron cross-section is about 1700 mb, with elastic and absorption about 600 mb each, and inelastic about 400 mb. Cross-sections for positive and negative pions are nearly the same because nuclei contain about the same number of protons and neutrons. These very large cross-sections mean that many pions will undergo some nuclear reaction within the target nucleus. In elastic and most inelastic reactions the scattered pion will not, because of its small mass, lose much energy. However, absorbed pions will lose all of their kinetic and mass energy. Of the four components of this intra-nuclear cross-section, the absorption probability within the interaction nucleus is roughly 30%. Figure 33 [113] shows absorption cross-sections for various nuclei as a function of pion energy.

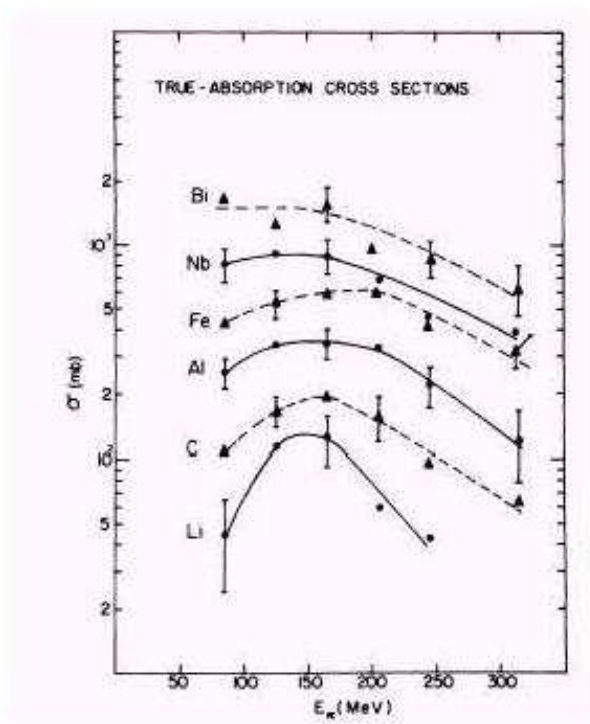


Figure 33: The absorption cross-sections for various nuclei as a function of pion energy.

Pion absorption cannot occur on a single nucleon due to energy and momentum conservation. The simplest absorption mechanism is on two nucleons. Because absorption appears to proceed mainly through $N-\Delta$ intermediate states, an isospin zero (np) pair is the primary candidate. Such an absorption for a positive pion would give two energetic protons whose kinetic energy nearly equaled the total pion energy. However, early studies of pion absorption found this was not the most probable mechanism.

In the 1990's two large solid angle detectors, the LAMPF BGO Ball and the PSI LADS detector, were built to study pion absorption. The somewhat surprising result from both experiments was that pion absorption is dominated by three body absorption [105]. For positive pions, the absorption on a $pnn$ triplet (leading to a $ppn$ final state) was the most common. This was observed even in $^4$He. The absorption in heavier nuclei also appears to proceed mainly through a three-body mechanism,

although increased initial state interactions (pion re-scattering) and final-state interactions (nucleon re-scattering) result in four to five nucleons being emitted. Typically the final-state contains more neutrons than protons. The absorption process, which is still not well understood theoretically, largely fills the available phase space thus giving a wide range of nucleon energies with little angular dependence. Because much of the energy is in neutrons, the visible energy is well below the total pion energy. Even in carbon more than half the energy is lost to unobserved particles, a fraction which increases with pion energy and with A [106].

The situation is worse for negative pions. Charge symmetry would indicate that the primary absorption should be on a $ppn$ triplet leading to a $pnn$ final state. In this case, most of the pion energy would be in neutrons, and hence effectively invisible. However, if the interaction vertex and one proton energy is known, and the angles of the outgoing neutrons are known, the total energy of the three nucleons can be estimated. Monte Carlo studies with realistic absorption models will be needed to determine the accuracies of such estimates.

Although neutral pions escaping the nucleus will decay, usually to two photons, the mean distance traveled before decay is a few nanometers, much greater than the size of the nucleus. Thus the absorption of neutral pions in the interaction nucleus must also be accounted for in any study of resonance production.

For MINER$\nu$A, studies with INTRANUKE have begun to explore the sensitivity to the probability of pion absorption in the interaction nucleus. Monte Carlo routines are being modified to treat pion absorption more realistically. Unfortunately there are essentially no measurements of pion absorption above 500 MeV. The fine spatial resolution and $4\pi$ acceptance of MINER$\nu$A will allow study of these interactions, especially in carbon.

### 8.3.2 Nuclear transparency

A second nuclear interaction process which affects the observed energy is final state interaction of a nucleon in the struck nucleus. An outgoing nucleon has a substantial probability of interacting in the nucleus. These probabilities have been measured, most recently at Jefferson Lab, with some precision. The experiments used $(e, e'p)$ coincidence reactions, and the cross-section for finding the scattered electron in the quasi-elastic peak was compared to the cross-section for finding the coincident proton.

Unlike pion absorption, there is little available information on what happens to the scattered nucleon. Of course, most either scatter from a single nucleon quasi-elastically or produce a pion (for protons above 600 MeV). Improving Monte Carlo routines to model this interaction should allow us to better estimate the total final state energy. As for pion absorption, the good resolution, neutron detection capability, and full solid angle coverage of MINER$\nu$A should allow measurement of the actual final states and help constrain the Monte Carlo models.

## 8.4 Nuclear Effects in MINER$\nu$A

To study nuclear effects in MINER$\nu$A, carbon, iron and lead targets will be installed upstream of the pure scintillator active detector. The currently preferred configuration involves a total of 9 planes, with each plane divided transversely into C, Fe and Pb wedges. As one proceeds from upstream to downstream, the C, Fe and Pb targets exchange (rotate) positions. A scintillator module of four views (X,U,X,V) separates each of the planes. The total mass is over 1 ton of Fe and Pb and somewhat over 0.5 ton of C. Since the pure-scintillator active detector acts as an additional 3-5 ton carbon target (CH),

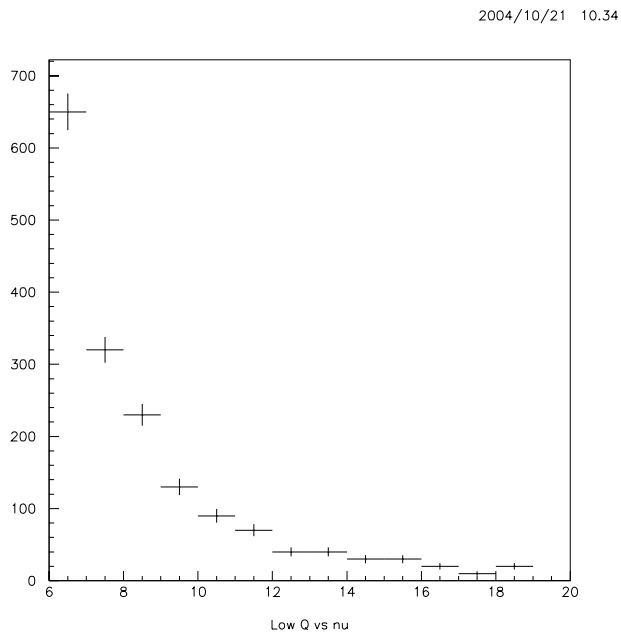


Figure 34: The expected event sample per target with $Q^2 \leq 0.4\text{GeV}^2$ and $\nu \geq 6$ GeV.

the pure graphite (C) target is mainly to check for consistency. For the standard four-year run described in the proposal, MINER$\nu$A would collect over 740 K events on Fe and Pb, 430 K events on C as well as 2.3 M events on the scintillator in the fiducial volume.

### 8.4.1 Measuring modified interaction probabilities

To measure this nuclear effect, the cross-section and resulting structure functions $F_2(x,Q^2)$ and $xF_3(x,Q^2)$ will be measured for the three target nuclei of C, Fe and Pb. For the standard 4-year run we expect around 740 K events per target distributed in $x$ depending on the W-region in question. For an A-dependent comparison in the DIS region ($W \geq 2$ GeV and $Q^2 \geq 1$ (GeV/c)$^2$) we would have 330 K events per target with 66 K events per target in the shadowing region ($x \leq 0.1$) and 20 K events per target in the high-$x$ region ($x \geq 0.5$).

To study the axial-vector nuclear shadowing effects expected at low $Q^2$ (non-DIS events) and low $\nu$ we will have 133 K events per target with $Q^2 \leq 1.0$ (GeV/c)$^2$ and $x \leq 0.1$. For example, the expected distribution of events with $Q^2 \leq 0.4$ (GeV/c)$^2$ and $\nu \geq 6$ GeV (the region where the largest differences from charged-lepton shadowing are expected) is shown in Figure 34. With these samples, MINER$\nu$A can measure the expected difference in lead to carbon shadowing for charged leptons compared to neutrinos to just under three standard deviations (statistical).

### 8.4.2 Measuring final state interactions

The NEUGEN Monte Carlo has been used to study MINER$\nu$A's sensitivity to nuclear effects. Nuclear effects in NEUGEN are controlled by the INTRANUKE processor. This processor incorporates a probability for pion absorption based on earlier electroproduction absorption studies and lower-statistics Ne/$H_2$ neutrino bubble chamber data. The observed phenomenon of hadron formation length, which increases the transparency and reduces final-state interactions, is incorporated. The particular model used

for pion absorption, which is currently being improved and updated, assumes that absorption eliminates a pion and the resulting nucleons are themselves either absorbed in the nucleus or are too low in energy to be observed.

To determine MINER$\nu$A's sensitivity to the predictions of this model, the assumed probability for pion absorption in INTRANUKE has been increased by three standard deviations and then decreased by the same amount, which essentially turns off pion absorption completely. The multiplicity and a simple, crude estimate of the visible hadron energy have been examined under these extreme conditions. Other nuclear effects such as intra-nuclear scattering and hadron formation length have not been altered from their nominal values. Figure 35 shows both the true and reconstructed multiplicity distributions for carbon. Unfortunately, the available tracking software fails to reconstruct many of the tracks. We expect this problem to be resolved when full pattern recognition and a more robust tracker become available. For the present study, we will use the true multiplicities.

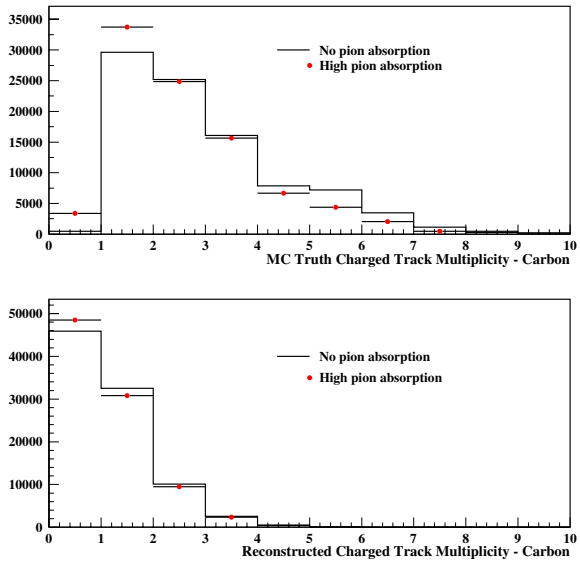


Figure 35: The shift in the true and reconstructed multiplicity distributions between the two values assumed for pion absorption on carbon described in the text.

The next series of figures show the predicted "asymmetry" of the true multiplicity and visible hadron energy. The asymmetry is defined as the percentage change under these extreme assumptions. That is, the bin contents at plus three standard deviations minus the bin contents at minus three standard deviations, divided by bin contents at minus three standard deviations. Figure 36 shows the asymmetry of the true multiplicity for carbon and iron. There is a dramatic effect for carbon, as the high absorption value increases the number of 0-track events by over a factor of six compared to the no-absorption case. This is because the other nuclear effects, being unchanged, are minimal for carbon. Since intra-nuclear rescattering increases as $A^{1/3}$ and the suppression due to hadron formation length decreases as $A^{1/3}$, non-absorption nuclear effects are minimal for carbon and already sizable for lead. If this model is realistic, the carbon multiplicity distribution should be quite sensitive to the probability of absorption.

Final determination of the visible hadronic energy will be an involved process for this experiment. For now, we use the most primitive estimate of this quantity, an uncorrected version derived from the total light output of the hadron shower. In the real data analysis this can be refined through measure-

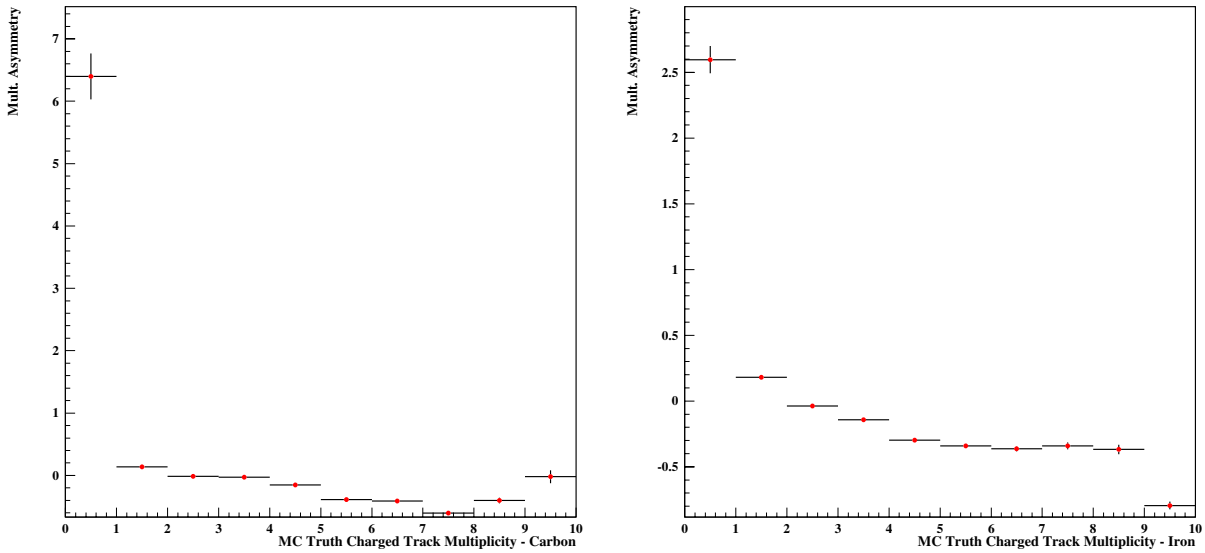


Figure 36: The fractional change in true multiplicity distributions between the two values assumed for pion absorption on carbon (left) and iron (right), as described in the text.

ments of stopping/decaying particles. With this crude estimate, the change in hadron energy for iron and lead are shown in Figure 37. There is a significant increase in the number of events with $E_H$ less than 3 GeV and a corresponding decrease in the number of events with higher $E_H$, as one would expect. MINER$\nu$A will collect several times these statistics and should be able to measure this effect at even higher hadron energy.

Since the incoming neutrino energy is not known *a priori*, the measured **muon** kinematics will be tested as a basis for comparing the visible hadron shower across nuclear targets to determine whether a nuclear correction-factor can be parameterized as a function of the observed muon angle and energy. The muon is relatively free from nuclear dependent effects and serves well as an A-independent normalization. For example, the quantity:

$$Q' = E_\mu \sin^2(\theta/2) \tag{13}$$

is representative of the 4-momentum transfer to the nucleon or quark (divided by $E_\nu$) and reflects the energy-momentum transferred to the hadronic vertex. The distribution of events in this quantity is peaked toward low $Q'$. with half the events below $Q' = 1.0$ GeV.

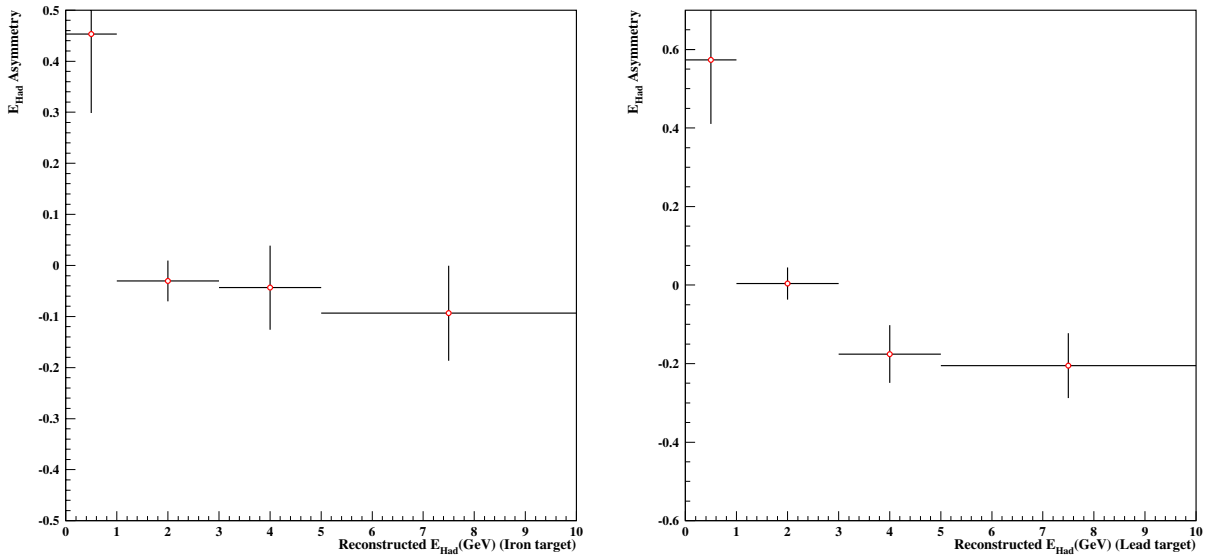


Figure 37: The fractional change in the visible hadron energy distributions between the two values of pion absorption on iron (left) and lead (right), as discussed in the text.

# Part II
# The MINER$\nu$A Project

# 9 NuMI Beam and Hall

MINER$\nu$A will run in the NuMI beamline, and be sited in the hall which currently houses the MINOS near detector. The NuMI beam is the most intense high-energy neutrino beam available today, and because of the available space, the hall itself is an ideal environment for neutrino experiments. It provides a well-shielded area with sufficient infrastructure to support MINOS as well as other neutrino experiments.

## 9.1 The MINOS Near Detector Hall

The MINOS Near Detector Hall[152] is a fully-outfitted experimental facility that can accomodate MINER$\nu$A with a limited number of additions to the infrastructure.

The hall is 45 m long, 9.5 m wide, 9.6 m high, with its upstream end just over 1 km from the NuMI target, at a depth of 106 m below grade. The MINOS near detector has been installed at the downstream end of the hall, and there is free space upstream amounting to, roughly, a cylinder 26 m in length and 3 m in radius. The neutrino beam centerline descends at a slope of $3.3^\circ$ and enters the MINOS detector at a height of 3 m from the floor.

Ground water is pumped from the NuMI/MINOS complex at a rate of approximately 270 gallons (980 l) per minute. The hall floors and walls are occasionally damp in places, and a drip cover will be used to protect MINER$\nu$A from moisture. The air is held at a temperature between $60^\circ$ F and $70^\circ$ F ($15^\circ$ C and $21^\circ$ C), and 60% relative humidity.

### 9.1.1 Utilities

The MINOS Service Building on the surface houses the access shaft to the Near Detector Hall and is the entry point for electrical, cooling, and data services to the hall. A 15-ton capacity crane, with a hook height of 18.5 feet (5.66 m), was used to lower the 3.47 ton MINOS detector planes to the hall. MINOS planes were moved within the hall using an overhead 15-ton crane, with 22 foot (6.7 m) hook height and a coverage along the beam axis of approximately 40 m.

Quiet power to the hall is provided by a 750 KVA transformer at the surface, which branches to a 45 KVA transformer for the muon monitoring alcoves, and two 75 KVA transformers for the Near Detector hall. The power needs of the MINOS detector account for the capacity of the 4 panelboards served by the two 75 KVA transformers, so additional panelboards for MINER$\nu$A will be installed by Fermilab. The estimated power consumption of MINER$\nu$A's electronics is less than 5000 W. The overall capacity for this additional load exists within the MINOS hall.

MINER$\nu$A's main non-quiet power need is for the magnet coils, with an estimated ohmic power loss of 30 kW. The MINOS magnet coil power supply is served by a 480 V line with 400 A capacity, but requires less than 80 kW of power. This should leave ample capacity for the addition of a power supply for the MINER$\nu$A coil on the same line.

The heat sink for the MINOS LCW cooling circuit is the flux of ground water collected in the MINOS sump. This cooling is adequate for MINOS, with an output water temperature of $70^\circ$ F. This should be sufficient to absorb the heat load of the MINER$\nu$A magnet, but would likely be too warm to effectively cool the power supplies for MINER$\nu$A's electronics. The relatively low heat load of the MINER$\nu$A electronics would likely be absorbed without problem by the MINOS hall air conditioning.

### 9.1.2 Detector placement

MINER$\nu$A will be placed 1.75 m upstream of MINOS. This will leave sufficient work space between the two detectors and will avoid interfering with the MINOS coil, which extends approximately 1.5 m upstream of MINOS, to the lower right in the view of Figure 38. To have the beam axis intersect the detector axis close to the center of the active plastic target, the lowest corner of MINER$\nu$A will be placed 1.10 m above the hall floor. The beam centerline would enter the detector at an elevation of 3.4 m from the floor (Figures 39 and 40).

MINER$\nu$A will impinge slightly on a "stay clear" egress space for the lower MINOS detector electronics racks. This will be resolved by extending the upstream part of the MINOS electronics platform and moving the stairs farther upstream.

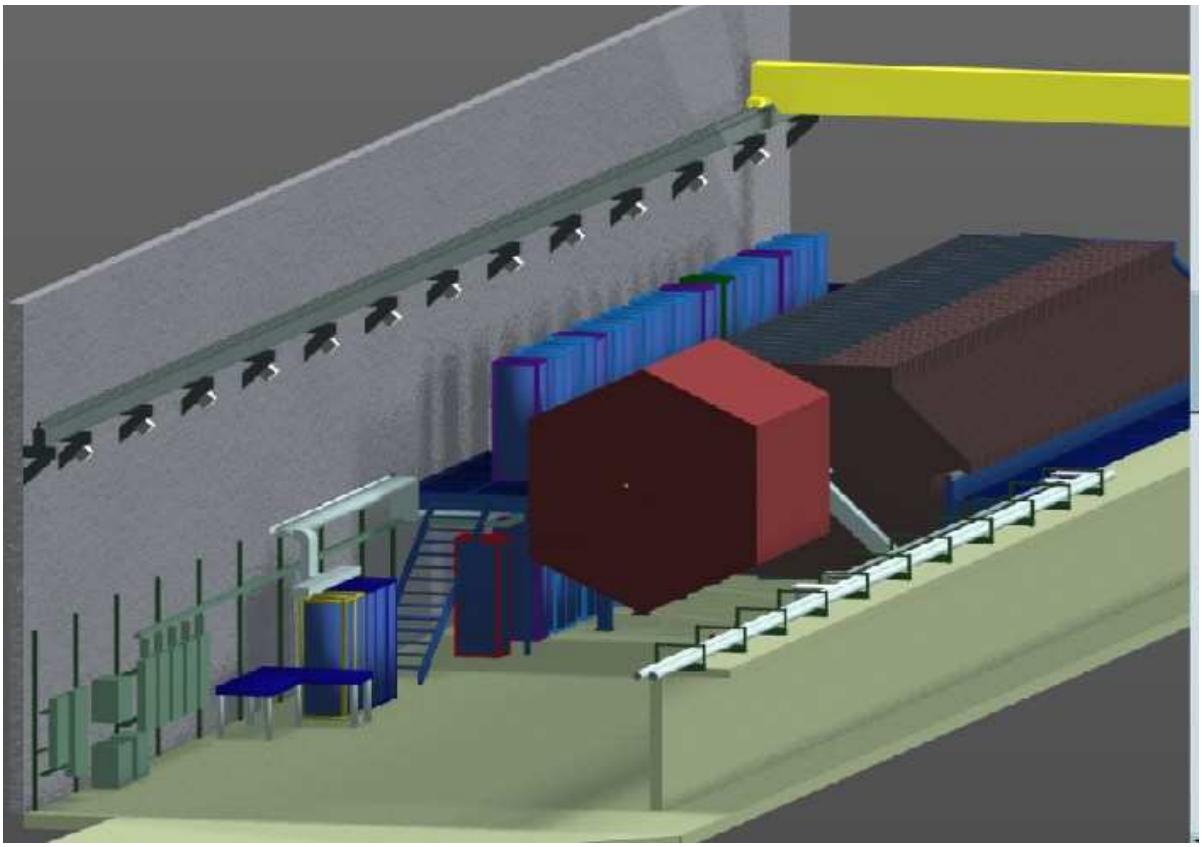

Figure 38: View of the proposed MINER$\nu$A detector, and the MINOS detector, looking dowstream.

### 9.1.3 Impact on MINOS

The impact on MINER$\nu$A's heat load and power consumption on MINOS can be made negligible through relatively minor additions to the hall infrastructure. Presence of the detector in the neutrino beam will cause an increase in the rate of activity in the MINOS detector, particularly in the first 20 planes forming the MINOS veto region. Given MINER$\nu$A's design, the expected event rate in the detector is $\approx$ 1.4 charged-current interactions per $10^{13}$ protons on target (POT). For a spill of $2.5 \times$

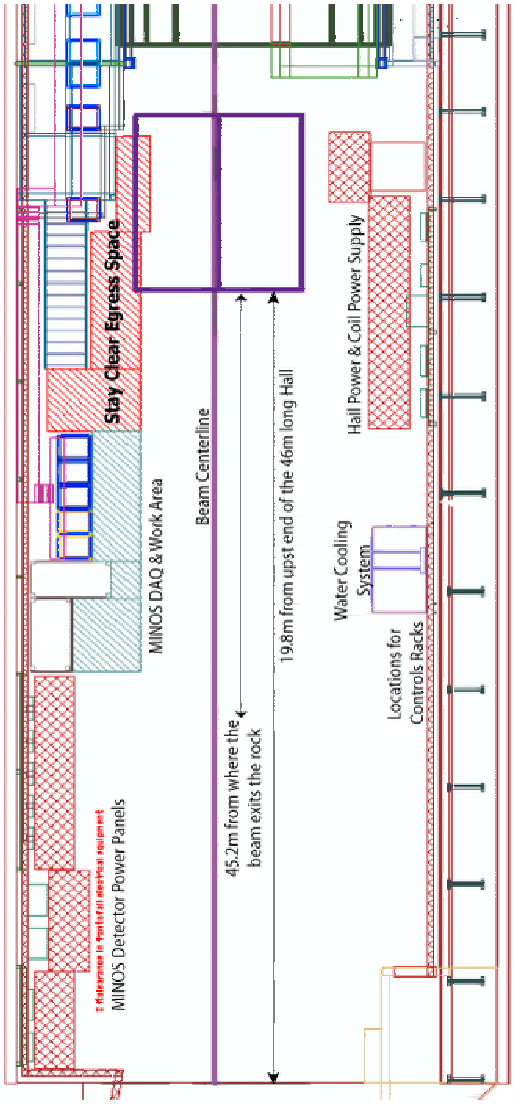


Figure 39: Plan view of MINER$\nu$A (purple outline near top of figure).

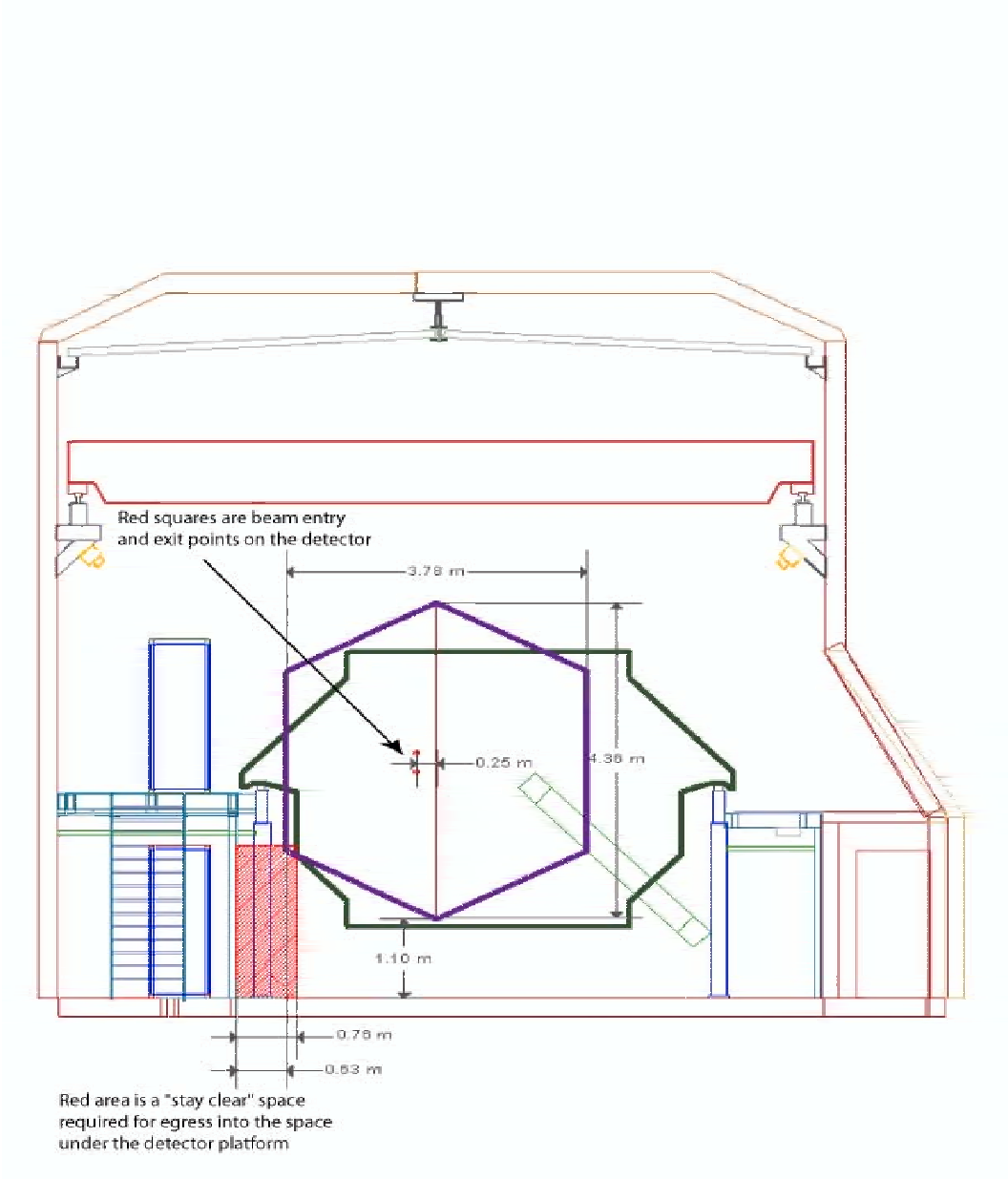


Figure 40: Front view of MINER$\nu$A.

$10^{13}$ POT this corresponds to 3.4 charged-current events, plus an additional 1.0 neutral-current event per spill. Since the vectors of all particles leaving MINER$\nu$A with a trajectory heading towards MINOS will be made available when MINER$\nu$A is taking data, this rate should be managable.

## 9.2 The NuMI Beam and MINER$\nu$A Event Sample

The NuMI neutrino beam is produced from $\pi$- and $K$-decay in a 675 m decay pipe beginning 50 m downstream of a double horn focusing system. At the end of the decay pipe a 10 m long hadron absorber stops the undecayed secondaries and non-interacting primary protons. Just downstream of the absorber, 240 m of Dolomite is used to range out muons before the $\nu$ beam enters the Near Detector Hall. Figure 41 shows the beamline and hall layout.

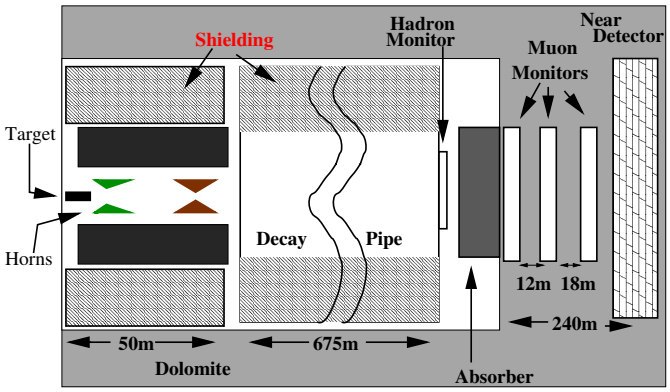


Figure 41: Layout of NuMI beamline components and near detector hall (not to scale).

### 9.2.1 Energy options

The neutrino energy spectrum of the NuMI beam can be adjusted by changing the distances of the target and second horn from the first horn, as in a zoom lens. The three configurations result in three beam energy tunes for the low- (LE), medium- (ME), and high-energy (HE) ranges respectively. However, to switch from one the beam mode to another requires down-time to reconfigure the target hall and a loss of beam time. An alternative which allows the peak energy to be varied is to change the distance of target from the first horn and leave the second horn fixed in the LE position. This can be accomplished remotely with a maximum target excursion of -2.5 m upstream of the first horn from its nominal low-energy position. Moving the target -1.0 m results in a "semi-medium" energy beam tune (sME), and -2.5 m produces a "semi-high" energy beam (sHE). These semi-beam configurations are less efficient and result in lower event rates than the ME and HE beams. A considerably more efficient sHE beam is possible with three-day downtime to move the target to its normal HE position of -4.0 m. This more efficient sHE(-4.0) beam would yield over 50% more events than the sHE(-2.5) beam. For MINOS, the beamline will be operating primarily at its lowest possible neutrino energy setting, to reach the lowest values of $\Delta m^2$. However, to minimize systematics, MINOS will also run in the sME and sHE configurations. The neutrino energy distributions for the LE, sME, and sHE running modes are shown in Figure 42.

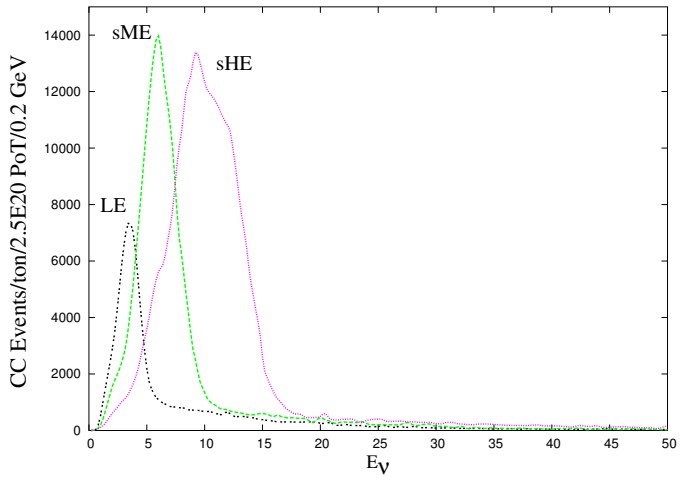


Figure 42: Neutrino energy distribution for charged-current interactions in three configurations of the NuMI beam corresponding to low-energy (LE), medium-energy (sME) and high-energy (sHE).

### 9.2.2 MINER$\nu$A event rates

Table 6 shows charged-current interaction rates per $10^{20}$ protons on target (PoT) per ton for different beams. The expected rates are about 20% lower than quoted in our November 2003 proposal, due to new hadron production spectra from the SPY experiment[157] recently incorporated in the NuMI beam Monte Carlo.

The same beam configurations with horn-currents reversed focus $\pi^-$ to create anti-neutrino beams. Rates for $\overline{\nu}_\mu$ charged-current interactions from anti-neutrino configurations (LErev, MErev, and HErev) are of great interest but have not yet been calculated with the new hadron production spectra. Running in these reversed ($\overline{\nu}$) modes would be highly desirable for MINER$\nu$A's physics program.

| Beam | CC $\nu_\mu$ |
|---|---|
| LE | 60 K |
| sME | 132 K |
| sHE | 212 K |

Table 6: MINER$\nu$A charged-current interactions per ton, per $10^{20}$ protons on target.

### 9.2.3 Baseline MINOS run plan

Table 7 shows the expected protons on target over a hypothetical four-year MINOS run. For this scenario, the total integrated rate in MINER$\nu$A would be 745 K $\nu_\mu$ charged-current interactions per ton. Table 9.2.3 shows the MINER$\nu$Asample (per ton) for different processes, assuming $9 \times 10^{20}$ protons on target.

| Scenario for PoT per year ($\times 10^{20}$) | | | | | | | |
|---|---|---|---|---|---|---|---|
| year | total PoT | LE | sME | sHE | LErev | MErev | HErev |
| 2006 | 3.0 | 3.0 | 0.0 | 0.0 | 0.0 | 0.0 | 0.0 |
| 2007 | 4.0 | 3.0 | 0.7 | 0.3 | 0.0 | 0.0 | 0.0 |
| 2008 | 4.0 | 0.0 | 0.0 | 0.0 | 2.5 | 1.0 | 0.5 |
| 2009 | 4.0 | 1.0 | 0.5 | 0.5 | 0.5 | 0.5 | 1.0 |
| Total | 15.0 | 7.0 | 1.2 | 0.8 | 3.0 | 1.5 | 1.5 |

Table 7: Hypothetical proton luminosity scenario for a four-year run.

| Process | CC/ton | NC/ton |
|---|---|---|
| Quasi-Elastic | 82 K | 27 K |
| Resonance | 156 K | 48 K |
| Transition | 164 K | 52 K |
| DIS | 336 K | 98 K |
| Coherent | 7 K | 3.3 K |
| Total ($\nu$) | 745 K | 228 K |

Table 8: MINER$\nu$A samples per ton for various processes, assuming $9 \times 10^{20}$ PoT. The detector fiducial mass is 3–5 tons Carbon, 1 ton Iron, and 1 ton Lead.

#### 9.2.4 Precision of neutrino flux prediction

One of MINER$\nu$A's significant advantages over previous wide-band neutrino scattering experiments will be better knowledge of the neutrino flux and energy spectrum. Since the NuMI beamline is designed for the MINOS oscillation experiment, considerable effort has been devoted to control of beam-related systematic uncertainties.

The largest source of uncertainty in the neutrino energy spectrum arises from the hadron ($\pi^{\pm}$ and $K$) prodution spectra. To reduce this uncertainty, a dedicated Fermilab experiment called MIPP (E-907)[158, 155] is directly measuring these hadron production spectra for various nuclear targets. One of the E-907 measurements will expose of the NuMI target itself to the 120 GeV Main Injector proton beam. Using the NuMI target material and shape, E-907's data will include secondary and tertiary hadron production, which significantly modified the spectra relevant for neutrino production. With input from E-907, the absolute neutrino flux and energy spectrum should be known to $\approx$ 3–5%.

For the absolute flux of neutrinos, a second uncertainty concerns the number of protons on target. With the planned NuMI primary proton beamline instrumentation[159], the number of protons on target will be known to within (1 – 3)%, the range being determined by control of the drift in the proton beam toroid devices.

To summarize, the energy spectrum of the NuMI beam should be known to (3 – 5)% and the absolute flux should also be known to (3 – 5)%.

# 10 The MINER$\nu$A Detector

## 10.1 Overview of Detector Design

For MINER$\nu$A to meet its physics goals, the detector must break new ground in the design of high-rate neutrino experiments. With final states as varied as high-multiplicity deep-inelastic reactions, coherent single-$\pi^0$ production and quasi-elastic neutrino scattering, the detector is a hybrid of a fully active fine-grained detector and a traditional calorimeter.

At the core of the MINER$\nu$A design is a solid scintillator-strip detector, similar in principle to the recently commissioned K2K SciBar [156]. The plastic inner detector serves as the primary fiducial volume, where precise tracking, low density of material and fine sampling ensures that some of the most difficult measurements can be performed. These include multiplicity counting in deep-inelastic scattering, tracking of photons, detection of recoil protons in low-$Q^2$ quasi-elastic events, and particle identification by $dE/dx$. A side view of the detector is shown in Figure 43.

The scintillator detector cannot contain events due to its low density and low $Z$, and therefore, the MINER$\nu$A design surrounds the scintillator fiducial volume with sampling detectors. At the low energies needed to study cross-sections of interest to neutrino-oscillation searches, many of the events contain sideways- and backward-going particles, so these sampling detectors extend to the sides, and even to the upstream part of the detector, where they also serve as high $A$ targets for study of nuclear effects. Finally, it is important to contain or measure the final-state muon in charged-current events, and for this purpose, the outer side detector of MINER$\nu$A is a magnetized toroid. Energetic muons at smaller angles will enter the MINOS near detector, where their momentum can be measured magnetically and/or by range.

Except for the upstream veto, the entire MINER$\nu$A detector is segmented transversely into an inner detector with planes of solid strips and an outer picture frame magnetized toroid (OD). For construction and handling convenience, a single plane of MINER$\nu$A incorporates both the inner detector and OD, which serves as the support structure. Two planes of scintillator are mounted in one frame, called a "module", as illustrated in Figures 45,46. There are three distinct orientations of strips in the inner detector, offset by 60°, and labelled X, U, and V.

A single module of the MINER$\nu$A active target has two X layers to seed two-dimensional track reconstruction, and one each of the U and V layers to enable a three-dimensional reconstruction of tracks. The 60° offset makes the hexagon a natural transverse cross-section for the detector. As shown, the scintillator strips extend the full length of the hexagon and range between 205 and 400 cm in length. The toroid steel/absorber is 10 cm thick in the veto; The magnetic properties of the OD are discussed in Section 10.4.

The center of the detector is the fully active inner detector (ID), whose plastic core represents the fiducial volume for most analyses in MINER$\nu$A. Calorimetric detectors in the central region of the detector are constructed by inserting absorber between adjacent planes, also shown in Figures 45,46. Lead alloy absorbers, 30 cm from the edge of the ID and 0.2 cm thick, are inserted between layers of scintillator and at the front of each module to serve as a side electromagnetic calorimeter. This part represents the largest part of the detector in length, and the outer calorimeter surrounding the fully active planes are the largest part of the detector in mass.

The inner detector is surrounded by the picture frames of absorber and scintillator strips that make up the outer detector (OD). The OD consists of six "towers" (one sixth of a hexagon). Note that the strips in the OD run only in one direction, in the bend plane of the magnetic field. Three-dimensional

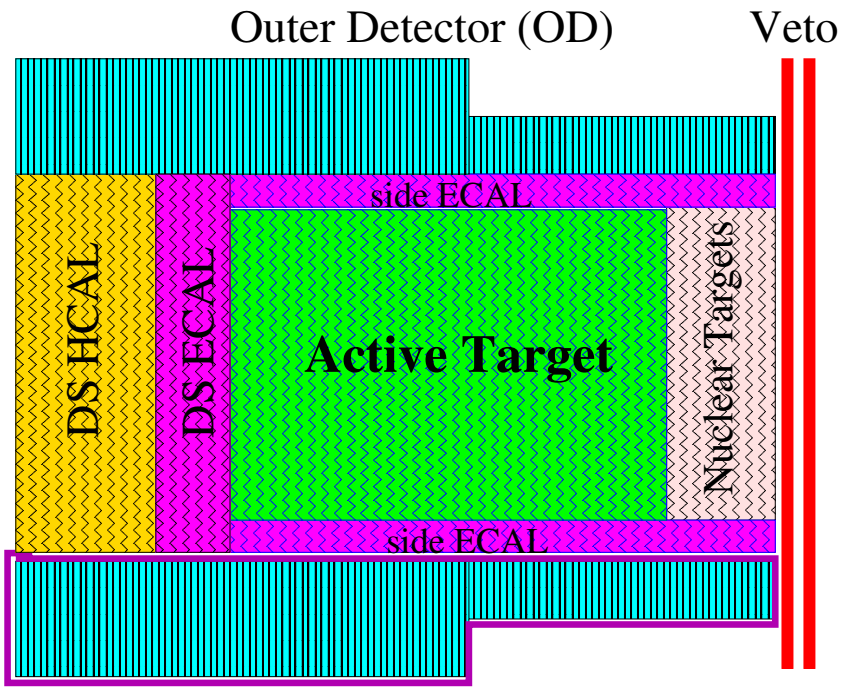


Figure 43: A side view schematic of the MINER$\nu$A detector

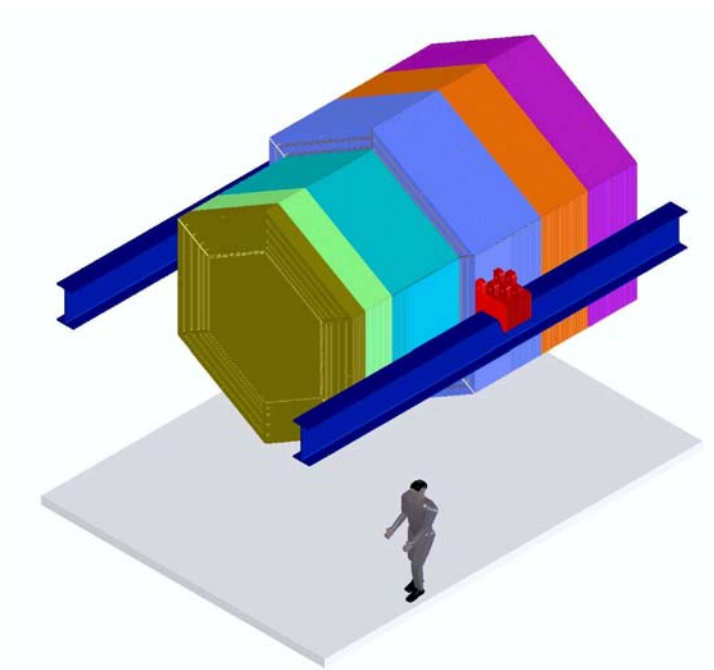

Figure 44: Outline of MINER$\nu$A detector to illustrate shape and scale. The veto wall is omitted for clarity.

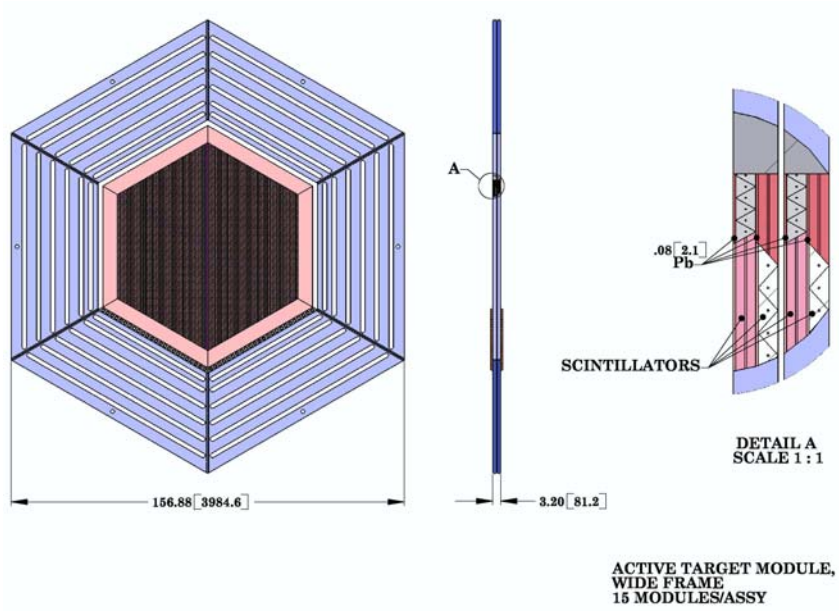


Figure 45: View of downstream active detector region. An expanded view of the area near the inner-outer detector interface is shown on the right.

tracks must therefore be matched from the inner detector and extrapolated outwards for an energy measurement or muon momentum measurement. A complication of the design is illustrated by the fact that the inner detector strips, which range in length from 120 to 240 cm, end inside the OD, and therefore bundled WLS fibers in a so-called "snout" must travel through the gap between the OD planes of each module to the detector edge. Note also the gaps for the muon toroid coil on the inner surfaces of the "5 O'clock" and "7 O'clock" sides of the OD. Magnetic flux will be isolated in each region of the OD, and will be prevented from leaking into the inner detector by gap between steel HCAL absorbers and the OD. The scintillator strips in the towers are square, with 1.9 cm sides, and arranged in rectangular layers of two (Figure 57).

In the inner detector, MINER$\nu$A's sensitive elements are extruded triangular scintillator strips, 1.7 cm height with a 3.3 cm base, with embedded wavelength-shifting fibers (details given in Section 10.2.1). To improve coordinate resolution while maintaining reasonably large strips, these elements are triangular and assembled into planes (Figure 56); this allows charge-sharing between neighboring strips in a single plane to interpolate the coordinate position.

The most up- and down-stream detectors are the hadronic calorimeters (HCALs) with 2.5 cm absorbers, one per plane downstream and one per module upstream, as shown in Figures 47 and 48. Next are the electromagnetic calorimeters, as shown in Figures 49 and 50. The electromagnetic calorimeters (ECALs) have 0.2 cm Pb alloy absorbers downstream, one per plane, and 0.8 cm Pb alloy absorbers upstream, one per module. The absorber only overlaps the inner detector and not the outer detector where it would represent a negligible fraction of the absorber material. The fine granularity of the ECAL ensures excellent photon and electron energy resolution as well as a direction measurement for each. In Figure 43, the upstream HCAL and ECAL are labeled as one device called "nuclear targets" since these planes serve all three purposes.

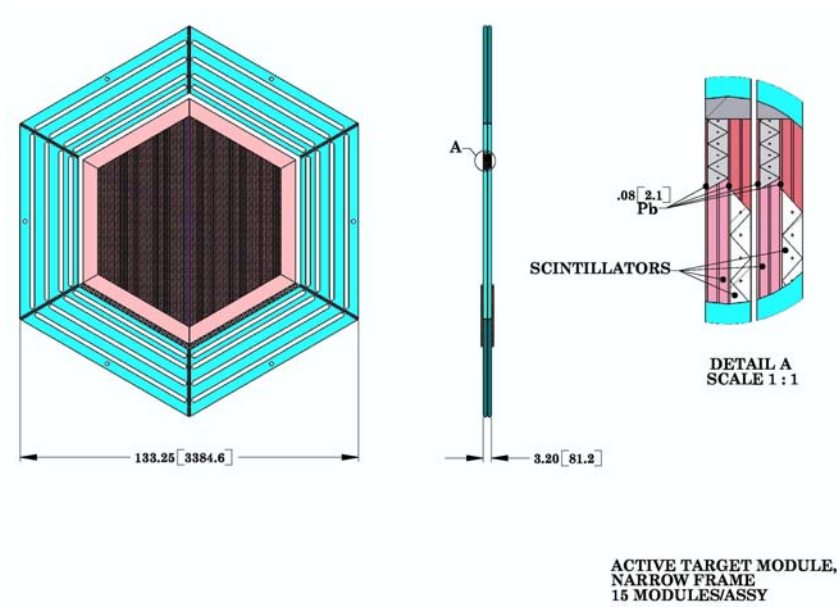


Figure 46: View of an upstream active detector module. An expanded view of the area near the inner-outer detector interface is shown on the right.

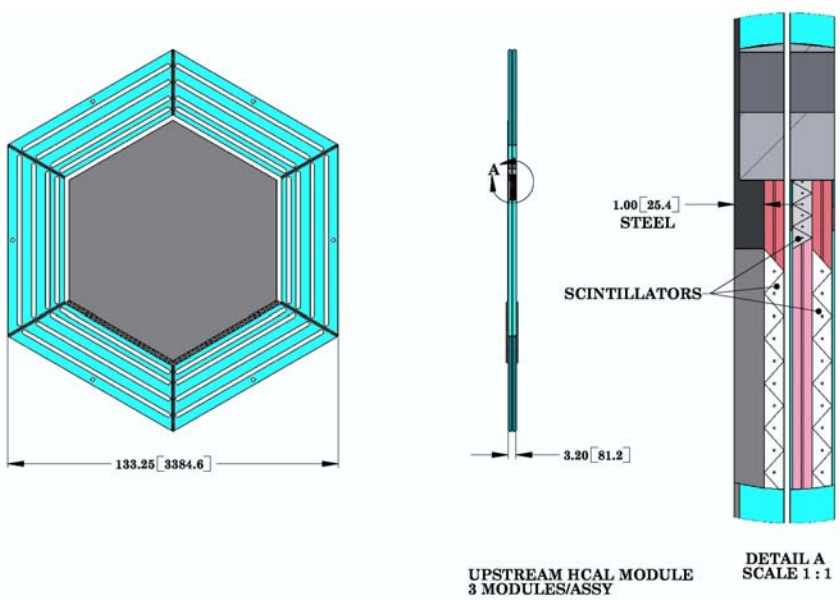


Figure 47: View of an upstream hadron calorimeter module. An expanded view of the area near the inner-outer detector interface is shown on the right.

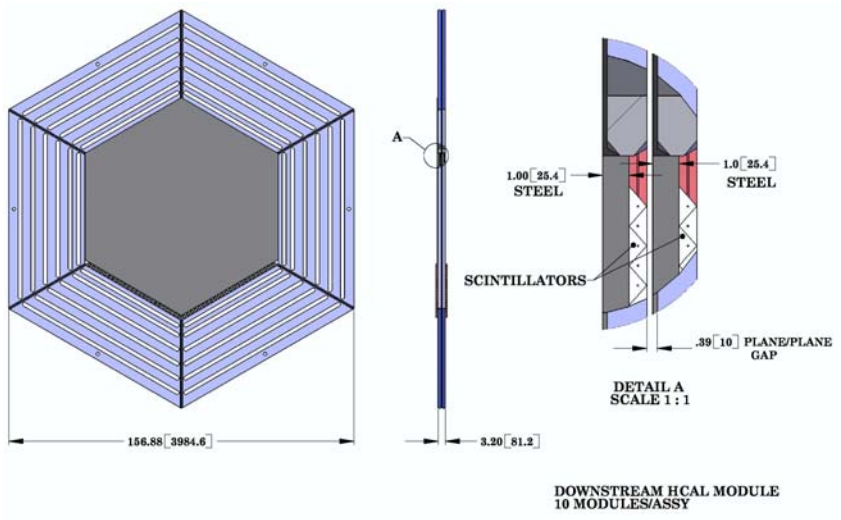


Figure 48: View of a downstream hadron calorimeter module. An expanded view of the area near the inner-outer detector interface is shown on the right.

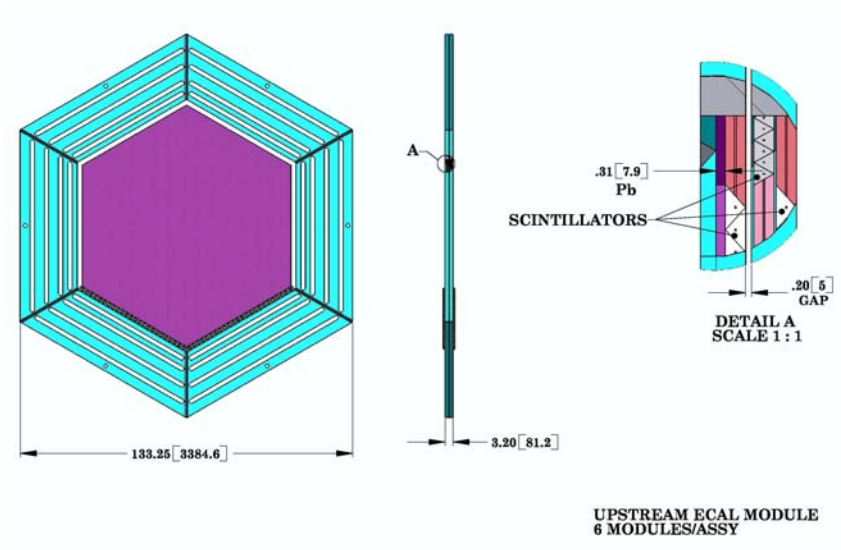


Figure 49: View of an upstream electromagnetic calorimeter module. An expanded view of the area near the inner-outer detector interface is shown on the right.

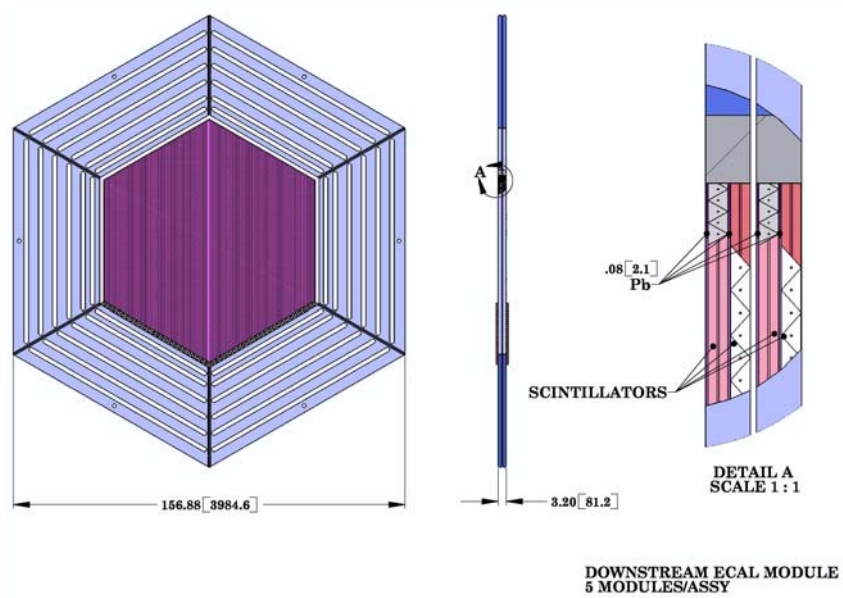


Figure 50: View of an downstream electromagnetic calorimeter module. An expanded view of the area near the inner-outer detector interface is shown on the right.

Note that MINER$\nu$A is, by design, entirely modular along the beam direction. Individual elements may be easily lengthened or shortened by omitting modules from the design or adding new modules. Hence, it would be easy to add a muon range stack at the downtream end of the MINER$\nu$A detector, if that should be required at a future date.

## 10.2 Scintillator

### 10.2.1 Scintillator extrusions

Particle detection using extruded scintillator and optical fibers is a mature technology. While in terms of size, MINER$\nu$A pales in comparison to MINOS, our system is similar in scale to other successful applications in the K2K SCIBAR detector, CDF plug calorimeter, and CMS HCAL. We have opted for a 1.7 cm height, 3.3 cm base triangular extrusion cross-section for the inner detector planes (Figure 51); this geometry allows refinement of spatial coordinates based on charge-sharing between adjacent strips (Figure 56). For the outer detector, strips will be square in cross-section, 1.9 cm on a side, arranged in rectangular groups of two (Figure 57).

Scintillator elements will be produced by the Northern Illinois Center for Accelerator and Detector Development (NICADD) at Northern Illinois University (NIU). NIU physicists and mechanical engineers have formed a collaboration to support development of the next generation of detectors at the Fermilab Scintillator Detector Development Laboratory. NICADD/NIU fully purchased and is sole owner of the NICADD/Fermilab extruder at the heart of the scintillator laboratory. NICADD and Fermilab jointly operate the extruder to ensure that the HEP community has access to affordable extruded scintillator. NICADD/NIU personnel have been responsible for commissioning the extruder; simulations, production, and prototyping of dies associated with specific detectors; and production of extrusions for

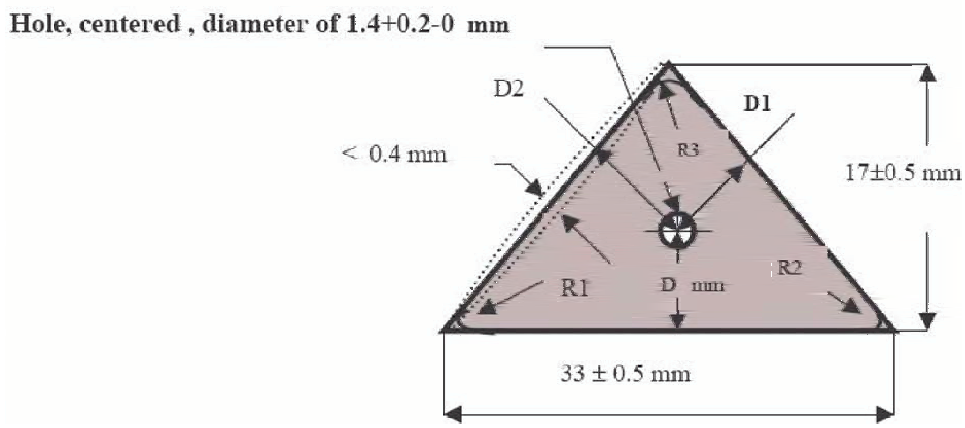


Figure 51: Specification for MINER$\nu$A's inner-detector scintillator extrusions.

prototypes and detector construction.

The key element in producing extruded scintillator is the metal die used to shape the final scintillator cross-section. Historically, development of the die has been more of an art than a science, marked by repeated redesigns and dependent on the die-maker's experience. To refine this process, NIU's mechanical engineering department formed a group to design dies through advanced computing and simulation techniques.

Figure 52 shows the die developed for MINER$\nu$A's first triangular extrusion prototypes in Summer 2004. A small number of these prototypes, with holes through the center of the bar for fiber insertion, were used successfully to detect cosmic-ray muons as part of our "Vertical Slice Test" (see Section 11.5). Figure 53 shows several of the first prototypes.

On-going R&D is focused on perfecting the extruded hole dimensions for a closer fit and more uniform light collection, which will improve MINER$\nu$A's response and sensitivity.

The 23 metric tons of extruded scintillator for the full MINER$\nu$A design will require a production run of approximately 18 weeks. Quality control procedures to ensure the light-yield of the finished product will be maintained by NIU personnel throughout production.

### 10.2.2 Wavelength-shifting fibers

MINER$\nu$A will read-out only one end of its wavelength-shifting (WLS) fibers. To maximize light collection, we will make the unread end of each fiber reflective using techniques developed at Fermilab (the expected improvement in light collection is quantified in Section 11.3). "Mirroring" consists of 3 steps: polishing the end to be mirrored, depositing the reflective surface on the fibers (a process called sputtering), and protecting the mirrors.

The fibers will be delivered in batches from one fiber preform. An automated fiber scanner available at Fermilab will determine if the attenuation length of the fiber is acceptable.

A technique called ice polishing is used to prepare the fibers prior to applying the reflective coating. Ice polishing can give a very good finish to many fibers at once. This technique is described in detail in [161].

The reflective coating is applied in a vacuum system dedicated to optical fiber mirroring at Fermilab. The number of fibers that can be sputtered per load depends on the diameter, but typically 1000–2000

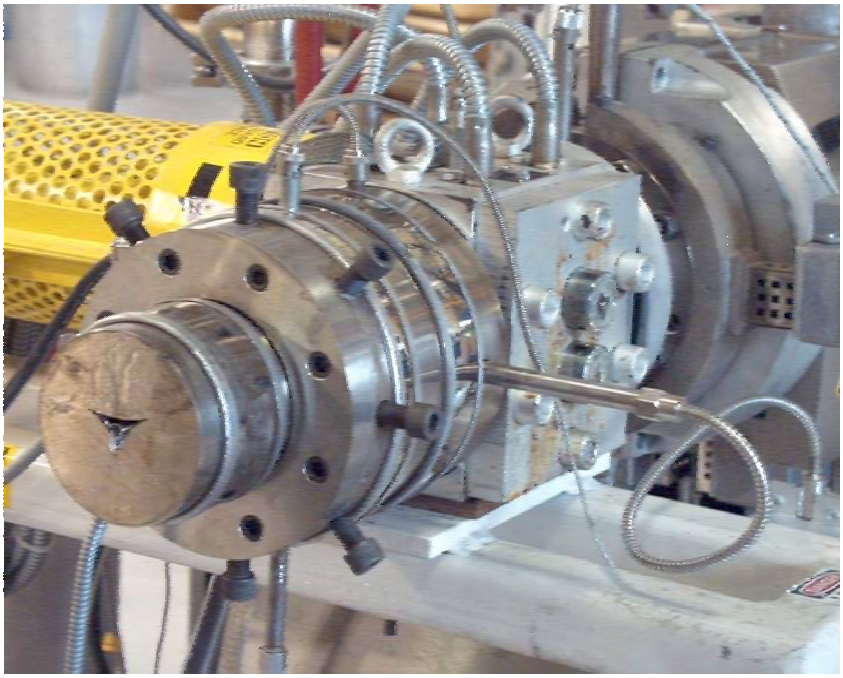

Figure 52: Die developed to produce scintillator bar prototypes for MINER$\nu$A's vertical slice test, mounted to the front of the NICADD extruder. The die is designed, using a finite-element thermal simulation, so the extruded bar will cool into the desired shape in Figure 51.

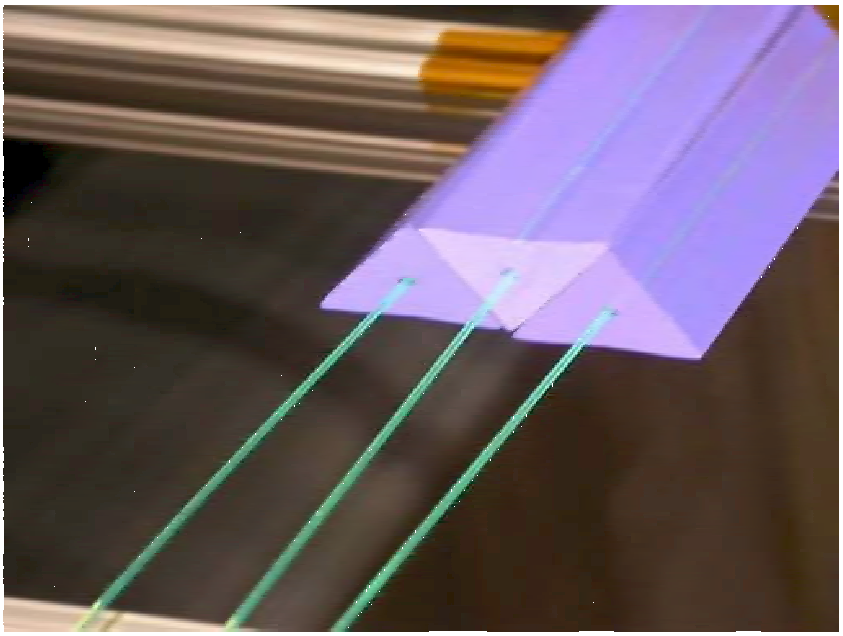

Figure 53: Prototype MINER$\nu$A scintillator bars, with wavelength-shifting fibers inserted.

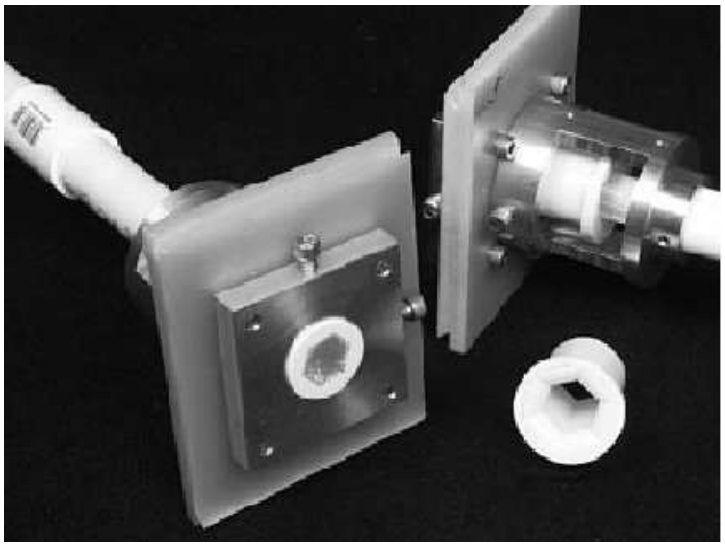

Figure 54: A urethane fixture in an aluminum/G10 frame for holding optical fibers during ice polishing.

fibers per pumpdown per unit can be coated. A 99.999% chemically pure aluminum coating is a applied for good reflectivity. The coating is approximately 2500 Angstroms thick and is monitored using an oscillating quartz crystal sensor device. The aluminized ends are protected with a coat of epoxy.

After this process, MINER$\nu$A will do a destructive measurement of the mirror reflectivity with production fibers, similar to one developed in the CDF plug upgrade. Light output is measured through the unmirrored end of a fiber with ultra-violet light incident on the fiber near the mirrored end. Then, the mirrored end is cut off at 45°, painted black, and the light yield is remeasured with the UV light at the same place. CDF measured an average mirror reflectivity of 90%, with 5.4% RMS variation [162].

### 10.2.3 Scintillator plane design

Scintillator extrusions, optical fibers, and optical connectors are assembled into scintillator planes. There are two varieties of scintillator assemblies: inner-detector (ID) planes and outer-detector (OD) towers. The planes incorporate light-tight skins and edge pieces; they also route the fibers from the ends of the scintillator strips to the outside of the detector. This task's interface with the optical readout system is at the optical connectors between green wavelength-shifting fibers and clear optical cables.

The ID planes are hexagonal assemblies of 128 strips in a single view (X, U or V). An ID plane is also called a "hex". The six OD towers of a complete detector module each consist of four or six OD modules, or stories, stacked radially outward. A single OD module has 2 roughly square strips nested to make a rectangular package. (We also considered a variant designed for improved resolution with four triangular strips, but we consider the 2 square strip design here as the default.) The layout of the ID and OD is shown schematically in Figure 55. A schematic cross-section of a hex is shown in Figure 56, while the cross-section of an OD scintillator module is shown in Figure 57.

The plane design is inspired by the successful MINOS near detector scintillator module assembly [152], but a few modifications are required to meet MINER$\nu$A's needs. Most significantly, the aluminum skins from the MINOS modules represent too much high-Z material for the MINER$\nu$A tar-

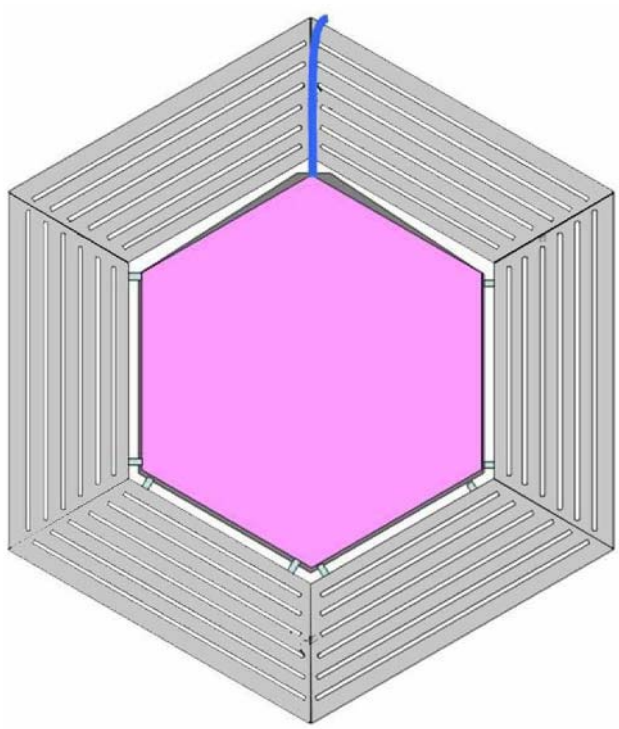

Figure 55: Schematic of a full (inner + outer) detector plane. The hexagonal ID plane is surrounded by six trapezoidal OD towers, each consisting of six OD modules, or stories.

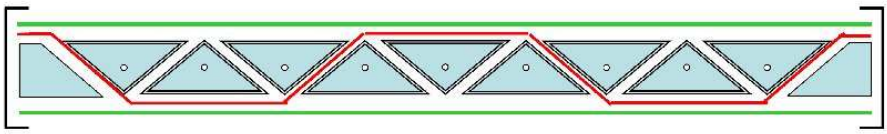

Figure 56: Schematic cross-section of an ID plane, or hex, assembly. The triangular scintillator strips are blue, the outer skins green, the inner web is red, and the outer edge seals are black.

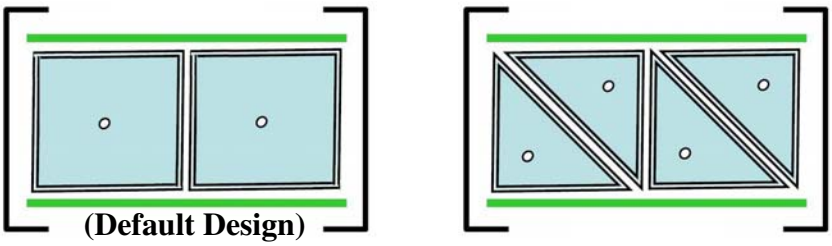


Figure 57: Schematic cross-section of a single OD tower scintillator module, or story. The design with two roughly square extrusions (left figure) is the default; we also considered a triangular design (right figure). The extrusions are blue, the outer skins are green, and the outer edge seals are black.

get region and are replaced with new materials. In addition, the triangular strip design uses an axial hole rather than a groove for better dimensional tolerances.

For light tightness and rigidity, each plane is wrapped in skins made from commercially laminated black Mylar layers with embedded threads of Kevlar. These skins are glued to form the assemblies. A web layer of the skin material is routed between the triangles to provide flat gluing surfaces and a robust connection between the outer skins. The edges of the modules contain small triangular extruded plastic strips to provide square edges to facilitate light sealing with a flexible black extruded PVC edge seal. The ends of the planes contain plates, called manifolds, made from black foamed PVC. On the readout end, these manifolds are partially grooved to route the fibers to their exit points at the end of the assembly. The green fibers are extended past the end of the inner hex in a flexible snout to the outside of the detector where a DDK optical connector is used to make a transition to a clear optical cable.

For eventual installation in the steel detector frames, the scintillator assemblies will have stamped and folded metal brackets attached at six locations around the perimeter of the hex. These tabs will be welded to the steel during detector module assembly. This process is similar to the H-clip mounting technique developed for the MINOS detectors. Next to the flexible snout a small guard piece ensures the fibers are not crushed. Finally, the lead foils of the side ECAL are glued to the skins at the outer radius of the planes.

Assembly of MINER$\nu$A scintillator planes will be undertaken at both Hampton University and the College of William and Mary. Both programs have extensive experience in detector production. Since the two institutions are located less than 25 miles from each other (and less than 15 miles from JLab), they form a natural team for undertaking a joint detector production program. This team will benefit from a collaborative prototyping program, and the joint set-up costs are minimal for this project.

All of the parts other than the scintillator strips, lead sheets, mirrored fibers, and optical connectors will be procured or fabricated by these two institutions. Bulk purchasing responsibilities will be shared by the two institutions, according to the particular strengths and experience of each.

### 10.2.4 Scintillator plane assembly

The module assembly process for MINER$\nu$A planes are based on those used in MINOS project. Labor requirements for prototyping and assembling the MINER$\nu$A scintillator planes are estimated from extrapolation of the as-realized MINOS far detector scintillator module production. The labor model for this construction is based on a mixture of full-time mechanical technicians and undergraduates, which is the same as employed for MINOS at University of Minnesota.

An overview of the four-day scintillator plane assembly process is briefly summarized here. Prior to the first day, we receive scintillator strips, fibers, optical connectors, and the various parts and supplies for construction. In the first day of the process, we initially cut the scintillator to length. Each strip of scintillator will come bar coded for tracking purposes. After that, the lower skin, fiber routing trays, survey fiducials, and lower strips are laid into position. A layer of adhesive is applied to the gaps between the strips and the web layer is positioned. We then cover the assembly with a vacuum seal and cure it overnight. On the second day, we lay the upper strips, insert fibers, apply a layer of glue, and lay the top skin. The assembly is again covered in a vacuum seal and cured overnight. On the third day we polish connectors, perform initial quality assurance, fix bad fibers, seal the ends, and glue a layer lead to the skin. The assembly is then covered a third time in a vacuum seal and cured overnight. The last day involves final quality assurance, fixing possible light leaks, and packaging for shipment. Each scintillator assembly's response will be mapped after shipping to Fermilab, after mounting in a detector

module frame, as described in Section 10.3.4.

MINER$\nu$A requires a total of 196 hexes and 1612 OD modules. We will produce an additional 12 hexes and 89 OD modules as spares. We assume 3% wasted components during production so the total part counts corresponds to 214 ID and 1612 OD assemblies.

## 10.3 Detector Modules

### 10.3.1 Module frames

The basic frame shape is shown in Figure 55, and is about 4.3 meters tall. Each frame serves several purposes: to hold the scintillator composing the inner detector, to serve as a skeleton for the outer detector, to provide a magnetic field outside the inner detector, and to support the lead for the electromagnetic calorimeter. Each frame holds two layers of scintillator, and there are a total of 98 frames. Because the detected particles produced in the fiducial volume will be lower-energy in the most upstream part of the detector, the thickness of the outer detector will be about 60 cm smaller in that region. The thickness of individual towers is 56 cm for the upstream section and 87 cm for the downstream section.

A number of factors were considered in the outer-detector frame design: material, thickness, production of the hex (from single plate or welded individual plates), and construction of slots. We discuss each of these in turn, with attention to factors that will affect construction and robustness of the resulting calorimeter.

Because the frame will be magnetized, it must be made of a material with good magnetic properties. We have chosen soft steel with the specifications used by MINOS. This is basically AISI 1006 (less than 0.06% C), with some additional requirements on other impurities. This alloy is not a stock item and will require a few month lead time to be produced.

We considered making the hexagon from a single plate, but the required width (about 3.7 meters) is larger than what is generally available, and cutting the center out would involve a great deal of waste (and cost). Instead, we will make each tower separately and weld the plates together at Fermilab. The individual towers are about 2.2 meters long and nearly one meter wide.

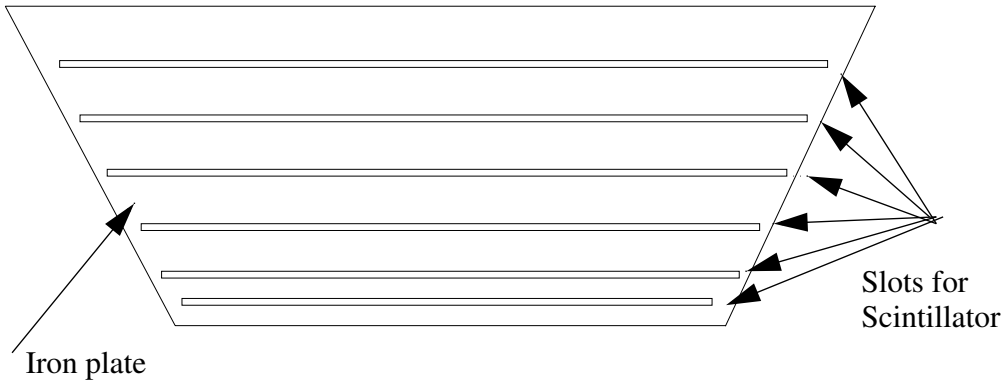


Figure 58: Schematic of one tower showing scintillator placement.

Each tower has six slots, as shown in Figure 58, nominally 1.6 cm (5/8 inch) wide to hold the scintillator. Our initial plan was to have each hexagon hold one layer of scintillator, so the plates would be approximately 1.6 cm thick. After discussion with the steel manufacturer and machine shops, we have instead decided to use 3.8 cm (1.5 inch) thick plates. From the steel production view, the thinner

plates would be difficult to make flat, and mills will charge more to make it. Cutting the slots in such a thin material would lead to warping of the plates, and welding would also be more problematic. While none of these problems were insurmountable, going to a thicker plate made the design less prone to problems and less expensive.

Cutting slots in the plate is a time consuming (and hence expensive) procedure. The cheapest technique appears to be flame cutting. This can be done to a precision of about 1.6 mm (1/16 inch), which is adequate for our purposes. It will require a somewhat wider slot (about 2 cm), which will necessitate increasing the width of the tower slightly to keep the same absorber thickness. This method will likely cause considerable warping of the plates (more than 1 cm) and change the magnetic properties near the cuts. Annealing the plates after cutting will both flatten the plates and give more uniform magnetic properties.

The normal method of handling plates of this size is with magnets. In order to avoid magnetizing the plates, we will need to cut some holes to allow the plates to be easily moved with a crane. In addition, holes will be drilled and tapped to allow attachment of the lead plates.

The number (588) and size (about 225 kg each) of these plates, as well as the need to flame cut the slots, puts their construction beyond the capabilities of a university shop.

Once the plates are constructed, they will be shipped to Fermilab for final assembly. The plates require welding only at the ends of the joints for mechanical strength. We do not expect the magnetic properties to be significantly affected by the small gap between plates. A finite element analysis showed the frame will sag less than 0.1 mm.

We have obtained non-binding quotes from Metals USA, Inc. for the steel and machining needed for this frames. The estimated delivery time is 6-8 months.

### 10.3.2 Calorimeters

The calorimeters are in three distinct regions: upstream of the active target, around the active target (the outer detector), and downstream of the active target. The upstream calorimeter will also provide a variety of nuclear targets (carbon, iron, lead).

**Upstream calorimeters and nuclear targets** To study differences in neutrino scattering from different nuclei, three nuclear targets, carbon, iron, and lead, will be mounted on the upstream side of the active target area. Scintillator planes identical to the central detector modules will be interleaved with the passive target/absorber material. The mass of the lead and iron will each be about one ton, and the carbon target in this region will be about half a ton. The nuclear targets will also serve as absorbers for the upstream calorimeter.

Our proposed arrangement, illustrated in Figures 49 and 47, is to have planes of a single material in this area. However, to reduce systematic errors in comparisons across different nuclear targets, we are considering using partial planes of multiple materials in a single layer for at least some modules. More studies are required to finalize this decision. The decision should not significantly affect the estimated cost because it involves only the arrangement of the layers.

**Side calorimeters** To provide electromagnetic calorimetry for particles exiting the sides of the fully-active central region, lead plates will be mounted on the frames and extend over part of the central scintillator region. Smaller plates will be mounted between the two scintillator layers contained in each frame. The plates will be approximately 2 mm thick. Pure lead plates are not strong enough to support

their own weight when attached with screws to the main frame, so we will use a Pb-Ca-Sn alloy which is considerably stronger than pure lead. Tests performed at Rochester with this alloy have confirmed that its strength is adequate.

The hexagonal frame also serves as the outer detector, with layers of iron and scintillator (as discussed above). The frame will serve as a ranger for lower energy particles and as a muon detector.

**Downstream calorimeters** The downstream electromagnetic calorimeter (ECAL) and hadron calorimeter (HCAL) are simple variations of the basic detector module - identical scintillator planes, but separated by absorbing material. The ECAL consists of sheets of lead alloy 2 mm (5/64 inch) thick (the same material as used for the side ECAL), which cover the entire hex frame, with layers of scintillator between the sheets. The HCAL will consist of 2.5 cm (1 inch) steel plates, also covering the entire frame, also with layers of scintillator between the plates.

### 10.3.3 Module assembly

As shown in Figures 45–50, MINER$\nu$A modules consist of two outer detector frames, two, three or four hex planes of scintillator in assemblies and 24 or 36 outer detector scintillator modules as described in Section 10.2.3, and the appropriate calorimetric absorbers for the type of modules. The completed assembly serves as a single structural unit of the detector which is assembled above ground, transported to the NuMI near hall and there installed on the detector support frame.

In brief, the assembly procedure consists of the following steps. Two outer detector steel frame trapezoids are arranged on strongbacks on a frame-table and skip welded into OD frames; lifting and mounting fixtures and frame fiducials are welded onto the frames; and necessary steel absorbers are welded or lead or graphite absorbers are screwed into the frame. At this point, the frame may be flipped to allow for scintillator installation if absorbers were screwed onto the frame face. Then, the hexagonal scintillator planes and OD modules with their associated fiber cable "snouts" are arranged onto the frame and tack welded into place on each frame. One of the two frames in the module is flipped and laid onto the other where the two are joined together with a module joining plate and the top strongback is removed. The completed module with its remaining strongback is then ready for mapping, and eventually for installation.

This work will be led by university (Rochester) technicians, resident at Fermilab, and will be assisted by FNAL welders and physicists who will run the mapping process. We plan to house the assembly facility in the New Muon Lab at FNAL because of good crane coverage and significant available floor space. Figure 59 shows technicians doing similar work during assembly of the MINOS near detector.

### 10.3.4 Module response mapping

Within MINER$\nu$A, two hexagonal planes of scintillator are physically combined into a structure called a "pan"; two pans are combined into inner-detector "modules". We will use a source scanner for quality control of each module before final installation and to map the local response of the detector. The source scanner moves a collimated source over the the broad face of the scintillator module, creating scintillation light at known positions.

Variation in local response is dominated by the attenuation length of wavelength-shifting fiber. A smaller contribution to the non-uniformity (1–2%) is due scintillator itself. The primary goal of mapping

Figure 59: Module assembly work for MINOS, closely analogous to the MINER$\nu$A initial (left) and final (right) assembly steps, being performed by technicians at the New Muon Lab. Note the use of the Lab's crane and floor space.

modules with the scanner is to measure the attenuation length of the fibers in each pan. The overall gain for each channel (including PMT response and loss in optical connections) will be determined with cosmic-ray and neutrino-induced muons in the experimental hall. Since most damaged fibers can be diagnosed visually, we will check the fibers for before and after installation. Hence the purpose of the scanner is to map the local response, not to calibrate gains or identify broken fibers.

A similar system, pictured in Figure 60, was employed used by MINOS. Our system will be built and operated based on the MINOS design. In the MINOS scanner, the short axis moves using a lead screw, and the long axis moves using using a rack and pinion system. The pinion gear and gear rack were manufactured by Martin Gear. The scanner moves at a rate of 0.15 m/sec along the short axis and 1 m/s along the long axis. The motors on both axes use servo motors made by Aerotek. Both motors employ planetary speed reducers (10:1 for the long axis, 4:1 for the short axis) made by Minarik. The carriage runs on a double side rail bearing combination made by Thompson. The scanner top is made of an aluminum honeycomb sandwich panel, called "Hexcel", made by Pacific Panel. The scanner sits on a Unistrut frame.

MINER$\nu$A's scanner will not be identical to MINOS' due to the different dimensions of the two detectors' scintillator components. The MINOS scanner covers an area 1.2 m by 10 m. MINER$\nu$A's needs to scan an area about 4 m square. By strengthening the carriage, we can extend its range in the short dimension from 1.2 m to 4 m. It may also prove more economical to construct the support frame from welded aluminum rather than Unistrut.

The scanner will employ a 5 mCi Cs-137 source, similar to the type used by MINOS, collimated by a machined lead cone. At least 5 cm of lead on the sides are required for collimation, with at least 2.5 cm of lead on top for shielding. The source will be mechanically connected to the lead cone to prevent removal. Fermilab's Safety Division will review and approve the final design to ensure the shielding is sufficient protect the scanner operators and others from exposure to hazardous levels of radiation.

The signal and readout system for the source scanner will be the MINER$\nu$A PMTs, PMT boxes and data-acquisition system.

The modules should be light tight when we scan them, but a tarp will be available to help track

Figure 60: The MINOS source scanner. MINER$\nu$A will construct a similar device to scan scintillator pans after construction to control quality and map local response.

down and fix light leaks that may have been created during transportation. Once a module is placed on the scanner and its light-tightness is verified, the scan will begin and run automatically overnight. We expect to scan one pan per day. Based on MINOS experience, the scanner can make 4 measurements per minute, including the movement of the source. Thus, we can do about 5000 individual measurements on each module, corresponding to 10 scans along the fiber direction, each scan involving 500 steps perpendicular to the scintillator strips. This will produce enough data to fit each fiber to a double exponential function, and provide a good description of its attenuation.

### 10.3.5 Detector stand

The detector stand will consist of two rails approximately 20 feet in length. Each rail is supported by four vertical posts of structural steel, with a structural steel bookend at the downstream end. The "keys," which lock the 4-plane module assemblies into the structure, are made of stainless steel (or a combination of stainless and brass) to prevent the supports from becoming magnetized. There will be 100 of these (2 each for 50 modules) and their manufacture will constitute most of the machinist's time for this item. The sum weight of all of the modules is estimated to be 211 tons plus a possible 91 tons for an eventual muon ranger, exclusive of cabling, electronics and other accoutrements. The preliminary design calls for the stand to support 400 tons.

We intend to build two support structures, one shorter structure for module assembly at the suface and one for support below ground in the MINOS near hall. The module assembly and the assembly stand itself would be at New Muon Lab. The underground support structure should also be assembled first on the surface, at the New Muon Lab. The purpose of the above-ground assembly is to test the structure itself and de-bug assembly procedures. It will be modified as necessary, then disassembled and moved underground to the MINOS hall. All critical welds will be made on the surface. Underground assembly will consist of rigging and bolting.

### 10.3.6 Module installation

The MINER$\nu$A installation is expected to proceed much like the MINOS near detector installation: a complete module will be placed on a strongback, driven from New Muon Lab to what is called the "MINOS shaft", then lowered down the shaft onto a cart at the base of the shaft. This cart then transports the module plus its strongback to the MINOS hall, where a second crane will pick up the strongback and module and place both on the detector support stand. Then the module will be connected to either the bookend or an already installed module, the strongback removed from the module, and brought back up to the surface.

This task is assumed to be straightforward, based on experience with the MINOS installation. It is possible that some materials left over from MINOS could be used in the fabrication of the strongback. Also, the cart that was used to transfer MINOS near detector planes while underground might only need some modifications to be used for MINER$\nu$A modules.

One attractive possibility is to assemble the modules on the strong back, and the individual pieces would therefore be lifted with slings and placed on the strongback. In this way an additional custom-built lifting fixture other than the strongback itself will not be necessary.

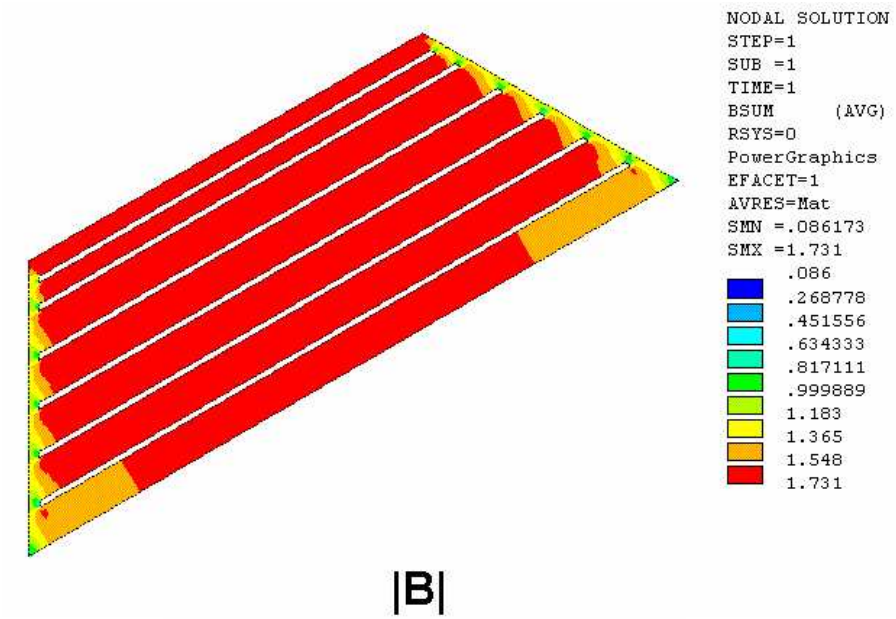


Figure 61: A preliminary calculation of the expected magnetic field ($|B|$ in Tesla) in MINER$\nu$A frames made from 1009 steel and energized by a 28,000 A current.

## 10.4 Magnetic Coil

This section describes the requirements of the MINER$\nu$A coil, and what these requirements imply for the coil design. Much of the design of the coil is borrowed from that of the MINOS near detector.

To achieve a high magnetic field and the best possible momentum resolution, the current must be high enough to saturate the low-carbon steel. Finite-element analysis calculations have shown that 28,000 A-turns will suffice, yielding a toroidal magnetic field of 1.6 T for 1009 low-carbon steel. The calculated field is shown in Figure 61 and the field in a radial slice is shown in Figure 62. The effect of the field will be to focus radially escaping negatively-charged tracks (i.e. muons) toward the MINOS near detector.

The coil turns will be installed through the completed detector modules and will be the final piece of heavy installation during detector construction. The space requirements and installation plan lead to a design with a minimum number of turns and high current per turn, as in the MINOS near detector [170]. This high current on the coil turns will require substantial cooling. A low-conductivity water (LCW) closed loop provides the coil-cooling for the conductor.

The coil consists of 11 approximately 5.5 m legs (bore and return) and 12 approximately 1.5 m-long sections to connect the bore and return legs (upstream and downstream).

Each coil leg is formed from $2.8 \times 3.8$ cm$^2$ rectangular cross-section aluminum conductors with a 1.66 cm diameter channels through their centers. The conductor is cooled by flowing LCW through the center channel. The cross-section of the one of these conductors is shown in Figure 63. The coil cross-section has 36 of these conductors.

Groups of six conductors are formed into planks (Figure 64). The electrical connections are made using edge-welded lap joints. An example of one of these joints from MINOS is shown in Figure 65. The current flows in parallel through the conductors within a plank. The lap joints require less installa-

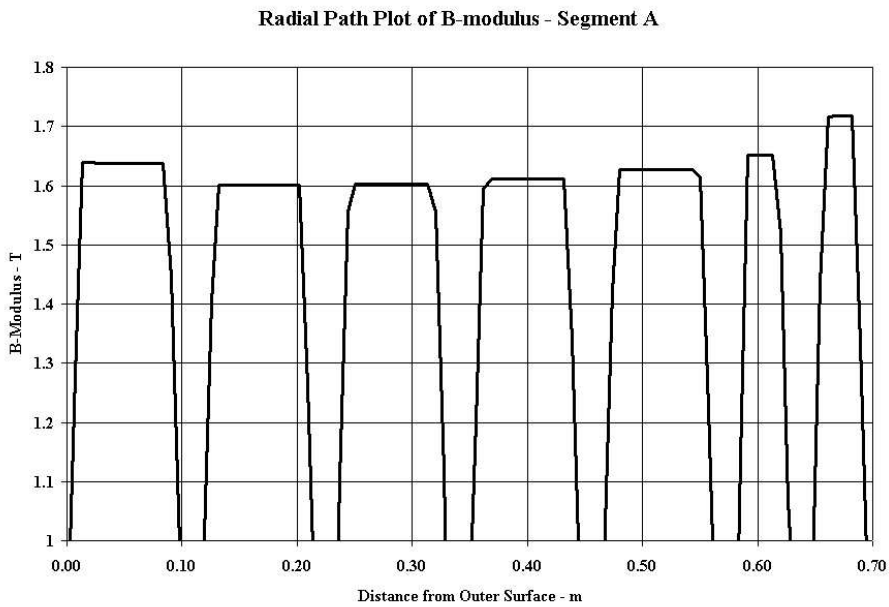


Figure 62: A preliminary calculation of the expected magnetic field ($|B|$ in Tesla) in a radial slice through a MINER$\nu$A frame made from 1009 steel and energized by a 28,000 A current.

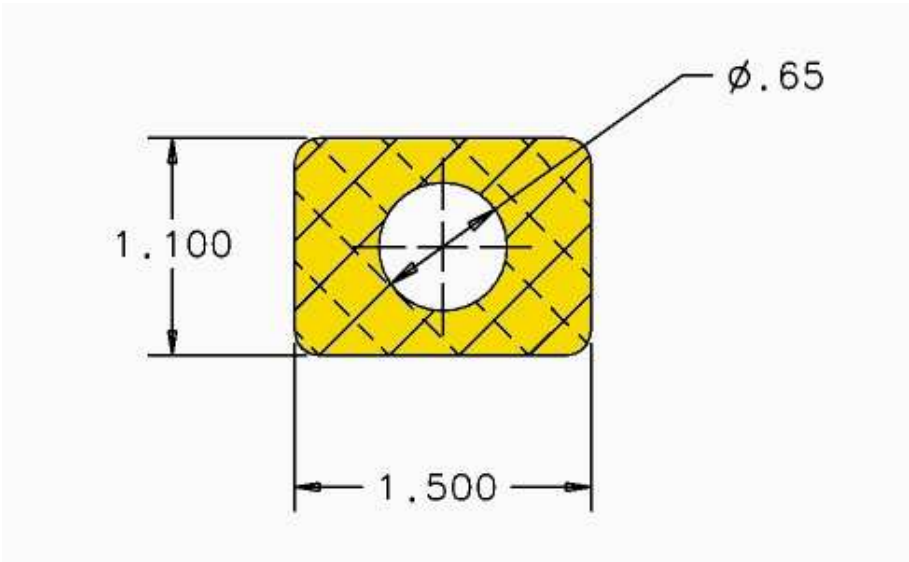


Figure 63: Cross-section of an aluminum conductor element. The dimensions shown are in inches.

Figure 64: Cross-section of a MINOS coil plank. An identical design is proposed for each turn of the MINER$\nu$A coil.

tion labor than designs requiring conductor-by-conductor in situ welding.

Input and output water manifolds will be located at all four corners of the device. Water passes through four planks before returning to the chiller, giving six separate parallel water circuits. The water flows in parallel within a plank. Flow calculations show that the flow rates in the different conductors within a plank are fairly well balanced [171].

There is only one electrical circuit. Each conductor carries up to 833 A and the coil is powered by a 5000 A supply.

### 10.4.1 Manufacture and installation

The pre-tested aluminum conductor is purchased from a vendor and delivered directly to the coil fabricator on spools where it is uncoiled, straightened, and cut to length. The ends of the conductors are prepared for welding in two ways: the hole is countersunk for a stainless-steel ferrule and the edges are beveled to allow for full penetration welds. The six conductors in a plank are welded together. Ferrules are inserted into the lap-joint pieces and mated with the conductors and then welded. The planks are wrapped in two layers of G10 and B-stage epoxy and heat cured. The finished planks are then pressure and flow tested prior to delivery to Fermilab.

After delivery the completed components are lowered into the NuMI near detector hall though the shaft using a special lifting fixture. Because the MINER$\nu$A coil will be significantly shorter than the MINOS near detector coil (5.5 m compared to 20 m), the installation will not be nearly as challenging.

The coil will be installed after the detector has been mounted. Planks are rigged into position using a special "spreader bar" lifting fixture to support the free end of the plank as it enters the bore. Note that the center segment of the coil assembly (six full-length planks) weighs about 100 kg. The planks are flexible, and could be easily damaged if overstressed. Before the lap connections are made the surfaces

Figure 65: Completed MINOS planks showing lap joint end pieces.

will be chemically cleaned and a surface coating will be applied. After a new plank is put in place, the lap-joint connection is completed. There is a relatively short time (minutes) between the preparation of the surface and the mating of the splice.

Before the installation can proceed, brackets are mounted on the steel support structure to support the return coil. Installation of the first four planks is somewhat different than the remainder of the planks. Rollers on the lifting fixture enable the planks to slide smoothly into the bore of the detector, where they rest on insulation in the central collar tube. The long return plank is then rigged into position on the support brackets under the detector. A short plank is rigged into position on the downstream end of the detector and connected to the first two planks. Each connection will be checked for electrical integrity. The water connections to each end of the planks will also be made. A second short plank is installed on the upstream side of the detector and is only connected to the return plank. This completes the first circuit of planks. After this point, the installed coil sections are self-supporting.

The remaining planks are installed in a helical pattern. First a bore plank is installed, then a downstream plank, then a return plank, and finally an upstream plane. As each plank is installed it is electrically connected to the previous plank and protective insulation installed. Final installation of the coil includes making connections to the power supply and tests of the LCW system.

### 10.4.2 Cooling systems

The coil cooling system will connect to the MINOS halls LCW cooling system. The coil cooling system will run at about 70 GPM and must carry off the 25 kW of heat generated by the coil power supply, coil, and power bus. Fermilab will install additional cooling to the detector hall accommodate this load.

### 10.4.3 Power system

The coil will be powered by a Fermilab PEI 150-5 supply running at 5 kA to deliver up to 5000 A or 833 A per conductor. The power supply has remote readout and remote control capabilities. The supply, cooling system, and interlocks will be provided by the Fermilab.

The supply's control and monitoring systems will be interfaced to the Fermilab ACNET control system in keeping with standard practice for analysis magnets. There will be a parallel read back to the MINER$\nu$A slow control systems and parallel read back and control for the magnetic calibration system. As in MINOS, manual connections at the supply will be used to change the control source.

The coil power supply will have a current regulator and precision readout to continuously monitor its current. In addition a resistance bridge will be installed to monitor for small changes in the resistance of the coil that could signal non-uniform heating or shorts. Thermal interlocks will also be provided in the event of excessive heating or loss of LCW flow.

The coil will also have a 5 kA mechanical reversing switch to allow the polarity to be reversed. The switch will have remote control and monitoring capabilities and will be interface to ACNET for control and the MINER$\nu$A slow control system for read back.

### 10.4.4 Magnetic calibration

Calibration of the magnetic field will be done by the installation of induction coils at several radii per plane. These coils will be read-out by a PC with Keithley scanning ADC and I/O board using a LabView program.

Although the coils themselves (called Bdot cables) must be purchased, all other hardware can be recycled from MINOS.

## 10.5 PMT's, Optical Boxes and Cables

### 10.5.1 Multi-anode PMT's

With an inexpensive active detector technology, the dominant equipment costs for MINER$\nu$A are photosensors and their associated read-out electronics. Our choices among the universe of available technologies is determined by the answers to three questions. First, is the light yield for a minimum-ionizing particle sufficient to support a low quantum-efficiency detector such as photomultiplier tubes (PMTs) or image intensifier tubes (IITs)? In MINER$\nu$A, there is sufficient light to use a $1/6$ quantum efficiency photocathode with a WLS fiber diameter of at least $1.2$ mm, as explained in Section 11.3. Second, is timing within the spill important or can a technology that integrates over a long window, such as IITs be used? We concluded that timing within the spill, both to flag overlapping events and measure time of flight and decay times at rest was important to our physics goals. Third, what level of technical risk, R&D time and cost is acceptable? We concluded that for MINER$\nu$A to begin data-taking as early as possible, and given the modest size of our collaboration and expected detector costs, we should choose low technical risk over lengthy R&D programs designed to reduce costs or improve performance.

In our design process, we considered four technologies for photosensors: multi-anode photomultiplier tubes (MAPMTs), IITs, avalanche photodiodes (APDs) and visible light photon counters (VLPCs). Ultimately, we chose a solution based on MAPMTs with a sensor+electronics cost (including EDIA and overhead but without contingency) of approximately $40 per channel, approximately divided between

$15 per channel for the sensor, $15 for the electronics and $10 for EDIA and testing. To defend this important decision, we discuss the alternatives mentioned above.

Image intensifying tubes coupled to CCDs are an appealing low-cost solution for reading out bundles of fibers, in part because the CCD itself is the final stage photosensor and readout device. This device is well-matched to the pulsed structure of a neutrino beam, with one readout corresponding to one beam pulse. Costs per channel are largely proportional to the total photocathode surface required, which is set by the number of channels and fiber diameter. Cross-talk in adjacent channels is a non-trivial issue, but can be addressed because of the high density of CCD channels relative to fiber granularity, even with intermediate spatially demagnifying stages. We were driven to relatively expensive CCD cameras because of the need maintain reasonable linearity. Our candidate system, based on Hamamatsu C8600 2-stage multi-channel plate (MCP) intensifiers and C7190 bombardment CCDs, was approximately $15 per channel, including photosensor and CCD readout but not including required demagnification optics. Nevertheless, a complete IIT/CCD system would likely still be half the cost of the chosen MAPMT solution. Our concerns about the system were the smaller effective dynamic range, even with relatively costly IIT/CCD systems, and the relatively low mean time to failure per device reported in other large systems (4 years per two stages in the CHORUS experiment). However, the missing capability for timing within a single main injector spill was enough for us to discard this otherwise promising option.

Avalanche photodiodes (APDs) were also considered because of their recent successful application in the CMS ECAL and their proposed use in the NuMI off-axis far detector. APDs are low gain ($\sim$100), high quantum efficiency (85% for Y11 WLS fibers) devices which offer significant cost savings in the photodetector. Complications of operation include the need to cool the sensors below room temperature to reduce noise, but this is a fairly easily solved problem as cryogenic temperatures are not required. The primary problem we identified with APDs for MINER$\nu$A was the need for significant electronics R&D to develop a low-cost system for controlling noise over the long NuMI spill. For MINER$\nu$A, we set a requirement of keeping the photosensor and electronics noise well below 10 delivered photon equivalents to maintain good sensitivity to minimum-ionizing particles (typically 70 photons in a doublet of triangular scintillators) and a low rate of detector noise. Over a 12 $\mu$s gate (the NuMI spill plus $2\tau_\mu$) at -10°C with an operating gain of 100 (optimal), the signal from 10 photons is 850 electrons and the noise on the best existing candidate electronics, the MASDA chip, is 900 electrons. To achieve the better signal-to-noise being pursued by the proposed NuMI off-axis R&D program requires design of a new ASIC, which would imply at least a one-year development project. In short, although the APD is a potentially promising technology, we were not convinced it could be in production on a timescale suitable for MINER$\nu$A.

The final alternative considered was the VLPC. These have a history of successful employment and electronics design in the D0 fiber tracker and pre-shower detectors. However, the costs for just the VLPCs themselves, even under optimistic assumptions about the outcome of future R&D, would exceed $50 per channel, and are thus significantly greater than the MAPMT solution. Given that the low quantum-efficiency solution gives sufficient resolution, it is difficult to justify the cost of VLPCs.

The MAPMT we have selected as our photosensor is the Hamamatsu R7600U-00-M64. These are an incremental design improvement from the R5900-00-M64 MAPMTs used in the MINOS near detector, and we expect much of the experience gained by the MINOS collaboration with these detectors to be applicable. In particular, we have confidence in costing the testing, housing for and optical connectors to the PMTs because of our ability to scale costs from the MINOS experience.

### 10.5.2 PMT testing

James Madison University (JMU) will build a test stand for evaluation of MINER$\nu$A's Hamamatsu M64 photomultiplier tubes (PMTs). The M64 PMT is currently used by MINOS, and the results of their tests have been submitted for publication [167]. Each MINER$\nu$A PMT will undergo a similar series of tests to verify its suitability for use in the experiment. Tubes passing specified acceptance criteria will then have their performance characterized in detail.

The JMU test stand is designed to test 5 M64 PMTs simultaneously, with an additional witness PMT for reference. The pixels of the M64 are arrayed in an $8 \times 8$ lattice. Bundles of 64 clear optical fibers will be connected to the pixel arrays of the six PMTs in the test stand. A wavelength-shifting (WLS) fiber bundle mounted on a computer-driven stepper motor table will allow illumination of any of the clear fiber bundles. The light intensity may be varied with a neutral density filter wheel between the clear and WLS fibers. A pulser-driven blue LED will serve as the light source for the test. Figure 66 shows a schematic of the test set-up.

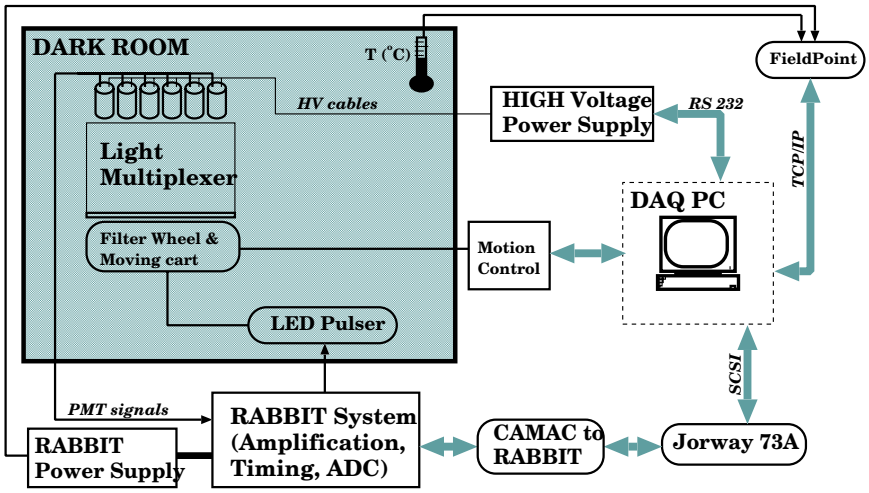


Figure 66: Schematic of the University of Athens MINOS PMT test stand and associated electronics which serves as a prototype for the JMU test stand to be constructed for this project. Note that we plan to replace the RABBIT system shown in this diagram with MINER$\nu$A electronics for the final test stand.

Each PMT will undergo a series of tests to qualify it for service in MINER$\nu$A and record the relative response of each pixel.

- Gain vs. voltage in the range 500–1000 V will be measured at a light level of 10–15 photoelectron using a stable pulsed LED source.

- Width of the single photoelectron peak will be measured using the same LED pulser with 0–1 photoelectrons per pulse.

- Linearity of charge response. Space charge effects in MAPMTs can be a problem due to the small size of the dynodes, and MINER$\nu$A relies on measurements of high $dE/dx$ for proton

identification and electromagnetic shower energy reconstruction. The filter wheel will be used to map the signal vs. light input relative to a low light standard.

- Quantum efficiencies will be measured by comparing light yields to those of the witness PMT which will, in turn, be calibrated against a Hamamatsu supplied standard.
- Dark current at operating voltage within a MINER$\nu$A ADC gate. A high number of pulses will be measured with the MINER$\nu$A gate to ensure that few of these gates are populated above a 1/3 photoelectron threshold from dark current.
- Inter-pixel cross-talk will be measured by illuminating single pixels over a variety of light levels and observing their nominally dark neighbors.

These tests will require an estimated 3 days for one batch of PMTs. For each test, 5000-10,000 pulses per pixel per setting will be acquired. For example, to test linearity we plan to acquire 5000 events per pixel using 12 different filter densities. The total number of pulses would be $64 \times 5000 \times 12 = 3.84 \times 10^6$. Assuming a data acquisition rate of 200 events/s this will result in 5.3 DAQ hours. Additional time would be required to move the light source in between measurements. Testing one third of MINER$\nu$A's MAPMTs will therefore take about 100 days.

JMU will plan for the capacity to test two thirds of the PMTs needed for MINER$\nu$A. Collaborators at the University of Athens, not supported by this proposal, will develop a parallel test stand to test the balance of the PMTs for the experiment.

### 10.5.3 PMT optical boxes

Design, fabrication, and testing of an operational array of 550 photo-multiplier tube (PMT) optical boxes is one of the critical tasks required in construction of MINER$\nu$A [168]. Realization of this array and its delivery to the surface staging area at Fermilab is the primary responsibility of the Tufts and Rutgers groups. Design and prototyping work for a MINER$\nu$A-specific PMT box is summarized below. MINER$\nu$A boxes, in contrast to optical boxes developed for the MINOS far detector ("MUX" boxes), will house a single M64 phototube per box. Unlike either the MINOS MUX boxes or "Alner boxes" of the near detector, the MINER$\nu$A design will use construction-standard steel extrusions reduce fabrication costs and improve magnetic shielding.

Based upon our current design and Tufts' invaluable 2001–2003 experience with production and testing of MINOS MUX boxes, a realistic projection of the costs and schedule has been assembled. Our construction model assumes two coordinated, independently operating assembly and testing sites, one at Tufts and the other at Rutgers. Our breakout of costs and schedules for instrumentation and startup of the factory lines, staffing, purchase and fabrication of component parts, quality assurance testing, and shipping, are detailed in Chapter 12.

**PMT box overview** In MINER$\nu$A, each PMT will reside in a single light-tight box to which optical cables carry the scintillation light from the detector's active regions. Within each box, the enclosed PMT will be in optical contact with polished ends of the bundled fibers which it reads out. This contact is made possible via termination of the fiber bundle in a "cookie" which holds the polished fiber ends. Registration of the fiber-loaded cookie to the PMT is mechanically precise by necessity; it is made possible by a rigid mounting framework which holds the PMT and cookie, whose relative positions are fixed via alignment pins. The fiber mounting cookie is a precisely-machined piece made of Noryll

plastic. In addition to the optical input cable, each PMT box has two electrical cables connected to its associated front-end board: one from a nearby low-voltage power fan-out (Section 10.7), and another for communication with the data-acquisition and slow-control system, which runs in a daisy-chain among twelve boxes (Section 10.6.3). Electrical and optical connections to the interior of each box will be made via endcap connector ports.

To minimize the length of clear fiber cables from the wavelength-shifting fibers to the PMT boxes, we will mount the PMT boxes on the upper surface of the detector itself, using mounting frames of aluminum and steel to provide an air-gap standoff between the optical boxes and the magnetized steel of the outer detector. Since an ambient magnetic field of several tens of Gauss will be present, which could degrade phototube performance, MINER$\nu$A optical boxes must provide magnetic shielding for the PMTs, as well as a light-tight enclosure. Specifically, the optical box must ensure that the internal ambient field is below 5 Gauss. Two features of the MINER$\nu$A design achieve this goal. First, the box walls will be 1/8-inch steel (3.17 mm), more than twice as thick as either of the MINOS models. Second, the MINER$\nu$A design is augmented by mu-metal foil surrounding the PMT, which further deflects the remnant magnetic field.

MINER$\nu$A's boxes must be mechanically rugged, protecting both the PMT and delicate fiber hook-up from accidental impacts. The boxes should also be amenable to rapid assembly and testing, and easily disassembled for component repair and replacement. With the latter in mind, we will mount the 64-channel front-end readout board outside each box, enclosed in a pre-shaped aluminum RF shield coverplate. Thus, maintenance of the read-out electronics and Cockroft-Walton HV supply will not require breaking the box's optical seal, or manipulating its optical cables.

**The MINOS "Alner" box** Successful operation of the MINOS far detector and CalDet hadronic calibration detector testifies to the general viability of the experiment's PMT optical box designs. Of the two MINOS box types, the "Alner" box used in CalDet and the near detector is a PMT-per-box implementation more closely aligned with MINER$\nu$A's requirements. Since the Alner box provides a natural starting point for a MINER$\nu$A-specific implementation, we briefly summarize its design.

Figures 67, 68 and 69 show front, back, and side exploded-view photographs of an Alner box. An attractive feature is apparent in Figures 67 and 68. The metallic box enclosure is a shell from which the innards are separated; the latter are mounted on a rigid structural frame which is inserted along the axis of the rectangular enclosure. This arrangement has obvious advantages for assembly and alignment of the fiber bundle, fiber cookie, and PMT, providing ready access to these pieces as shown in Figure 69. We have adopted the same strategy in our MINER$\nu$A implementation.

**MINER$\nu$A optical box design** The Alner box enclosure (to the left in Figures 67 and 68) is made from thin-wall flat plate which is creased and welded into the finished shape. An equivalent structure is obtainable more economically with construction-standard hollow steel extrusions of rectangular cross section. These can be capped at each end using steel "lids" which are stepped around the circumference. In this MINER$\nu$A design, the internal support frame is mounted between these lids; the lids will also carry all of the connector ports. The front lid is smaller than the rear one, allowing axial insertion (as in the Alner box). Standard steel extrusions provide - at lower cost - walls more than double the thickness of Alner boxes, and a modest improvement in magnetic shielding. The original Alner design provided for internal thin-steel magnetic shielding surrounding the PMT, but this was later deemed unnecessary. In our implementation however, interior magnetic shielding is a necessity. A relatively

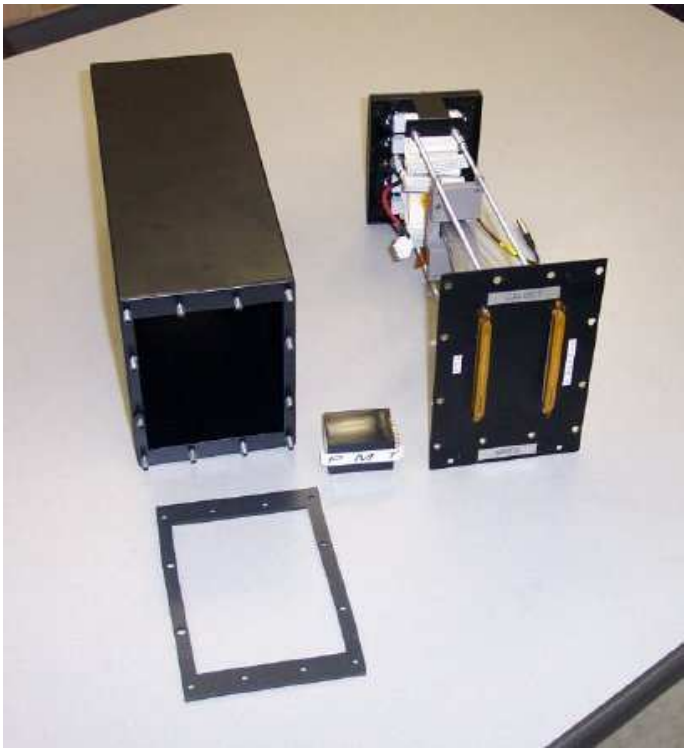

Figure 67: Front view of an “Alner box”, the PMT optical box used for signal readout in the MINOS CalDet and near detector.

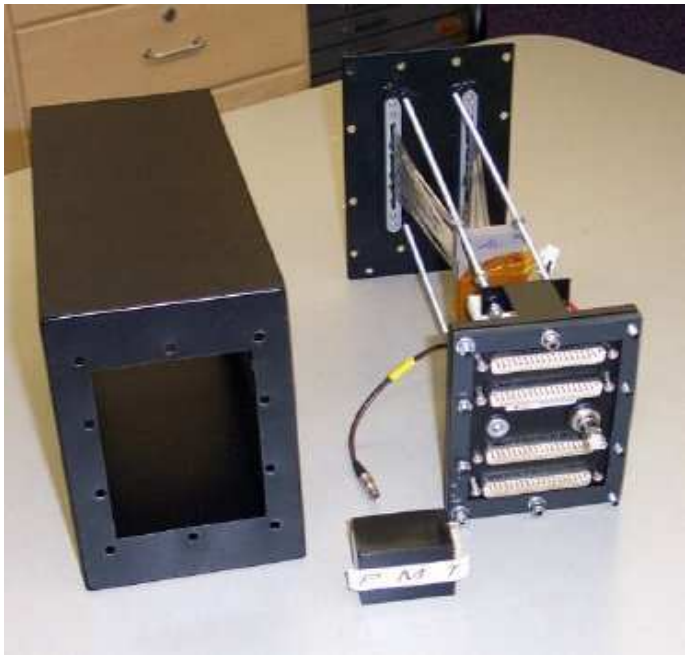


Figure 68: Rear view of a MINOS "Alner box". The framework which holds the fiber cookie and PMT is inserted axially into the surrounding steel enclosure. A similar scheme is used in the MINER$\nu$A design.

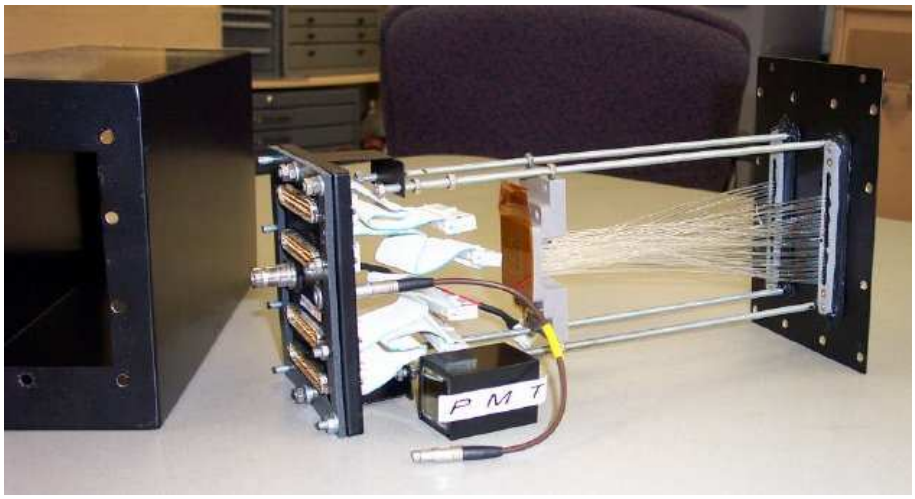


Figure 69: Interior of an Alner optical box. Optical fibers enter via connectors through the backplate and terminate on the cookie. The M64 phototube (foreground) is mounted on registration pins in front of the cookie. Cables provide low voltage and signal connections to the PMT from connectors which breach the front plate.

tight internal shielding surface is achievable using commercially available mu-metal foil; pre-shaped mu-metal forms are also under study.

### 10.5.4 Fiber connectors and optical cables

MINER$\nu$A will use optical connectors from Fujikura/DDK (generically referred to as DDK connectors). These connectors were originally developed for the CDF Plug Upgrade by DDK, in consultation with Tsukuba University. Since then, they have been used by several other experiments (FOCUS, STAR, and D0).

The DDK connectors consist of a ferrule, clip, and box (Figure 70). They snap together without screws and pins. DDK will make a new ferrule die/design for our 1.2 mm diameter fibers, keeping the outside dimensions of the ferrule identical to the current model; thus, other parts of the connector do not need to be redesigned.

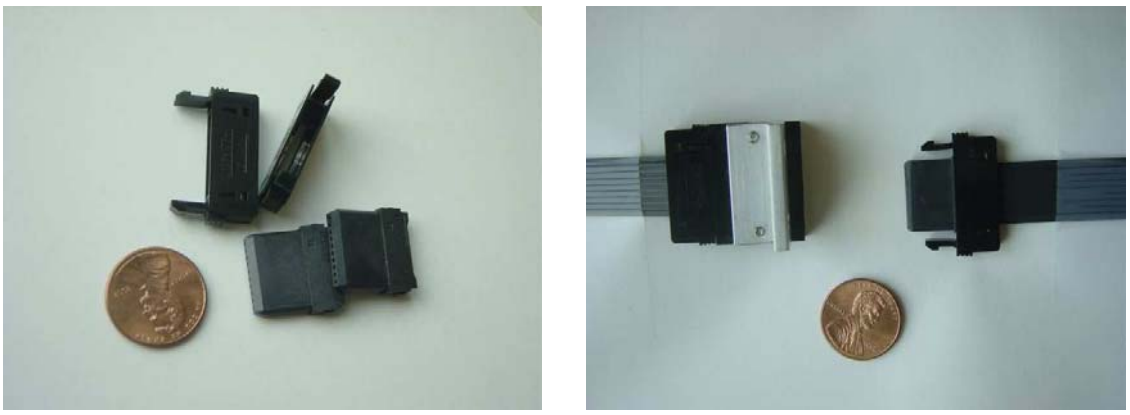

Figure 70: DDK connector parts. At left, examples of the ferrules (bottom) and the clip (top). At right, two completed CDF cables with the box to which they connect. The aluminum angle bolted onto the box is used to hold the box on an aluminum cover.

After mechanically measuring the connectors and performing quality control tests on the fiber, we will assemble wavelength-shifting (WLS) fiber pigtails[5], clear fiber cables, and clear fiber pigtails (the other end of these fibers will be inserted into the acrylic "cookie" for connection to a PMT, see Section 10.5.3).

A sample of fibers from each batch will have their attenuation length checked using a procedure developed by CMS. Fibers will be checked for breaks or cracks during and at the end of assembly. The quality of light transmission for each fiber will be checked once the connectors are mounted.

Our fabrication and polishing procedure was used by the CDF and CMS collaborations on DDK connectors and cables. For the CDF Plug Upgrade, a significant Fermilab effort was devoted to developing a method to polish the DDK connectors. A procedure for polishing one connector at a time is described in [161]; since then, Fermilab has developed a machine we can use to polish 10 optical connectors simultaneously. Fermilab will design a fixture for this machine to hold the DDK connectors.

[5]A "pigtail" is a fiber bundle with a DDK connector on one end; a "cable" is a fiber bundle with connectors on both ends.

Figure 71: The MSU light-tight boot for DDK connectors.

We will use a light-tightening scheme similar to one developed by the Michigan State University nuclear physics group, who used DDK connectors in a large electromagnetic calorimeter. The bulk of the cable is light-tight thanks to an opaque sheath placed around the fiber between the two ends. The region at the connector is made light-tight by placing an RTV (room temperature vulcanizing) silicone rubber boot around the end of the sheath and connector, as shown in Figure 71.

## 10.6 Electronics

### 10.6.1 Electronics overview

The requirements for the MINER$\nu$A electronics are summarized in Table 9. These requirements are motivated by the experiment's physics goals, which include:

- Fine-grained spatial resolution, exploiting charge-sharing between neighboring scintillator strips,
- Identification of $\pi^{\pm}$, $K^{\pm}$ and $p$ using dE/dx information,
- Efficient pattern-recognition, using timing to identify track direction and separate interactions occuring during a single spill,
- Ability to identify strange particles, and muon decay, using delayed coincidence, and
- Negligible deadtime within a spill.

The average data rate expected for MINER$\nu$A ($\sim$ 100 kByte/second) and the relatively modest duty-factor of the NuMI beam (one $\sim$ 10 $\mu$s spill every 2 seconds) are far from demanding by the standards

of modern high-energy physics experiments. To minimize costs and technical risks, we have studied a number of existing solutions, including those used for the MINOS design. Major components of the electronics system include the front-end boards, the PMT and electronics housing, slow control and readout systems. Extensive prototyping and integration testing will be performed for all components prior to production of the final modules.

### 10.6.2 Front-end electronics

The front-end boards digitize timing and pulse-height signals, provide high-voltage for the photomultiplier tubes (PMTs), and communicate with VME-resident readout controller modules over an LVDS token-ring. For easy access in connection, testing and replacement, the boards are mounted *outside* the light-tight PMT housing assemblies. Pulse-heights and latched times will be read from all channels at the end of each spill.

The front-end board for MINER$\nu$A is designed around the D0 TRiP ASIC which is a redesign of the readout ASIC for the D0 fiber tracker and preshower. As discussed below, the TRiP chip has suitable capabilities for use in MINER$\nu$A. The most significant technical risks have already been addressed by our successful 2004 R&D program, using a prototype board fabricated using available TRiP chips from D0. Results from the prototype board are discussed in detail in the R&D section of the MINER$\nu$A Technical Design Report.

**Requirements and design features** Each front-end board will service one PMT (64 channels) which will require 4 TRiP chips per board. The TRiP chips will be controlled by a commercial FPGA (Field-Programmable Gate Array) using custom firmware. A prototype of this firmware has already been developed and successfully operated during our R&D studies. In addition to digitization of charge and timing information, the front-end boards will also supply high-voltage to the PMT and communicate with the downstream readout system over an LVDS (Low-Voltage Differential Signaling) link. Figure 72 shows the basic design of the board and the main components. Table 10 summarizes the channel counts for the final design.

| Parameter | Value | Comments |
|---|---|---|
| Active spill width | 12 $\mu$sec | Spill plus $2 \times \tau_\mu$ |
| Repetition Time | $> 1.9$ sec | |
| Number of channels | 37478 | |
| Occupancy per spill | 2% | LE beam, $2.5 \times 10^{13}$ POT/spill |
| Front-end noise RMS | $< 1$ PE | |
| Photodetector gain variation | 4.5 dB | Extremes of pixel-to-pixel variation |
| Minimum saturation | 500 PE | Proton range-out or DIS event |
| Maximum guaranteed charge/PE | 50 fC | Lowest possible charge at highest gain |
| Time resolution | 3 ns | Identify backwards tracks by TOF |
| | | Identify decay-at-rest $K^\pm$, $\mu^\pm$ |

Table 9: Electronics design requirements and parameters for MINER$\nu$A

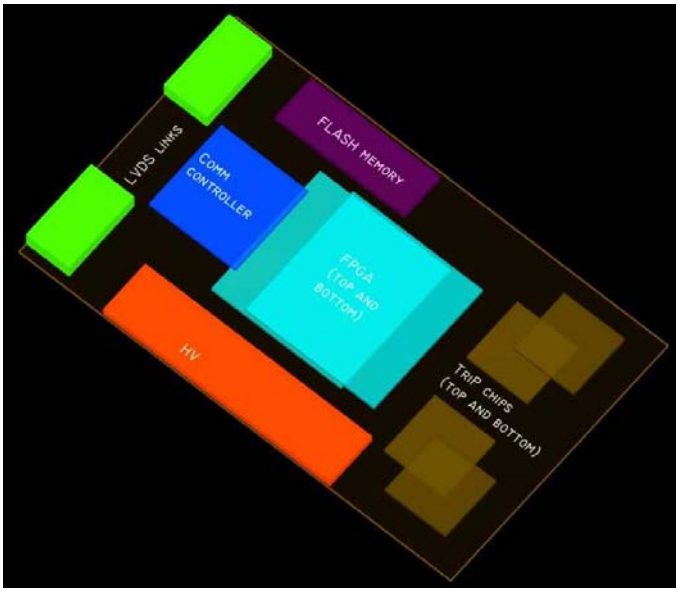


Figure 72: Simplified schematic of the front end electronics final board.

| **Item** | **Quantity** |
|---|---:|
| Front-end boards, including spares(15%) | 580 |
| PMT's serviced per board | 1 |
| PMT channels serviced per board | 64 |
| ADC channels per board | 128 (64 low-gain and 64 high-gain) |
| TDC channels per board | 64 |
| TRiP chips per board | 4 |
| LVDS interfaces per board | 2 (1 send + 1 receive) |
| HV channels per board | 1 |
| Power consumption per board (including PMT HV) | 7 Watts |

Table 10: MINER$\nu$A front-end board channel summary.

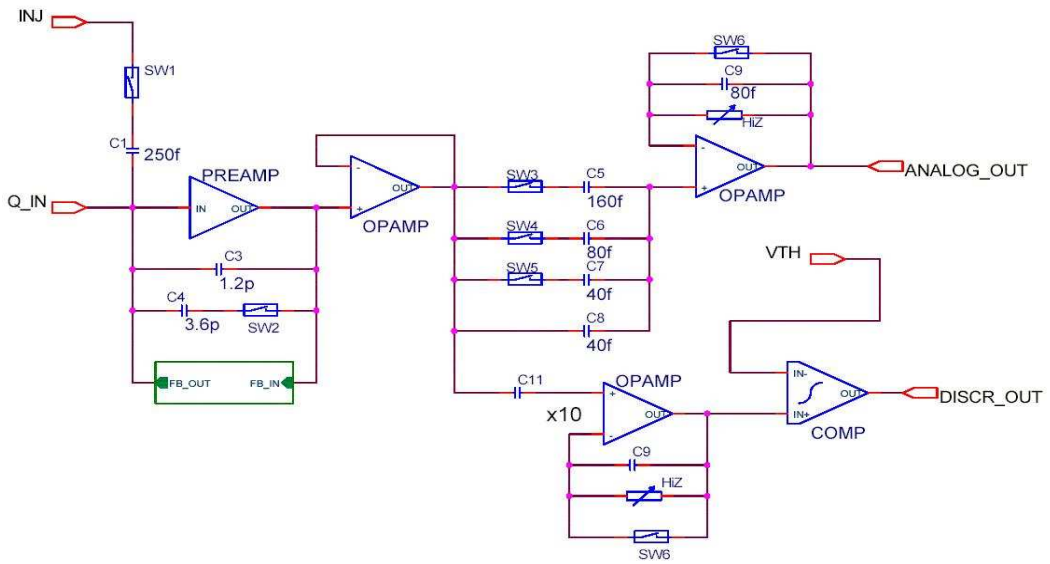


Figure 73: Simplified schematic of the front end electronics of the TRiP chip.

**The TRiP chip and digitization** The heart of the system is the D0 TRiP ASIC. The TRiP chip was designed by Abder Mekkaoui of the Fermilab ASIC group and has undergone extensive testing by D0 [169]. Its analog readout is based on the SVX4 chip design. Each TRiP chip supports 32 channels for digitization, but only half that number of channels for discrimination and timing. A simplified schematic of the TRiP ASIC is shown in Figure 73. The pre-amplifier gain is controlled by jumper SW2 and has two settings which differ by a factor of four. The gain of the second amplifier stage is controlled by jumpers SW3-SW5. We will set the chip to the lowest gain setting for the preamp and largest integration capacitor. This gives a linear range with a maximum charge readout of 5 pC. The "ANALOG_OUT" goes into a analog pipeline, which is identical to the one used on the SVX4 chip and 48 cells deep. To gain dynamic range, MINER$\nu$A will increase the input range of the electronics by using a passive divider to divide charge from a single PMT anode among two TRiP channels with a ratio of a factor of 10. This "high range" channel, then, will give a equivalent total readout charge of 50 pC. Each TRiP channel will be digitized by a 12-bit ADC.

Based on Monte Carlo studies of proton identification by dE/dx, the MINER$\nu$A design requires no saturation below 500 photoelectrons (PE) and RMS noise well below 1 PE. Matching this to the 5 pC charge limit, the highest gain anodes in a tube would be set at 100 fC/PE and therefore the lowest gain anodes would be run at 33 fC/PE. In MINER$\nu$A the integration time for the ADC will be 10–12 $\mu$s, much less than the hold time for the charge in the capacitor of 100 $\mu$s. The prototype MINER$\nu$A board has been tested explicitly with a 10 $\mu$s gate, and the measured pedestal RMS was $< 2$ fC. This will put a single photoelectron approximately a factor of 10 above the pedestal RMS, well within our requirements. The maximum PMT gain for the lowest gain anode will be 50 fC/PE, safely within the desired parameters above.

**Timing** Only one of every two input channels to the TRiP chip has a latched discriminator output (latch) which can be used for timing information. Hence, only the lower range channels will feed the

latch whose output will then go into an FPGA. With appropriate firmware, internal logic of the FPGA can be used measure timing with a granularity of 5 ns. To measure the time of the latch firing accurately, the RF/2 reference clock from the Tevatron (approximately 25 Mhz) is multiplied by four in a PLL and phase shifted by 90 deg to form a quadrature clock that is used inside the FPGA to form a digital TDC with least bit resolution of 2.5 ns. This feature has also been tested on the prototype board and a timing resolution consistent with the 2.5 ns least count timing resolution of the TDC's has been achieved. The reset time for the latch is only 15 ns, so inside a spill the latch will be in the ready state by default. When the signal exceeds a threshold of 1.5 PE, the latch will fire. After storing the time, the latch is reset, incurring minimal deadtime.

Each board includes its own high-frequency phase-locked oscillator, which provides a local clock signal for the FPGA logic. Global synchronization is provided using an external counter-reset reference signal distributed over the LVDS interface from the VME readout boards once every second, and originating with a MINOS timing module which is, in turn, synchronized to the NuMI beam.

**High-voltage** A resonant mode Cockroft-Walton high-voltage generator, mounted on a daughter card, will provide power to each board's PMT. The daughter-card design will allow a malfunctioning high-voltage supply to be easily replaced without changing the main readout board. A controller based on the Fermilab RMCC chip, very similar to one already being developed for the BTeV experiment, will allow the PMT voltage to be monitored, adjusted or disabled under computer control, using the LVDS interface to the board.

**LVDS interface** As detailed in Section 10.6.3 each front-end board will be a member of a chain (or token-ring) connected by LVDS to a VME-resident readout controller. As such, the front-end boards require two LVDS connections, one to receive data from the previous member, and another to transmit data to the next. The LVDS interface transmits all information to and from the board (at 53 MHz), including:

- Transmission of digitized timing and charge data from the front-end board to the VME readout controller,
- Write access to the front-end memory buffers, for diagnostics,
- Configuration of the TRiP chip registers (thresholds, gains, etc) for data-taking,
- Reprogramming of the flash ROM containing the front-end board's FPGA firmware, and
- High-voltage control and monitoring messages.

The first prototype front-end board used in our 2004 R&D studies was designed to accommodate an LVDS interface, which will be commissioned and tested in early-2005.[6] This subsystem represents the most significant remaining technical risk in the electronics (now that the TRiP digitization and timing scheme has been successfully tested), as the latency in propagating signals from one front-end board to another via LVDS limits the number of boards that may be linked in a single chain, and hence the number of chains (and VME readout boards) required to service the full detector. The latency tolerance

[6]For testing and commissioning the board's core digitization functionality, an alternative parallel-port interface was used during initial R&D studies.

is constrained by the need to transmit a global timing synchronization signal to all front-end readout boards. As explained in Section 10.6.3, pending prototype testing we estimate approximately 100 ps jitter may be introduced by each link in the chain. As the least count of our TDCs is 2.5 ns (which is itself considerably better than required, since each track will have numerous timing measurements) we have conservatively limited the design length of each LVDS chain to 12 boards, which represents a factor of two safety margin ($12 \times 100\,\mathrm{ps} = 1.2\,\mathrm{ns}$) from a single TDC count. As LVDS is a mature technology, used in many consumer applications, this risk is a relatively mild one, which in the worst case would require fabrication of a small number of additional VME readout boards and/or a modest compromise in timing resolution which will not noticeably degrade the experiment's physics capabilities. Based on results from the first prototype, the final version of the LVDS interface will be designed and incorporated into the second (64-channel) prototype, and the full token-ring communication protocol defined, for testing together with a prototype of the VME readout controller.

**FPGA and firmware** The internal behavior of the front-end board is supervised by an FPGA operating as a finite-state machine, making the system programmable and highly flexible. As noted, during commissioning of the first prototype version of the board during 2004 R&D, the most mission-critical and timing-sensitive elements of the firmware (controlling the TRiP chip's buffering and TDC functionality) have already been developed and successfully tested. For the production boards, logic to interpret commands and exchange data over the LVDS interface, and control the on-board Cockroft-Walton high-voltage supply will also be required. This additional logic can be developed and tested using the full 64-channel prototype version to be built during 2005.

Persistent storage for the firmware is provided by an onboard flash PROM, which is read by the FPGA on power-up and can be re-written under computer control. As such, it will be possible to reprogram the FPGA logic of all boards remotely even after they are installed, if necessary.

### 10.6.3 Data acquisition and slow control

MINER$\nu$A's data acquisition (DAQ) requirements are relatively modest, as the average data rate expected in the NuMI beam is only 100 kByte/second and a two-second window for readout is available after each $\sim 10\ \mu$s spill. Moreover, the predictable timing of the beam obviates the need for a complicated trigger - instead, a gate is opened just prior to arrival of the beam, and all charge and timing information from the entire detector is simply read-out after the spill is complete. The slow-control system is also relatively simple, with each PMT powered by its own local Cockroft-Walton HV supply (resident on its associated front-end board).

The DAQ and slow-control system is therefore essentially a communication network for distributing information (synchronization, high-voltage commands, and exceptionally, updated firmware) to the front-end boards and funnelling event data collected from them to the main data acquisition computer. The system consists of the following components:

- The main DAQ computer, including a VME interface board,
- Two VME crates containing a total of 11 custom-built Chain Read-Out Controller (CROC) modules, with each CROC controlling four LVDS chains,
- 42 LVDS chains (CAT-5e network cable), with each chain linking 12 front-end boards, and
- A third VME crate, containing timing, diagnostic and logic modules.

Due to the distributed nature of the front-end digitizer/high-voltage boards, the central DAQ and slow-control system itself can be easily accommodated in a single electronics rack.

**LVDS token-ring chains** As explained in Section 10.6.2, the front-end digitizer boards are daisy-chained into 42 LVDS token rings of 12 boards each. Data is transfered over the LVDS at 53 MHz, a frequency much higher than required for data readout, but necessary to transmit precision synchronization reset signals to the front-end digitizer boards. Both ends of a chain terminate in a custom built VME chain read out controller (CROC) module described below. The number of digitizers on a chain is limited by the allowable jitter in the high-precision timing information transmitted to each digitizer board over LVDS. As LVDS is a one-way protocol, each digitizer board must receive the period global synchronization signal from the previous member of the chain on one connection, and re-transmit it to the next member on a second connection. Pending bench tests with our 16-channel prototype front-end board, to be completed by early 2005, we estimate that each board in a chain will introduce approximately 100 ps of jitter; thus a chain consisting of 12 boards would translate into roughly 1.25 ns timing jitter (worst case). This represents a factor of two safety margin over the 2.5 ns least-count timing resolution of the front-end TDC's. In the unlikely event the jitter introduced by a chain of 12 front-end boards proves unacceptable, even with this large safety factor, the number CROC modules (and hence chains) could be increased, allowing each chain to have fewer members.

LVDS signals will be transmitted around a ring on standard, commercially-available fire-resistant and halogen-free CAT-5e network cable approved by Fermilab safety division for underground use. The LVDS chains will also be used to transmit configuration and slow-control messages to the cards.

**Chain read-out controller (CROC) modules** Each CROC module will control four LVDS chains, requiring a total of 11 CROCs (plus spares) for the entire detector. These modules will reside in two VME crates alongside a crate controller and a MINOS timing distribution module.

The readout controller modules have the following functions:

1. Prior to the arrival of a NuMI spill, as signaled by the VME-resident MINOS timing module,[152] to reset the timing counters of each front-end board and open a 10$\mu$sec gate to collect data from the spill.

2. Upon completion of a NuMI spill, to initiate readout of front-end digitizer data over the four associated LVDS rings, into internal RAM.

3. Upon completion of the parallel readout of all four chains, to raise an interrupt with the main DAQ computer, indicating that event data is available. The PVIC/VME interface/crate controller allows VME interrupts to be received directly by the main computer.

4. The internal RAM of each CROC is memory-mapped to the host computer's PCI bus, allowing block transfer of event data via the PVIC/VME interface/crate controller. The relatively long NuMI duty cycle ($\sim$2 seconds) and low data rate (under 1MB per spill for the entire detector) ensures that no deadtime will be associated with the readout itself.

5. Once per second, to globally synchronize the detector's TDCs over LVDS using a high-precision refresh signal from the MINOS timing module. The need for this synchronization drives the choice of LVDS for the readout chains, as opposed a lower performance alternative such as Ethernet.

6. Upon command of the main data acquisition computer, to control and monitor the Cockroft-Walton high-voltage power-supplies on the front-end digitizer boards, and to configure the firmware of these boards at run-startup.

**Ancillary electronics and DAQ computer** Communication between the main data acquisition computer will be via commercially available PVIC/VME link, allowing block data transfers to and from VME and interrupts to be received by the computer in response to the NuMI spill gate.

A trigger scaler and TDC to monitor the NuMI timing signals, and a programmable pulse generator to simulate them during beam-off periods, along with other any additional logic needed for monitoring and calibration, will reside in the third VME crate. All VME components will be installed underground, within about 20 meters of the detector.

The main DAQ and slow-control computer will be located near the VME electronics, in the NuMI hall, with two high-speed TCP/IP links (one for data, one for monitoring and control messages) to the Fermilab network. A relatively modest, dual-CPU server model will be more than adequate for our purposes. One CPU will be dedicated to real-time data acquisition, and the other will handle control messages and monitoring. An on-board, RAID-5 disk cluster with sufficient capacity to store several weeks of data will serve as a buffer for the data, pending transfer to offline processing nodes and permanent storage.

| Component | Number | Comments |
|---|---|---|
| Channels | 30992 | WLS Fibers |
| Front-end boards | 503 | One per PMT, plus 15% spare |
| Readout Token Rings | 42 | 12 PMTs/ring |
| VME Readout Cards | 11 | 4 rings/card, plus five spare |
| VME Crates | 3 | Plus one spare |
| VME PVIC Interface | 3 | One per crate, plus one spare |
| PVIC/PCI Interface | 1 | Plus one spare |
| DAQ Computer with RAID system | 1 | Data rate is 120 kByte/spill |

Table 11: Parts count for MINER$\nu$A electronics design

## 10.7 Power and Safety Systems

### 10.7.1 Quiet power

The current design calls for a complement of electronics and DAQ components that will not quite fill one electronics rack. The sum power draw of these items is estimated to be 3 kW.

Also in the rack will be a Fermilab-provided low-voltage power supply for the front-end boards mounted in the individual PMT boxes. The power required per PMT box will be approximately 7 W, requiring a total capacity of 5 kW. Total Quiet power required for read-out electronics, DAQ computer, front-end electronics and the PMTs is therefore about 8 kW.

To accomodate this, and any other currently unforeseen quiet power needs, Fermilab has agreed to add another 75 kVA transformer to the two 75kVA and one 45kVA transformers already serving MINOS. Like the three existing transformers, MINER$\nu$A's would be fed from the main 750 kVA quiet

power transformer, at 480 V. Unused taps with sufficient current capacity exist on this line. Fermilab will also supply electrician labor to install the transformer, conduits, and panel boards.

### 10.7.2 Magnet power supply

MINER$\nu$A will use 48 turns at 500 amps (24 kA-turns) to power the magnetic component of the detector. A 240 kW PEI power supply will likely be used for the MINER$\nu$A magnet, and would need to supply 500 A at an estimated 60 V. Unused PEI 240 supplies are available at Fermilab, and will be refurbished at Fermilab expense.

The MINOS magnet will draw an estimated 80 kW on a power supply fed by a 400 A/480 V transformer. Accounting for efficiencies of the supplies, the MINOS and MINER$\nu$A magnet power supplies combined should draw less than 200 kVA (236A) from the 400 A/480 V transformer. Fermilab will add a seperate disconnect for the new power supply.

### 10.7.3 Power distribution

As described above, the MINER$\nu$A PMT boxes will each require 48 V volts, and will consume approximately 7 W of power. Analytic Systems has a rack-mounted, 1 kW 48 V power supply which could then supply power for 100 PMT's (model number PWS1000R-110-48). We would use 6 of these supplies, located at the electronics racks. Due to space constraints the racks will likely be many meters from the detector itself. Long cables will go from the six power supplies to fanouts located much closer to the detector, and then shorter cables will go from each fanout to the different PMT boxes located on the detector.

### 10.7.4 Safety considerations

There are a number of hazards that are associated with the installation and operation of the MINER$\nu$A detector: there are mechanical hazards due to the underground nature of the installation and the transport of equipment weighing several tons. There are electrical hazards associated with not only the operation of the electronics, but also hazards associated with the operation of the coil to provide the magnetic field. Finally, there are additional hazards due to the fact that the experiment is to be installed and operated in a deep underground location which has occasional moisture coming from the ceiling. Each of these hazards will be addressed and mitigated in accordance with OSHA, (Occupational Safety and Health Administration) and NFPA (National Fire Protection Association) regulations, as well as the guidelines documented by FESHM (Fermilab Environmental Safety and Health Manual).

The detector stand, the bookends that keep the detector planes straight, and all lifting fixtures associated with transporting the various kinds of detector planes will be designed by Fermilab engineers and reviewed and tested accordingly before they are used underground. Although the coil itself might be fabricated by an outside contractor, the design of the coil will also proceed through Fermilab engineers.

The overall philosophy for MINER$\nu$A data-taking is to be parasitic to MINOS data-taking, and the appropriate safety features will be implemented in the detector design to ensure that this is true from a safety standpoint as well.

For example, the MINER$\nu$A coil power supply will be adequately shielded to ensure that a separate Lock-out Tag-out (LOTO) procedure will not be required to access the Near Detector Hall while the MINER$\nu$A magnet coil is energized. There will also be adequate drip protection above both the

MINER$\nu$A detector and coil power supply, since the drip ceiling that covers the MINOS Near Detector does not extend past the MINOS detector itself.

Safety features will also be installed on the MINER$\nu$A electronics racks that are similar to those on the MINOS near detector racks. Specifically, the electronics racks will have smoke detection, water drip sensors, air flow, temperature, and humidity sensors.

All the cables that extend to and from the electronics racks, including those that reach the fanouts and from the fanouts themselves to the PMT boxes on the detector proper will be fire-retardant and will be suitable for use underground as defined by Fermilab ES& H section. .

Once the detector, power distribution, and PMT box design is finalized then the current amount of fire protection that is located in the Near Detector Hall will be evaluated to see if additional protection (beyond what is located in the electronics racks) is needed.

# 11 Detector Simulation and Performance

This section outlines the event simulation and reconstruction software used to optimize the detector's design and quantify its physics capabilities, and R&D studies carried out to validate many key elements.

Much of the simulation software has been borrowed from other experiments, where it has been thoroughly validated. The detector simulation and reconstruction software has been developed specifically for MINER$\nu$A, but is based on widely-used libraries and algorithms. MINER$\nu$A-specific hardware tests, culminating in a small vertical slice of the detector, to record data from cosmic-ray muons, were carried out over the summer of 2004.

## 11.1 Event Generators

The MINER$\nu$A simulation software interfaces with two event generators that model neutrino interactions with matter: NEUGEN[114] and NUANCE[33]. NEUGEN was originally designed for the Soudan 2 experiment and is now the primary neutrino generator for the MINOS experiment. NUANCE was developed for the IMB experiment and is currently used by the Super-Kamiokande, K2K, MiniBooNE and SNO collaborations. Both have evolved from "proprietary" programs designed for atmospheric neutrino studies into freely-available, general-purpose utilities that aim to model neutrino scattering over a wide range of energies and for different nuclear targets. Total charged-current cross-sections calculated by NUANCE (Figure 75) and NEUGEN (Figure 74) are compared with data below. As the results of the two generators agree with each other (to within the depressingly large range of uncertainties in available data)[117], they have been used interchangeably for the present studies.

As in the past, future studies of neutrino oscillation and searches for nucleon decay will rely heavily on the best possible description of neutrino interactions with matter. Neutrino event generators are tools which encapsulate our understanding of this physics in an easily usable and portable form. Practically, they serve two related functions: to allow the rates of different reactions with the experimental target to be calculated, by providing total exclusive and inclusive cross-sections, and to simulate the dynamics of individual scattering events, by sampling the differential cross-sections. Many comparable packages are available to the collider physics community, and have been incrementally improved for decades, forming a common basis for discussion of different models and phenomena. One important goal of MINER$\nu$A is to improve the quality of neutrino Monte Carlo event generators, and thereby enhance the physics reach of many future experiments.

MINER$\nu$A will attack this problem from both experimental and theoretical directions. Experimentally, MINER$\nu$A will make definitive measurements of dozens of exclusive and inclusive cross-sections, across the range of energies most important for future oscillation and nucleon-decay experiments, with a well-controlled flux, and on a variety of nuclear targets. The era of 25% uncertainties and marginally-consistent cross-section data for even the simplest neutrino reactions will end with MINER$\nu$A; for the first time it will be possible to validate the details, and not merely the gross features, of competing models.

At the same time, MINER$\nu$A will be a natural focus of attention for theorists and phenomenologists developing these models. NEUGEN and NUANCE are two of the most sophisticated neutrino-physics simulations in the world, but NUANCE models quasi-elastic scattering with the 1972 calculation of Smith and Moniz[34], and both programs use the Rein–Sehgal[58] resonant production model which dates from 1981. That no other widely-accepted models for these, the most fundamental neutrino–nucleon reactions, have emerged in the last quarter century is sobering evidence that an experiment like

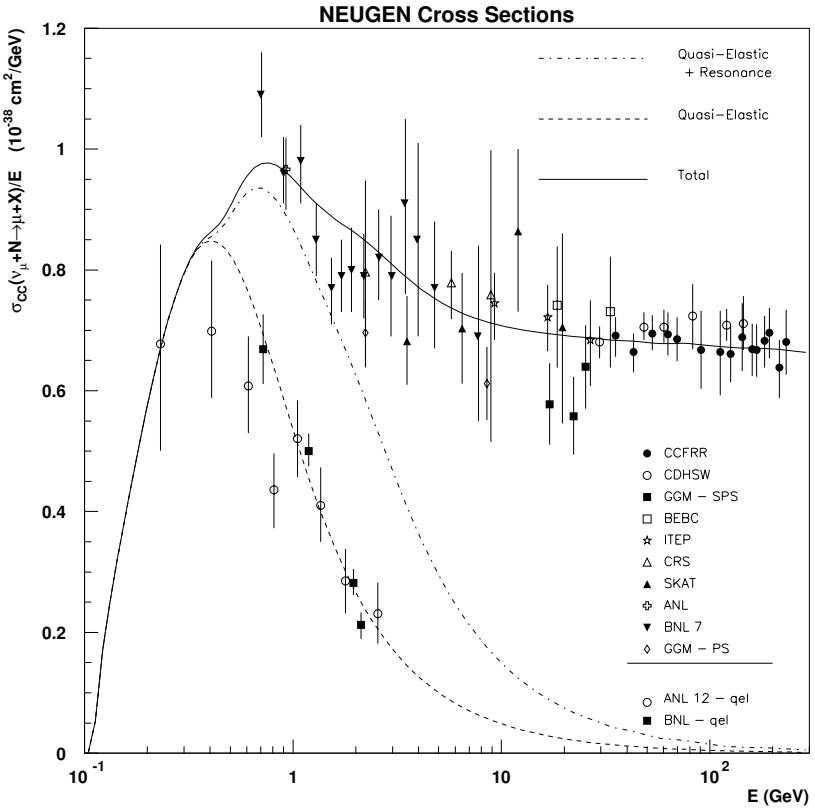


Figure 74: The NEUGEN prediction for the $\nu_\mu$ charged-current cross-section ($\sigma/E_\nu$) from an isoscalar target compared with data from a number of experiments. Quasi-elastic and resonance contributions are also shown.

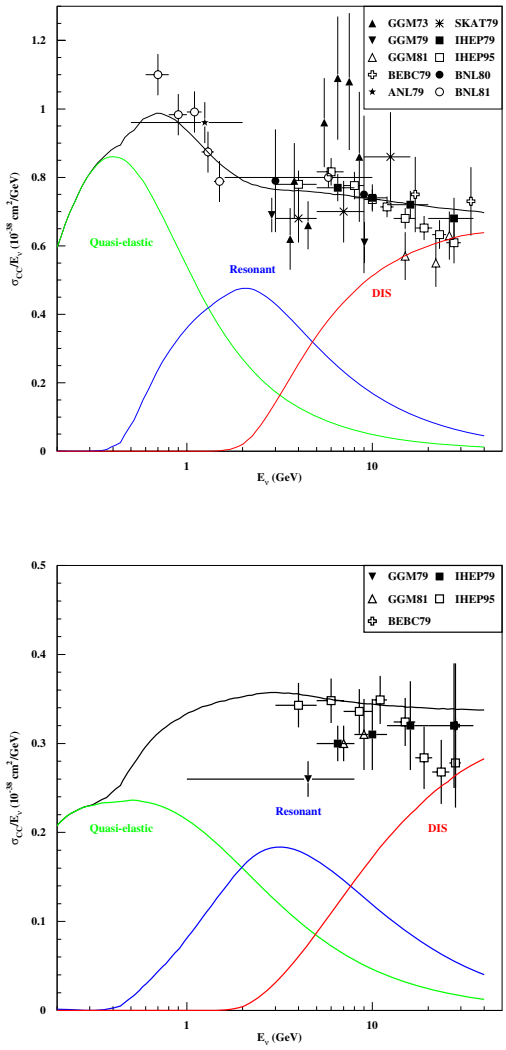


Figure 75: Total neutrino (top) and anti-neutrino (bottom) cross-sections divided by energy versus energy compared to the sum of quasi-elastic, resonant, and inelastic contributions from the NUANCE model. The sum is constructed to be continuous in $W$ ($\equiv$ mass of the hadronic system) as follows. For $W > 2$ GeV the Bodek-Yang model is used. The Rein-Sehgal model is used for $W < 2$ GeV. In addition, a fraction of the Bodek-Yang cross-section is added to the Rein-Sehgal cross-section between $W = 1.7$ GeV and $W = 2$ GeV. The fraction increases linearly with $W$ from 0 to 0.38 between $W = 1.7$ and $W = 2$ GeV.

MINER$\nu$A is long overdue. New, high-quality data is the surest way to catalyze theoretical ingenuity, and MINER$\nu$A will provide the former in abundance. Through our contacts with these theorists, and ability to translate well-tested, state-of-the-art models into universally-available and widely-adopted software, MINER$\nu$A will serve as a conduit for expertise from a diverse collection of disciplines into the high-energy neutrino physics community.[7]

## 11.2 Detector Response Simulation

Simulation of neutrino interactions in MINER$\nu$A is carried out by a GEANT3-based Monte Carlo program. This program combines a flexible description of the detector geometry, the NuMI neutrino beam flux from the beam simulation, neutrino interaction physics from either of the two generators and simulation of the scintillator response with the standard tracking and particle interaction routines available in GEANT.

### 11.2.1 GNuMI flux interface

The output of the GNuMI simulation of the beamline is a set of files recording the neutrino flux in 0.5 GeV bins for a nominal number of protons on target. The flux files are in a standard format and hence can be interchanged with no additional modifications to the code. In this way different beam configurations can be easily studied. An option exists to generate interactions with a flat energy spectrum. In this case, beam weights are stored in an output ntuple. This is particularly useful if one wishes to study the effect of different beam configurations without furthur Monte Carlo running.

### 11.2.2 Event generator interface

The Monte Carlo simulation program can be configured to accept neutrino interactions from either NEUGEN3 or NUANCE. The results of a neutrino interaction can be passed to the simulation in a number of ways. By default, the event generation routines in NEUGEN3 are usually called from within the simulation itself. In this mode, the code chooses a neutrino energy from the flux files, samples the density of material along the neutrino path; chooses a vertex and nucleus type, calls the kinematics generator and inserts the list of particles thus obtained into the GEANT data structures. This is not the only mode of generation. As a stand-alone generator, NUANCE provides events in either a text or ntuple format and so a provision is made to read in events from a standard external format. NEUGEN3 has been modified to write out events in the same format, so that the results of both generators may be compared in a consistent manner.

### 11.2.3 Geometry

Flexibility drives the design of the detector geometry code. The size, segmentation, material and shape of all components of the detector can be set and altered almost entirely from input datacards. The detector is logically divided into longitudinal sections. Each section can have different dimensions, strip sizes and absorber widths. In addition the absorbers in each section can be be constructed from

[7] This trend is already beginning, thanks to collaborative work sparked by the NUINT series of workshops. The BBA–2003 quasi-elastic form-factor fits (see Chapter 2) and Bodek–Yang duality-inspired model of deep-inelastic scattering (Section 6) have recently been implemented in NUANCE, and NEUGEN is exploring Benhar's spectral-function approach[172] to nuclear binding effects.

segments of differing material and widths. The geometry description is sufficiently abstract that minor changes in detector design may be accommodated merely by changing the datacard, allowing for fast detector reconfiguration and easy bookkeeping.

### 11.2.4 Hits and digitizations

Particles are tracked through the GEANT geometry in the standard manner. When a particle traverses a sensitive detector volume the particle type, volume identifier, entrance and exit points and energy deposition (including Landau and other fluctuations) are recorded as a hit. When GEANT has finished tracking the event, the hits are considered and converted to digitizations. There are as many digitizations as there are strips hit. Multiple hits on a single strip are condensed into one digitization, although information on which tracks contributed to the digitization is stored. These digitizations are then passed to the event reconstruction program.

### 11.2.5 Photon transport

The GEANT detector simulation assumes "ideal" light collection, and records the raw energy deposited in each channel. During event reconstruction, the energy deposited is converted to a number of detected photo-electrons. The scale factor between energy deposited and expected photo-electrons detected is determined by a standalone optical simulation validated for MINOS (see Section 11.3): the expected number of photo-electrons is smeared by Poisson statistics, and a 10% channel-to-channel Gaussian smearing reflecting a conservative estimate of remaining systematics after calibration and attenuation corrections.

## 11.3 Optical Simulation

MINOS has shown that co-extruded solid scintillator with embedded wavelength shifting fibers and PMT readout produces adequate light for MIP tracking and can be manufactured with excellent quality control and uniformity in an industrial setting. The performance characteristics of the MINOS scintillator modules produced at the three 'module factories' are now well known, both through measurements taking with radioactive sources post-fabrication at the factories and through measurements of cosmic rays at Soudan. We intend to use this same technology for the active elements of MINER$\nu$A.This section describes the light yield studies that were carried out in order to demonstrate that the proposed design produces enough light.

The basic active element in the MINERvA detector is a co-extruded triangular scintillator strip with a wave-length shifting fiber threaded through a small circular hole that runs through the middle of the strip. Like MINOS, the scintillator strips are polystyrene (Dow 663) doped with PPO (1 % by weight) and POPOP (0.03% by weight), co-extruded with a reflective coating of $TiO_2$ loaded polystyrene [174]. The strip cross-section is a triangle of width 3.3 cm and height 1.7 cm. Strip lengths vary throughout the detector and range from 1.4 meters to 2.2 meters in the inner tracking detector to 4 meters for the calorimeter sections. The WLS fiber (Kurrary Y11) is 1.2 mm in diameter. The WLS fibers are spliced to clear fibers which are mated to the PMT face. One ended readout is used, and the far strip/fiber end are mirrored.

Studies indicate that for a triangular extrusion, average light levels above 3.9 photo-electrons/MIP are required in the inner detector in order to obtain good particle identification (shown in Section 11.4.5). Coordinate resolution, vertex finding, and track pointing are also affected by light levels, but to a lesser

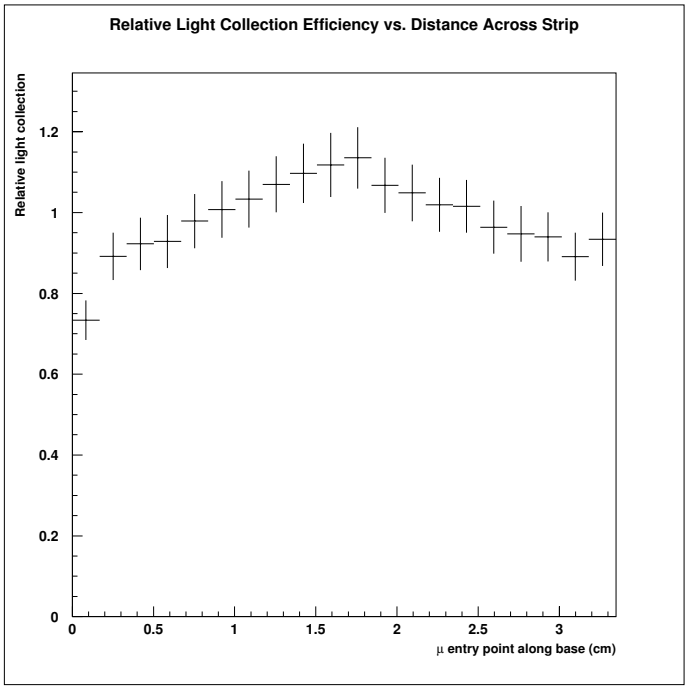


Figure 76: Relative light collection efficiency across the 3.35 cm triangular width of the scintillator extrusion.

extent. For this design we have targeted an average light level of 7.8 PE/MIP, which includes a safety factor of 100%. This safety factor accounts for some ad hoc assumptions in the simulations as well as possible effects from degradation of the scintillator over time.

The basic ingredients for the MINERvA light studies are the known characteristics of the MINOS modules and a photon transport Monte Carlo written by Keith Ruddick [165]. The average light yield from a MINOS scintillator module is 4.25 photo-electrons/MIP at a distance of 4 meters, and attenuation in the fiber is well described in terms of a double exponential: [173]:

$$\mathrm{N(x) = A(exp(-x/90cm) + exp(-x/700cm))} \tag{14}$$

The photon transport Monte Carlo (LITEYLDX) is used to calculate, for a given 'configuration' (strip geometry, fiber diameter, and fiber placement), the number of photons trapped in the fiber for a MIP entering at a particular position. This information is then used to determine a relative light collection efficiency for a particular configuration compared to MINOS strips. With the overall normalization and attenuation curve from MINOS one can then calculate the amount of light for any particular configuration. Figure 77, for instance, shows the relative light output for triangular extrusions when the strip thickness, fiber diameter and fiber placement are varied. As expected, light output is nearly proportional to the strip thickness, and is greatest when the fiber is placed at the center of gravity of the strip. Figure 76 shows the relative light collection efficiency for a triangular extrusion where the entry point of the minimum ionizing particle is varied across the strip width, and indicates that the collection efficiency varies by $\pm 10\%$ over the strip width.

The overall light levels from 3 lengths of strips are shown in Figure 78. Here we have assumed a 90% reflectivity from the mirror end of the strip, and in all cases a 1 meter WLS 'pigtail' from the end

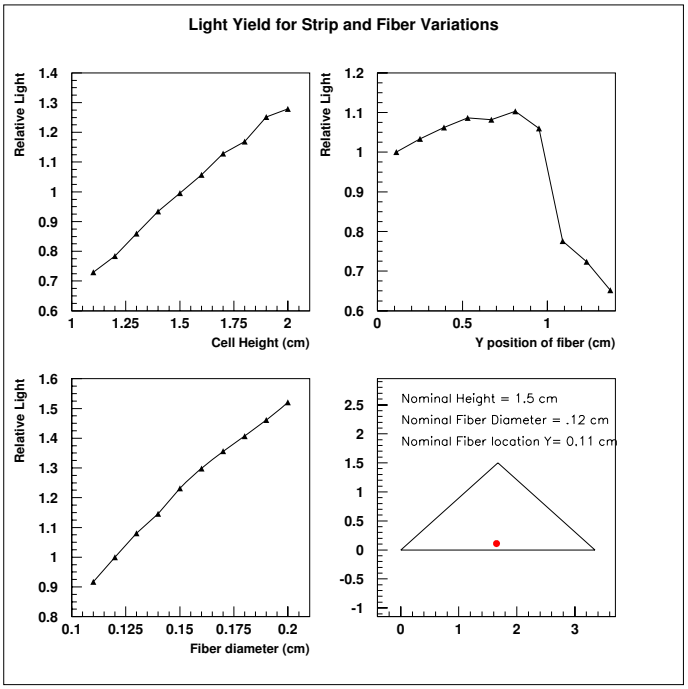


Figure 77: Relative light levels for different strip widths and fiber diameters.

of the near end of the strip to the PMT face. Clear fiber lengths and connectors are not included. In the MINOS near detector, the far strip end was not mirrored, here we assume the strip ends are mirrored with 100% reflectivity. Because the light produced in the scintillator is generally collected within a few cm of the MIP crossing location, this approximation only affects the calculation of collection efficiency at the very far end of the strip. Shown are the light levels predicted for 3 strip lengths. In each plot, the lowest curve corresponds to light collected from reflections off the mirrored end, the middle line corresponds to light travelling directly from the MIP to the readout end, and the upper line is the sum. As the figure shows, the light level in the inner tracking detector, with a maximum length of 2.2 m, meets the design requirement of 7.8 PE/MIP over the entire length.

## 11.4 Performance of Reconstruction Algorithms

The output of the detector simulation is a list of digitizations for each strip. We have developed a basic reconstruction program which takes this list and reconstructs the tracks and vertices in an event.

### 11.4.1 Pattern recognition

For our design studies, we have adopted "omniscient" pattern recognition based on Monte Carlo truth information. All hits generated by a given track (ignoring channels with overlap) are used to reconstruct the track. Development of a fully-realistic pattern-recognition algorithm to associate hits to track candidates has not been undertaken as yet due to manpower and time constraints. We are confident that the three-dimensional XUXV modular design of the detector, and its relatively modest occupancy, will allow highly-efficient pattern recognition and track identification. Visual inspection of events through

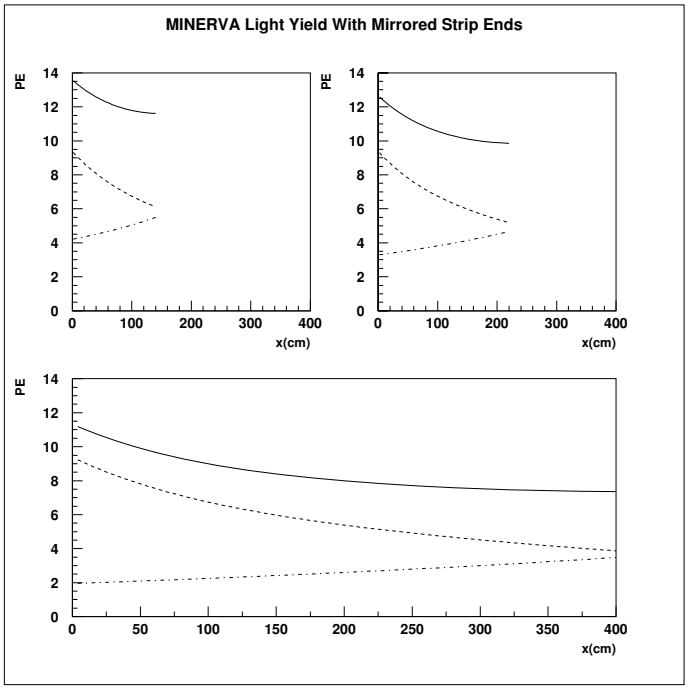


Figure 78: Light yield vs. distance along strip for MINER$\nu$A scintillator strips with one-ended readout with a mirrored end. Dot-dashed line is light collected from reflections off the mirrored end, dashed line is light travelling directly to the readout end; solid line is the sum.

the graphical interface of the detector simulation program reinforces this conclusion.

### 11.4.2 Coordinate reconstruction

Tracks generating hits in at least six scintillator planes of the inner detector, including three planes of the X view, can be reconstructed. Coordinates are estimated from the raw, smeared digitizations, using only planes which have one or two strips hit. Tracks at high angles to the detector axis may pass through more than two strips in a single plane, and it should be possible to recover these higher-multiplicity hits with a more sophisticated algorithm. For single hits, the coordinate is taken as the center of the strip. For dual hits, the position is interpolated using the charge-sharing between between strips, with a small geometrical correction based on the estimated crossing angle.

The coordinate resolution for a large test sample of single and double hits can be measured directly using the residuals obtained when each coordinate is excluded, in turn, from the track's fit. This coordinate resolution is parameterized as a function of the track's crossing angle, and used to assign errors to coordinates in the fitter.

### 11.4.3 Track reconstruction

Reconstructed coordinates are used to fit each track using a Kalman filter algorithm[175]. For this proposal, tracking performance has only been studied in the non-magnetic region of the detector; the track model is perforce a strictly linear one. Neglect of the magnetic field is justified because mission-critical

resolutions are determined by performance of the fully-active (non-magnetized) volume, and since coordinate resolution for the strips should not depend on the presence of a magnetic field. The momentum resolution for charged tracks in a magnetic field can be reliably estimated from the coordinate resolution, momentum and field strength. As long tracks may pass through many radiation lengths of scintillator and absorbing material, the Kalman filter's ability to correctly account for multiple Coulomb scattering ("process noise") is essential. The algorithm can optionally be used to exclude outliers from the fit.

Figure 79 shows the expected hit residuals, impact parameter and angular resolution for muons from a sample of quasi-elastic interactions, assuming triangular strips of 3 cm width and 1.5 cm thickness (close to the final design values). Hit resolutions of $\sim 3\,\mathrm{mm}$ and angular resolutions of $< 0.5^\circ$ are expected. The coordinate resolution is degraded to approximately 1.5 cm if rectangular strips are employed instead of triangular ones, since interpolation based on charge is no longer possible.

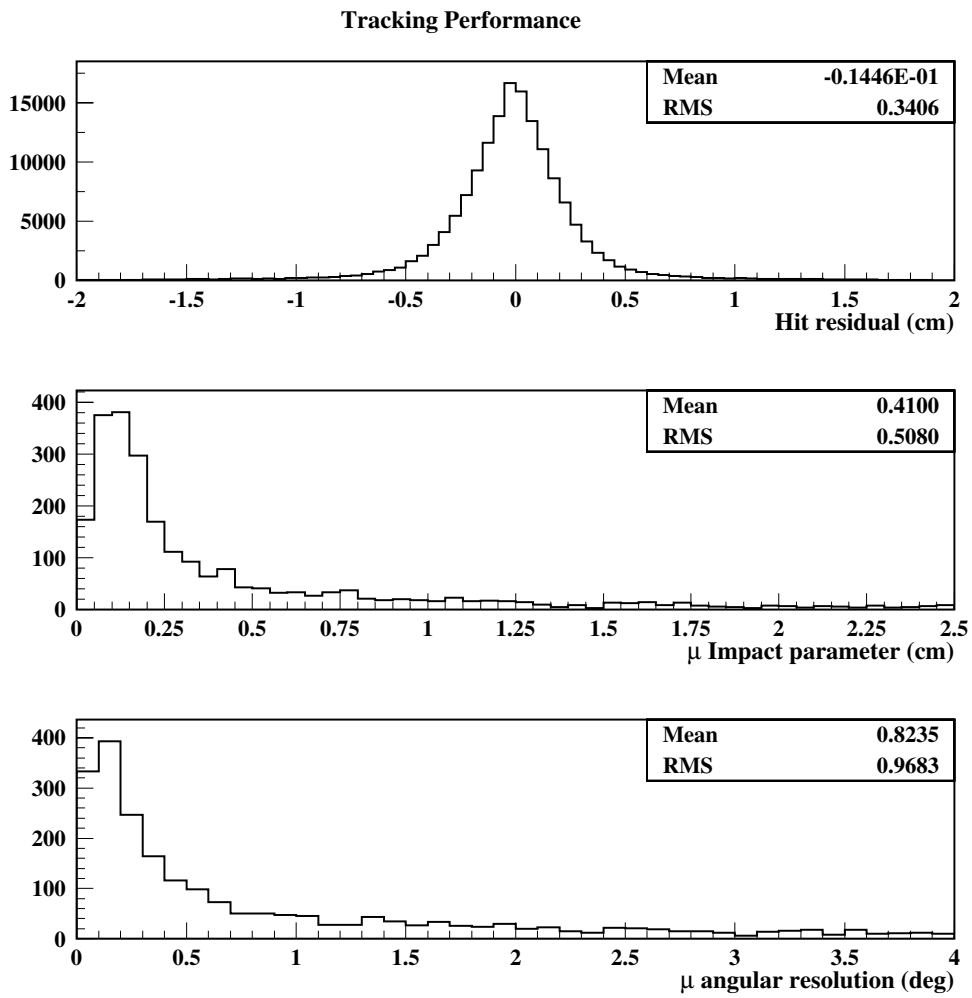


Figure 79: Performance of the tracking algorithm on muons from from a sample of simulated charged-current quasi-elastic interactions. Shown are (top) the hit residuals, (middle) the impact parameter of the muon with the vertex and (bottom) the muon angular resolution.

### 11.4.4 Vertex reconstruction

In this study, reconstructed tracks are associated to vertices using Monte Carlo truth information. The vertex positions are then fit using a Kalman filter algorithm. Track directions at the vertex are updated taking account of the constraint. This is equivalent to a least squares fit, but mathematically more tractable since it does not involve inversion of large matrices and can be easily extended to a helical track model. The primary vertex resolution for a sample of simulated quasi-elastic interactions with two visible tracks is shown in Figure 80. The transverse (longitudinal) vertex postion can be measured to a precision of better than (slightly more than) a centimeter.

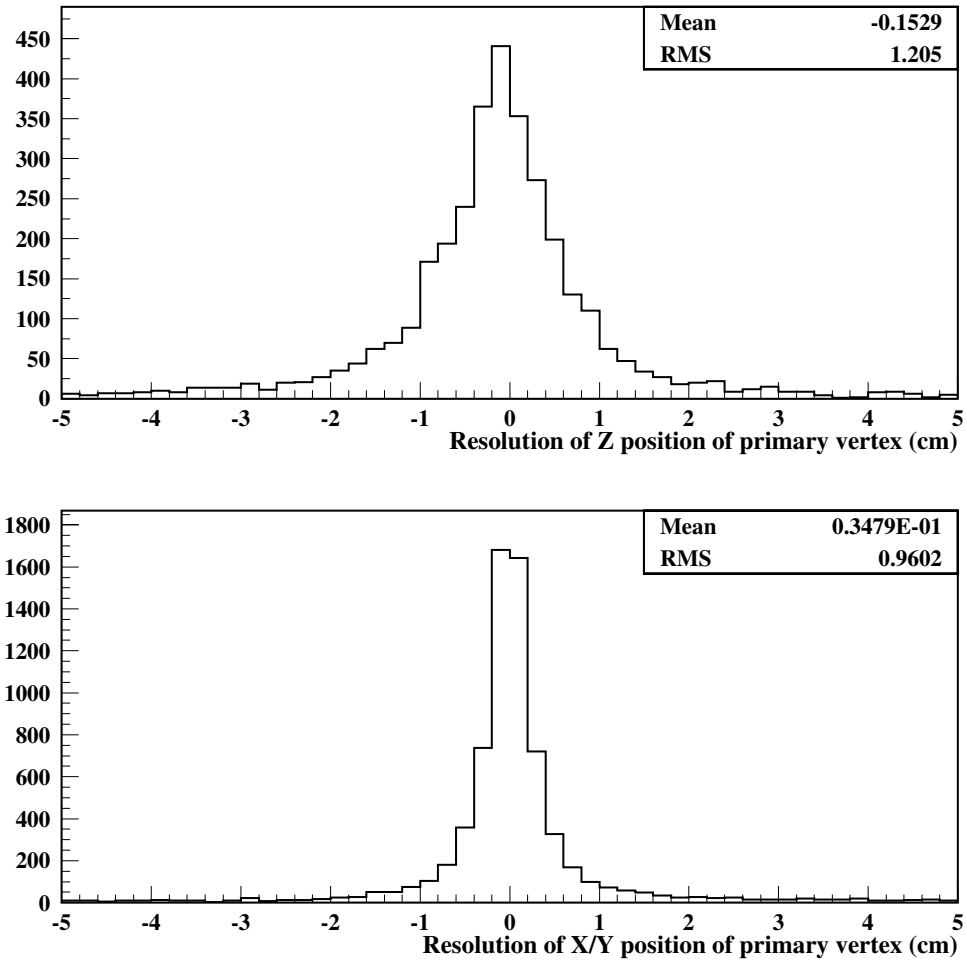


Figure 80: Reconstructed vertex resolution for two track charged current quasielastic events. Shown are (top) the resolution in the longitudinal position of the vertex (Z) and (bottom) the resolution of the transverse position of the vertex (X and Y).

### 11.4.5 Particle identification

Particle identification in MINER$\nu$A will rely on measuring specific energy loss ($dE/dx$) as well as topology (hadron and electromagnetic showers, decay signatures).

**Electromagnetic showers** Electromagnetic showers are easily identifiable by their diffuse track and characteristic $dE/dx$ profile in the fully-active central detector and energy deposition in the electromagnetic calorimeters. In addition, the fine granularity of MINER$\nu$A allows us to distinguish electrons and photons, when the primary vertex is known, using distance to shower onset and shower length. Figure 81 shows the distance between the electromagnetic shower origin and the true primary vertex for charged-current $\nu_e$ interactions and $\pi^0$ production. The figure also shows the length of the showers, measured in MINER$\nu$A scintillator planes, or 1.75 cm of polystyrene. For neutral pions the length is from the beginning of the first showering photon to the end of the second one.

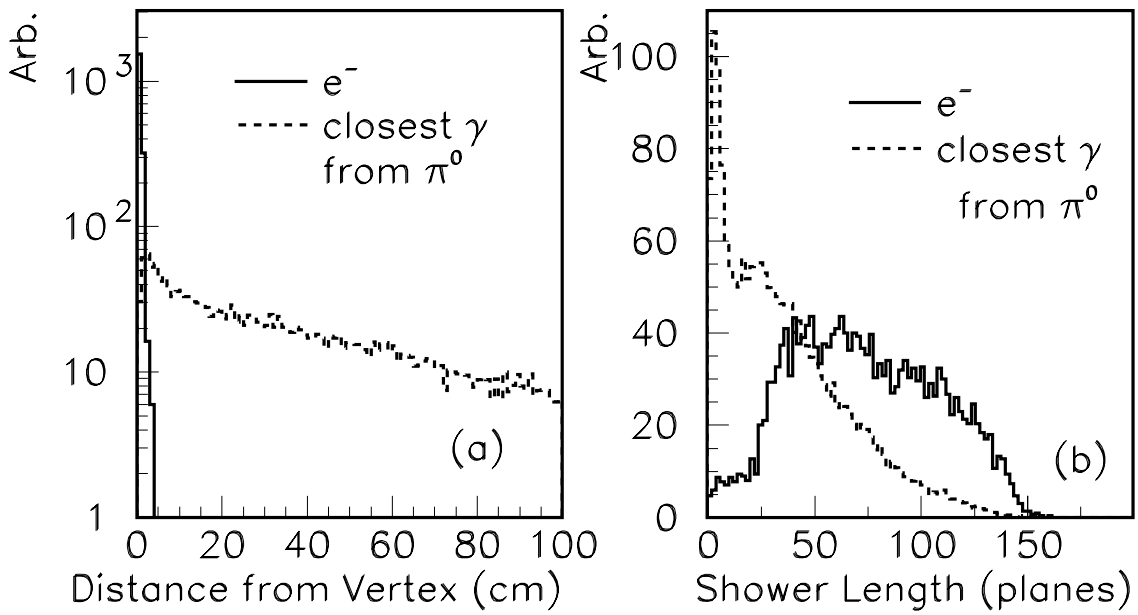


Figure 81: (a) The distance in centimeters between the neutrino vertex, which can be determined from a proton track, and the start of the most upstream electromagnetic shower, for both electrons and photons from neutral pions. (b) The shower length in units of scintillator planes, for electrons and neutral pions.

**$\pi^0$ reconstruction** With the surrounding ECALs for containment, MINER$\nu$A's $\pi^0$ reconstruction capabilities are excellent. This is essential, since $\pi^0$ are a major source of background for $\nu_e$ appearance oscillation experiments. As discussed in Section 3.3.3 and shown in Figure 14, MINER$\nu$A's low density and high granularity make it an excellent photon tracker, able to accurately reconstruct the vertex and kinematics even for coherently-produced $\pi^0$'s with no accompanying charged tracks.

**Muons** Energetic muons can be identified by their penetration of material in the calorimeters and/or MINOS near detector. Muons with a momentum measurement in the magnetic field, or which stop inside the detector can be distinguished from protons and kaons by $dE/dx$. In addition, the delayed $\mu \to e$ decay signature can be detected.

**Charged hadrons** Hadrons can be identified as such by their interactions in the inner detector and/or hadron calorimeters. Hadrons which stop without interacting or have their momentum measured by the magnetic field can also be distinguished as $\pi$, $K$ or $p$ with good efficiency using $dE/dx$.

**dE/dx analysis** Specific energy loss ($dE/dx$) will be an important tool for particle identification in MINER$\nu$A. For tracks which stop in the inner detector, the charge deposited near the end of the track (corrected for sample length) can be compared with expected curves for, *e.g.,* the $\pi^{\pm}$, $K^{\pm}$ and proton hypotheses. This technique does not require an independent momentum measurement, since the range ($x_{stop}$, in g/cm$^2$) from the stopping point to a given sampling point is closely correlated with the momentum at the sampling point. The algorithm is calibrated by fitting the expected $dE/dx$ vs. $x_{stop}$, and the standard deviation of this quantity, $\sigma_{dE/dx}$, as a function of $x_{stop}$ for the three different particle types (see Figure 82). The measured $dE/dx$ for a track is compared to the expected value at each sample, to form $\chi^2$ estimators reflecting the goodness of fit to each of the three particle identification hypotheses:

$$\chi^2(\alpha) = \sum_{i=1}^{N_{sample}} \left[ \frac{\left(\frac{dE}{dx}\right)_i^{obs} - \left(\frac{dE_\alpha}{dx}\right)_i^{exp}}{\sigma_i^\alpha} \right]^2,$$

where the sum runs over all measured samples, and $\alpha = \{\pi, K, p\}$. The hypothesis $\alpha$ with the minimum $\chi^2$ is assigned to the track. The frequency of misidentification can be visualized most easily by plotting the difference $\Delta\chi^2$ between the correct $\chi^2$ (for the particle's true type) and the smallest of the two (incorrect) others (Figure 83). With this naïve $dE/dx$ analysis, MINER$\nu$A correctly identifies 85% of stopping kaons, 90% of stopping pions, and $> 95\%$ of stopping protons. A similar analysis can be applied to tracks with momenta measured in the magnetic regions of the detector.

### 11.4.6 Energy reconstruction and containment

**Muons** The energy of muons from charged-current interactions will be measured using range and/or curvature in the magnetized regions of MINER$\nu$A and the MINOS spectrometer. For muons stopping in the detector, the momentum resolution will be $\frac{\Delta p}{p} \sim 5\%$. If the MINOS detector is used, the momentum resolution will be 13%[152].

**Electromagnetic showers** For electromagnetic showers, the estimated energy resolution is $6\%/\sqrt{E(GeV)}$.

**Hadronic calorimetry** Containment of hadronic energy is a significant design consideration, as it assists in meeting many of the experiment's physics goals. Studies show that the visible hadronic component of quasi-elastic and resonant events in the fully-active central region of the detector are completely contained, apart from secondary neutrinos and low-energy neutrons. Figure 84 shows the fraction of escaping visible hadronic energy for deep-inelastic reactions in several hadronic energy ranges, and figure 85 shows the probability that a deep-inelastic event will leak visible energy as a function of the true hadronic energy. Only for hadronic energies greater than 8 GeV is there any significant probability of leakage and only above 15 GeV is the average fraction of escaping energy greater than 10%. The fraction of deep-inelastic interactions with hadronic energies over 15 GeV in the low-energy, semi-medium

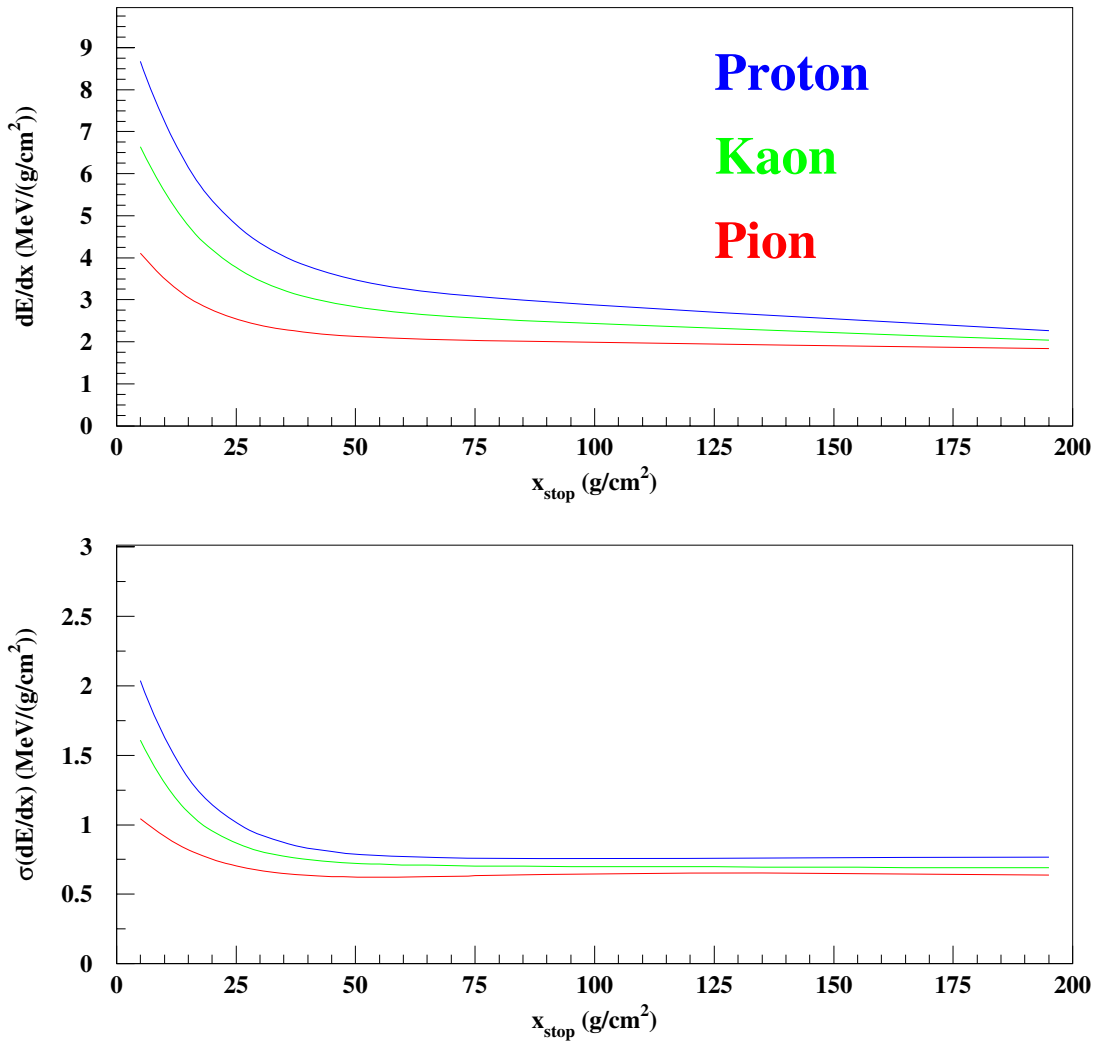


Figure 82: The top figure shows the average specific energy loss $dE/dx$ for stopping $\pi^{\pm}$, kaons and protons, vs. range from the stopping point (in g/cm$^2$), for the simulated MINER$\nu$A inner detector. The bottom figure shows the estimated standard deviation of the energy loss, which is used to form a $\chi^2$ estimator for particle identification.

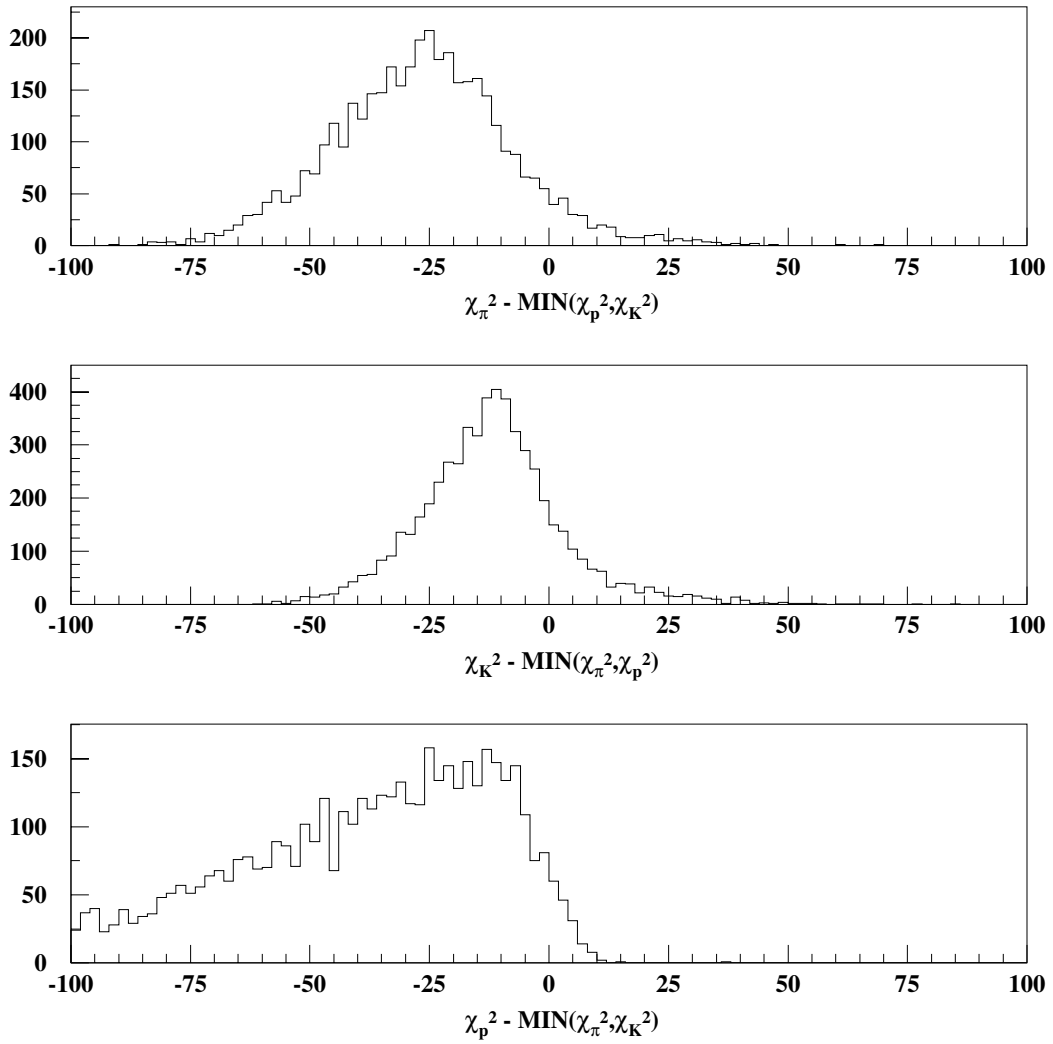


Figure 83: The three plots show the $\Delta\chi^2$ $dE/dx$ estimator for simulated and reconstructed charged pions(top), kaons(middle) and protons(bottom) stopping in the inner detector. Tracks with $\Delta\chi^2 < 0$ are correctly identified.

or semi-high energy beams is $< 1\%$, and so visible energy leakage should be insignificant. These estimates ignore downstream components beyond the forward hadron calorimeter, such as the MINOS detector, and are therefore conservative.

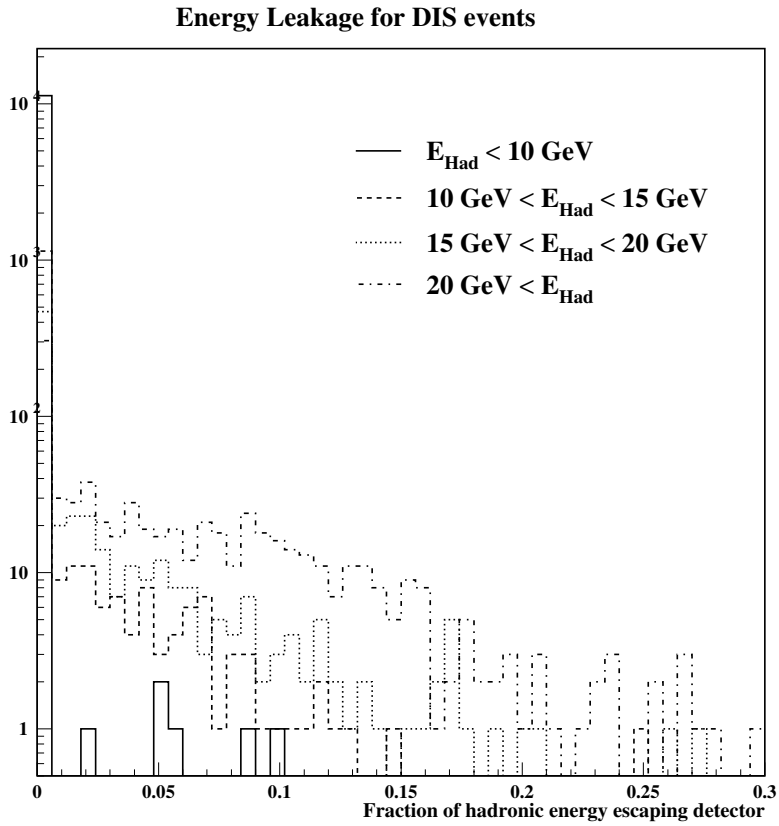


Figure 84: Fraction of hadronic energy escaping the detector for deep-inelastic scattering in the fully-active central region.

To study MINER$\nu$A's calorimetric $E_h$ resolution, the detector response to a neutrino sample generated throughout the inner detector by NUANCE, on carbon and hydrogen targets, was simulated. From this simulated sample, events where all hadronic fragments were contained within MINER$\nu$A were used. Hits from lepton tracks in charged-current interactions are excluded from the following analysis.

In a fully-active scintillator calorimeter, the total light yield should be essentially proportional to $E_h$. (The proportionality is not unity due to escaping neutrinos, rest masses of charged pions, nuclear binding energy in the initial and secondary reactions and other nuclear effects such as pion absorption.) While the central inner detector volume is fully active, there are also regions with passive iron or lead absorber sandwiched between scintillators. In these sampling calorimeter regions, not all energy deposited results in scintillation light, so the light yield is corrected accordingly.

Figure 86 shows reconstructed $E_h$ vs. true $E_h$ computed from the kinematics of the incoming and outgoing leptons. The relative deviation of the reconstructed energy from the true $E_h$, $\Delta E_h/E_h$, multiplied by $\sqrt{E_h}$ is shown in figure 86, giving a average resolution for reconstruction of $E_h$ of $\frac{\Delta E_h}{E_h} =$

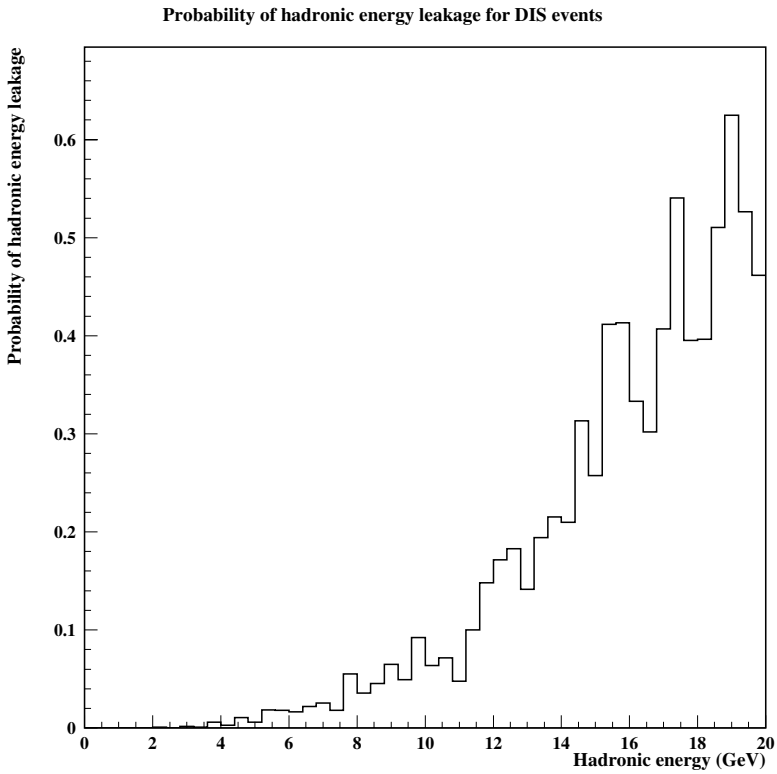


Figure 85: Probability that visible hadronic energy from a deep-inelastic event escapes undetected vs. total hadronic energy.

$\frac{23\%}{\sqrt{E_h(\mathrm{GeV})}}$. This $1/\sqrt{E_h}$ resolution has some energy dependence and is best represented by

$$\frac{\Delta E_h}{E_h} = 4\% + \frac{18\%}{\sqrt{E_h(\mathrm{GeV})}}.$$

### 11.4.7 Event categorization

Particle identification and event classification will play a central role in the analysis of data from MINER$\nu$A. One possible method of event classification is use of artificial neural network (ANN) techniques.

Event classification will be based on on topological characteristics as well as on particle ID. Separation of CC from NC interactions will be based on muon identification. Detection of muon decays for low energy muons stopping in the carbon gives the potential for accurate CC identification even at high y $_{Bj}$. In each such class further event identification will be based on other particle ID, energy/momentum measurements and kinematics. Neural networks are designed for such categorization and have been frequently used in the analysis of data from high energy physics experiments (see, for example, the DONUT[160] experiment).

## 11.5 R&D Studies

In Summer 2004, the collaboration began an extensive hardware R&D program in the following areas:

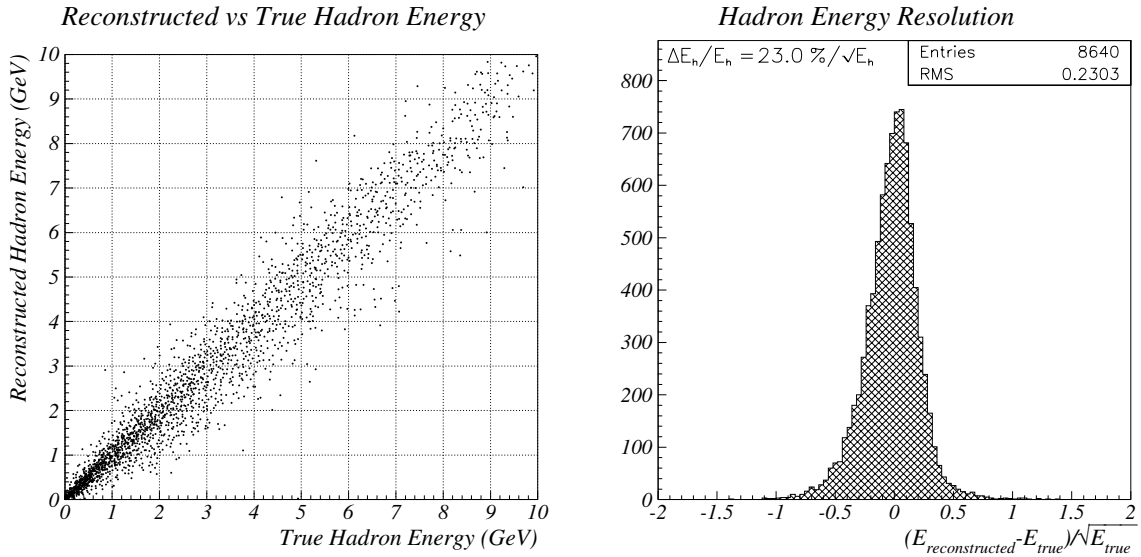


Figure 86: The left graph shows on the vertical axis the the hadronic energy $E_h$ reconstructed from scintillator output in MINER$\nu$A vs. the true $E_h = E_\nu - E_\mu$. Right figure shows the relative deviation of the fit, $(\Delta E_h/E_h)\sqrt{E_h}$.

- Testing of triangular scintillator extrusion die
- Study of fiber optical and mechanical properties
- Development of a prototype front-end digitizer board (FEB)
- Tests of the FEB and scintillator system in a "Vertical Slice Test" (VST)
- Developing a scheme for the mechanical support of the planes of iron and scintillator bars
- Constructing and testing a full module (*XUXV* views) inner/outer detector prototype

Significant progress has already been made on the first four items, as discussed below. Preparations for the remaining tasks are underway.

### 11.5.1 Scintillator extrusions

Triangular scintillator prototypes have been produced using the NICADD/FNAL extrusion facility. Bars of the design dimensions have been successfully extruded, and a $\sim$1.5 mm hole through the center, for fiber insertion, has been integrated into the process. These test bars were used in the VST described below.

### 11.5.2 Optical fibers

MINER$\nu$A will use optical fiber for light collection. This fiber travels from the scintillator to the photosensor and must be bent along this path. Fibers were tested to study light loss and cracking at different curvatures, and determine the angle at which fibers can be safely bent in the mechanical design of the detector. The fiber tested was Y-11 (green) WLS S-35 J-type fiber, made by Kuraray, with 1.2- and 1.5-mm diameters.

Light loss in the fiber results from several effects: attenuation, geometric loss from bending, cracks, and optical coupling at the ends. These effects must be understood to select the appropriate fiber for the experiment.

Bending tests were performed in a dark box. A light mixer, which is a diffusing piece of plastic, was glued to a PMT and served to disperse the light from the fiber evenly before hitting the surface of the PMT. A R580-17 model 1.5 inch diameter PMT, made by Hamamatsu, was used for these tests. The other end of the fiber was fed into a tile. The tile is a $0.5 \times 4 \times 4$ in$^3$ piece of scintillator with a groove in the center of one of the broad sides. The broad ends of the tile were covered with Tyvek and the narrow sides were painted with white titanium dioxide paint. Grooved tiles with different diameters were used for tests with 1.2 and 1.5 mm fibers. The signal was generated by gamma decays from a 1.9 mCi Cesium-137 source, Compton scattering in the tile scintillator. The PMT current was measured with a picoammeter read-out by computer. For the bending tests, fiber was wrapped around cylinders with diameters ranging from 0.5 to 4.5 in, with the fibers making between 0.25 and 2 turns around the cylinder in different runs. Control fibers, prepared exactly like the fibers being tested, but not wrapped around the cylinder, were used to check the stability of the set-up. The results of the tests are summarized in the tables below.

| | **# of Wraps** | | | | | | | | | |
|---|---|---|---|---|---|---|---|---|---|---|
| **Diameter (in)** | 0 | 1/4 | 1/2 | 1 | 2 | 0 error | 1/4 error | 1/2 error | 1 error | 2 error |
| 2 | 1.000 | 0.966 | 0.942 | 0.949 | 0.919 | 0.005 | 0.007 | 0.006 | 0.007 | 0.007 |
| 2.5 | 1.000 | 0.976 | 0.971 | 0.965 | 0.949 | 0.004 | 0.006 | 0.006 | 0.006 | 0.006 |
| 3.5 | 1.000 | 0.992 | 0.983 | 0.976 | 0.969 | 0.005 | 0.007 | 0.007 | 0.006 | 0.006 |
| 4.5 | 1.000 | 0.989 | 0.992 | 0.982 | 0.971 | 0.005 | 0.005 | 0.006 | 0.009 | 0.006 |

Table 12: Fraction of original signal surviving for different bend diameters, using 1.2 mm fiber.

| | **# of Wraps** | | | | | | | |
|---|---|---|---|---|---|---|---|---|
| **Diameter (in)** | 0 | 1/4 | 1/2 | 1 | 0 error | 1/4 error | 1/2 error | 1 error |
| 2 | 1.000 | 0.952 | 0.918 | 0.885 | 0.008 | 0.008 | 0.008 | 0.008 |
| 2.5 | 1.000 | 0.962 | 0.936 | 0.926 | 0.004 | 0.006 | 0.006 | 0.005 |
| 3.5 | 1.000 | 0.976 | 0.968 | 0.956 | 0.004 | 0.006 | 0.006 | 0.005 |
| 4.5 | 1.000 | 0.977 | 0.986 | 0.965 | 0.005 | 0.006 | 0.006 | 0.006 |

Table 13: Fraction of original signal surviving for different bend diameters, using 1.5 mm fiber.

While the 1.5 mm fiber gives higher light yield, it is much easier to break. Limits for minimum bend diameter can be set at 2 inches for the 1.2 mm fiber and 2.5 inches for 1.5 mm fiber. MINER$\nu$A plans to use the 1.2 mm fiber, unless it proves impossible due to lower light yield.

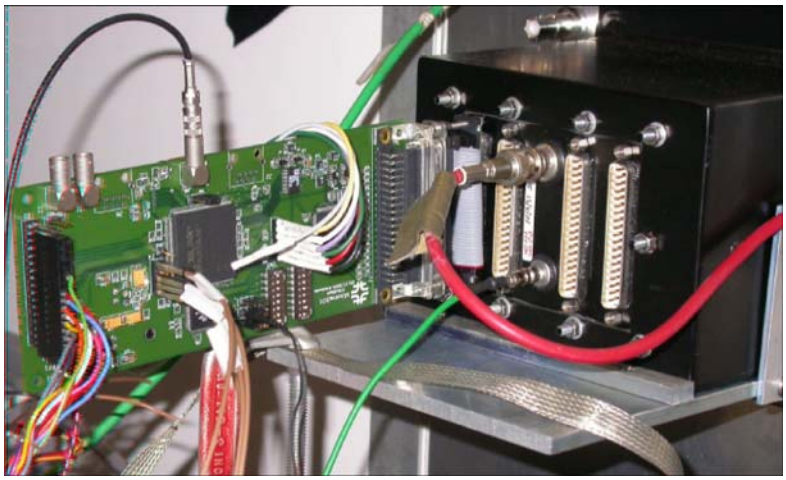

Figure 87: Photo of prototype readout board connected to a MINOS CalDet box.

### 11.5.3 Front-end prototype

A 16-channel FEB prototype, based on the TRiP chip, was designed and tested at FNAL. The essential elements are a TRiP chip (providing discimination, shaping, and an analog pipeline), high- and low-gain 10-bit ADCs, TDCs with 1.5 ns least-count, and an FPGA controller. Readout to the parallel port of a PC can be internally or externally triggered. On the bench, the board achieves the charge and timing resolution necessary for MINER$\nu$A. After commissioning and testing with pulser input, the prototype was used to read a real PMT as part of the vertical slice test (see Figure 87).

### 11.5.4 Vertical-slice test

To test the scintillator, front-end board and readout scheme, a small plane of the triangular bars were constructed at FNAL. Fibers from the bars were attached to a MINOS Near Detector M64 MAPMT housed in a MINOS CalDeT PMT box. Figure 88 shows a schematic of the VST set-up.

**Single photo-electron and noise measurement** The trigger for readout was either generated internally or by a set of scintillator paddles deployed above and below the prototype MINER$\nu$A plane to tag cosmic-ray muons. Tests of both these modes of operation proved successful. Using a blue LED flasher to excite the green fiber we were able to observe the single PE peak using this setup (Figure 89). The noise level, integrating over the nominal 10 $\mu$s NuMI spill time, was $<$2 fC (see Figure 90). This is much less than the measured charge of 30 fC from a single photo-electron using the lowest expected operating HV for the PMTs. Both high- and low-gain ADC channels were tested and functioned as expected.

The TDC channels where tested using the LED flasher by varying the time between the 10 $\mu$sec gate leading edge and the LED excitation pulse. The TDC values for the triggered channels displayed the expected linear response, with a time resolution better than 3 ns.

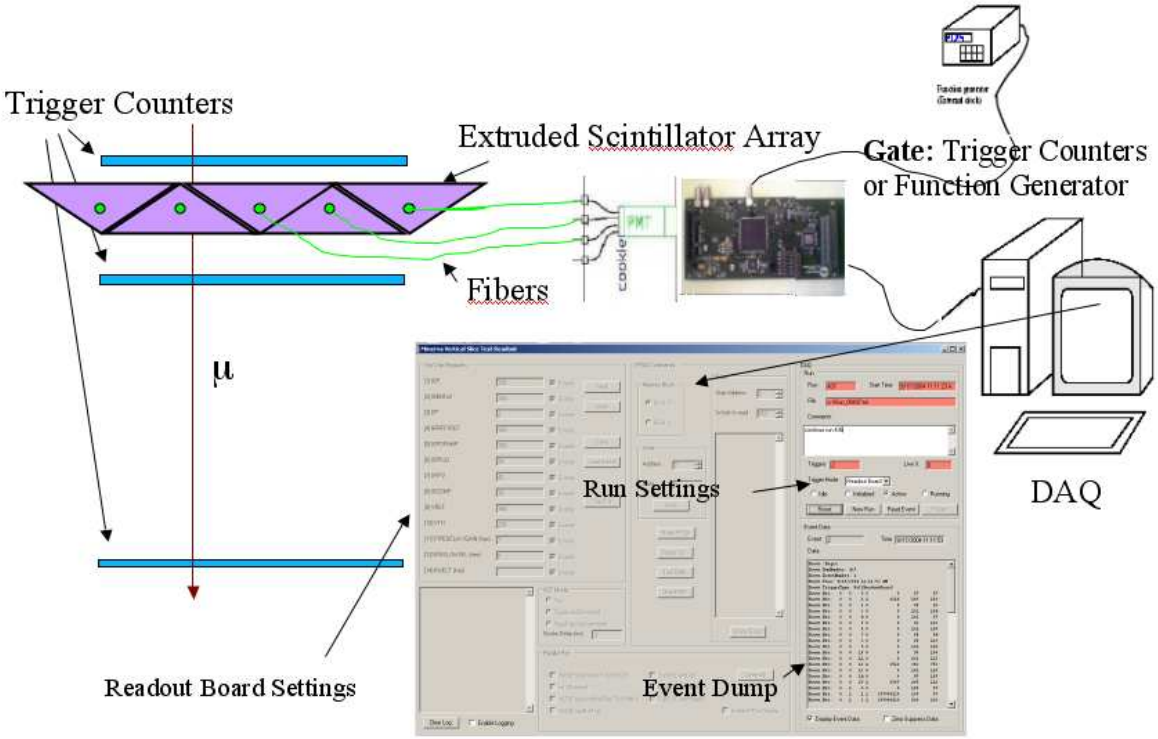


Figure 88: Schematic of vertical slice test set-up.

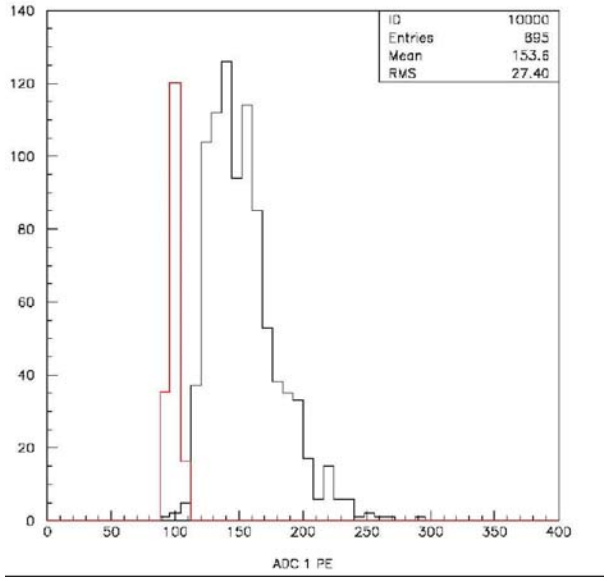


Figure 89: Single PE peak in high-gain ADC counts, measured with an LED pulser at very low occupancy. The pedestal peak in in red.

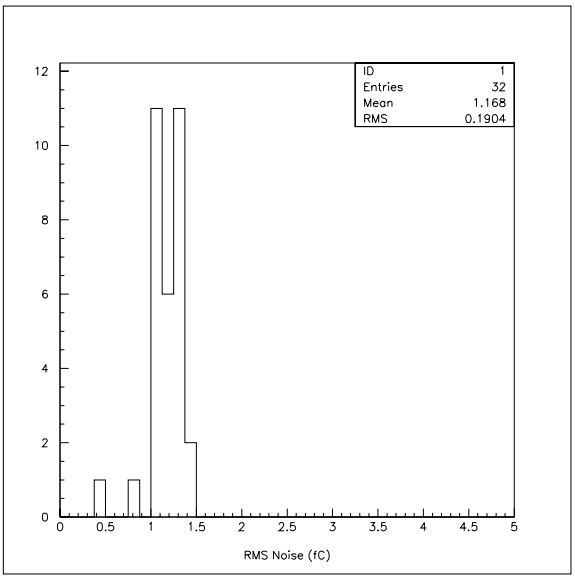


Figure 90: Pedestal RMS distribution for 32 ADC channels.

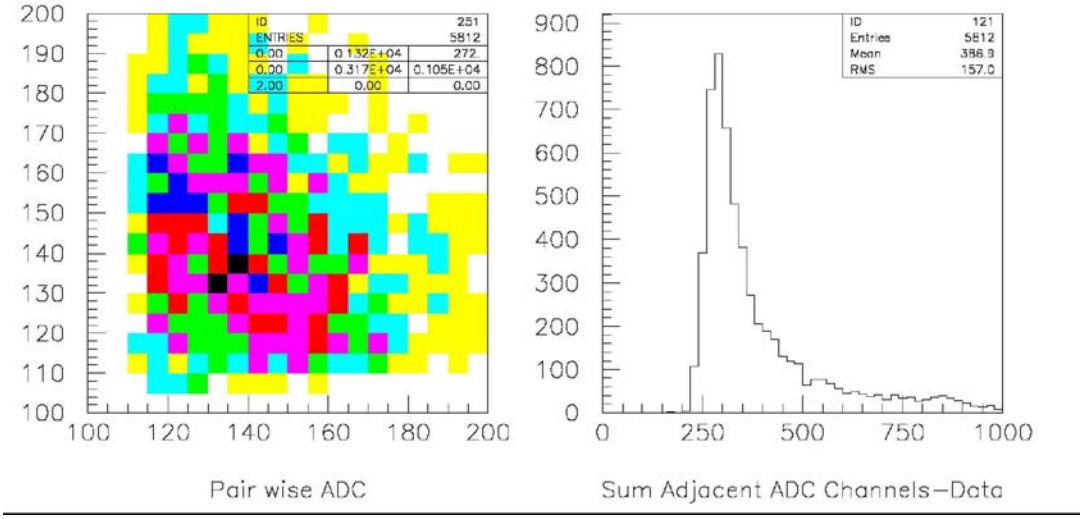


Figure 91: Left: Scatter plot of adjacent ADC counts for cosmic-ray muons. Right: Total light-yield for adjacent strips, using low-gain ADC channels.

**Cosmic-ray muon light-yield** Light yield from a single scintillator layer was measured using external triggers from cosmic ray muons. Vertical muons will excite two triangular scintillator strips in the layer, so anti-correlation between ADC values for adjacent channels is expected, and observed (Figure 91). The sum of adjacent ADC channels displays a clear peak and the expected tail from Landau variation and radiative energy loss. Combining the results of the single-PE and the cosmic ray measurements, the muon light-yield per layer is $\sim 10$ PE/layer for the light output.

For the real detector (after correcting for the different fiber lengths and an additional connector), these measurements imply a yield of $\sim 7.5$ PE/layer for minimum-ionizing particles. Note that VST measurements were performed with no optical coupling between the fibers and bars (air only). Based on MINOS studies, optical coupling should increase the light-yield by about a factor of two [176]. When this difference is accounted for, the measured light-yield agrees with predictions from the MINOS optical simulation (Section 11.3). The next round of measurements, in early 2005, will include optical coupling to confirm this agreement.

# Part III
# Bibliography

## References


[1] Kamiokande Collaboration, S. Hatakeyama *et al.*, Phys. Rev. Lett. **81** (1998) 2016; Soudan-2 Collaboration, W. W. Allison *et al*, Phys. Lett. **B 449** (1999) 137; MACRO Collaboration, Ambrosio *et al*, Phys. Lett. **B434**, 451 (1998)

[2] Y. Fukuda et al., *Phys. Rev. Lett.* **81** (1998) 1158; Erratum **81** (1998) 4279, B.T. Cleveland et al., *Astrophys. J.* **496** (1998) 505. W. Hampel et al. (GALLEX Collaboration), *Phys.Lett.* **B 447** (1999) 127., J.N. Abdurashitov et al. (SAGE Collaboration), *Phys. Rev.* **C 60** (1999) 055801 [astro-ph/9907113]

[3] Q.R. Ahmad *et al.* Phys.Rev.Lett.**89** (2002) 011302 nucl-ex/0204009

[4] Y. Fukuda *et al.*, Phys.Rev.Lett.**81** (1998) 1562 [hep-ex/9807003]; M. Sanchez et al., Phys. Rev. **D 68**, 113004 (2003)

[5] KamLAND Collaboration (K. Eguchi et al.), Phys.Rev.Lett.**90** (2003) 021802 [hep-ex/0212021]

[6] K2K Collaboration (M.H. Ahn et al.), Phys.Rev.Lett.**90** (2003) 41801 [hep-ex/0212007]

[7] B. Pontecorvo and J. Exptl, Theoret. Phys. **34** 247 (1958); Z. Maki, M. Nakagawa and S. Sakata, Prog. Theor. Phys. **28**, 870 (1962).

[8] M. Maltoni *et al*, submitted to New J. Phys, [hep-ph/0405172]

[9] By CHOOZ Collaboration (M. Apollonio et al.), Phys.Lett.**B466** (1999) 415 [hep-ex/9907037]

[10] W. Grimus and L. Lavoura, Phys. Lett. **B572**, 189 (2003); A. Aranda, C.D. Carone, R.F. Lebed, Phys. Rev. **D62**, 016009 (2000).

[11] "A Long Baseline Neutrino Oscillation Experiment at Fermilab", E.Ables *et al*, FERMILAB-PROPOSAL-0875, Feb. 1995, 241pp.

[12] "NOVA: Proposal to build an Off-Axis Detector to Study $\nu_\mu \rightarrow \nu_e$ oscillations in the NuMI Beamline", I. Ambats *et al.*, FERMILAB-PROPOSAL-0929, Mar 2004.

[13] Y. Itow *et al*, "The JHF-Kamioka Neutrino Project", KEK report 2001-4, June 2001. [hep-ex/0106019]

[14] C.H. Llewellyn Smith, Phys. Rep. **3C** (1972).

[15] J. Arrington, nucl-ex/0305009.

[16] M. K. Jones *et al.*, Phys. Rev. Lett **84**, 1398 (2000); O. Gayou *et al.*, Phys. Rev. Lett **88**, 092301 (2002).

[17] H. Budd, A. Bodek and J. Arrington, To be published in *Proceedings of the Second Workshop on Neutrino-Nucleus Interactions in the Few-GeV Region (NUINT02),* Irvine, California (2002), arXiv:hep-ex/0308005.

[18] V. Bernard, L. Elouadrhiri, U.G. Meissner, J. Phys. **G28** (2002).

[19] G. Zeller (private communication).

[20] K. Tsushima, Hungchong Kim, K. Saito, nucl-th[0307013].

[21] T. Kitagaki *et al.*, Phys. Rev. **D26**, 436 (1983) .

[22] S. J. Barish *et al.*, Phys. Rev. **D16**, 3103 (1977).

[23] N. J. Baker *et al.*, Phys. Rev. **D23**, 2499 (1981).

[24] W.A. Mann *et al.*, Phys. Rev. Lett. **31**, 844 (1973).

[25] J. Brunner *et al.*, Z. Phys. **C45**, 551 (1990).

[26] M. Pohl *et al.*, Lett. Nuovo Cimento **26**, 332 (1979)

[27] L.B. Auerbach *et al.*, Phys. Rev. **C66**, 015501 (2002).

[28] S.V. Belikov *et al.*, Z. Phys. **A320**, 625 (1985).

[29] S. Bonetti *et al.*, Nuovo Cimento **38**, 260 (1977)

[30] K.L. Miller *et al.*, Phys. Rev. **D26** (1982) 537.

[31] H. Budd, A. Bodek and J. Arrington, [arXiv:hep-ex/0308005]; A. Bodek, H. Budd and J. Arrington, [arXiv:hep-ex/0309024] (to be published in Proceedings of CIPANP2003, New York City, NY 2003.)

[32] H. Budd, A. Bodek and J. Arrington, To be published in *Proceedings of the Third Workshop on Neutrino-Nucleus Interactions in the Few-GeV Region (NUINT04),* Laboratori Nazionali del Gran Sasso - INFN - Assergi(2004), arXiv:hep-ex/0410055.

[33] D. Casper, Nucl. Phys. Proc. Suppl. **112**, 161 (2002).

[34] R. A. Smith and E. J. Moniz, Nucl. Phys. **B43**, 605 (1972 ) ; E. J. Moniz *et al.*, Phys. Rev. Lett. **26**, 445 (1971); E. J. Moniz, Phys. Rev. **184**, 1154 (1969).

[35] Ghent Theory group in Belgium, Jan Ryckebusch (jan@inwpent5.UGent.be).

[36] G. P. Zeller, (2003), hep-ex/0312061.

[37] B. Z. Kopeliovich and P. Marage, Int. J. Mod. Phys. **A8**, 1513 (1993).

[38] D. Rein and L. M. Sehgal, Nucl. Phys. **B223**, 29 (1983).

[39] A. A. Belkov and B. Z. Kopeliovich, Sov. J. Nucl. Phys. **46**, 499 (1987).

[40] C. A. Piketty and L. Stodolsky, Nucl. Phys. **B15**, 571 (1970).

[41] E. A. Paschos and A. V. Kartavtsev, (2003), hep-ph/0309148.

[42] Super-Kamiokande and K2K, C. Mauger, Nucl. Phys. Proc. Suppl. **112**, 146 (2002).

[43] BooNE, J. L. Raaf, (2004), hep-ex/0408015.

[44] MiniBooNE, J. Monroe, (2004), hep-ex/0408019.

[45] K2K, T. Ishida, Prepared for 1st Workshop on Neutrino - Nucleus Interactions in the Few GeV Region (NuInt01), Tsukuba, Japan, 13-16 Dec 2001.

[46] B. Z. Kopeliovich, (2004), hep-ph/0409079.

[47] H. Faissner *et al.*, Phys. Lett. **B125**, 230 (1983).

[48] E. Isiksal, D. Rein, and J. G. Morfin, Phys. Rev. Lett. **52**, 1096 (1984).

[49] CHARM, F. Bergsma *et al.*, Phys. Lett. **B157**, 469 (1985).

[50] CHARM-II, P. Vilain *et al.*, Phys. Lett. **B313**, 267 (1993).

[51] BEBC WA59, P. P. Allport *et al.*, Z. Phys. **C43**, 523 (1989).

[52] BEBC WA59, P. Marage *et al.*, Z. Phys. **C31**, 191 (1986).

[53] SKAT, H. J. Grabosch *et al.*, Zeit. Phys. **C31**, 203 (1986).

[54] C. Baltay *et al.*, Phys. Rev. Lett. **57**, 2629 (1986).

[55] V. V. Ammosov *et al.*, Yad. Fiz. **45**, 1662 (1987).

[56] E632, S. Willocq *et al.*, Phys. Rev. **D47**, 2661 (1993).

[57] E. Paschos and A. Kartavtsev, Private Communication.

[58] D. Rein and L. M. Sehgal, Annals Phys. **133**, 79 (1981).

[59] D. Drakoulakos *et al.* MINER$\nu$A Collaboration, arXiv:hep-ex/0405002, pgs. 49 - 61, pgs. 201 - 210.

[60] E. A. Paschos, M Sakuda, J. Y. Yu, Phys. Rev. **D69**, 014013 (2004).

[61] G. M. Radecky *et al.*, Phys. Rev. **D25** 1161 (1982).

[62] T. Kitagaki *et al.*, Phys. Rev. **D34** 2554 (1986).

[63] M. Sakuda and E.A. Paschos, Nucl. Phys. B (Proc. Suppl.) **112** 89 (2002); M. Sakuda, http://www.ps.uci.edu/ nuint/slides/Sakuda.pdf

[64] R. Gran, To be published in *Proceedings of the Third Workshop on Neutrino-Nucleus Interactions in the Few-Gev Region (NUINT04),*

[65] N.J. Baker *et al.*, Phys. Rev. D **24**, 2779 (1981).

[66] A. Alavi-Harati *et al.*, Phys. Rev. **87** 132001 (2 001).

[67] P.G. Ratcliffe, Phys. Rev. **D59**, 014038 (1999).

[68] N. Cabibbo *et al.*, Semileptonic Hyperon Decay and CKM U nitarity, [arXiv:hep-ph/0307214] (July 2003).

[69] T. Alexopoulos *et al.* (KTeV Collaboration), Phys. Rev. Lett. **93**, 181802 (2004).

[70] T. Nakano *et al.*, [arXiv:hep-ex/0301020]; V.V. Barmin
em et al., [arXiv:hep-ex0304040]; S. Stepanyan [arXiv:hep-ex/0307018].

[71] R. Jaffe and F. Wilczek, Di-quarks and Exotic Spectroscopy, [ar Xiv:hep-ph/0307341] (July 2003).

[72] D. Drakoulakos *et al.* [Minerva Collaboration], fine-grained detector in the NuMI beam," arXiv:hep-ex/0405002. Pgs. 99 - 108, 192 - 200.

[73] B.Z. Kopeliovich, hep-ph/0409079.

[74] M.K. Jones *et al.*, Phys. Rev. **C48**, 2800 (1993); R.D. Ransome *et al.*, Phys. Rev. **C46**, 273 (1992); R.D. Ransome *et al.*, Phys. Rev. **C45**, R509 (1992).

[75] D. Rowntree *et al.*, Phys. Rev. **C60**, 054610 (1999); B. Kotlinksi *et al.*, Eur. Phys. J. **A9**, 537 (2000).

[76] E. A. Paschos, M. Sakuda, I. Schienbein and J. Y. Yu, arXiv:hep-ph/0408185.

[77] M. Arneodo, Phys. Rept. **240**, 301 (1994).

[78] G. Piller and W. Weise, Phys. Rept. **330**, 1 (2000).

[79] B. L. Ioffe, V. A. Khoze, and L. N. Lipatov, *Hard processes: Phenomenology, Quark-Parton Model* (Elsevier Science Publishers, North Holland, 1984).

[80] G.B. West, Ann. Phys. **74** (1972) 464.

[81] S. V. Akulinichev, S. A. Kulagin, and G. M. Vagradov, Phys. Lett. B **158**, 485 (1985); S. V. Akulinichev, S. Shlomo, S. A. Kulagin, and G. M. Vagradov, Phys. Rev. Lett. **55**, 2239 (1985).

[82] S. A. Kulagin, Nucl. Phys. A **500**, 653 (1989).

[83] C. Ciofi degli Atti and S. Liuti, Phys. Rev. C **41**, 1100 (1990).

[84] F. Gross and S. Liuti, Phys. Rev. C **45**, 1374 (1992).

[85] S. A. Kulagin, G. Piller and W. Weise, Phys. Rev. C **50**, 1154 (1994).

[86] S. A. Kulagin, W. Melnitchouk, G. Piller, and W. Weise, Phys. Rev. C **52**, 932 (1995).

[87] S. A. Kulagin, Nucl. Phys. A **A 640**, 435 (1998).

[88] W. Melnitchouk, A. W. Schreiber and A. W. Thomas, Phys. Rev. D **49**, 1183 (1994).

[89] J. Gomez, *et al.,* Phys. Rev. D **49**, 4348 (1994).

[90] S. I. Alekhin, S. A. Kulagin and S. Liuti, Phys Rev. D **69**, 114009 (2004).

[91] S. A. Kulagin and R. Petti, paper in preparation.

[92] T. H. Bauer, R. D. Spital, D. R. Yennie and F. M. Pipkin, Rev. Mod. Phys. **50**, 261 (1978) [Erratum-ibid. **51**, 407 (1979)].

[93] C. A. Pickety, and L. Stodolsky, Nucl. Phys. B **15**, 571 (1970).

[94] S. L. Adler, Phys. Rev. **135**, B963 (1964).

[95] R. J. Glauber, Phys. Rev. **100**, 242 (1955).

[96] V. N. Gribov, Sov. Phys. JETP **29**, 483 (1970) [Zh. Eksp. Teor. Fiz. **56**, 892 (1969)] ; Sov. Phys. JETP **30**, 709 (1970) [Zh. Eksp. Teor. Fiz. **57**, 1306 (1969) ].

[97] B. Z. Kopeliovich, and P. Marage, Int. J. Mod. Phys. A **8**, 1513 (1993).

[98] S. A. Kulagin, arXiv:hep-ph/9812532.

[99] E. A. Paschos and L. Wolfenstein, Phys. Rev. D **7**, 91 (1973).

[100] G. P. Zeller *et al.* [NuTeV Collaboration], Phys. Rev. Lett. **88**, 091802 (2002) [Erratum-ibid. **90**, 239902 (2003)] [arXiv:hep-ex/0110059].

[101] S. A. Kulagin, Phys. Rev. D **67**, 091301 (2003) [arXiv:hep-ph/0301045].

[102] S. A. Kulagin, arXiv:hep-ph/0406220.

[103] S. A. Kulagin, arXiv:hep-ph/0409057.

[104] R. Merenyi *et al.*, Phys. Rev. D **45**, 743 (1992), W. A. Mann *et a l.*, unpublished.

[105] C.H.Q. Ingram, Nucl. Phys. A **684**, 122 (2001).

[106] M. K. Jones *et al.*, Phys. Rev. C **48**, 2800 (1993).

[107] M. Nakahata *et al*, Nucl. Instrum. Meth. **A421**, 113 (1999); E. Blaufuss *et al*, Nucl. Instrum. Meth. **A458** 638 (2001).

[108] M. Diwan and J. Nelson, NuMI-NOTE-STEEL-0639 (2000)

[109] PhD Thesis of C. Smith, University College London, London, 2002 *Calibration of the MINOS Detectors and Extraction of Neutrino Oscillation Parameters*; PhD Thesis of R. Nichol, University College London, London, 2003 *Calibration of the MINOS Detectors*

[110] PhD thesis of M. A. Kordosky, University of Texas at Austin, August 2004 *Hadronic Interactions in the MINOS Detectors*

[111] PhD thesis of P. L. Vahle, University of Texas at Austin, August 2004 *Electromagnetic Interactions in the MINOS Detectors*

[112] E. A. Paschos, L. Pasquali and J. Y. Yu, Nucl. Phys. B **588**, 263 (2000) and E. A. Paschos, J. Y. Yu and M. Sakuda [arXiv:hep-ph/0308130].

[113] D. Ashery *et al.*, Phys. Rev. **C23**, 2173 (1981).

[114] H. Gallagher, Nucl. Phys. Proc. Suppl. **112**, 188 (2002)

[115] NuMI Fluxes courtesy of Mark Messier

[116] The simulation assumed the active material was resistive plate chambers and the absorber was particle board (hydrocarbons).

[117] G.P.Zeller, submitted to proceedings of 2nd International Workshop on Neutrino - Nucleus Interactions in the Few GeV Region (NUINT 02), Irvine, California, 12-15 Dec 2002 [hep-ex/0312061]

[118] W. Melnitchouk, R. Ent, C.E. Keppel, accepted by Physics Reports.

[119] Sabine Jeschonnek and J.W. Van Orden, Phys. Rev. D **69**, 054006 (2004).

[120] F. E. Close and Nathan Isgur, Phys. Lett. B **509**, 81-86 (2001).

[121] R. Ent, C. E. Keppel, I. Niculescu, PRD **62**, 073008 (2000).

[122] I. Niculescu *et al.*, Phys. Rev. Lett. **85**, 1182-1185 (2000).

[123] C.E. Carlson and N.C. Mukhopadhyay, Phys. Rev. D **47**, 1737 (1993).

[124] F.E. Close and F.J. Gilman, Phys. Rev. D **7**, 2258 (1973).

[125] T. Abdullah and F.E. Close, Phys. Rev. D **5**, 2332 (1972).

[126] M. Diemoz, F. Ferroni, and E. Longo, Phys. Rev. **130**, 293 (1986).

[127] R. Belusevic and D. Rein, Phys. Rev. D **38**, 2753 (1988); Phys. Rev. D **46**, 3747 (1992).

[128] J. Arrington, R. Ent, C.E. Keppel, J. Mammei, and I. Niculescu, nucl-ex/0307012, submitted to Phys. Rev. Lett.

[129] SPIN0 ref

[130] G. R. Farrar and D. R. Jackson, Phys. Rev. Lett. **35**, 1416 (1975).

[131] KUHL ref

[132] U.K. Yang and A. Bodek, Phys. Rev. Lett. **82**, 2467 (1999).

[133] Lai:1994bb ref

[134] A. Bodek and U.K. Yang, Nucl. Phys. B (Proc. Suppl.) 112 70 (2002); Eur. Phys. J. **13**, 241 (2000).

[135] Gargamelletwist ref

[136] Varvell:1987qu

[137] J.C. Webb *et al.* [FNAL E866/NuSea Collaboration], hep-ex/0302019.

[138] See http://www.phys.psu.edu/∼cteq/ for a summary of CTEQ work; H. L. Lai *et al.* [CTEQ Collaboration], Phys. Rev. D **51**, 4763 (1995); H. L. Lai *et al.*, Eur. Phys. J. **12**, 375 (2000).

[139] V. A. Radescu *et al.* [NuTeV Collaboration].

[140] Jefferson Lab Experiment E03-012, approved.

[141] F.E. Close and W. Melnitchouk, Phys. Rev. C **68**, 035210 (2003); hep-ph/0302013.

[142] F.E. Close, F.J. Gilman, and I. Karliner, Phys. Rev. D **6**, 2533 (1972).

[143] F.E. Close and F.J. Gilman, Phys. Lett. B **38**, 541 (1972).

[144] X. Ji, Phys. Rev. Lett. **78**, 610 (1997).

[145] X. Ji, Phys. Rev. **D55**, 7114 (1997).

[146] A. V. Radyushkin, Phys. Lett. **B380**, 417 (1996).

[147] A. V. Radyushkin, Phys. Lett. **B385**, 333 (1996).

[148] J.C. Collins, L. Frankfurt, and M. Strikman, Phys. Rev. **D56**, 2982 (1997).

[149] A. V. Radyushkin, Nucl. Phys. **A711**, 99 (2002).

[150] M. Vanderhaeghen, Nucl. Phys. **A711**, 109 (2002).

[151] M. Diehl, hep-ph/0307382 (2003).

[152] MINOS Collaboration, "MINOS Technical Design Report", NuMI-NOTE-GEN-0337 (1998).

[153] N. V. Mokhov, "The MARS Monte Carlo", FERMILAB FN-628 (1995); N. V. Mokhov and O. E. Krivosheev, "MARS Code Status", FERMILAB-Conf-00/181 (2000); http://www-ap.fnal.gov/MARS/.

[154] N. Mokhov and A. Van Ginneken, J. Nucl. Sci. Tech. **S1**, 172 (2000).

[155] M. Messier (private communication)

[156] Y. Hayato, To be published in *Proceedings of the Second Workshop on Neutrino-Nucleus Interactions in the Few-GeV Region (NUINT02),* Irvine, California (2002).

[157] G. Ambrosini *et al.* [NA56/SPY Collaboration], Eur. Phys. J. C **10**, 605 (1999).

[158] P-907: Proposal to Measure Particle Production in the Meson Area Using Main Injector Primary and Secondary Beams, May 2000

(http://ppd.fnal.gov/experiments/e907/Proposal/E907_Propsal.html)

[159] NuMI Technical Design Handbook

(http://www-numi.fnal.gov/numiwork/tdh/tdh_index.html)

[160] K. Kodama *et al.*, Nucl. Phys. Proc. Suppl **98**, 43-47 (2001)

[161] E. Gallas & J. Li., "Polishing Optical Fibers for the D0 ICD in Run II", FNAL-TM-2062, 1998.

[162] P. de. Barbaro, et. al., "Quality Control Studies of Scintillating Tile/Fiber Megatile Productin for the CDF End Plug Upgrade Hadron Calorimeter", UR-1371/ER40685-821, CDF Note 2778.

[163] N. Pearson (Minnesota), private communication.

[164] D. Michael (CalTech) and T. Chase (Minnesota), private communication.

[165] K. Ruddick (Minnesota), private communication.

[166] J. Grudzinski (Argonne), private communication.

[167] N. Tagg, et al., "Performance of Hamamatsu 64-anode photomultipliers for use with wavelength–shifting optical fibres," NuMI-PUB-SCINT 1040, [physics/0408055].

[168] The MINER$\nu$A Collaboration, "*Proposal to perform a high-statistics neutrino scattering experiment using a fine-grained detector in the NuMI beam*", Fermilab Proposal P-938, e-print hep-ex/0405002; see Sect. 16.5.2.

[169] "MCM II and the Trip Chip", J. Estrada, C. Garcia, B. Hoeneisen and P. Rubinov, August 2002, FERMILAB-TM-2226.

[170] J.K. Nelson, "The MINOS Magnets", DPF2000, NuMI-703, August 2000.

[171] J.K. Nelson, J. Kilmer, "Overview of the design of the MINOS Near detector Coil," NuMI-L-523, August 1999;
J. Kilmer, R.W. Fast, R. Currier, and R. Stanek, "Specifications for Aluminum Conductor," NuMI-L-411, September 1998;
A. Lee, private communication.

[172] O. Benhar, [arXiv:nucl-th/0307061].

[173] L. Mualem (private communication).

[174] MINOS Collaboration, P. Adamson *et al.*, IEEE Trans. Nucl. Sci. **49**, 861 (2002).

[175] R. Fruhwirth, Nucl. Inst. Meth. **A262**, 444 (1987).

[176] "Studies of Extruded Plastic Scintillator for MINOS", Karol Lang and Todd Soesby, NuMI-NOTE-L-250, Feb 1997.